




2019

Optimum Design of Axial Flux PM Machines based on Electromagnetic 3D FEA

Narges Taran

University of Kentucky, narges.taran@uky.edu

Author ORCID Identifier:

 <https://orcid.org/0000-0002-1677-9229>

Digital Object Identifier: <https://doi.org/10.13023/etd.2019.429>

[Right click to open a feedback form in a new tab to let us know how this document benefits you.](#)

Recommended Citation

Taran, Narges, "Optimum Design of Axial Flux PM Machines based on Electromagnetic 3D FEA" (2019).
Theses and Dissertations--Electrical and Computer Engineering. 145.
https://uknowledge.uky.edu/ece_etds/145

This Doctoral Dissertation is brought to you for free and open access by the Electrical and Computer Engineering at UKnowledge. It has been accepted for inclusion in Theses and Dissertations--Electrical and Computer Engineering by an authorized administrator of UKnowledge. For more information, please contact UKnowledge@lsv.uky.edu.

STUDENT AGREEMENT:

I represent that my thesis or dissertation and abstract are my original work. Proper attribution has been given to all outside sources. I understand that I am solely responsible for obtaining any needed copyright permissions. I have obtained needed written permission statement(s) from the owner(s) of each third-party copyrighted matter to be included in my work, allowing electronic distribution (if such use is not permitted by the fair use doctrine) which will be submitted to UKnowledge as Additional File.

I hereby grant to The University of Kentucky and its agents the irrevocable, non-exclusive, and royalty-free license to archive and make accessible my work in whole or in part in all forms of media, now or hereafter known. I agree that the document mentioned above may be made available immediately for worldwide access unless an embargo applies.

I retain all other ownership rights to the copyright of my work. I also retain the right to use in future works (such as articles or books) all or part of my work. I understand that I am free to register the copyright to my work.

REVIEW, APPROVAL AND ACCEPTANCE

The document mentioned above has been reviewed and accepted by the student's advisor, on behalf of the advisory committee, and by the Director of Graduate Studies (DGS), on behalf of the program; we verify that this is the final, approved version of the student's thesis including all changes required by the advisory committee. The undersigned agree to abide by the statements above.

Narges Taran, Student

Dr. Dan M. Ionel, Major Professor

Dr. Aaron Cramer, Director of Graduate Studies

Optimum Design of Axial Flux PM Machines based on Electromagnetic 3D FEA

DISSERTATION

A dissertation submitted in partial fulfillment of the requirements for the
degree of Doctor of Philosophy in the College of Engineering at the
University of Kentucky

By

Narges Taran

Lexington, Kentucky

Director: Dr. Dan M. Ionel, Professor and L. Stanley Pigman Chair in Power
Lexington, Kentucky 2019

Copyright© Narges Taran 2019

ABSTRACT OF DISSERTATION

OPTIMUM DESIGN OF AXIAL FLUX PM MACHINES BASED ON ELECTROMAGNETIC 3D FEA

Axial flux permanent magnet (AFPM) machines have recently attracted significant attention due to several reasons, such as their specific form factor, potentially higher torque density and lower losses, feasibility of increasing the number of poles, and facilitating innovative machine structures for emerging applications. One such machine design, which has promising, high efficiency particularly at higher speeds, is of the coreless AFPM type and has been studied in the dissertation together with more conventional AFPM topologies that employ a ferromagnetic core.

A challenge in designing coreless AFPM machines is estimating the eddy current losses. This work proposes a new hybrid analytical and numerical finite element (FE) based method for calculating ac eddy current losses in windings and demonstrates its applicability for axial flux electric machines. The method takes into account 3D field effects in order to achieve accurate results and yet greatly reduce computational efforts. It is also shown that hybrid methods based on 2D FE models, which require semi-empirical correction factors, may over-estimate the eddy current losses. The new 3D FE-based method is advantageous as it employs minimum simplifications and considers the end turns in the eddy current path, the magnetic flux density variation along the effective length of coils, and the field fringing and leakage, which ultimately increases the accuracy of simulations.

After exemplifying the practice and benefits of employing a combined design of experiments and response surface methodology for the comparative design of coreless and conventional AFPM machines with cores, an innovative approach is proposed for integrated design, prototyping, and testing efforts. It is shown that extensive sensitivity analysis can be utilized to systematically study the manufacturing tolerances and identify whether the causes for out of specification performance are detectable.

The electromagnetic flux path in AFPM machines is substantially 3D and cannot be satisfactorily analyzed through simplified 2D simulations, requiring laborious 3D

models for performance prediction. The use of computationally expensive 3D models becomes even more challenging for optimal design studies, in which case, thousands of candidate design evaluations are required, making the conventional approaches impractical. In this dissertation a new two-level surrogate assisted differential evolution multi-objective optimization algorithm (SAMODE) is developed in order to optimally and accurately design the electric machine with a minimum number of expensive 3D design evaluations.

The developed surrogate assisted optimization algorithm is used to comparatively and systematically design several AFPM machines. The studies include exploring the effects of pole count on the machine performance and cost limits, and the systematic comparison of optimally designed single-sided and double-sided AFPM machines. For the case studies, the new optimization algorithm reduced the required number of FEA design evaluations from thousands to less than two hundred.

The new methods, developed and presented in the dissertation, maybe directly applicable or extended to a wide class of electrical machines and in particular to those of the PM-excited synchronous type. The benefits of the new eddy current loss calculation and of the optimization method are mostly relevant and significant for electrical machines with a rather complicated magnetic flux path, such is the case of axial flux and of transvers flux topologies, which are a main subject of current research in the field worldwide.

KEYWORDS: Axial flux permanent magnet, electric machines, eddy current losses, optimization, 3D finite element analysis, kriging meta-model.

Author's signature: Narges Taran

Date: November 20, 2019

Optimum Design of Axial Flux PM Machines based on Electromagnetic 3D FEA

By
Narges Taran

Director of Thesis: Dr. Dan M. Ionel

Director of Graduate Studies: Dr. Aaron Cramer

Date: November 20, 2019

To Mohsen

ACKNOWLEDGEMENTS

First and foremost, I would like to thank my advisor, Professor Dan M. Ionel, who has been a constant source of knowledge, encouragement, and inspiration from the day I joined the SPARK Laboratory and the ECE Department at the University of Kentucky, and whose untiring support has enabled and shaped this dissertation in more ways than I can count. Under his caring tutelage, I learned how to work hard, individually, and as part of a team, productively accomplish goals, and pursue highest intellectual ambitions. I am deeply indebted to him not only for directing my PhD studies with dedication and foresight but also for always believing in me and my potential for success. I am grateful for all his teachings on technical and professional matters alike. Whether I needed his technical insights, mentoring on designing electric machines, or advice for future career, the door of his office was always open. I am thankful to him for enriching my PhD studies beyond what I would have thought possible only a few years ago.

I am very grateful to Dr. Vandana Rallabandi, a singularly knowledgeable mentor with whom I was lucky enough to work during her postdoctoral fellowship at the SPARK laboratory. I am proud to count her a close friend. I would also like to thank all my colleagues in the SPARK Laboratory for their support and friendship.

The support of the National Science Foundation through Grant # 1809876 in the last period of my research is gratefully acknowledged. My great appreciation is also due for the support over the years of University of Kentucky, the L. Stanley Pigman endowment, Regal Beloit Corp., and ANSYS, Inc.

At Regal Beloit Corp., special thanks are due to Professor Dean Patterson for his constant support and illuminating answers to my many questions, to Dr. Greg Heins for his guidance, including expert practical design, prototyping and testing, and to

Dr. Mark Thiele for sharing his industrial expertise whenever I needed it. At ANSYS, Dr. Ping Zhou and Mr. Mark Solveson provided expert advice and technical insights for which I am very grateful. At UK, I am especially thankful for the support of my Ph.D. Committee members Professors Aaron Cramer, Caicheng Lu, Joseph Sottile, and Mirosław Truszczyński.

I would like to thank my parents, who taught me to be purposeful, courageous, and confident. They have selflessly put aside their own dreams to watch me live out mine and for that, and much more, I am grateful beyond words.

My most special gratitude goes to my husband, Mohsen Jabbari, for accompanying me through my PhD years with his calming presence, generosity, and love.

Narges Taran

November, 2019

Contents

ACKNOWLEDGEMENTS	iii
List of Tables	x
List of Figures	xxii
1 Introduction	1
1.1 Background	1
1.2 Literature Review	5
1.3 Research Objectives and Original Contributions	11
1.4 Dissertation Outline	15
1.5 Publications	16
2 A New Hybrid Method for Three-Dimensional Calculation of Wind- ing Eddy Current Losses	19
2.1 Introduction	20
2.2 Eddy Loss Calculation Methods	22
2.2.1 Analytical Method	22
2.2.2 Numerical Methods	23
2.2.3 Hybrid Method using 2D Numerical Models	25
2.2.4 Proposed Hybrid Method using 3D Numerical Models	29
2.3 Case Studies	34
2.3.1 Air Cored Axial Flux PM Machine	34
2.3.2 Open Slot Stator Core Axial Flux PM Machine	38
2.4 Results and Discussion	42

2.5	Experimental Study	46
2.6	Summary	47
3	Design of Experiments and Response Surface Methodology in Electric Machine Design	50
3.1	Introduction	51
3.2	Coreless and Conventional AFPM Motors for Solar Cars	52
3.2.1	Solar Car Electric Motor Specifications	53
3.2.2	Winding Factor Calculation for Air-gap Concentrated winding	56
3.2.3	Specifications and Design Considerations of the Coreless AFPM Motor	63
3.2.4	Factors and Responses for DOE and RSM	67
3.2.5	Selection of Best Designs	69
3.2.6	Comparison and Experimental Validation	73
3.2.7	Speed Range Extension of Coreless Machines	78
3.3	A Systematic Study on the Effects of Dimensional and Materials Tolerances	83
3.3.1	IEEE 1812 Testing Guide: Open-Circuit and Short-Circuit Tests	85
3.3.2	Case Study for Dimensional and Material Tolerances	86
3.3.3	Design of Experiments (DOE) and Virtual Tests	89
3.3.4	Discussion	94
3.4	Summary	98
4	A New Two-level Surrogate Assisted Multi Objective Differential Evolution Optimization Algorithm	101
4.1	Introduction	102
4.2	Kriging Surrogate Modeling	104
4.3	Novel Optimization Algorithm	105
4.3.1	Initial sample pool	107
4.3.2	Initial generation for each iteration of interior loop	108
4.3.3	Interior level	108

4.3.4	3D FEA of promising designs	108
4.3.5	Stopping criterion:	108
4.4	Algorithm Implementation, Validation and Design Examples	109
4.5	Comparing Optimization Results	113
4.6	Reference Design and Search Space Specification	114
4.6.1	Broad search space specification	116
4.6.2	Iterative search space specification	116
4.6.3	Biased search space specification	116
4.6.4	Example Study and the Biased Search Space Definition	117
4.6.5	Comparing the Result of Different Search Space Assignment Methods	119
4.7	Summary	123
5	Optimization Case Studies	125
5.1	Introduction	125
5.2	Systematic Exploration of the Effects of Pole Count on Optimum De- sign of Ultra-high Efficiency Fractional hp Axial Flux PM Machines .	126
5.2.1	Problem Formulation for Analysis and Optimization	126
5.2.2	Optimization Results and Discussion	133
5.2.3	Optimal Design Selection	135
5.2.4	Identification of Trends	138
5.2.5	Characteristics of Optimum Designs	142
5.2.6	Prototyping and Experimental Validation	145
5.3	Systematic Optimization and Comparison of Single-sided and Double- sided AFPM Machines	147
5.3.1	Analytical Evaluation	149
5.3.2	Sensitivity Analysis	154
5.3.3	Overload Capability	157
5.3.4	Design Topologies and Optimization Setup	158
5.3.5	Pareto front designs	161
5.3.6	Mass components breakdown	164

5.3.7	Loss components breakdown	165
5.3.8	Efficiency Maps	168
5.4	Summary	169
6	Conclusions	174
6.1	Summary and Conclusions	174
6.2	Original Contributions	179
6.3	Recommendations for Future Work	182
	References	185
	Vita	204

List of Tables

2.1	ADDITIONAL AC COPPER LOSSES IN THE WINDINGS DUE TO EDDY CURRENTS, CALCULATED WITH DIFFERENT FEA AND HYBRID METHODS FOR OPEN-CIRCUIT AND FULL LOAD OPERATING CONDITIONS.	46
3.1	Specifications and main dimensional properties of the NGM SC-150 (conventional) AFPM motor.	57
3.2	Torque density and fundamental winding factor for 16 pole 12 coil topology with different number of stator disks.	64
3.3	All the designed machines produce 28 Nm at 400 rpm.	66
3.4	Geometrical input variables for the parametric model of the conventional (cored) machine.	69
3.5	Geometrical input variables for the parametric model of the coreless machine.	69
3.6	Reference model and selected designs for the conventional motor, at 400 rpm, for application with one driving wheel. Estimations are done suing regression models and 2D and 3D FEA.	71
3.7	FEA results of the selected designs for the coreless motor for application with two driving wheels, at the rated speed of 400 rpm. All designs have mechanical air-gap of 1.85 mm.	71
3.8	Main specifications of the reference machines considered for the experimental validation of the 3D FEA study.	78
3.9	Geometrical variables (fig. 3.26). A tolerance of ± 0.1 mm for geometrical variables has been considered.	88

3.10	SmCo rare-earth magnets and ceramic ferrites with a nominal remanence of 1.1 T and 0.4 T, respectively, have been studied together with the possible inadvertent substitution of the lamination grade.	88
3.11	Theoretical Maximum Variations for the Open-circuit Voltage (Back EMF) and Core Losses.	93
4.1	The RMS estimation error of predictions made by 3 surrogate models, for magnet eddy losses of an example AFPM machine.	105
4.2	The results of the optimization algorithm presented in Fig. 4.1 for the test function (DTLZ2) with different number of objectives and variables. The results are the average of 5 runs for each scenario.	109
4.3	Optimization variables of the conventional machine.	110
4.4	Optimization variables of the coreless machine.	110
4.5	The optimization variables and their assigned limits.	118
4.6	The number of 3D FEA design evaluations by the surrogate assisted optimization.	120
5.1	Independent optimization variables and corresponding limits, exemplified for the configuration with 40 poles.	131
5.2	Number of generations, FE models, and kriging surrogate models for each optimization study.	135
5.3	The per-unit value of representative optimum designs for different pole counts. The total mass, cost, and loss of the selected 20 pole design represent the base.	139
5.4	Minimum flux density within Neodymium magnets of the optimum designs selected on the knee of the Pareto front.	141
5.5	The experimental and calculated results for the ultra high efficiency axial flux SPM machine rated at 0.75 hp. The calculated value of the efficiency uses 3D FEA results and a 6 W mechanical loss component.	147
5.6	Independent optimization variables and their corresponding limits.	160

List of Figures

1.1	Schematic general radial and axial flux PM machines: (a) exploded view and (b) assembled view of a model radial flux machine, (c) exploded view and (d) assembled view of a model axial flux machine.	3
1.2	Example manufactured PM machines: (a) typical steps for manufacturing, exemplified for a radial flux line-fed PM motor [1], (b) exploded view of a general-purpose radial flux induction motor [1], and (c) and example 1 hp axial flux PM machine [2].	4
1.3	Varieties of double sided AFPM machines: (a) single-rotor double-stator, (b) single-stator double rotor, and (c) single-stator double-rotor.	7
1.4	(a) The NN- or SS-type AFPM machine configuration. The stator yoke is necessary to provide the magnetic flux path. (b) The NS-type AFPM machine where the stator yoke in the middle can be eliminated.	7
1.5	(a) Two machine topologies can be considered in order to utilize the advantages enabled by WBG devices: coreless machine for higher speed and MAGNUS machine for lower speed applications. (b) Examples of axial flux machines, power electronics and controls illustrating the best practices of employing WBG devices for motor drives.	14
2.1	Illustration of wires with circular and rectangular cross section.	23
2.2	The geometries employed for the FE models of the case study open slot AFPM machine. (a) Simplified 3D model, (b) 3D model with turn-by-turn representation, (c) simplified 2D model, and (d) 2D model with detailed turn-by-turn representation of the wire conductors.	25

2.3	Typical eddy current path considered in 2D analysis has a go and return path along the conductor and does not include end coil sections.	26
2.4	The magnetic flux density in the conductors of a concentrated precise wound coil placed in the slots of the case study open slot AFPM machine calculated with 2D (a) and 3D (b) FEA and illustrating the multi-dimensional variation of the field.	27
2.5	(a) Schematic of a coil side placed around the tooth displaying conductor identification numbers. (b) The flux density in each conductor, obtained by space sampling 2D and 3D FEA results, respectively. The 2D FEA typically results in an over estimation, especially for the conductors at the top slot and closest to the tooth.	28
2.6	The magnetic flux density in the conductors of an example AFPM coreless machine calculated with 3D FEA. For such machines, the winding is directly exposed to the airgap field, the magnitude and multi-dimensional variation of which can be substantial, resulting in significant eddy current losses.	29
2.7	(a) The flux density sampling planes employed by the new hybrid 3 FEA method stacked in the direction of the main current flow. (b) Three-dimensional sampling is performed also in order to take end effects into account. The axial cross section schematic depicts the coil span and the in inner and outer diameter as used in (2.5).	31
2.8	Eddy current paths with different length along the coil side.	34
2.9	The 3D model of the coreless machine under study. Each turn is separately modeled and meshed.	36
2.10	A zoomed view of the tetrahedral meshes in the conductors of the coreless machine.	36
2.11	The general 2D model for sampling flux density values employed in the hybrid method. The coil cross section marked with dashed box is zoomed in to show the location of four sampling points in the center of round conductors.	37

2.12	The flux density in the sampling points shown in Fig. 2.11 at different time steps.	37
2.13	(a) Flux density obtained from the 3D FEA model of the coreless machine case study, illustrating the lower values closer to the end turns. (b) The current density distribution.	38
2.14	The 2D FEA model of the coreless machine under study: (a) flux density distribution and (b) current density distribution in conductors at open-circuit operation.	38
2.15	The 3D FEA model of the AFPM machine under study with open slot stator core.	39
2.16	The 2D FEA model of the optimally designed AFPM machine with open slot stator core in which the circular conductors are utilized and placed further away from the slot opening: (a) flux density distribution and (b) current density distribution in conductors at open-circuit operation.	39
2.17	The open slot bound coils with (a) 29 turns, (b) 23 turns, and (c) 14 turns.	40
2.18	The winding dc and additional open-circuit eddy current ac losses with different number of turns at rated load.	40
2.19	The 2D FEA model of the AFPM machine with open slot stator core, employing square conductors: (a) flux density distribution and (b) current density distribution in conductors at open-circuit operation. Note the reduction in flux density and current density compared to circular conductors in Fig. 2.16.	41
2.20	The additional eddy current copper losses at open circuit calculated with FEA for cases with circular and square conductors. The overall conductor area in both cases is maintained the same.	42
2.21	The mesh for the coil in the case study of the open slot AFPM machine. The turns closer to the slot opening are meshed finer.	42

2.22	(a) The flux density observed by the conductors. The reduced flux density at the ends is due to the fringing and leakage. (b) The current density distribution.	43
2.23	The 3D mesh plot for the turn-by-turn model of the AFPD machine with open slots.	44
2.24	The 3D model of the prototype machine. The mesh can be fine for (a) all conductors or (b) only for the top conductors that cause the majority of open-circuit eddy current losses.	47
2.25	The prototype machine with spacers.	48
2.26	The prototype machine without spacers.	48
2.27	The measurements of ac copper loss and validation of 3D FEA calculations.	49
3.1	Gato del Sol IV solar car from University of Kentucky.	54
3.2	The 36 slot stator of the NGM SC-M150 motor installed in Gato del Sol IV solar car together with its 12 pole rotor.	54
3.3	Exploded view of the 3D model of the NGM SC-M150 motor with 36 stator slots and 12 rotor poles.	54
3.4	The 3D model and electromagnetic field for (a) the conventional, and (b) the coreless machines considered.	56
3.5	Schematic of a coreless stator and rotor employing a plastic composite structure for mounting and supporting magnets and coils.	56
3.6	Radial cut-out of a concentrated coil.	59
3.7	Coil pitch angle variation with diameter. The magnets are included in the plot and are transparent.	59
3.8	Analytical and numerical calculation of axial component of flux density at different axial positions for a coreless AFPD machine.	61

3.9	(a) Pitch factor, and (b) distribution factor in circumferential direction with respect to coil width to pole pitch ratio; and (c) distribution factor with respect to coil height to pole pitch ratio, plotted at different harmonics for a 16 pole 12 coil topology with concentrated coreless winding.	62
3.10	Fundamental winding factor for the 12 coil 16 pole topology.	63
3.11	Flux lines of multi-disk AFPM machines with different number of disks.	63
3.12	Dimensional variables selected as factors for DOE of (a) conventional, (b) coreless machine.	68
3.13	The responses of the conventional machine obtained from central composite DOE. (a) Three-dimensional plot and (b) the contour plot.	70
3.14	The responses of the multi-disk coreless machine obtained from full factorial DOE. (a) Three-dimensional plot and (b) the contour plot.	70
3.15	Projection of the DOE results and selected designs for the conventional motor. Designs marked with ★ are selected in order to have approximately the same torque as the reference machine and minimum losses.	71
3.16	Projection of the DOE results and selected designs for the coreless motor. Designs marked with ★ are selected in order to have half the torque of the reference machine and minimum losses and mass.	72
3.17	(a) The reference design, (b) the selected design 3 of conventional machine, (c) the selected design 1 of coreless machine. Taking advantage of the symmetrical geometry, only $\frac{1}{6}^{th}$ of the conventional machine and $\frac{1}{4}^{th}$ of the cored machine have been analyzed.	73
3.18	(a) Conventional and (b) coreless AFPM machine designs with changing air-gap. The selected design 3 in Table 3.6 and design 1 in Table 3.7 are marked with ■.	74

3.19	Special concentrated-winding multi-disk laboratory prototype employed for validating the 3D FEA parametric design study. The detailed fine finite element mesh and current density vectors in the coils calculated from 3D FEA are represented on the left.	76
3.20	The 3D model of the commercially available distributed winding coreless AFPM machine produced by MARAND for in-wheel drive solar cars.	77
3.21	Torque versus total losses of conventional and coreless designs, compared to prototype and commercial machines employed in solar powered vehicles. Required torque is 56 Nm for single active wheel or 28 Nm for car designs with two active wheels, respectively.	78
3.22	The exploded view of 3D FEA model for a two-phase AFPM motor with wave windings. Each of the two stators has a two-phase winding.	79
3.23	Illustration of the proposed technique for rotation of one of the stators with respect to the other for higher speed operation in constant power zone.	82
3.24	Traction characteristics of a WAVED coreless motor. The proposed stator rotation technique is employed in order to produce constant power operation by reducing the equivalent flux linkage.	83
3.25	Flux density distribution and flux lines for the case studies: the spoke-type motor with high-energy rare-earth SmCo magnets (left) and the same design but with ceramic ferrite magnets (right).	87
3.26	Overview of the geometrical design variables for the case studies. The model was analyzed with the ANSYS Maxwell software.	88
3.27	The per unit regression coefficients calculated for open-circuit based on FEA virtual tests for the motor with ceramic ferrite magnets; (a) back emf, i.e. voltage, (b) core losses. Note the different scales on the y-axis. The bar corresponding to lamination material , M, in (b) is truncated as it reaches up to 0.23.	91

3.28	The per unit regression coefficients calculated for short-circuit based on FEA virtual tests for the motor with ceramic ferrite magnets; (a) d-axis inductance, (b) current. Note the different scales on the y-axis.	92
3.29	The per unit regression coefficients for the input factors most significantly affecting the output performance. Results based on FEA virtual tests for the spoke-type motor with (a) rare earth SmCo magnets, and (b) ceramic ferrite magnets.	93
3.30	Example simple scenario for the spoke-type machine with ferrite magnets where only W_{Fe} is out of specification. As I_{sc} and V_{oc} comply with the design predictions, the design variables influencing their value are most probably as specified. This leaves lamination grade M the highest possible out of specification tolerance causing discrepancy in W_{Fe} .	97
3.31	Example scenarios for the spoke-type machine with ferrite magnets and illustrations of the simplifications employed in the identification process of non-conformant tolerances. I_{sc} out of specification values necessitates considering B_r and/or h_{ib} variations. If the other two geometrical parameters also deviate in the same direction (a), the possibilities of g_o and g_{ns} out of spec deviations are low; if they deviate in the opposite direction (b), all or part of the manufacturing tolerances are out of specification.	97
4.1	The two-level optimization algorithm with an interior loop based on DE and kriging surrogate models.	106
4.2	The optimization results for the commercial motor at the rated torque of 56 Nm, using (a) the conventional MODE, (b) the 2 level SAMODE, and (c) the Pareto fronts obtained from the two algorithms. The darker colors in (a) and (b) represent the designs evolved in more recent generations.	111

4.3	The optimization results for a coreless AFPM motor at the rated torque of 28 Nm, using (a) the conventional MODE, (b) the 2 level SAMODE, and (c) the Pareto fronts obtained from the two algorithms. The darker colors in (a) and (b) represent the designs evolved in more recent generations. . .	112
4.4	Employing the surrogate model is estimating designs in order to fill in the gaps in Pareto front.	113
4.5	Three different methods of specifying search space are illustrated in the flowchart of the two-level kriging surrogate assisted optimization algorithm. The steps in dashed boxes are specific for different search space assignment approaches.	115
4.6	The geometrical variables employed in design optimization.	118
4.7	The sensitivity analysis within the range of $\pm 20\%$ of the reference design variables, and within an extended range to examine the possibility of further reduction in loss.	119
4.8	The Pareto front designs obtained from the two-level surrogate assisted optimization with three different methods for search space assignment. The reference design is providing the per-unitization base.	120
4.9	The search space defined with different methods, for the multi-objective optimization of the spoke machine design. All the designs shown in the plot are evaluated with 3D FEA. The reference design is providing the per-unitization base.	122
4.10	The distribution of variables for the Pareto front designs obtained using different search space assignments.	123
5.1	The geometrical independent variables included in the process of design optimization. The variables are introduced to the algorithm as ratios.	130
5.2	The 3D flux lines distribution of an exemplified design with 40 poles.	131
5.3	The effects of optimization variables on dc copper loss of designs with different pole count, represented by per-unitized regression coefficients.	133
5.4	The effects of optimization variables on core loss of designs with different pole count, represented by per-unitized regression coefficients. .	134

5.5	The effects of optimization variables on cost function of designs with different pole count, represented by per-unitized regression coefficients.	134
5.6	All designs evaluated in 3D FEA for the 30 pole configuration and the Pareto optimal designs represented by filled circles.	135
5.7	The fitted curve on the Pareto front and the calculated knee point, based on (5.4), marked with the red star symbol (★). The point $T = 0.2$ is where further reduction in loss causes at least 5 ($\frac{1}{0.2} = 5$) times more increase in the cost. The point $T = 5$ is where further reduction of cost causes at least 5 times more increase in loss.	138
5.8	Pareto fronts obtained for the machines with different pole count, employing 3D FEA models. A representative design of each topology is marked with a star symbol (★). The per-unit system is based on the representative design with the highest efficiency which is the 20 pole topology marked with a red star symbol (★).	139
5.9	The mass, cost, and loss components of the design on the knee point of the Pareto front obtained from the optimization studies with different number of poles.	140
5.10	Flux density distribution in magnets of the optimum designs with (a) 40, (b) 30, (c) 20, and (d) 10 poles at the rated load. Note that the color scale is identical and ranges from 0.2 T to 1.5 T.	141
5.11	Distribution of the design variables for the Pareto front designs obtained with different pole counts.	143
5.12	Pareto front obtained for the machine with 30 poles, divided into three zones, the vertical section (zone 1) where further reduction in loss requires at least 5 times more increase in cost, the knee in the middle (zone 2), and the horizontal section (zone 3) where further reduction in cost requires at least 5 times more increase in loss.	144

5.13	Distribution of the design variables at different zones of the Pareto front for the topology with 30 poles. This topology is selected due to the its extended asymptotic Pareto front on both sides, illustrated in Fig. 5.12.	144
5.14	The optimum designs obtained for the configuration with 30 poles. (a) The design with minimum loss on the Pareto front, (b) the design with minimum cost on the Pareto front, (c) the design on the knee of the Pareto front with a trade-off between cost and loss.	145
5.15	The overall Pareto front (filled markers) and all of the evaluated designs (hollow markers). The prototyped design is selected to have a high efficiency, marked with a star symbol (★).	146
5.16	The ultra high efficiency AFPM machine, rated for 5.4 Nm at 1050 rpm, selected for prototyping based on the comprehensive optimization study with 3D FEA models. (a) The stator with a core OD of approx. 170 mm and (b) the assembled motor.	147
5.17	The measured efficiency map of the prototyped machine. The performance of the machine at its rated torque and speed is marked with a star symbol (★).	148
5.18	The 3D parametric models of the two AFPM machines under study: (a) single-stator single-rotor, and (b) YASA with two rotors.	150
5.19	The 3D FEA parametric model of three topologies considered for preliminary evaluations; (a) the YASA structure, (b) the single sided machine with half the total magnet volume as the YASA (S1M), and (c) the single sided machine with the same total magnet volume as the YASA (S2M).	151
5.20	D-axis flux linkage at different q-axis currents, per-unitized based on λ_d of the YASA machine at open-circuit. The reduction in λ_d due to i_q is considerably higher for the single sided machines due to greater saturation.	151

5.21	Flux density distribution with pure q-axis excitation for (a) the YASA machine, and (b) the S1M machine, at the current density of $25 A/mm^2$. The stator teeth and rotor core operate in saturation, which explains the reduction in d-axis flux at high q-axis currents.”	152
5.22	The sensitivity analysis of the (a) electromagnetic torque, (b) stator core loss, and (c) power factor for single sided and YASA topologies. The horizontal dashed lines distinguish the insignificant factors with maximum effect being less than 5% variation in the response, within the studied range.	156
5.23	The torque production of YASA, S1M and S2M topologies (a) with ferrite magnets, and (b) with Neodymium magnets.	157
5.24	Flux density distribution at high magnetic and electric loading, current density of $25 A/mm^2$ with Neodymium magnets. Figure (d) and (c) are similar except for an additional air-gap in the latter.	158
5.25	The reference AFPM motor employed for the base design and experimental validation: (a) the test set-up, (b) the stator, (c) the oil cooling jacket.	159
5.26	The experimental validation of the FEA simulations.	159
5.27	The Pareto fronts for the topologies optimally designed for different envelopes: (a) outer diameter of 200 mm, (b) outer diameter of 300 mm, and (c) both diameters.	162
5.28	The distribution of variables for optimum designs with total outer diameter of (a) 200 mm, (b) 300 mm.	163
5.29	The slot width and depth variation of Pareto front designs of (a) the single sided and (b) the YASA machine.	163
5.30	The breakdown of mass components for the Pareto front designs of the topologies studied for an outer diameter of 200 mm. Similar trends were observed for the machines designed for the larger envelope with an outer diameter of 300mm.	165

5.31	The breakdown of loss components for Pareto front designs of the topologies studied for an outer diameter of 200 mm. Similar trends were observed for the machines designed for the larger envelope with an outer diameter of 300mm.	166
5.32	Distribution of eddy current losses in the magnets of (a) the selected YASA optimal design and (b) the selected single-sided AFPM machine optimal design.	166
5.33	The additional winding losses due to eddy currents at rated load for the selected single sided and YASA optimum designs.	168
5.34	Distribution of eddy current losses in the winding with 20 turns per coil of (a) the selected YASA optimal design and (b) the selected single sided AFPM machine optimal design.	168
5.35	Distribution of eddy current losses in the winding with 11 turns per coil of (a) the selected YASA optimal design and (b) the selected single sided AFPM machine optimal design.	169
5.36	The electromagnetic efficiency maps calculated by 3D FEA for the two representative designs with similar mass and loss: (a) single sided design, (b) the YASA design, and (c) the difference between efficiency maps of the two designs (the efficiency of the YASA machine subtracted from the single sided).	170

Chapter 1

Introduction

1.1 Background

Electric machines are increasingly employed in industrial and household applications, such that approximately half of the electrical energy worldwide is being consumed by electric machines. Moreover, new technological trends, such as electric vehicles and wind turbines, specify new requirements that open up an advanced realm for electric machine designers to explore and improve upon. Among the recent advancements and requirements are: the use of permanent magnets (PM) in synchronous machines for field excitation or assisting the excitation which requires special care to avoid demagnetization and thermal issues related to magnets, speed range extension without employing larger inverter ratings, optimally designing the machine that is cost and performance competitive, taking multi-physics specifications of the electric machine into account in design optimization process such as electromagnetic, mechanical and thermal properties, designing motors that can operate efficiently for an entire driving cycle, and reducing the noise and cost.

Increasing the environmental concerns and considering the abundant application

of electric machines have raised the importance of designing efficient machines. From customer and manufacturer point of view minimum cost is also among the most important design considerations. The designer needs to take these two counteracting factors, i.e., efficiency and cost, into account in addition to the performance requirements that ensure an applicable design. Moreover, designing an electric machine is inherently a complicated task with many interacting factors and variables. These make a multi-objective optimization approach an absolute necessity for the successful design of electric machines.

Among the many varieties of electric machines, this dissertation is focused on the axial flux permanent magnet (AFPM) synchronous types which are acclaimed for their high efficiency, torque density, and compact structure. Such machines are also referred to as disc- or pancake-shape machines due to the flat shape of rotor and stator. Common radial flux machines include cylindrical and concentric rotor and stator. As shown in Fig. 1.1, in the case of AFPM machines windings are placed such that their active part is oriented along the radial direction. The field excitation magnets are placed on the rotor such that the air-gap flux flows in the axial direction. This is contrary to the more common radial flux PM machine structures where the rotational movement is obtained by magnetizing the PMs in the radial direction and placing the conductors along the axial direction. Manufactured PM machines are exemplified in Fig. 1.2.

The magnetic flux for an AFPM machine in the air-gap flows in the axial direction, while in the rotor and stator core the magnetic flux is in both axial and circumferential directions. The flux leakage occurs in three dimensions. Also, the

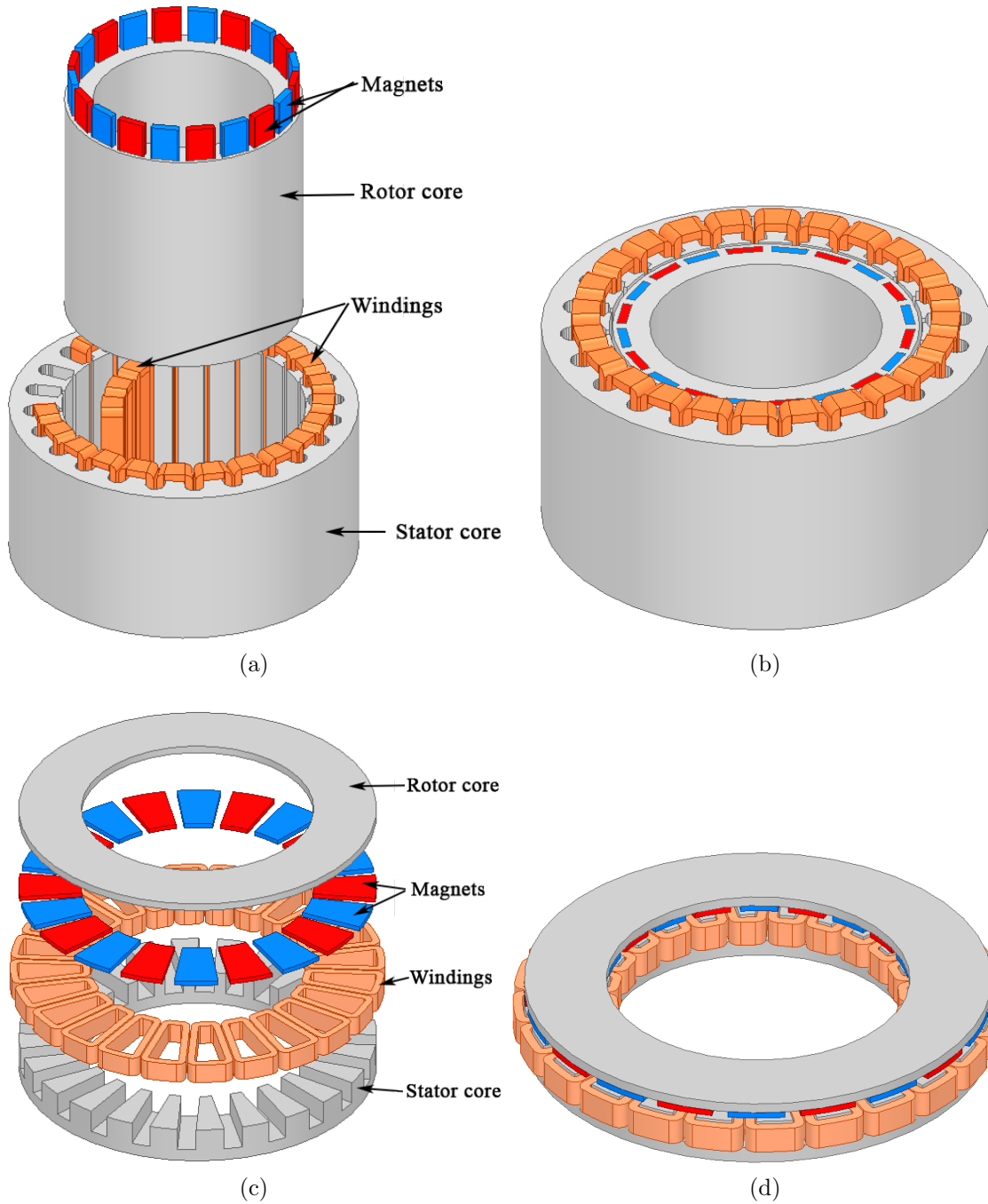
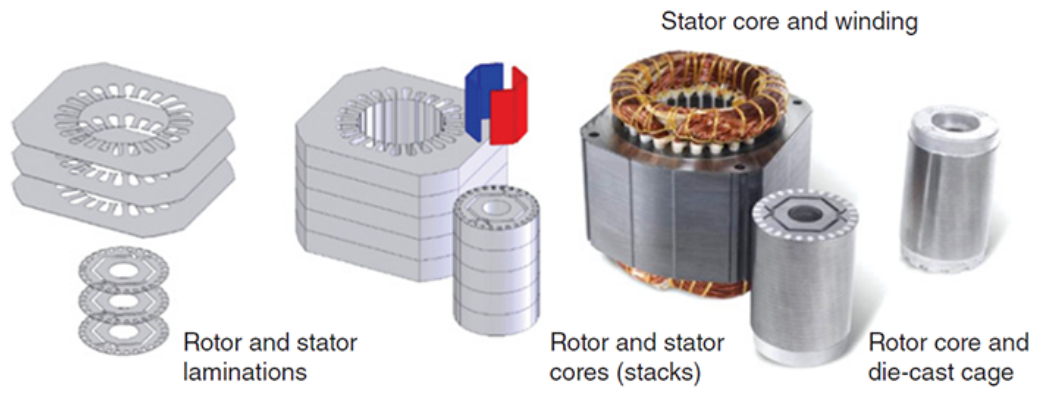
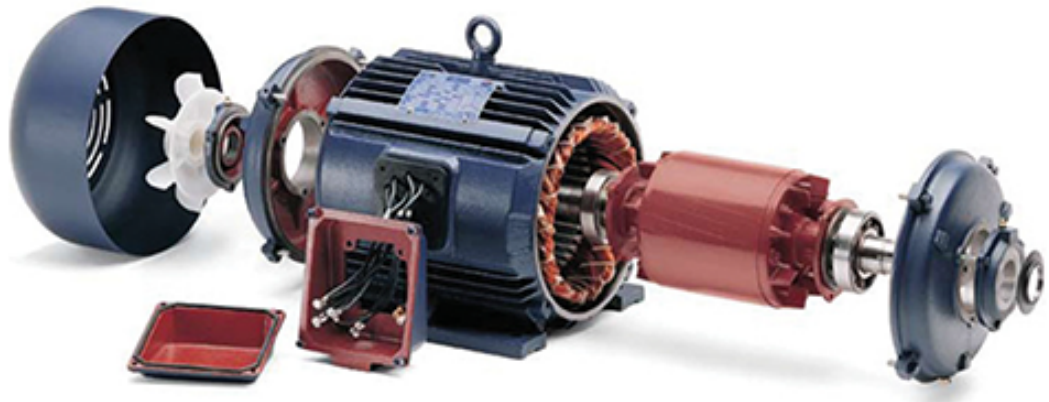


Figure 1.1: Schematic general radial and axial flux PM machines: (a) exploded view and (b) assembled view of a model radial flux machine, (c) exploded view and (d) assembled view of a model axial flux machine.

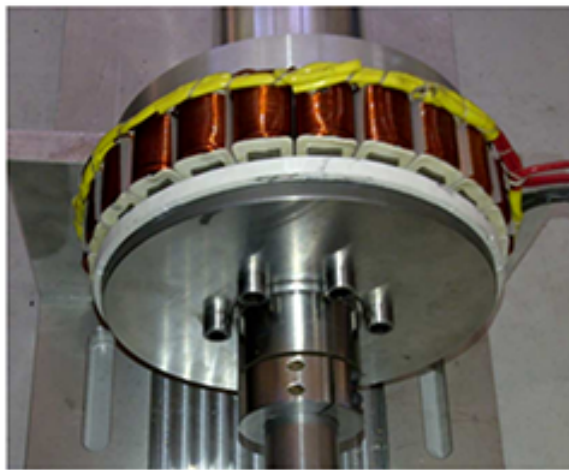
tooth width variation in the radial direction makes the stator core in the inner diameter prone to saturation. Two-dimensional or quasi-3D models cannot capture the effects of end coils and overhang. These are some of the reasons necessitating the use



(a)



(b)



(c)

Figure 1.2: Example manufactured PM machines: (a) typical steps for manufacturing, exemplified for a radial flux line-fed PM motor [1], (b) exploded view of a general-purpose radial flux induction motor [1], and (c) and example 1 hp axial flux PM machine [2].

of computationally expensive 3D models for AFPM machines.

Generally, thousands of design evaluations are required to identify the optimum designs. Therefore, the use of time-consuming 3D finite element analysis (FEA) models with conventional algorithms is simply unaffordable. One of the main contributions of this dissertation is proposing a new two-level surrogate assisted differential evolution multi-objective optimization. This algorithm reduces the required number of FEA design evaluations from thousands to less than two hundred making employment of accurate 3D FEA feasible.

This dissertation systematically addresses the 3D effects related to the performance assessment of axial flux machines that are previously ignored or oversimplified. Other examples of the challenges addressed, in addition to the proposed optimization method, are calculating winding eddy current loss that is inherently difficult to estimate, and winding factor calculation of coreless AFPM machines with minimum simplifying assumptions.

1.2 Literature Review

The earliest electric machines were developed in the form of axial flux [3]. The first working prototype of an axial flux machine recorded was M. Faraday's disc (1831) which was also reported in Nikola Tesla's Patents [3, 4]. Until recently, high-volume manufacturing methods and balancing of the stator and rotor magnetic attraction forces, which are major challenges for AFPM, limited their development, such that the radial flux is a dominant topology in practical implementations. The invention of stronger rare-earth magnets in the mid 20th century, in addition to the attractive

flat aspect ratio, high torque density and efficiency of AFPMM machines have prepared the way for these machine topologies to again draw the attention of the scientific community for additional exploration and investment.

The two main structures of AFPMM machines are single sided and double sided. Single sided AFPMM machine includes only one stator and one rotor disc as shown in Fig. 1.1d. Double sided AFPMM machine can be sub-categorized into single rotor sandwiched between two stators, shown in Fig. 1.3a, and single stator sandwiched between two rotors. The stator winding layout of the double rotor structure depends on the magnets orientation; if the two magnet poles facing each other mounted on opposing rotors are identical, configuration in Fig. 1.3b or 1.3c both can work. Such AFPMM machines are also known as NN (north-north) or SS (south-south) type [5]. If the magnets facing each other with opposite poles, NS (north-south) type, the winding layout as shown in Fig. 1.3c is not practical. The NN and NS type AFPMM machines are demonstrated in Fig. 1.4. In the case of NS AFPMM machines, the flux will not circumferentially flow through the stator. Therefore, the stator yoke becomes electromagnetically dispensable and may be eliminated or be very thin. The NS structure with eliminated stator yoke is referred to as yokeless and segmented armature (YASA) machine [6, 7]. The YASA machine is studied in depth in chapter 5. The configuration shown in Fig. 1.3c is commonly referred to as the TORUS machine [8]. Another classification of AFPMM machines can be PM dc commutator machines, PM brushless dc and synchronous machines, and induction machines [3].

Similar to radial PM excited machines, AFPMM machines can be grouped into surface mounted PM (SPM) machines with equal d- and q-axis inductance and interior

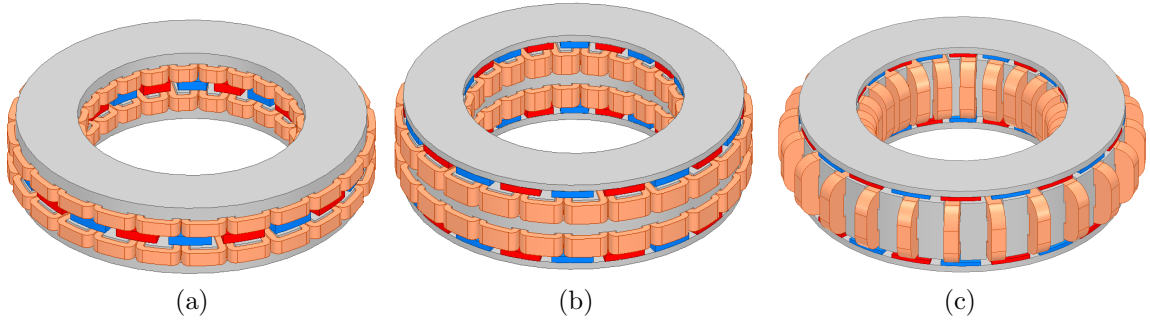


Figure 1.3: Varieties of double sided AFPM machines: (a) single-rotor double-stator, (b) single-stator double rotor, and (c) single-stator double-rotor.

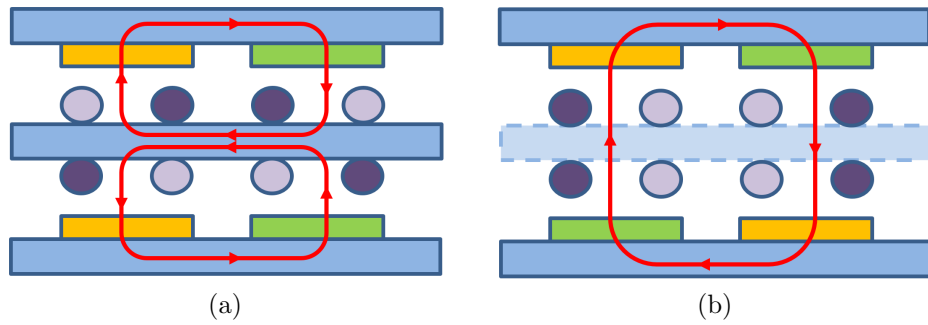


Figure 1.4: (a) The NN- or SS-type AFPM machine configuration. The stator yoke is necessary to provide the magnetic flux path. (b) The NS-type AFPM machine where the stator yoke in the middle can be eliminated.

PM (IPM) machines with saliency causing L_d and L_q to vary. The SPM AFPM machines are the dominant form mainly due to simplicity of the structure and manufacturing [9, 10]. There is some attention toward spoke-type IPM AFPM structure [11]. However, contrary to radial flux PM machines, v-type IPM is the least popular form of AFPM machines [12]. This can be attributed to the manufacturing difficulties.

The main advantageous of AFPM machines can be listed as:

- different form factor that may best suit certain applications
- high efficiency [13–15]
- high torque density and compactness [15, 16]

- possibility of machine structures that their radial counterparts are not easily achievable, such as YASA [6, 7], TORUS [14], stackable multi-stator or multi-rotor layout [17, 18], and coreless (also known as air-cored or air-wound) machines [19].

The main disadvantages of AFPM machines are [3]

- axial magnetic force that may cause difficulties in assembling the machine and keeping the uniform axial air-gap
- manufacturing challenges, such as cutting slots in laminated cores and other methods of making slotted stator cores
- higher cost.

The advantages and disadvantages of AFPM machines have been weighed against each other in numerous applications including the disk spindle drives in computers [20, 21], electric bicycles [22–24], airplanes [18, 25, 26], electric cars [19, 27, 28], generators and wind turbines [29, 30], fans [31], etc.

The disc shape topology has opened up many possibilities for variants, where their counterparts in the more conventional radial air-gap form involve a high degree of mechanical complexity. Radial flux machines can be inner rotor and outer stator or the other way around and they are rarely designed in multiple-stator or multiple-rotor layouts. AFPM machines are stackable, meaning that with some modification even after fabrication, by simply adding more discs of rotor and stator alternatively, the power production can increase. This forms a multi-disc AFPM machine [18]. The radial flux machines lack such flexibility. Other examples of innovative topologies

of AFPM machines are the coreless machine also known as air-cored, air-wound, or ironless machines [3] which are discussed in various chapters in this dissertation.

Main advantages of coreless machines can be listed as no stator core losses, lowest rotor losses, high(est) efficiency throughout a wide speed range, virtually no cogging and ripple torque, and low(est) noise. Disadvantages are high(est) cost because of large PM quantity, high AC winding losses (special wire and windings such as Litz wire is needed), heating of inner stators, ultra-low inductance (necessitating employment of special electronics), and unsuitable for high-speed constant power operation.

The sizing equations and analytical approaches of designing AFPM machines have been developed in earlier publications such as [8, 13, 32–34]. The more accurate numerical methods, such as FEA have been used for performance estimation of AFPM machines [8, 35] and simplifications such as quasi-3D methods are introduced to increase the speed of numerical analysis while maintaining the accuracy, although only to some extent [9, 36]. A short description of the differences between these methods is explained below.

The fastest design performance estimation approach may be the analytical method sizing equations, which includes overly simplifying assumptions, hence the results usually have higher estimation errors. Two-dimensional FEA can be used which includes an axial cut and unrolling of the AFPM machine to somewhat look like a linear machine. The depth (third dimension of the 2D representation) of this *linear* machine would be radial thickness of AFPM machine, i.e., inner diameter subtracted from the outer diameter. In some cases 2D FEA may be reliable. For instance, general coreless AFPM machines that have minimum 3D leakage and fringing, may

be significantly accurately analyzed using 2D finite element methods. This is due to elimination of stator teeth with varying saturation level and different radii. However, more common AFPM machines, and particularly spoke-type AFPM machines, have a strong variation in their electromagnetic properties at different radii and require consideration of their 3D nature.

Quasi-3D methods can find a balance between accuracy of the estimation and the speed. Using quasi-3-D modeling, the axial flux PM machine is segmented circumferentially at different diameters. Each segment is modeled in 2D, resulting in several linear machines each representing the performance at a corresponding diameter. The overall performance of the axial flux machine is obtained by summing the performance of these individual linear machines. The approach can take different magnet shapes and variation of tooth width in the direction of the machine radius into account. However, it ignores the end turns leakage and fringing.

Three-dimensional FEA is the most accurate method which takes all aspects of AFPM machine's 3D nature into consideration. This method divides the geometry into tetrahedral mesh elements and uses numerical methods to calculate the vector potential of each node. Maxwell equations are used to obtain magnetic properties. Shape functions are used to interpolate magnetic properties between the nodes. The finer the meshes, the more accurate the results, which also increases the computational cost and time.

Extensive literature review on more detailed aspects of designing AFPM machines is distributed throughout this dissertation and included in each chapter. These include methods for calculating eddy current losses in chapter 2, design methodologies in

chapters 3 and 4, winding factor calculation in chapter 3, design considerations in chapter 5, the emergence and evaluation of different configuration of AFPM machines in chapter 5.

1.3 Research Objectives and Original Contributions

Statement of the problem:

The most accurate approach for modeling, and consequently estimating the performance of AFPM machines is 3D FEA which is capable of capturing the radially varying saturation in the teeth, leakage flux in end turns, 3D flux path and fringing and variation of flux density and torque production capability in different diameters. However, due to large mesh size (over 200,000 up to millions of tetrahedral mesh elements, depending on the machine size and design problem under study) the analysis takes a significantly long time to solve, compared to more approximate methods.

To optimally design an electric machine, the use of optimization algorithms is needed. Such algorithms require thousands of design evaluations before reaching to the best design. Each design evaluation needs to be carried out by either one of the approximate methods including analytical, 2D FEA, and quasi-3D, or by a more accurate method such as 3D FEA. Approximate methods are faster although diminish the confidence in achieving the best possible design and adversely impact the fidelity and robustness of the final result, particularly in the case of AFPM machines. The use of accurate 3D FEA is simply unaffordable by conventional optimization methods

as evaluating thousands of 3D finite element models may take an unreasonable time.

Another issue specific to some machine design problems is the large search space. This may be the case when for example the number of poles is added to optimization variables. The best choice for the number of poles becomes more complicated due to the freedom recently achieved through the emergence of wide band gap (WBG) devices. WBG based motor drives have the capability of significantly increasing the switching frequency. This enables using ultra-high polarity electric machines.

Increasing number of poles may achieve a higher power density (due to reduced yoke thickness and end coils), however it can increase hysteresis and eddy current losses. Larger rotor polarity requires a proportional increase in the number of stator slots and coils, which, for given main dimensions, may become too small to be practically manufacturable. Furthermore, in such constructions, the slot width may become comparable to the coil insulation width leading to very poor slot filling, increased winding resistance and conductor losses. The best compromise between pros and cons of the increased pole number is achieved in a balanced pole count, indicated by the optimization algorithm.

Approach:

A challenge of optimally designing electric machines, particularly PM excited machines, arises when winding eddy current losses are considerable. In this dissertation these ac winding loss components are calculated through a hybrid method that bridges the gap between accurate time-consuming and approximate fast methods. The developed hybrid analytical/numerical estimation of winding eddy current losses takes 3D effects into account and requires only a general crude 3D FEA. Employment of 3D

FEA crude models within the optimization can be handled as explained in the following paragraph. Therefore, inclusion of winding eddy current loss in the optimization objectives and fitness functions is enabled.

The methods previously used for systematic design of electric machines are re-introduced with novel applications. Examples are innovatively employing extensive design of experiments and response surface methodologies for tracing the manufacturing tolerances, and application of design of experiments in assigning the reference design and appropriate ranges of optimization variables.

A new optimization algorithm is developed. This algorithm is referred to as two-level kriging surrogate assisted multi-objective optimization. The algorithm is capable of noting the most promising designs and evaluating only such designs with 3D FEA while thousands of designs are evaluated using a surrogate method, known as kriging meta-model which can be viewed as a local interpolation method.

As a result of increased speed in the optimization process, larger design problems can be solved. Examples of such design problems are including the number of poles as a design variable, or stretching the variables range to be very wide. These would generally require large number of design evaluations to ensure global optimization as the exploration of the best design needs to be done in a larger search space. With the overall faster method achieved, such extensions are feasible.

Due to enhancements in WBG based motor drives, higher polarity machines are becoming more and more attractive. The manufacturing issues associated with higher

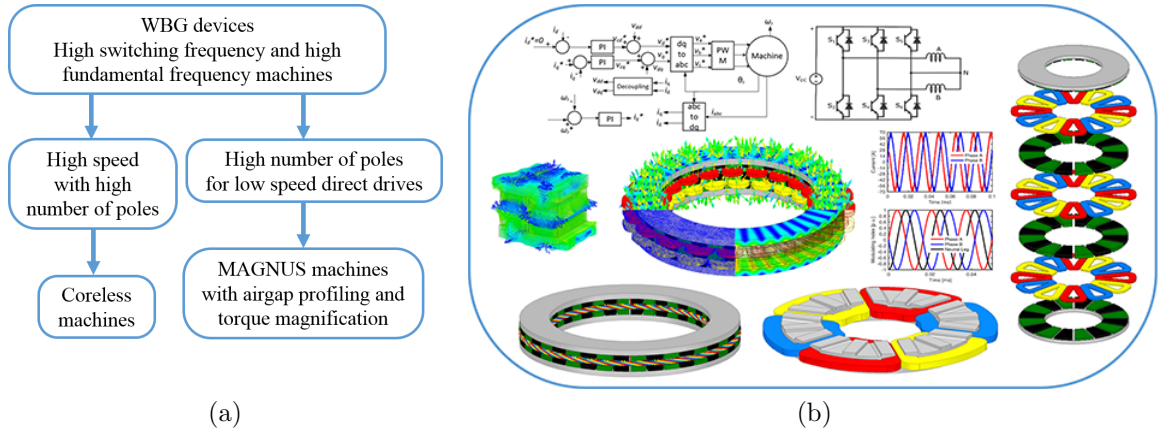


Figure 1.5: (a) Two machine topologies can be considered in order to utilize the advantages enabled by WBG devices: coreless machine for higher speed and MAGNUS machine for lower speed applications. (b) Examples of axial flux machines, power electronics and controls illustrating the best practices of employing WBG devices for motor drives.

polarity machines in a given diameter, such as saturated teeth and reduced coil cross-sectional area can be handled by innovative machine topologies such as flux modulation or vernier machines, referred to as MAGNUS, and coreless AFPM machines. Figure. 1.5 represents the application of such machine structures with WBG based drives. A coreless machine eliminates stator core and consequently removes tooth saturation and core loss issues. A MAGNUS machine employs smaller number of slots and still has a high performance with high polarity due to flux modulation principles. Contributions to axial flux version of MAGNUS machines are made, for example in [37–39], however, they are not included in the dissertation. Coreless machines are studied in detail in several sections of the dissertation.

Other contributions:

Some other detailed aspects of design and performance evaluation of APFM machines have been addressed. These include:

- developments on AFPM coreless machine design for traction application (such as comparison with conventional AFPM, speed range extension, etc.)
- systematically exploring the limits of efficiency and cost and the effect of pole count on fractional hp AFPM machines
- establishing the guidelines for design areas where single rotor or double rotor AFPM machine is the best choice
- introducing a systematic approach for selecting the ideal design as a post-processing step of multi-objective optimizations
- accurate winding factor calculation for coreless AFPM machines

1.4 Dissertation Outline

In order to address the accurate and systematic design and performance estimation of AFPM machines the following chapters have been included.

Chapter 2 proposes a method for calculating eddy current losses taking 3D effects into account. This hybrid analytical/numerical approach is a trade-off between speed and accuracy and can be used for optimization purposes. Chapter 3 discusses systematic application of design of experiments (DOE) and response surface methodology (RSM) in designing AFPM machines. A new approach of appropriating the information provided by RSM and extensive sensitivity analyses is proposed. This method can be used for narrowing down the possible out of specifications tolerances due to processes involved in manufacturing. The newly developed optimization algorithm is

proposed and elaborated in chapter 4. Two AFPM machine cases studies are included to compare the results of this method with more conventional differential evolution algorithm. In chapter 5, two more complicated case studies are included exhibiting the systematic design approach achieved through employing the new algorithm. Conclusions, and future works are provided in Chapter 6.

1.5 Publications

The main elements covered in this dissertation have been peer reviewed and published in:

- Taran, N., and Ionel, D. M., “A Hybrid Analytical and FE-based Method for Calculating AC Eddy Current Winding Losses Taking 3D Effects into Account,” Proceedings, IEEE ECCE 2019, Baltimore, MD, (October 2019) [40]
- Taran, N., Ionel, D. M., and Dorrell, D. G., “Two-Level Surrogate-Assisted Differential Evolution Multi-Objective Optimization of Electric Machines Using 3D FEA”, IEEE Transactions on Magnetics, Vol. 54, No. 11, pp. 1-5, 5p (2018) [41]
- Taran, N., et al., “Systematically Exploring the Effects of Pole Count on the Performance and Cost Limits of Ultra-high Efficiency Fractional hp Axial Flux PM Machines”, IEEE Transactions on Industry Applications, 11p, 2020 [42]

An additional number of 2 journal papers and 9 conference proceeding papers have been published with 1 of them under current review of development for journal publication:

- Taran, N., et al., “A Systematic Study on the Effects of Dimensional and Materials Tolerances on PM Synchronous Machines based on the IEEE Std 1812”, IEEE Transactions on Industry Applications, Vol. 55, No. 2, pp. 1360-1371, 11p (2019) [43]
- Taran, N., et al., “Coreless and Conventional Axial Flux Permanent Magnet Motors for Solar Cars”, IEEE Transactions on Industry Applications, Vol. 54, No. 6, pp. 5907-5917, 10p (2018) [44]
- Taran, N., et al., “Systematic Comparison of Two Axial Flux PM Machine Topologies: Yokeless and Segmented Armature versus Single Sided,” Proceedings, IEEE ECCE 2019, Baltimore, MD, (October 2019) [45]
- Taran, N., et al., “WAVED: A Coreless Axial Flux PM Motor for Drive Systems with Constant Power Operation,” IEEE Transportation Electrification Conference and Expo ITEC 2019, Novi, MI, (June 2019) [46]
- Taran, N., et al., “Design Optimization of Electric Machines with 3D FEA and a New Hybrid DOE-DE Numerical Algorithm”, IEEE International Electric Machines and Drives Conference IEMDC 2019, San Diego, CA. (May 2019) [47]
- Taran, N., et al., “A Comparative Study of Methods for Calculating AC Copper Loss in Permanent Magnet Machines”, IEEE International Electric Machines and Drives Conference IEMDC 2019, San Diego, CA. (May 2019) [48]
- Taran, N., et al., “Torque Production Capability of Axial Flux Machines with

Single and Double Rotor Configuration”, Proceedings, IEEE ECCE 2018, Portland, OR, 6p (Sep 2018) [49]

- Taran, et al., “Exploring the Efficiency and Cost Limits of Fractional hp Axial Flux PM Machine Designs”, Proceedings, IEEE ECCE 2018, Portland, OR, 6p (Sep 2018) [50]
- Taran, N., et al., “A Comparative Study of Coreless and Conventional Axial Flux Permanent Magnet Synchronous Machines for Low and High Speed Operation”, Proceedings, IEEE ECCE 2017, Cincinnati, OH, pp. 321-327 (Oct 2017) [51]
- Taran, N., et al., “A Comparative Study of Conventional and Coreless Axial Flux Permanent Magnet Synchronous Motors for Solar Cars”, Proceedings, IEEE IEMDC 2017, Miami, FL, 7p (May 2017) [52]
- Taran, N., et al., “On the Effect of Design Tolerances on the Performance of Synchronous PM Machines Evaluated According to the IEEE Std 1812”, Proceedings, IEEE IEMDC 2017, Miami, FL, 7p (May 2017) [53]
- Taran, N. et al. “Evaluating the Effects of Electric and Magnetic Loading on the Performance of Single and Double Rotor Axial Flux PM Machines”, *under preparation*.

Chapter 2

A New Hybrid Method for Three-Dimensional Calculation of Winding Eddy Current Losses

This chapter explores different methods of estimating the additional ac winding loss due to eddy currents for AFPM machines and proposes a new hybrid analytical and numerical FE-based method, demonstrating its applicability for axial flux electric machines. The method takes into account 3D field effects in order to achieve accurate results and yet greatly reduce computational efforts.

A comparative study of 2D and 3D FEA, and hybrid numerical and analytical methods is performed. The case study AFPM machines include a machine with open slots and a coreless configuration. These machine topologies are expected to present a substantial amount of ac winding loss, which would therefore need to be considered during optimal design. This chapter also includes other discussions relevant to the subject matter such as the selection of the number of turns, the effect of the conductor cross section shape, the placement of each turn for the two machines under study, and the meshing of the turns for FEA based methods. Further, a measurement method for additional open-circuit winding losses is proposed.

2.1 Introduction

The eddy currents are the result of exposure to alternating magnetic field and cause additional copper loss and temperature rise. The alternating magnetic field can be due to the ac current inside the same conductor (skin effect), or the ac current flowing in the adjacent conductors (proximity effect). In case of a permanent magnet (PM) excited electric machine, the magnetic field causing eddy currents may also be due to the leakage flux of the rotor PMs passing over the stator coils (open circuit copper loss). This third source of ac copper loss is discussed far less frequently in literature while it can be more significant than the proximity losses [54, 55], especially where frequency is not very high. The open-circuit copper loss is sometimes integrated with the proximity loss [56].

Analytical and numerical methods for estimating such ac winding losses have been previously developed and published, e.g. [54, 57–63]. Analytical methods are more straightforward to use, but typically employ many simplifying assumptions, leading to approximate results. Numerical techniques, such as finite element analysis (FEA), may be more accurate with the downside of a laborious set-up process and substantial computer resource requirements. Two-dimensional FEA is used in many studies [64–67] while 3D FEA has been employed only very recently in few works [56, 68].

In order to bridge the gap, hybrid methods have been proposed [69–71]. These methods generally employ the 2D FEA calculated flux density in one coil cross section in order to provide a trade-off between accuracy and computational speed. However,

due to end effects, flux leakage and fringing, the flux density observed by the winding in different cross sections may not be identical and hence employing a 2D FEA model may not suffice. For machines with considerable flux leakage at the ends, hybrid methods that utilize 2D FE models can overestimate the losses. Additionally, the accuracy is negatively affected because 2D models cannot take into account the end path of the eddy currents. The possible problems associated with sampling the flux density from a 2D FE model are discussed in more detail later in the chapter. Furthermore, it should be noted that electrical machines, such as those of the axial flux type, in which the flux density in the slots and winding conductors vary both in the axial and radial directions, have a substantially three dimensional magnetic flux path and require adequate 3D FE models.

In this chapter a new hybrid method with minimal simplifying assumptions is proposed. The analytical formulation is derived and the results are compared with meticulous 3D FEA with the windings modeled in detail and wire-by-wire. The method is illustrated on example axial flux permanent magnet (AFPM) machines with concentrated coils around the teeth and open slots, and with a coreless stator structure, respectively.

This chapter further contributes to the subject matter by studying AFPM machines and comparing hybrid numerical and analytical, 2D and 3D FEA approaches of calculating additional ac conductor loss. The comparison of quicker and less accurate methods with meticulous 3D FEA results is especially important for AFPM machines as the 2D models for such machines may be overly simplified considering the 3D flux linkage and leakage flux paths. The case studies include two topologies

where significant values of additional copper loss due to the magnet flux is expected, namely, open slot and air cored PM machines. This chapter also proposes a novel measurement approach which is then employed to validate the 3D FEA calculations.

2.2 Eddy Loss Calculation Methods

2.2.1 Analytical Method

The analytical methods for calculating eddy current loss, P_{eddy} , have been attempted previously. Majority of these approaches originate from the following

$$P_{eddy} = \frac{1}{R} \left(\frac{d\phi}{dt} \right)^2, \quad (2.1)$$

where R is the resistance and ϕ is the magnetic flux seen by the conductors. It can be shown that for a machine with N_c coil sides with the length of ℓ , N_t turns per coil with circular cross section as shown in Fig. 2.1a, and N_s strands per turn with diameter of d , assuming no magnet flux leakage on the end coils and all of the coil region exposed to a space uniform flux density of B_a varying sinusoidally in time, the eddy current loss can be estimated by

$$P_{eddy} = \frac{\pi \ell N_c N_t N_s d^4 B_a^2 \omega^2 \sigma}{128}, \quad (2.2)$$

where ω is the electrical angular speed and σ is the conductivity of the coil. Similarly, for the case with rectangular cross section conductors in Fig. 2.1b, these losses can be calculated as

$$P_{eddy} = \frac{\ell N_c N_t N_s w h \omega^2 \sigma}{24} (w^2 B_{az}^2 + h^2 B_{a\phi}^2), \quad (2.3)$$

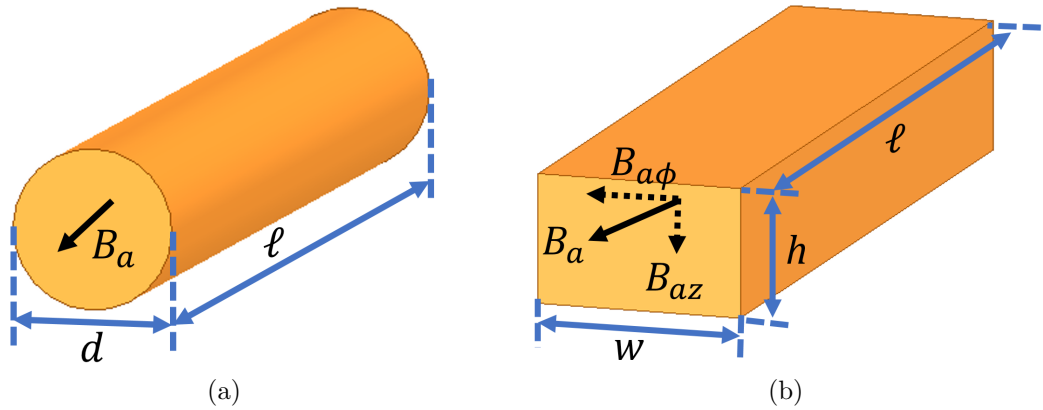


Figure 2.1: Illustration of wires with circular and rectangular cross section.

where B_{az} and $B_{a\phi}$ are the axial, in z direction, and tangential, in ϕ direction, component of the flux density as shown in Fig. 2.1b. The assumption of uniform B_a in many cases is not accurate due to skin effect, larger leakage flux at the top of the slots, circulating currents in parallel conductors, etc. The accuracy of simple calculations such as (2.2) and (2.3), varies for different machine structures. For example, in machines where conductors are placed in slots, each turn experiences a different flux density such that the conductors closer to the slot opening cause the majority of the losses and the calculations need to be performed individually and then integrated. Also, if the conductor diameter is significantly larger than skin depth, the variation of B_a inside each turn is considerable.

2.2.2 Numerical Methods

Two- and three-dimensional FEA models can be used to estimate the ac winding losses. Two-dimensional FEA is easier to set up and is faster, making it particularly suitable for large-scale parametric and optimization studies. However, a major disadvantage is that it cannot take into account the variations in the third dimension. On

the other hand, three-dimensional models can take end effects and 3D flux paths into account, but have the drawbacks of being laborious to set up and computationally expensive.

It is possible to model the coils in detail, in a turn-by-turn and wire-by-wire approach in order to numerically calculate the ac winding losses. However, this is a complicated task, difficult to parametrize and to employ in an optimization algorithm. The winding ac loss estimation requires fine meshing according to the skin depth, while the flux density can be estimated with a more coarse mesh.

Four types of geometries employed for the FEA modeling of the example slotted AFPM machine studied are shown in Fig. 2.2. These include 2D and 3D models with a general large equivalent single turn coil, Figs 2.2a and 2.2c, and detailed turn-by-turn models of the conductors, Figs. 2.2b and 2.2d.

Electric machines are more commonly modeled with one equivalent turn, as shown in Figs 2.2a and 2.2c. To obtain the eddy current losses directly from the available commercial FEA software, detailed models such as the ones shown in Figs 2.2b and 2.2d are required. Hybrid method for calculating winding eddy current losses, which will be discussed in the next part, can use only a general model.

If all the conductors are modeled and meshed correctly considering the skin depth, the mesh size would be very large (over 8 million elements in the case studies considered here). This necessitates use of high performance computing (HPC) systems and supercomputers. Another approach could be to fine mesh only the turns that cause the majority of the losses. For instance, as it will be shown, for the open-slot AFPM machine most of these losses happen at the top three layers of the winding.

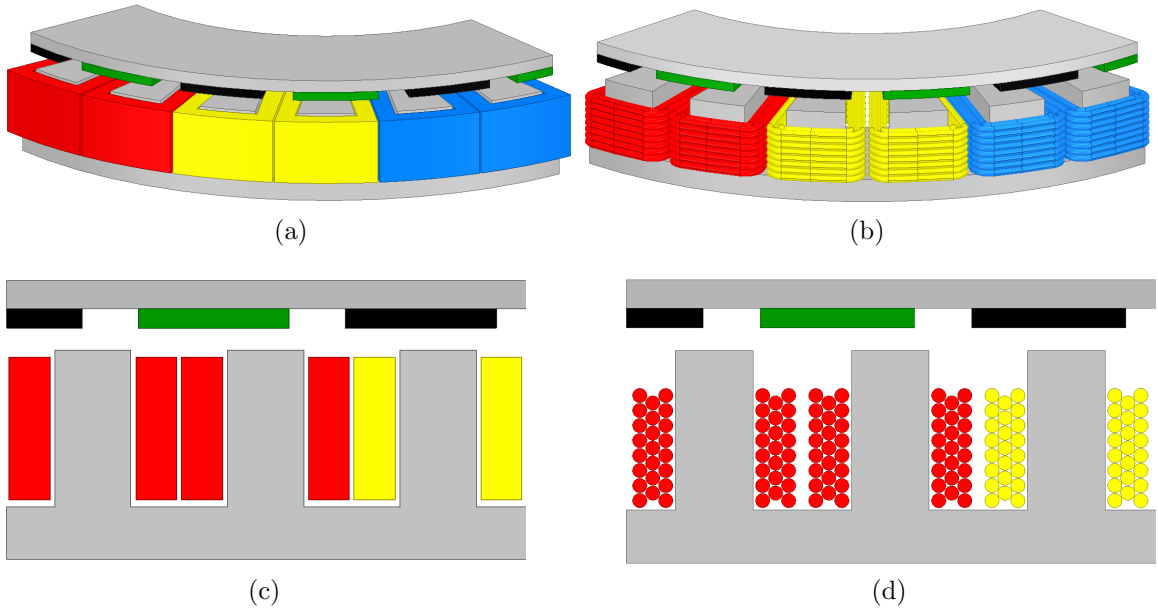


Figure 2.2: The geometries employed for the FE models of the case study open slot AFPM machine. (a) Simplified 3D model, (b) 3D model with turn-by-turn representation, (c) simplified 2D model, and (d) 2D model with detailed turn-by-turn representation of the wire conductors.

Therefore, the rest of the turns can be meshed coarsely.

2.2.3 Hybrid Method using 2D Numerical Models

Hybrid methods may provide, in principle, a satisfactory compromise between accuracy and computational efforts for estimating the ac eddy current component of copper losses. For such methods, a combination of analytical equations and FEA is employed [69, 70]. Typically, flux density values are sampled from the simplified coil cross section representation of a 2D FE model, e.g. shown in Fig. 2.2c. The flux density is then used with analytical equations in order to calculate the eddy current losses.

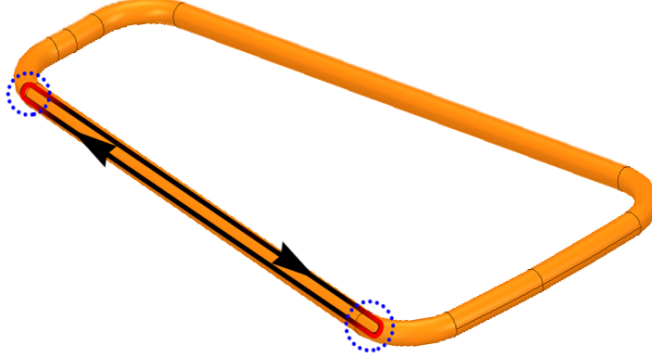


Figure 2.3: Typical eddy current path considered in 2D analysis has a go and return path along the conductor and does not include end coil sections.

Although hybrid methods may lead to more accurate estimations than pure analytical methods, they have the risk of inaccuracy due to the fact that they disregard 3D effects. Neglecting end paths, as shown in Fig. 2.3 may result into underestimation of resistance and hence overestimation of eddy current losses. The end turn paths become a larger contributor to the resistance of the eddy current paths for shorter coils, i.e., lower stack length in case of radial flux machines or larger split ratio in case of axial flux machines. Therefore, it is necessary to consider the entire path of the eddy current loop. One typical approach is to employ correction factors, such as:

$$K_s = 1 - \frac{\tanh\left(\frac{\pi L_{eff}}{d_c}\right)}{\frac{\pi L_{eff}}{d_c}} \quad (2.4)$$

where L_{eff} is the effective length of the coil and d_c is the conductor diameter. The above formulation of the correction factor, K_s , has been originally introduced for the calculation of eddy current losses in the screened-rotor of an induction motor [72] and later adopted for the rotor retaining can of PM excited machines [73]. In our study, K_s is employed for calculating winding eddy current losses.

Another reason for possible overestimation of eddy current conductor losses by 2D

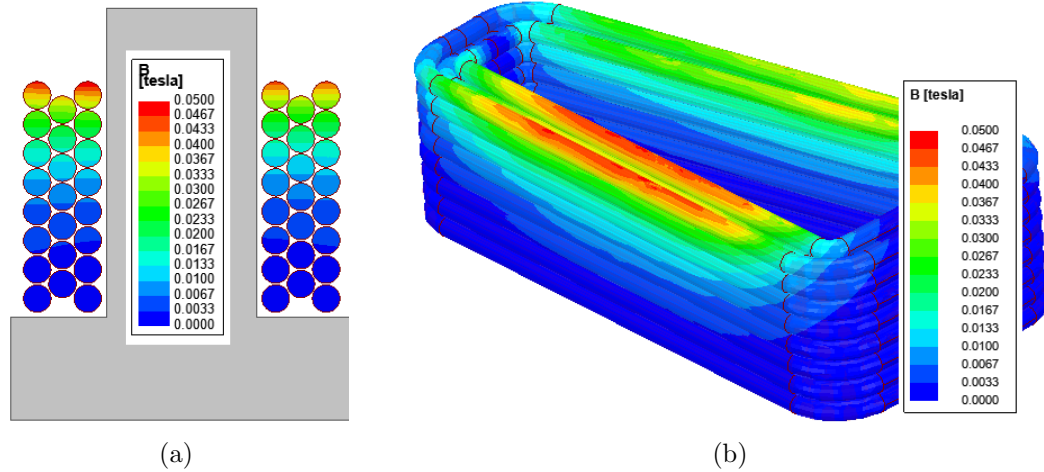


Figure 2.4: The magnetic flux density in the conductors of a concentrated precise wound coil placed in the slots of the case study open slot AFPM machine calculated with 2D (a) and 3D (b) FEA and illustrating the multi-dimensional variation of the field.

methods may be attributed to not considering the magnetic field fringing and leakage, and hence neglecting the reduction of the flux density towards the ends, as illustrated in Fig. 2.4. Hybrid methods that employ 2D models ignore the fringing in the third dimension and typically result in larger and constant values of the flux density along an entire coil side. Moreover, for axial flux machines the non-linear magnetic field along the radial direction can largely vary and sampling the flux density at only one particular diameter may not be truly representative of the flux density throughout the entire coil.

For an example AFPM machine, the magnitude of the flux density in each of the winding turns placed in the slot and surrounding a tooth was estimated with one sample per conductor using 2D and 3D models, respectively (Fig. 2.5). The 3D samples are taken for each conductor in 21 equally distanced radial locations and then integrated. The 2D model was set-up at the mean diameter. The 2D model

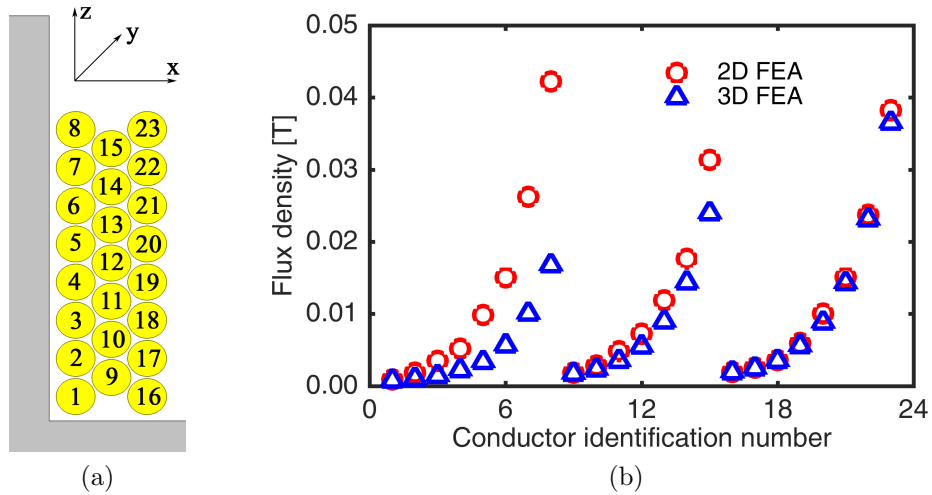


Figure 2.5: (a) Schematic of a coil side placed around the tooth displaying conductor identification numbers. (b) The flux density in each conductor, obtained by space sampling 2D and 3D FEA results, respectively. The 2D FEA typically results in an over estimation, especially for the conductors at the top slot and closest to the tooth.

overestimation of the flux density, particularly for the turns that are closer to the top of the slot and closer to the teeth, is noticeable.

The coreless AFPM machine example in Fig. 2.6 is illustrative of the typical very large 3D variation of the flux density in the stator windings. In order to account for this, one solution would be to study multiple 2D models representative of slices at different radial coordinates and combine their contributions [74]. An increased number of 2D slices would increase, in principle, the accuracy of the simulation at the expense of increased computational time, but won't still account for the end field, which makes the use of 3D models worthwhile even more so.

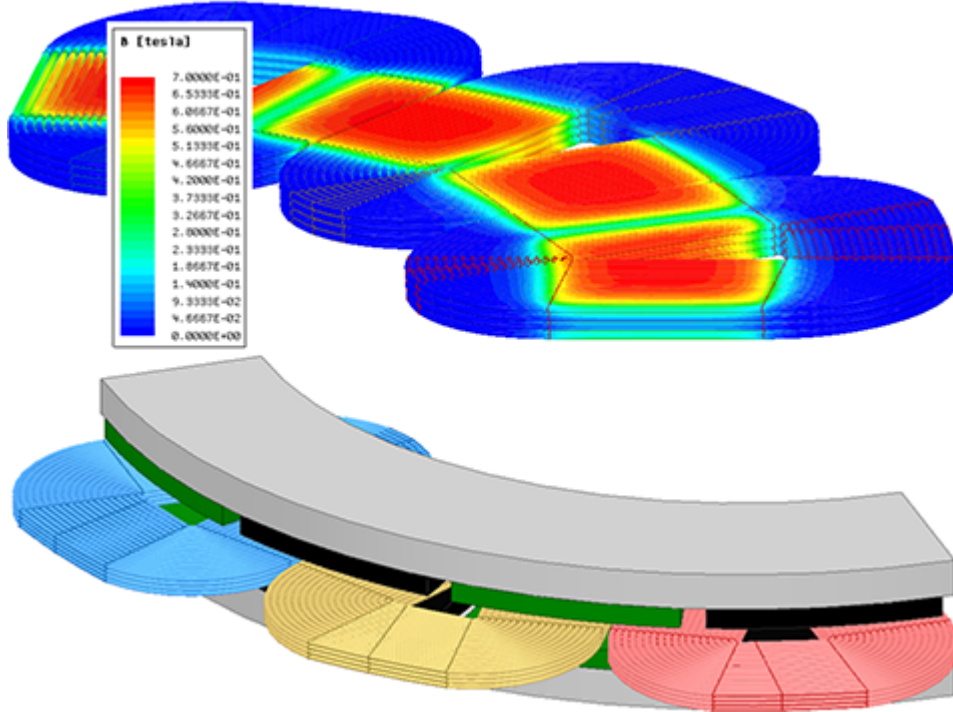


Figure 2.6: The magnetic flux density in the conductors of an example AFPM coreless machine calculated with 3D FEA. For such machines, the winding is directly exposed to the airgap field, the magnitude and multi-dimensional variation of which can be substantial, resulting in significant eddy current losses.

2.2.4 Proposed Hybrid Method using 3D Numerical Models

The new method proposed here employs a simplified 3D FE model with a single equivalent turn per coil as shown in Fig. 2.2a. The model can be solved as a magnetostatic field problem or as a transient problem with motion. The motivation for this approach is that the mesh required for satisfactorily accurate flux density calculations is substantially less dense than the mesh required for eddy current calculations in the winding conductors, resulting in faster solving and significantly lower computational resource requirements.

Considering N_L sections in the radial direction and a precise winding configuration, as shown in Fig. 2.7a:

$$\begin{aligned}
P_{n_\phi, n_z, n_L} &= [x_n, y_n, z_n] ; \\
n_\phi &= 1, \dots, N_\phi ; \quad n_z = 1, \dots, N_z ; \quad n_L = 1, \dots, N_L ; \\
x_n &= \frac{ID}{2} \cos\left(\frac{\theta_{in}}{2}\right) \left(1 - \frac{n_L}{N_L}\right) + \frac{OD}{2} \cos\left(\frac{\theta_{on}}{2}\right) \frac{n_L}{N_L} ; \\
y_n &= \frac{ID}{2} \sin\left(\frac{\theta_{in}}{2}\right) \left(1 - \frac{n_L}{N_L}\right) + \frac{OD}{2} \sin\left(\frac{\theta_{on}}{2}\right) \frac{n_L}{N_L} ; \\
\theta_{in} &= \theta_i + 2 \arcsin\left(\frac{d_c(2n_\phi - 1)}{ID}\right) ; \\
\theta_{on} &= \theta_o + 2 \arcsin\left(\frac{d_c(2n_\phi - 1)}{OD}\right) ,
\end{aligned} \tag{2.5}$$

where P_{n_ϕ, n_z, n_L} are the Cartesian coordinates of the n^{th} point to be sampled for the flux density value; N_L , the number of sampling planes stacked in the direction of the effective length of the coil with an equal distance of $\Delta L = \frac{L_{eff}}{N_L}$ between them; N_ϕ and N_z , the number of turns in the circumferential and axial directions, respectively, as shown in Fig. 2.7a; ID and OD the inner and outer diameters; θ_i and θ_o the inner and the outer coil span angles, as illustrated in Fig. 2.7b.

It should be noted that for random windings, methods such as the one described in [69] maybe further developed for 3D application in conjunction with the new techniques described in this chapter. Also, it is important to carefully adapt the flux density sampling to the problem. For example, if the real conductor dimensions are larger than the skin depth and the variations of flux density inside each conductor may be considerable, multiple flux samples in each plane are needed.

The eddy current losses for a circular conductor can be calculated based on a

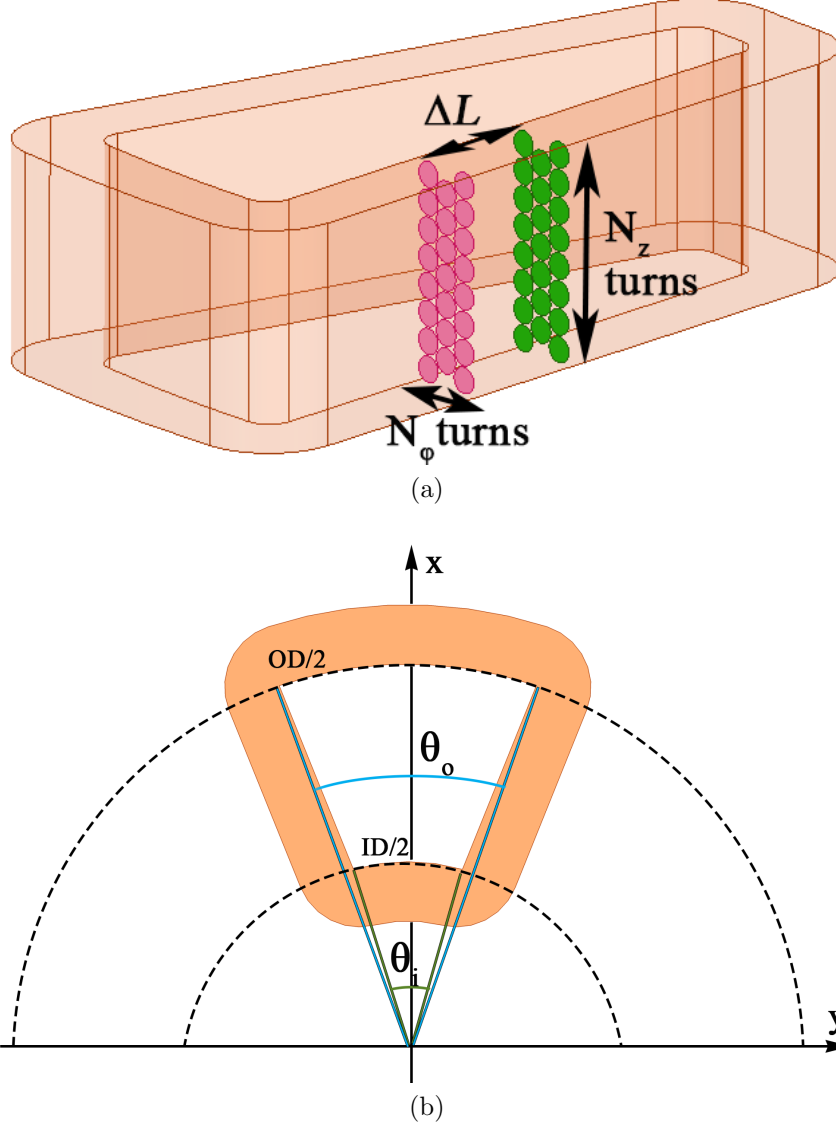


Figure 2.7: (a) The flux density sampling planes employed by the new hybrid 3 FEA method stacked in the direction of the main current flow. (b) Three-dimensional sampling is performed also in order to take end effects into account. The axial cross section schematic depicts the coil span and the in inner and outer diameter as used in (2.5).

general analytical formulation:

$$P_{eddy} = \frac{1}{R} \left(\frac{d\Phi}{dt} \right)^2; \quad dR = \frac{(L_{eff} + 2r)\rho}{\sqrt{\frac{a_c^2}{4} - r^2}} dr \quad (2.6)$$

where R is the resistance; Φ , the magnetic flux through the conductors; and ρ the conductor resistivity. Each conductor cross section can be divided into M segments

as shown in Fig. 2.3. Assuming constant flux density for each segment, one field sample per segment may suffice.

Therefore, the eddy current loss for one coil side with $N_\phi \times N_z$ turns can be estimated as:

$$\begin{aligned}
P_{eddy} &= \frac{4L_{eff}^2}{\rho} \sum_{n_\phi=1}^{N_\phi} \sum_{n_z=1}^{N_z} \sum_{h=1}^{\infty} \sum_{m=1}^M \dots \\
&\left[\left(\frac{d}{dt} \left(\frac{1}{L_{eff}} \int_{ID}^{OD} B_{m,h} \left(\frac{D}{2}, n_\phi, n_z \right) dD \right) \right)^2 \int_{r_{m1}}^{r_{m2}} \frac{r^2 \sqrt{\frac{d_c^2}{4} - r^2}}{(L_{eff} + 2r)} dr \right] \\
&= \frac{L_{eff}}{2\rho} K_s \sum_{n_\phi=1}^{N_\phi} \sum_{n_z=1}^{N_z} \sum_{h=1}^{\infty} \sum_{m=1}^M \dots \\
&\left[\left(\frac{d}{dt} \left(\frac{1}{L_{eff}} \int_{ID}^{OD} B_{m,h} \left(\frac{D}{2}, n_\phi, n_z \right) dD \right) \right)^2 (f(r_{m2}) - f(r_{m1})) \right] ; \\
f(r) &= r \sqrt{\frac{d_c^2}{4} - r^2} (2r^2 - \frac{d_c^2}{4}) + \left(\frac{d_c^2}{4} \right)^2 \arctan \frac{r}{\sqrt{\frac{d_c^2}{4} - r^2}} ,
\end{aligned} \tag{2.7}$$

where $B_{m,h}$ is the h^{th} harmonic of the flux density in the m^{th} section for the conductor associated with n_ϕ and n_z at the diameter D . The flux density of the m^{th} section includes the flux density of all sections that are inscribed in it (i.e. $B_m = \sum_{mi=1}^m B_{mi}$).

If the conductors are sufficiently small, the flux density throughout the conductor cross section may be assumed constant. Taking the variation of B along the effective length from inner to outer diameter into account, and neglecting the harmonics content, the eddy current losses of the machine with N_c coil sides are derived as:

$$\begin{aligned}
P_{eddy} &= \frac{\pi L_{eff} N_c d_c^4 \omega_e^2 K_s}{128\rho} \dots \\
&\sum_{n_\phi=1}^{N_\phi} \sum_{n_z=1}^{N_z} \left[\frac{1}{L_{eff}} \int_{ID}^{OD} B \left(\frac{D}{2}, n_\phi, n_z \right) dD \right]^2 .
\end{aligned} \tag{2.8}$$

A discrete sampling along radial direction with N_L samples can be performed in which case the coordinates of the sample points in the general 3D FEA model can be

obtained from (2.5).

Both (2.7) and (2.8) assume that within the coil side the largest eddy current flow path follows the entire active length of the coil with shorter paths being possible, as shown in Fig. 2.8. The following equation, in which different eddy current paths inside one conductor are specified with the index k , takes this effect into consideration:

$$P_{eddy} = \frac{\pi L_{eff} N_c d_c^4 \omega_e^2 K_s}{128 \rho} \sum_{n_\phi=1}^{N_\phi} \sum_{n_z=1}^{N_z} \sum_{k=1}^{k_{max}} C_k \cdot B_{path,k}^2, \quad (2.9)$$

where C_k is the coefficient adjusting the resistance of each current path and $B_{path,k}$ is the flux density within the k^{th} current path. In the case of an odd number of samples, N_L , along the coil side:

$$k_{max} = \frac{N_L + 1}{2}, \quad C_k = \frac{2 + 4(k - 1)}{N_L},$$

$$B_{path,k} = \frac{1}{1 + 2(k - 1)} \sum_{n=\frac{N_L+1}{2}-(k-1)}^{\frac{N_L+1}{2}+(k-1)} B_n. \quad (2.10)$$

For an even number of samples:

$$k_{max} = \frac{N_L}{2}, \quad C_k = \frac{4k}{N_L},$$

$$B_{path,k} = \frac{1}{2k} \sum_{n=\frac{N_L}{2}-(k-1)}^{\frac{N_L}{2}+k} B_n. \quad (2.11)$$

Equation (2.9), which comprehensively represents the discrete implementation of the proposed new hybrid 3D FEA method, was employed in the following case studies.

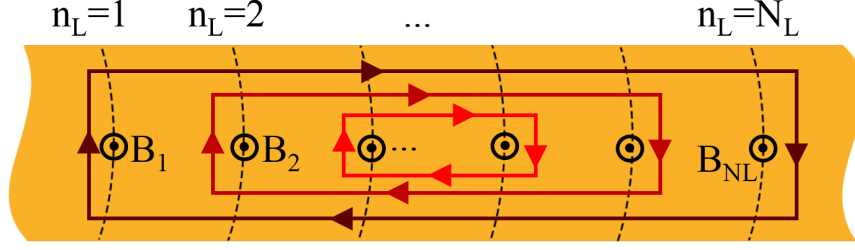


Figure 2.8: Eddy current paths with different length along the coil side.

2.3 Case Studies

2.3.1 Air Cored Axial Flux PM Machine

In case of an AFPM machine with double rotor structure such that PMs of opposite polarity face each other, magnetic flux from one rotor flows into the other without traveling circumferentially through the stator core, which may thus be eliminated, leading to the removal of associated loss and cogging torque, although at the cost of a higher electromagnetic air-gap.

Previously published papers have mostly focused on conventional AFPM machines, which include a ferromagnetic core, e.g. [2, 75–77]. Coreless AFPM machines have been studied less frequently. Some examples include the multiobjective optimal design of coreless AFPM machines, discussed in [78–80], fractional slot winding configurations [81], and applications of such machines in wind turbine generators, [82, 83], electric vehicles, [19, 84], and airplanes, [18, 85].

Air-cored PM machines (also known as coreless or ironless electric machines) are attractive options for high speed applications due to the elimination of the stator core loss. On the other hand, all the conductors are exposed to the air-gap flux density hence have larger eddy currents, which is more critical at higher speeds. This

forces the application of thinner conductors and a larger number of turns and strands, necessitating the consideration of expensive Litz wires. Therefore the estimation of ac copper loss in the design stage in air-cored machine topologies is of utmost importance.

The axial component of flux density in AFPM air-cored configurations can be calculated reasonably accurately [86, 87] using the following

$$B_{az} = \sum_{\nu=1}^{\infty} B_{\nu} \cosh\left(\frac{\nu\pi}{\tau_p} z\right) \cos\left(\nu\phi\frac{p}{2}\right), \quad (2.12)$$

where ϕ is the angular position of the conductor; z axial position of the conductor, B_{ν} maximum flux density of the ν^{th} harmonic, τ_p pole pitch, p number of poles. This makes the use of fast and pure analytical methods for air cored machines more convenient.

The exemplified coreless machine in this study is shown in Fig. 2.9 and Fig. 2.10. For this 16 pole machine with 12 air-cored coils it was estimated that 72 turns can give the desired torque constant. All turns are in series and Litz wire application is not included. In order to calculate the winding losses using the hybrid method, a general time transient 2D FEA model is analyzed and flux density values are sampled in the coordinates of the center of each turn. The flux density is obtained by recording the variation of flux density in time.

Due to the axial symmetry shown in Fig. 2.11 and Fig. 2.12 the flux density observed by points 1 and 4, and also points 2 and 3 are the same. Furthermore, due to the rotation of the rotor, modeling the flux density variation with time for a single column of turns is sufficient. This indicates that modeling only 2 turns may suffice. This is especially interesting in case of the detailed and computationally expensive

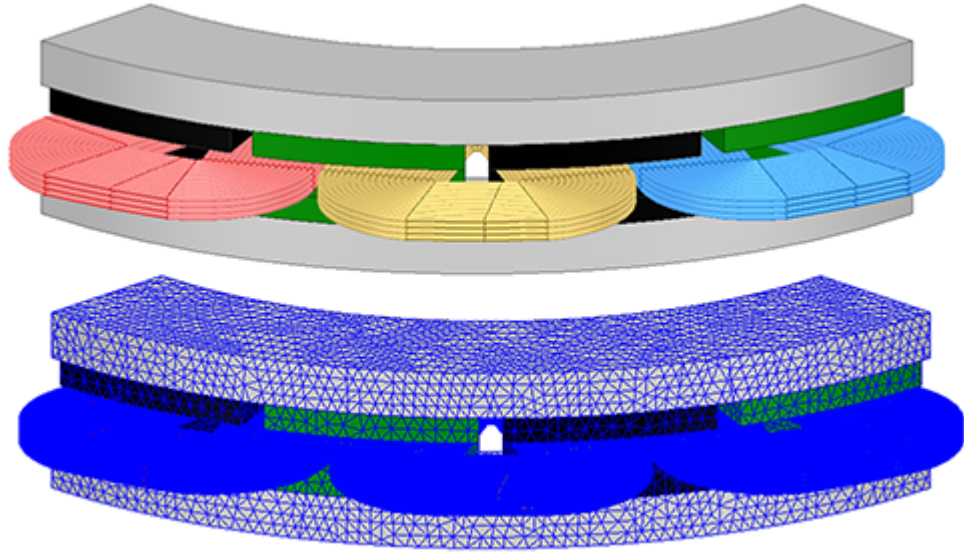


Figure 2.9: The 3D model of the coreless machine under study. Each turn is separately modeled and meshed.

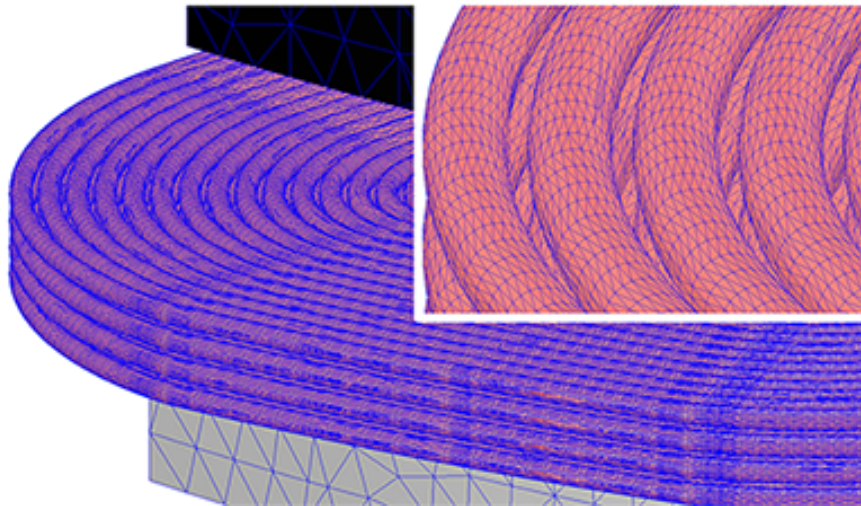


Figure 2.10: A zoomed view of the tetrahedral meshes in the conductors of the coreless machine.

FEA models [2]. Considerable reduction in computational efforts and mesh size (90% less number of mesh elements) is achieved by modeling only two turns for the coreless machine case study without affecting the accuracy of the results. It should be noted that such approaches for reducing the modeling efforts are applicable for eddy current loss calculation at open-circuit or cases where proximity effects are not considerable

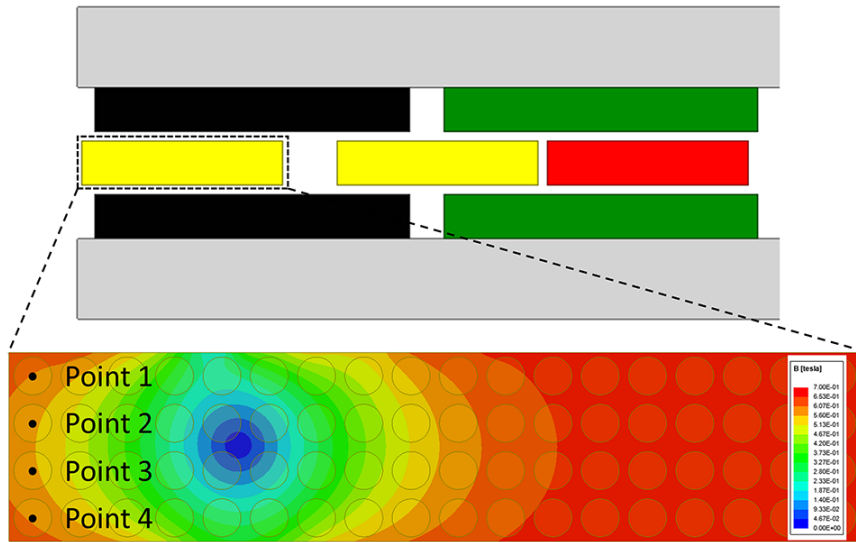


Figure 2.11: The general 2D model for sampling flux density values employed in the hybrid method. The coil cross section marked with dashed box is zoomed in to show the location of four sampling points in the center of round conductors.

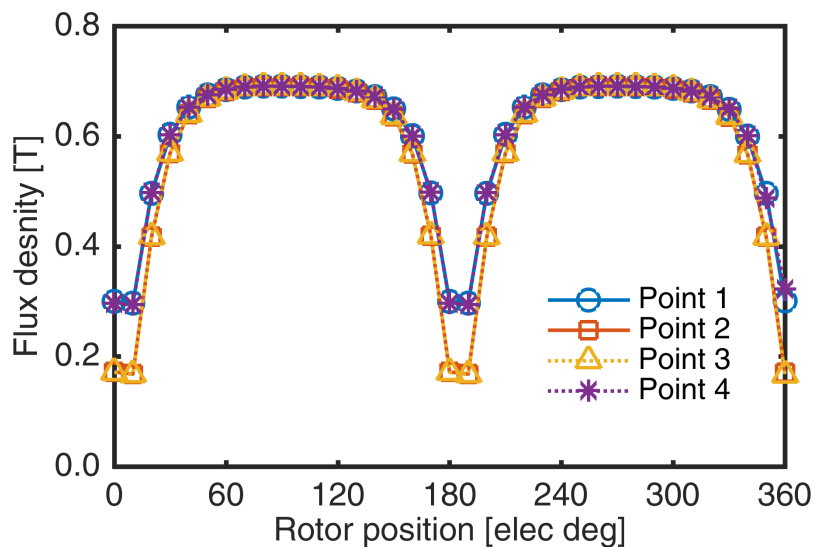


Figure 2.12: The flux density in the sampling points shown in Fig. 2.11 at different time steps.

and the eddy losses are mostly caused by the magnet flux. The calculation results are presented in a following section in comparison with eddy current losses of the second case study.

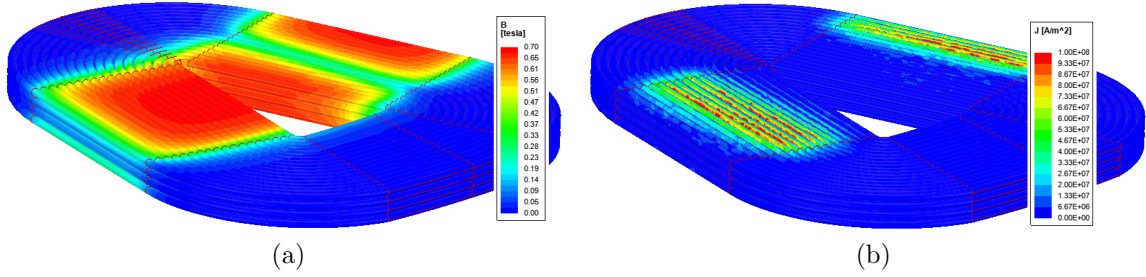


Figure 2.13: (a) Flux density obtained from the 3D FEA model of the coreless machine case study, illustrating the lower values closer to the end turns. (b) The current density distribution.

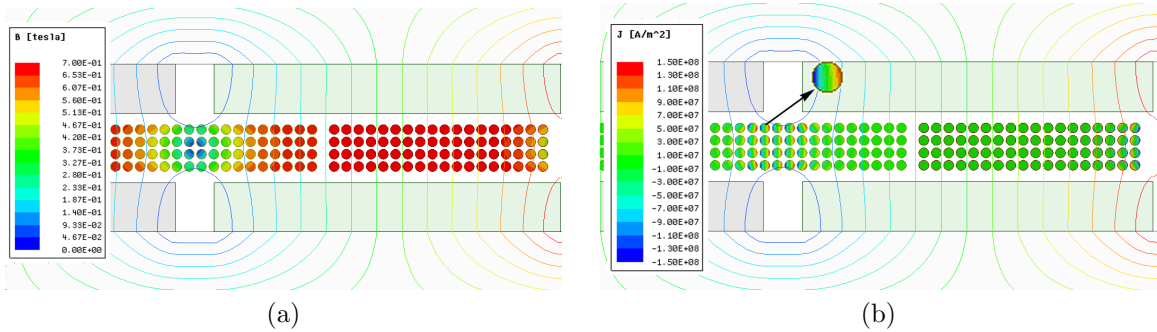


Figure 2.14: The 2D FEA model of the coreless machine under study: (a) flux density distribution and (b) current density distribution in conductors at open-circuit operation.

2.3.2 Open Slot Stator Core Axial Flux PM Machine

The second case study is an AFPM machine that employs a stator core with open slots, 20 poles and 24 slots. The 3D model of the optimally designed topology is presented in Fig. 2.15. The open slot machines due to their larger flux leakage, are prone to eddy currents and additional copper loss. The turns located on top of the slot experience larger flux density and hence have higher loss. Therefore each turn has a separate B_a which may not be uniformly distributed, necessitating separate calculation and data sampling for each turn.

Larger flux density and hence eddy current for conductors closer to the slot opening

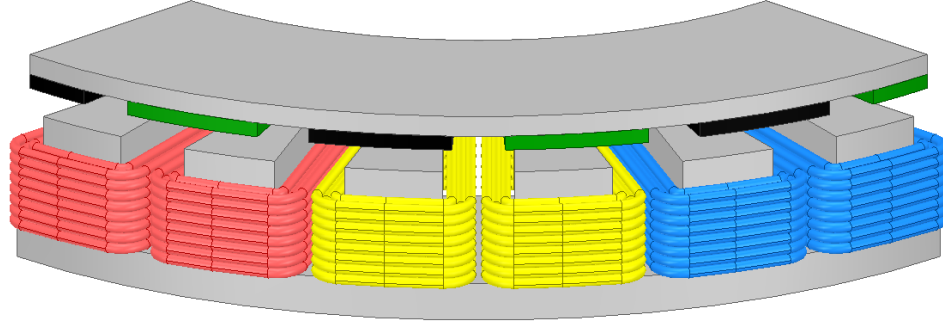


Figure 2.15: The 3D FEA model of the AFPM machine under study with open slot stator core.

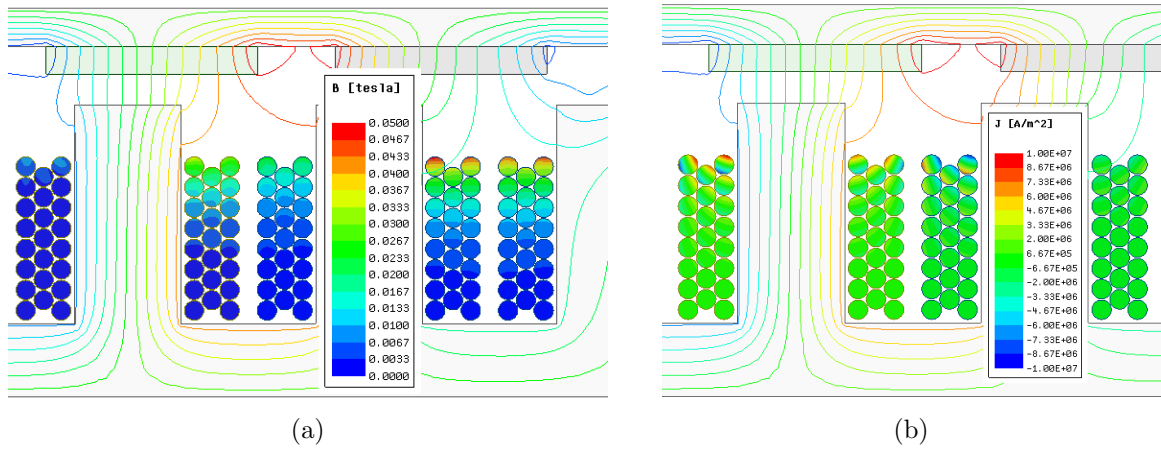


Figure 2.16: The 2D FEA model of the optimally designed AFPM machine with open slot stator core in which the circular conductors are utilized and placed further away from the slot opening: (a) flux density distribution and (b) current density distribution in conductors at open-circuit operation.

can be observed in Fig. 2.16. The eddy current losses can be reduced by placing conductors further away from the slot opening, Fig. 2.17. However, this reduces slot fill factor and hence requires increasing the current density and dc copper loss. The number of turns can be selected based on this trade-off between dc and additional ac copper losses. For this case study, the number and placement of the turns is selected to achieve the minimum copper losses at the rated frequency. The calculations are performed for different number of turns. As seen in Fig. 2.18, in this machine, 23 turns achieve the best balance between dc and ac components of copper losses. Other

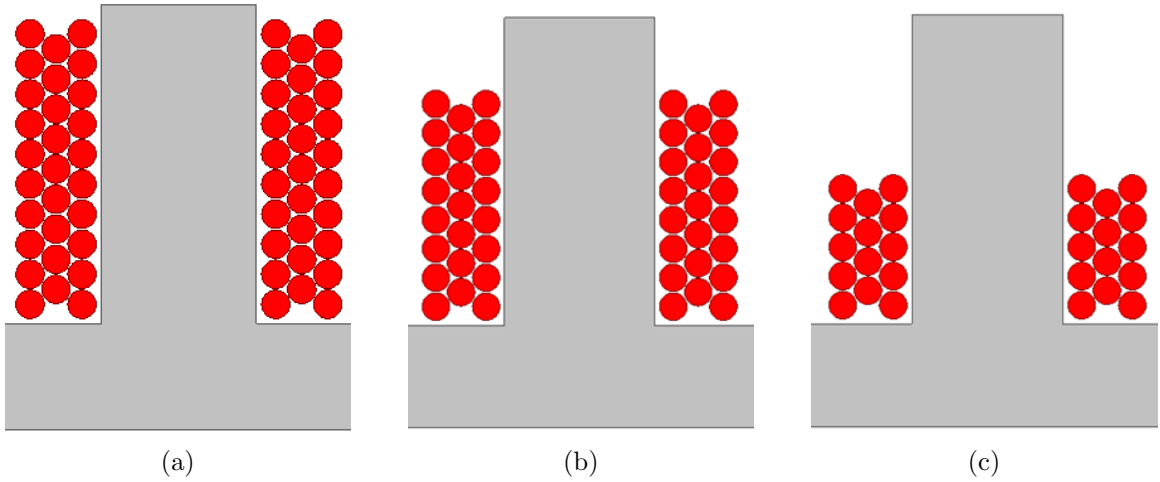


Figure 2.17: The open slot bound coils with (a) 29 turns, (b) 23 turns, and (c) 14 turns.

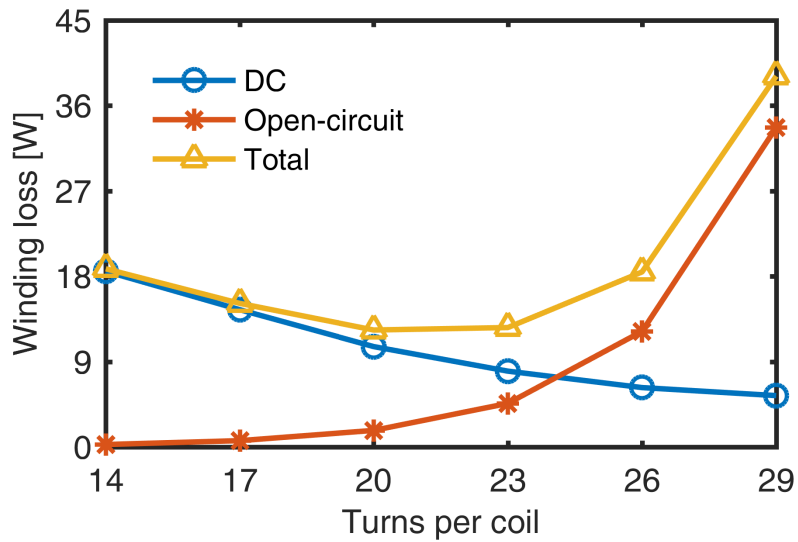


Figure 2.18: The winding dc and additional open-circuit eddy current ac losses with different number of turns at rated load.

solutions, such as the use of larger number of strands with smaller cross section can reduce the ac component of the copper loss, while reducing the fill factor and increasing the cost.

Another solution to reduce only the ac copper losses without increasing other losses is to employ conductors with square cross section, as shown in Fig. 2.19. The

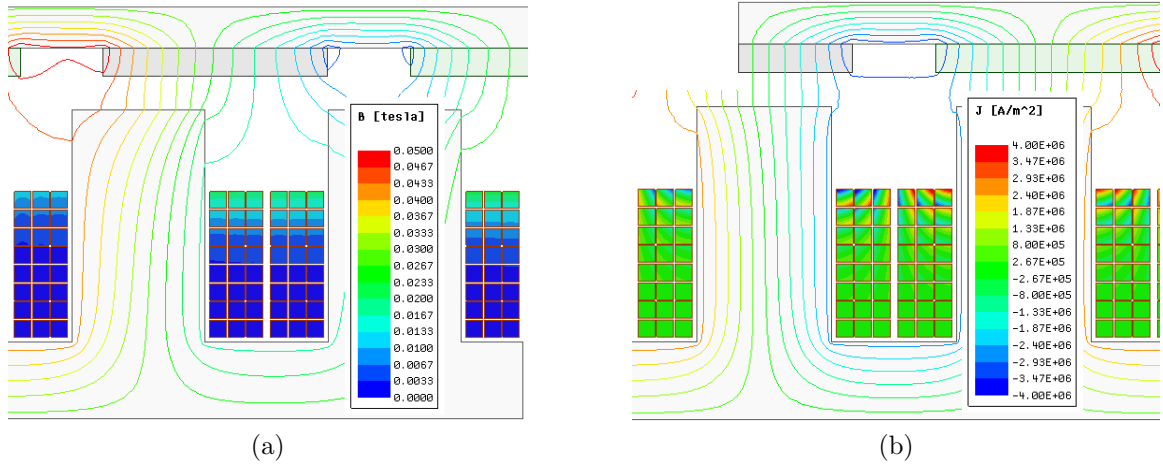


Figure 2.19: The 2D FEA model of the AFPM machine with open slot stator core, employing square conductors: (a) flux density distribution and (b) current density distribution in conductors at open-circuit operation. Note the reduction in flux density and current density compared to circular conductors in Fig. 2.16.

square shape of the wires helps in condensing the coil for the same overall conductor area, thus making it possible to locate the conductors further away from the air-gap, while maintaining the same dc copper losses. For this case study, the square wire dimensions are selected to give the same overall conductor area as the circular wires. The amount of reduction in losses for the machine under study is presented in Fig. 2.20. For this example study, it was observed that if the conductors with square cross section are placed at the same slot depth as the circular one, the overall conductor losses reduces due to greater slot fill factor, although the eddy current losses in both types of conductors are the same.

The mesh plot in Fig. 2.21 shows fine mesh for the turns closer to the slot opening and coarser mesh for the conductors located deeper in the slot. This reduces the computational efforts while maintaining the accuracy of the results.

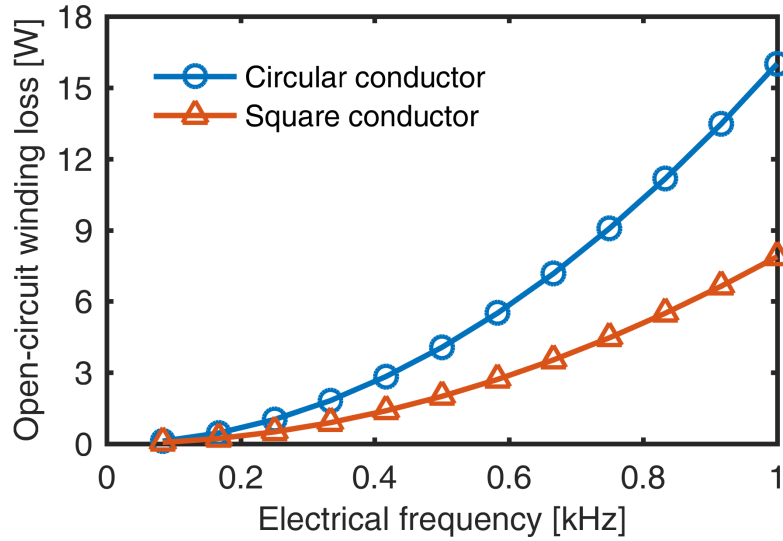


Figure 2.20: The additional eddy current copper losses at open circuit calculated with FEA for cases with circular and square conductors. The overall conductor area in both cases is maintained the same.

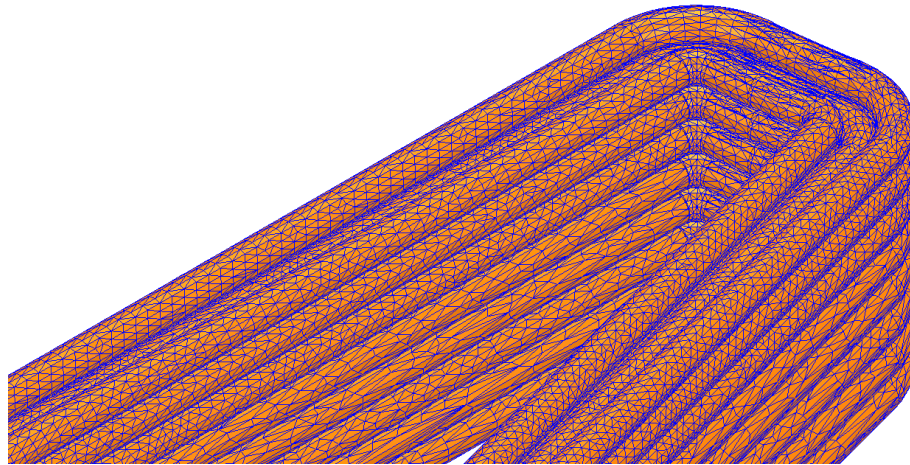


Figure 2.21: The mesh for the coil in the case study of the open slot AFPM machine. The turns closer to the slot opening are meshed finer.

2.4 Results and Discussion

The eddy current losses for each case study machine has been estimated using four methods. The calculations were performed for open-circuit and load, at a fundamental frequency of 1.6 kHz for the open-slot machine and at 480 Hz for the coreless

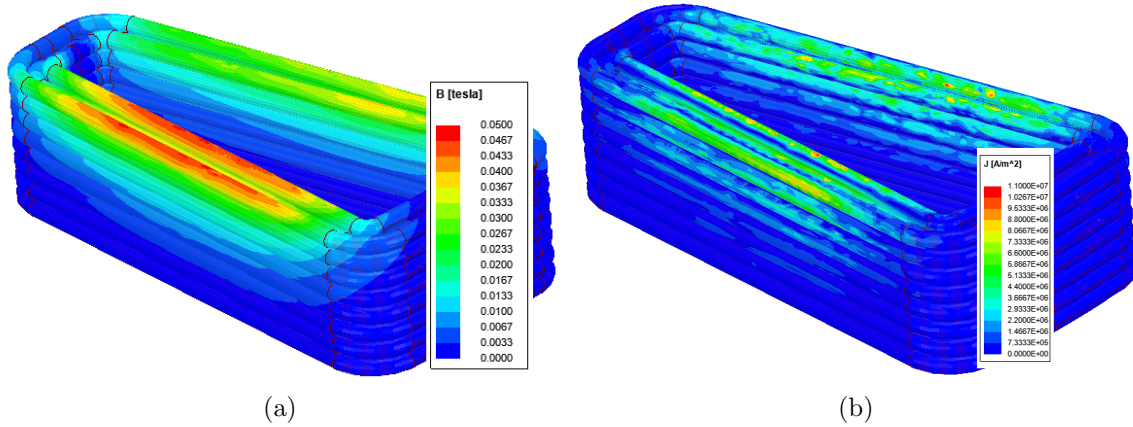


Figure 2.22: (a) The flux density observed by the conductors. The reduced flux density at the ends is due to the fringing and leakage. (b) The current density distribution.

design, respectively. A coreless machine operating at higher frequencies would typically require the use of Litz wire.

The results for different methods presented in Table 2.1 include only the additional ac induced eddy current losses in the windings and not the steady-state dc-type loss component due to the main supply current. The four calculation methods considered are:

- **3D FEA:** time-transient 3D FEA with detailed turn-by-turn, i.e., wire-by-wire, representation of the winding coils (considered the most accurate method),
- **Hy-3D:** the new hybrid method with samples of flux density obtained from a simplified 3D model (the proposed method),
- **2D FEA:** time-transient 2D FEA with turn-by-turn wire-by-wire representation of the winding coils,
- **Hy-2D:** a hybrid method with samples from a simplified 2D FEA.

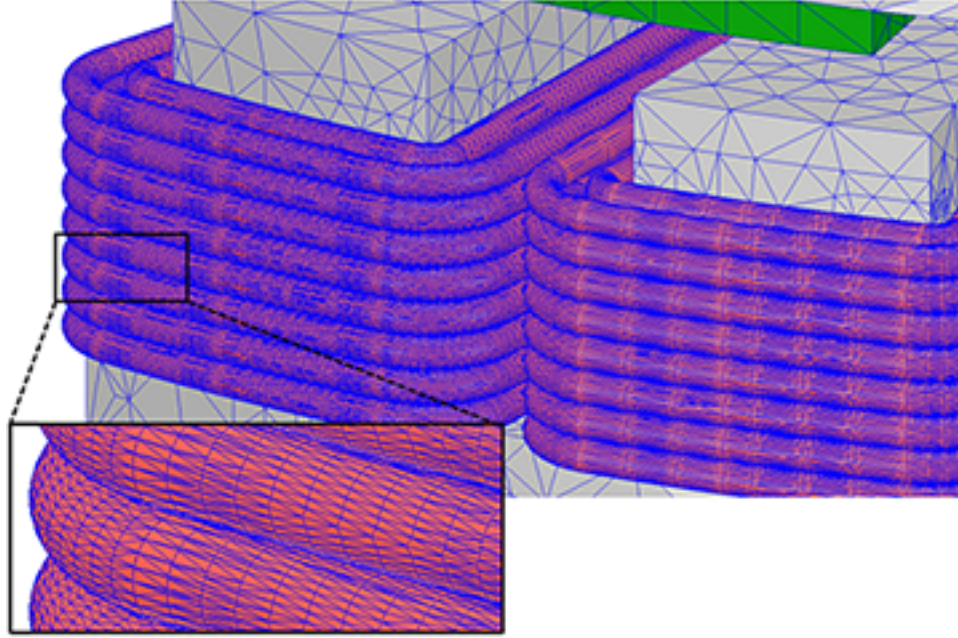


Figure 2.23: The 3D mesh plot for the turn-by-turn model of the AFPM machine with open slots.

An example mesh plot used with the first method, the detailed time-stepping 3D FEA, is presented in Fig. 2.23. The hybrid methods studied, i.e., Hy-3D and Hy-2D, employed time-transient analysis. Nevertheless, in principle magnetostatic analysis and adaptive meshing may also be used, which could further reduce the computational time. High performance computing system with 2 nodes and 32 cores per node are employed for large FEA calculations.

The additional eddy current losses calculated for the coreless machine example are significantly larger due to the winding conductors being exposed to the air-gap flux density. The results show increase in the additional winding loss for load operating conditions. This is because the varying flux density is not only originated from magnets, but also the ac current flowing in the neighboring conductors as well as the ac current inside the same conductor can induce additional eddy currents. Another

reason may be attributed to the increased variation of the flux density due to armature reaction, causing distortion and asymmetry in flux lines.

The new Hy-3D method takes into account the effect of end turns in the return path of eddy currents through the use of the correction factor, K_s , introduced in (2.4). The calculated K_s value is 0.98 for both machines, meaning that in these cases, the correction due to the end winding is minimal and the differences in results between methods may be substantially associated with the 3D field variation along the active sides of the coils.

In Table 2.1, the first method listed, the 3D FEA, is considered as the most accurate approach and its results serve for reference. For the example open slot machine, the estimation differences for the Hy-3D, 2D FEA, and Hy-2D methods are 3%, 16%, and 11% at open-circuit, respectively and 8%, 28%, and 11% on load, respectively, illustrating the advantages of the new Hy-3D method in terms of satisfactory estimation. It should be noted that for the coreless machine studied, the 2D based methods simply fail to provide any estimations suitable even for basic engineering calculations.

Although the new Hy-3D method takes longer to solve than 2D based algorithms, it is faster by one order of magnitude than the reference full 3D FEA and it is applicable for a wide range of problems. The saving in time becomes more significant when the ac copper loss calculation needs to be employed in the optimization. Any improvement in the speed will be multiplied by the number of required design evaluations by the optimization algorithm. Therefore, for optimization purposes, reducing the time one order of magnitude per design would achieve at least 3 orders of magnitude faster optimization.

Table 2.1: ADDITIONAL AC COPPER LOSSES IN THE WINDINGS DUE TO EDDY CURRENTS, CALCULATED WITH DIFFERENT FEA AND HYBRID METHODS FOR OPEN-CIRCUIT AND FULL LOAD OPERATING CONDITIONS.

AFPM machine	Eddy current loss	3D FEA	Hy-3D	2D FEA	Hy-2D
Coreless	Open-circuit [W]	420.5	424.0	611.7	520.3
Open slot	Open-circuit [W]	35.7	36.7	41.4	39.5
Open slot	Full load [W]	44.7	48.5	57.0	49.4
Approximate FEA computational time		37 hours	35 minutes	2 minutes	12 seconds

2.5 Experimental Study

The experiments and FEA validation is performed for a prototype AFPM machine with open slot and square conductors. The 3D FEA can be done by meshing all the conductors or only the top conductors that are responsible for the majority of the losses, as illustrated in Fig. 2.24. The computational efforts can be reduced without significant effect on the FEA results.

The separation of loss components, particularly ac and dc copper losses is a difficult task [2, 56, 64, 66]. The proposed method for open-circuit copper loss involves measurements performed with two distinct coil placements that have different clearances from the top of the slot.

First, the coils are placed closer to the air-gap by the help of 2 spacers. The motor with a spacer implementation is shown in Fig. 2.25. Then the spacers are removed, as shown in Fig. 2.26, the coils are placed at the bottom of the slot. The spinning loss, which includes the mechanical losses, such as friction and windage, stator core losses, open circuit copper, and PM losses, is measured in both scenarios. As confirmed by the numerical computations, the additional copper loss caused by the eddy currents when the conductors are placed further away from the top of the slot is

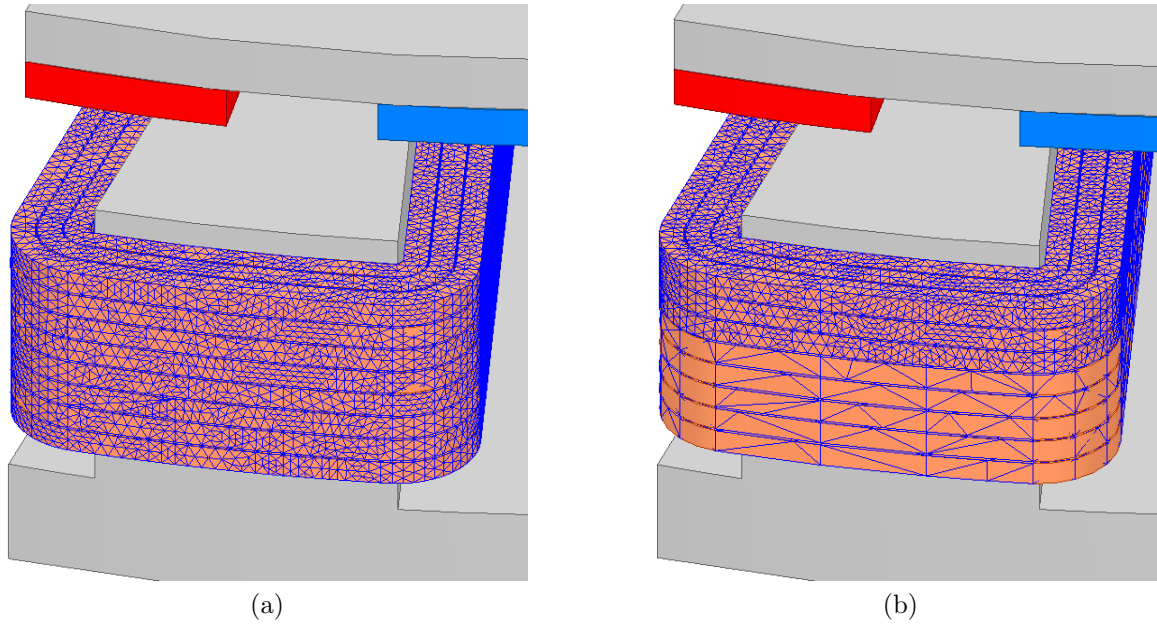


Figure 2.24: The 3D model of the prototype machine. The mesh can be fine for (a) all conductors or (b) only for the top conductors that cause the majority of open-circuit eddy current losses.

negligible. Therefore the additional (open-circuit) ac copper losses can be calculated by subtracting the two spinning loss measurements. The back EMF was ensured to be the same for the two measurements.

The measurements are performed at different rotational speeds and the results presented in Fig. 2.27. The FEA estimations are in good agreement with measurement, particularly for the larger speeds where the loss value is larger and hence more feasible to measure.

2.6 Summary

A new hybrid analytical-FEA method for calculating ac eddy current losses in electrical machine windings has been proposed. The new method is studied with special application for axial flux designs, such as those of the PM synchronous type. The



Figure 2.25: The prototype machine with spacers.

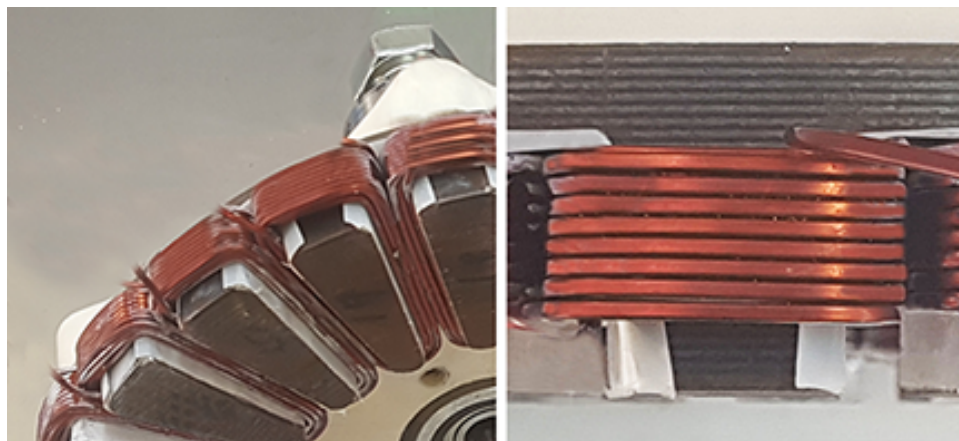


Figure 2.26: The prototype machine without spacers.

proposed approach brings a major improvement above more conventional FEA based hybrid methods by considering the variation of the flux density in a 3D dimension, namely radial in the case of an axial flux machine and axial for a radial flux machine.

The computational results for two case studies of AFPMP machines show that the new method is superior to other hybrid FE techniques in terms of accuracy and that its results satisfactorily compare with reference detailed 3D FEA, while reducing the computational time by one order of magnitude. The new method achieves a trade-off between speed and precision, making it suitable for different stages of the design process of an electrical machine including the optimization.

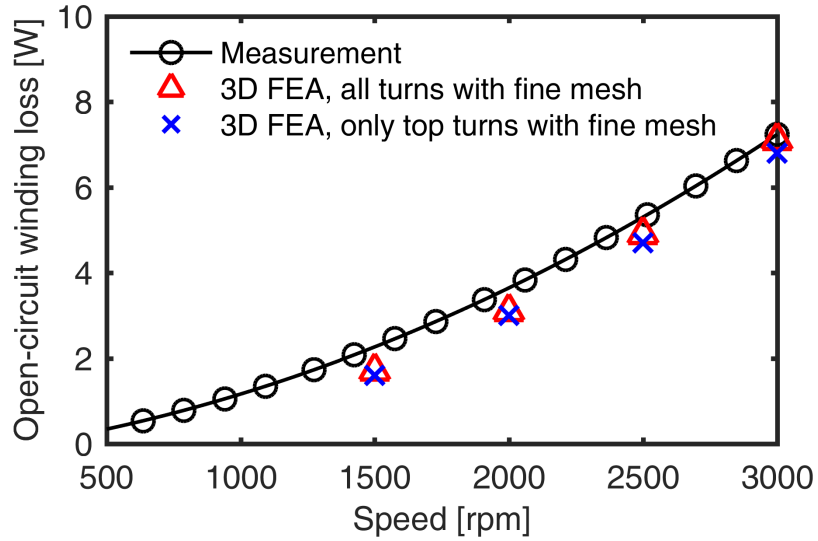


Figure 2.27: The measurements of ac copper loss and validation of 3D FEA calculations.

An approach for the measurement of ac winding loss is proposed and conducted for an open slot AFPM machine. The measurements are in close agreement with the results from 3D FEA. Other matters discussed are the selection of the number of turns, the comparison of circular and square conductors, and approaches for reducing mesh size and hence FEA computational time.

Chapter 3

Design of Experiments and Response Surface Methodology in Electric Machine Design

A systematic method to optimally design an electric machines is to employ design of experiments (DOE) and response surface methodology (RSM). These two approaches, i.e., DOE and RSM, are statistical designs methodologies that plan specific experiments (designs, in case of electric machine) and analyze the resulting data so that valid and objective conclusions are obtained [88]. The results can be employed for sensitivity analysis, robust design, selection of optimization variables, etc.

In this chapter two example studies of application of DOE and RSM in the process of designing an electric machines are provided. The first study employs RSM to statistically design the machine. This is a common usage for a fast optimization. The second study innovatively employs DOE and RSM in tracing down the manufacturing tolerances. This is used to narrow down the possible out of specification properties of prototyped machines in order to point out the cause(s) of discrepancy between design and actual performance.

3.1 Introduction

Response surface methodology (RSM) is essentially a set of mathematical and statistical methods used to aid in finding a particular solution for a system in which several input variables influence the performance. The input variables (factors) need to be independent of each other. The performance of the system can be measured by output parameters (responses) as a function of factors. The observed trends can be employed to select an optimum design. A regression model (response surface), can be used to relate the factors to the output parameters. A 2^{nd} order polynomial function is expressed in the following,

$$\begin{aligned}
 Y = & \beta_0 + \sum_{i=1}^{d_\nu} \beta_i X_{Ci} + \sum_{i=1}^{d_\nu} \beta_{ii} X_{Ci}^2 + \\
 & \sum_{i=1}^{d_\nu} \sum_{j=i+1}^{d_\nu} \beta_{ij} X_{Ci} X_{Cj} , \tag{3.1} \\
 X_{Ci} = & \frac{x_i - (x_{i,max} + x_{i,min})/2}{(x_{i,max} - x_{i,min})/2} ; i = 1, 2, \dots, d_\nu,
 \end{aligned}$$

where Y is a response parameter; β , the regression coefficient; d_ν , the number of factors, x_i , the i^{th} input factor; and X_{Ci} , the normalized (coded) value of the i^{th} factor. Factors may be normalized as shown in (3.1). $X_{Ci} = 0$ represents the specified values of the factors with zero manufacturing error, and β_0 is a representation of response parameter in this reference situation. β_{ii} and β_{ij} illustrate second order effects and interaction between the factors.

By fitting such regression curves, many fast design performance evaluations can be performed in a short time, sensitivity analysis can be executed, and as it is shown in different sections of this dissertation, other innovative advantages can be extracted,

such as defining the range of design variables and narrowing down the manufacturing tolerances.

The accuracy of the outcomes of such studies highly depends on the resolution of design of experiments. Full factorial designing, that include all the possible combination of design variables, with many levels can capture the relation between responses and factors more accurately, however, they are computationally expensive and in some cases not necessary. In most cases, carefully assigned fractional factorial designs, with reduced number of required experiments (FEA design evaluations in case of an electric machine design problem) can achieve reasonable results. Some common methods are Central Composite designs, Box-Behnken designs, and taguchi methods. The details of each of these methods can be found in various sources including [88, 89]. In the following sections, examples of implementation of DOE and RSM are presented.

3.2 Coreless and Conventional AFPM Motors for Solar Cars

Some of the advantages and properties of coreless machines is previously discussed in Section 2.3.1. The coreless AFPM machines configurations may be a suitable option for in-wheel drive application.

In case of the in-wheel (direct-wheel) drive systems, the motor is embedded inside the wheel, which offers the potential to eliminate some of the mechanical components, consequently simplifying the system. The solar cars with three wheels, can be configured to have two front wheels and one rear driving wheel with the motor inside.

The cars with four wheels can have two rear driving wheels. In this study, both cases are included. The machines considered for use in solar cars with one or two driving wheels are: a conventional single rotor–single stator core machine, based on a commercially available NGM SC-M150 motor [90] and a coreless multi-disk configuration with air-gap concentrated windings. The comparative study is based on the design of experiments (DOE) and response surface methodology (RSM), and several thousand candidate designs for both types of machines are studied. During the course of the comparison, the main dimensions of both machines are maintained the same, to ensure that they accommodate inside the same wheel. The DOE and RSM techniques are used to observe the relative trend between performance parameters and select the best designs.

3.2.1 Solar Car Electric Motor Specifications

The reference motor for this study is represented by the NGM SC-M150 unit that has been used in the Gato del Sol IV solar car at University of Kentucky, Fig. 3.1. This motor, which has a 36 slot stator core with distributed windings and a 12 pole rotor core with surface mounted PMs, as shown in Fig. 3.2, has been modeled in 3D (Fig. 3.3) and analyzed by the transient electromagnetic FEA.

The power system includes a solar panel connected to a boost converter performing the function of maximum power point tracking which feeds the 3 phase inverter driving the traction motor. A Li-ion battery is used to power the machine during shading, when high bursts of power are required, and also to absorb power during regenerative braking.



Figure 3.1: Gato del Sol IV solar car from University of Kentucky.

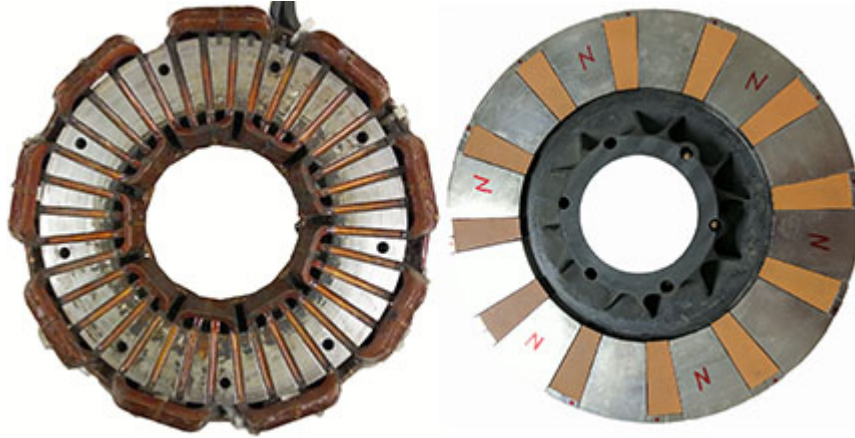


Figure 3.2: The 36 slot stator of the NGM SC-M150 motor installed in Gato del Sol IV solar car together with its 12 pole rotor.

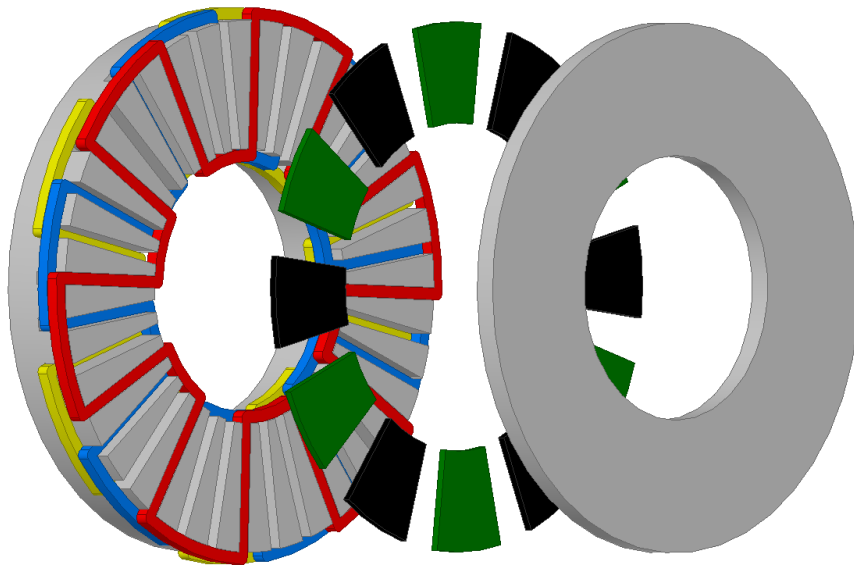


Figure 3.3: Exploded view of the 3D model of the NGM SC-M150 motor with 36 stator slots and 12 rotor poles.

In addition to electromagnetic considerations, mechanical challenges of a small air-gap in AFPM motors should be taken into account. For a thinner air-gap, the smallest amount of arching of the axle, caused by unsprung mass, becomes problematic. Therefore, it is preferred to use the largest air-gap possible while maintaining the performance parameters. The specification of the reference motor (Table 3.1) limits air-gap thickness between 1.8 to 5 mm. One objective of this study is to re-design the NGM SC-150 machine, in order to meet the rated torque requirements with the largest possible air-gap, as well as minimum losses and mass.

Another objective is to design a coreless machine to be employed with two driving wheels in the same solar vehicle, with minimum loss and mass, and the largest feasible air-gap. The 3D model representation with flux lines and flux density distribution of both machines under study are illustrated in Fig. 3.4. In case of the coreless machine, the required mechanical support for the discs in the middle can be provided by advanced engineering composite plastic materials, as represented in Fig. 3.5. These materials have good thermal properties, low weight, and no extra losses [91] and [92].

In AFPM machines the torque is directly proportional to the cube of the diameter, hence, employing largest feasible diameter is recommended which is 248 mm and limited by the dimensions of the wheel. The yokes also perform as part of the frame of the wheel, therefore the total axial length is constant and dictated by the wheel dimensions.

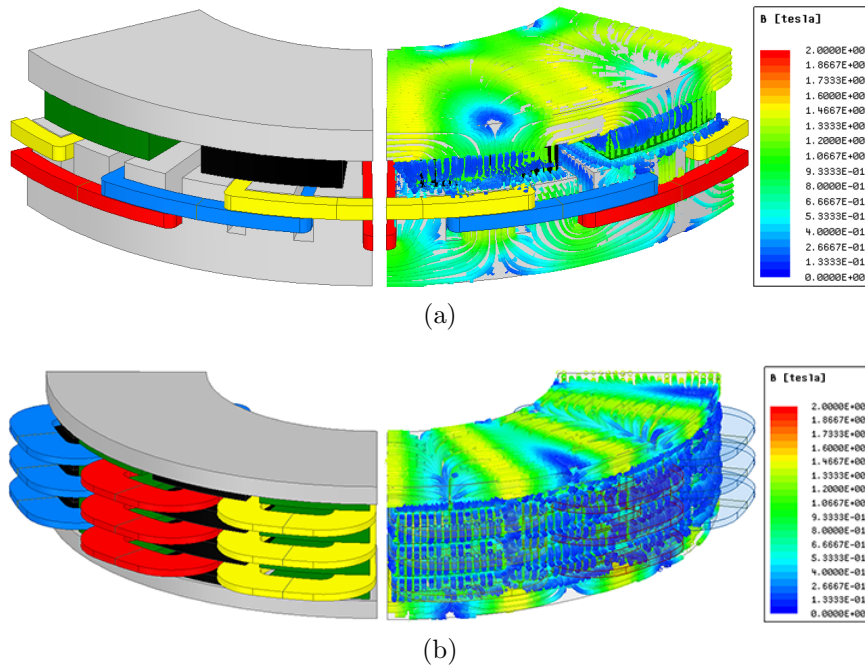


Figure 3.4: The 3D model and electromagnetic field for (a) the conventional, and (b) the coreless machines considered.

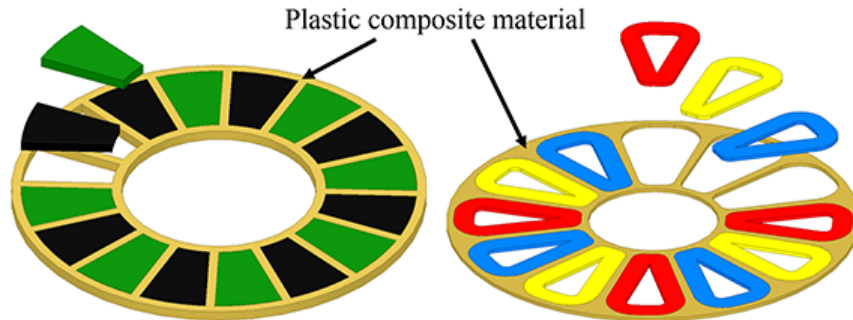


Figure 3.5: Schematic of a coreless stator and rotor employing a plastic composite structure for mounting and supporting magnets and coils.

3.2.2 Winding Factor Calculation for Air-gap Concentrated winding

The fundamental winding factor is an index used to compare winding configurations. Elimination of stator core and slots results in removing mechanical constraints of positioning coil sides. For the coreless machine, concentrated windings are considered due to their shorter end coils, lower copper mass, and less manufacturing

Table 3.1: Specifications and main dimensional properties of the NGM SC-150 (conventional) AFPM motor.

Rated Torque	56 Nm
Rated speed	400 rpm
Air gap	1.8-5 mm
Active outer diameter	248.0 mm
Total axial length	52.5 mm
Steel mass	11.2 kg
PM mass	0.6 kg
Copper mass	2.2 kg
Total active mass	14.0 kg
Number of poles	12
Number of slots	36
Number of coils per phase	6

complexity as compared to the distributed winding.

Winding factor is defined as the ratio of the induced electromotive force (EMF) to the EMF that would have been induced in the ideal case. The ideal situation is considered where the induced EMF in all conductors have identical phases and maximum magnitude. In case of a conventional AFPM machine this is achieved for full-pitch, non-skewed winding, with one slot per pole per phase. For a non-skewed conventional machine, winding factor, k_w , can be represented by the product of pitch factor, k_p , and distribution factor, k_d . In case of a coreless machine, the coils are exposed to the continuously varying air-gap flux density. This causes the induced EMF in adjacent conductors, even in the same coil side, to have different phases from one another. Moreover, in the axial direction, conductors closer to PMs will have EMF with a higher magnitude. Such that only conductors at the closest layer to PMs have the maximum EMF. Therefore, additional distribution factors in circumferential and axial direction need to be taken into account. As explained in the following, the effect of phase shift between EMF of adjacent conductors is captured by $k_{d\phi}$ and the effect

of varying magnitude by axial position is captured by k_{dz} .

So far, efforts in estimating winding factor for coreless machines has been executed with over-simplifications. Studies are conducted overlooking the distribution factor in the axial direction or neglecting the gap between phase bands [18, 93, 94]. The calculations dedicated to linear coreless machines [95, 96] do not consider the variation of coil pitch to pole pitch ratio with respect to diameter which is the case for AFPM coreless machines.

For a fractional-slot concentrated winding, in a machine with a slot pole combination such as 12-slot 8-pole or 24-slot 16-pole, the distribution factor is unity. However, in case of air-gap concentrated windings employed in coreless machines, the distribution factor within the same coil band, in the axial and circumferential directions, should be considered. The winding factor, k_{wn} , can be calculated as

$$k_{wn} = k_p \cdot k_{d\phi} \cdot k_{dz} , \quad (3.2)$$

where n is the harmonic order, and $k_{d\phi}$ and k_{dz} are distribution factors in circumferential and axial direction, respectively.

Pitch factor: Considering a concentrated coil, with cylindrical cut at an arbitrary diameter represented in Fig. 3.6 and 3.7, the ration of the phasor sum to arithmetic sum of n^{th} harmonic of the induced EMF in two coil sides can be estimated as

$$k_p = \left| \frac{E - Ee^{-j\frac{n\pi\tau_c}{\tau_p}}}{E + E} \right| = \sin \left(\frac{n\pi\tau_c}{2\tau_p} \right); \quad \tau_c = \frac{\pi D}{N_c} - W_c , \quad (3.3)$$

where τ_c and τ_p are coil and pole pitch, D is the diameter, N_c number of coils per stator disk, and W_c is the coil width. It is important to note that the ratio of coil

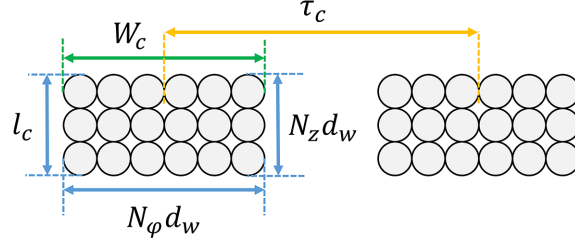


Figure 3.6: Radial cut-out of a concentrated coil.

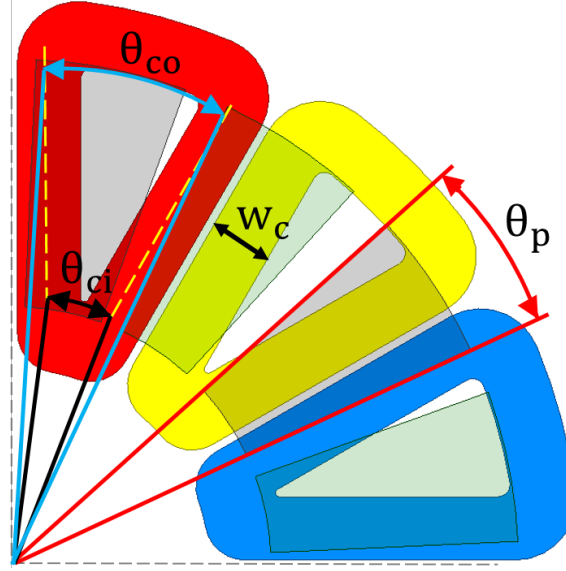


Figure 3.7: Coil pitch angle variation with diameter. The magnets are included in the plot and are transparent.

pitch to pole pitch angle, $\frac{\theta_c}{\theta_p}$, varies with diameter, as shown in Fig. 3.7, resulting in varying $\frac{\tau_c}{\tau_p}$. Therefore, for an accurate estimation of pitch factor, integration of (3.3) from inner to outer diameter is performed. It can be shown that the maximum fundamental pitch factor is attained at $\frac{w_c}{\tau_p} = \frac{p}{N_c} - 1$.

Distribution factor in the circumferential direction: For coreless machines with air-gap concentrated windings, distribution factor within the same coil band, in the

circumferential direction, can be calculated as

$$k_{d\phi} = \frac{\sin\left(\frac{\pi W_c}{2\tau_p}\right)}{N_\phi \sin\left(\frac{\pi d_w}{2\tau_p}\right)}, \quad (3.4)$$

where d_w is the diameter of each conductor and N_ϕ is the number of turns in coil band in circumferential direction and can be estimated as $N_\phi = \frac{W_c}{d_w}$. In coreless winding the use of Litz wire with thin conductors is common, which results in

$$d_w \approx 0 \rightarrow k_{d\phi} = \frac{2\tau_p}{\pi W_c} \sin\left(\frac{\pi W_c}{2\tau_p}\right). \quad (3.5)$$

Variation of τ_p with diameter should be taken into account through an integral form of (3.5). Larger $k_{d\phi}$ is expected to be obtained with smaller coil width.

Distribution factor in axial direction: The axial component of flux density in a coreless machines is a function of angular position, ϕ , and axial position, z , such that a higher flux density is seen by conductors closer to PMs. This effect is more significant in case of a thicker coil and larger electromagnetic air-gap. The z component of flux density can be obtained by

$$B_z(\phi, z) = \sum_{n=1}^{\infty} B_n \cosh\left(\frac{n\pi}{\tau_p} z\right) \cos\left(n\phi \frac{p}{2}\right). \quad (3.6)$$

Detailed calculations of B_n can be found in [95, 97]. Figure 3.8 represents that this analytical estimation of B_z for an example design is in agreement with the numerical results obtained from FEA.

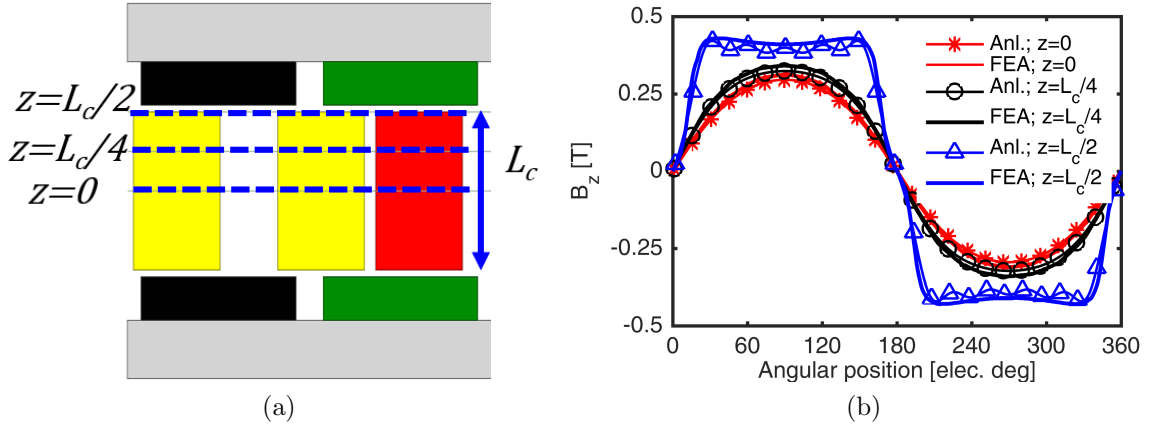


Figure 3.8: Analytical and numerical calculation of axial component of flux density at different axial positions for a coreless AFPM machine.

Based on (3.6) the winding factor in axial direction can be calculated from

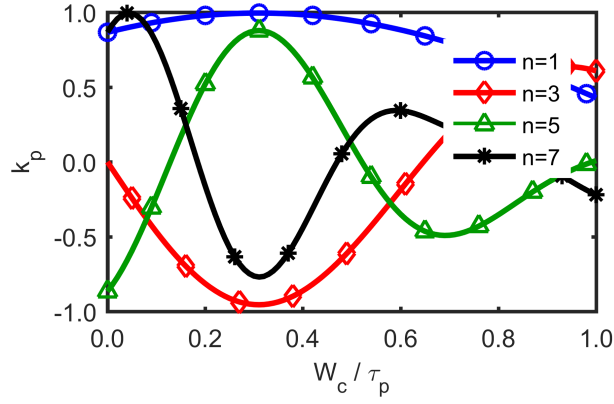
$$k_{dz} = \frac{2 \sum_{i=1}^{N_z/2} \cosh\left(\frac{n\pi d_w}{2\tau_p}(2i-1)\right)}{N_z \cosh\left(\frac{n\pi L_c}{2\tau_p}\right)} = \frac{\tanh\left(\frac{n\pi L_c}{2\tau_p}\right)}{N_z \sinh\left(\frac{n\pi d_w}{2\tau_p}\right)}. \quad (3.7)$$

Considering that Litz wires are employed yields,

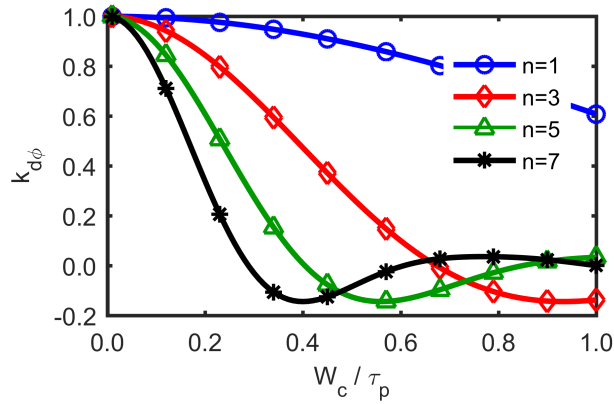
$$d_w \approx 0 \rightarrow k_{dz} = \frac{2\tau_p}{n\pi L_c} \tanh\left(\frac{n\pi L_c}{2\tau_p}\right). \quad (3.8)$$

Again, due to diameter dependent τ_p , integration of (3.8) should be considered.

The variation of winding factor components with respect to $\frac{W_c}{\tau_p}$ and $\frac{L_c}{\tau_p}$ at different harmonics, for a 16 pole 12 coil topology, is plotted in Fig. 3.9. The fundamental winding factor variation, illustrated in in Fig. 3.10, shows that largest winding factor is obtained when the coils are axially as thin as possible and the coil width is closer to $\left(\frac{p}{N_c} - 1\right) \cdot \tau_p$.



(a)



(b)

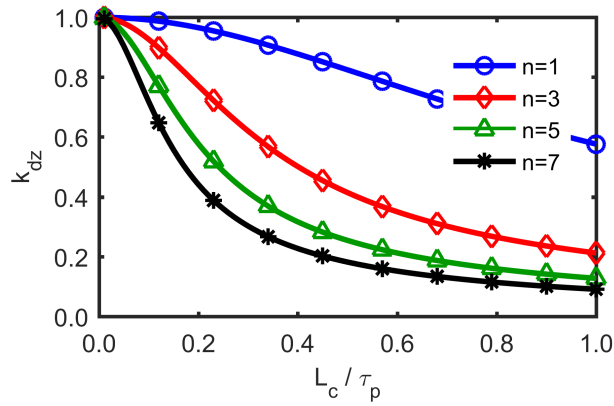


Figure 3.9: (a) Pitch factor, and (b) distribution factor in circumferential direction with respect to coil width to pole pitch ratio; and (c) distribution factor with respect to coil height to pole pitch ratio, plotted at different harmonics for a 16 pole 12 coil topology with concentrated coreless winding.

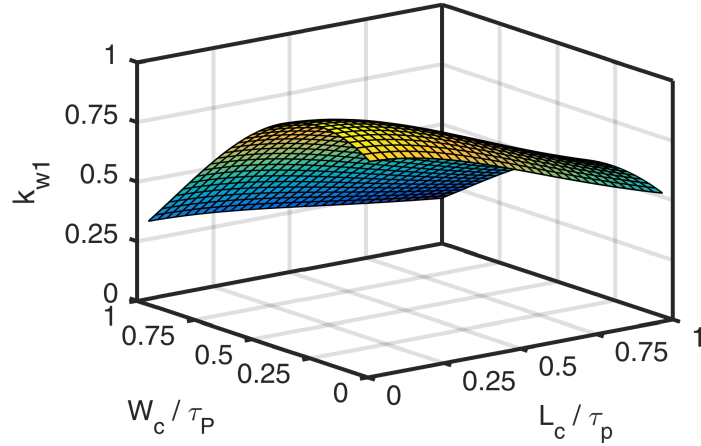


Figure 3.10: Fundamental winding factor for the 12 coil 16 pole topology.

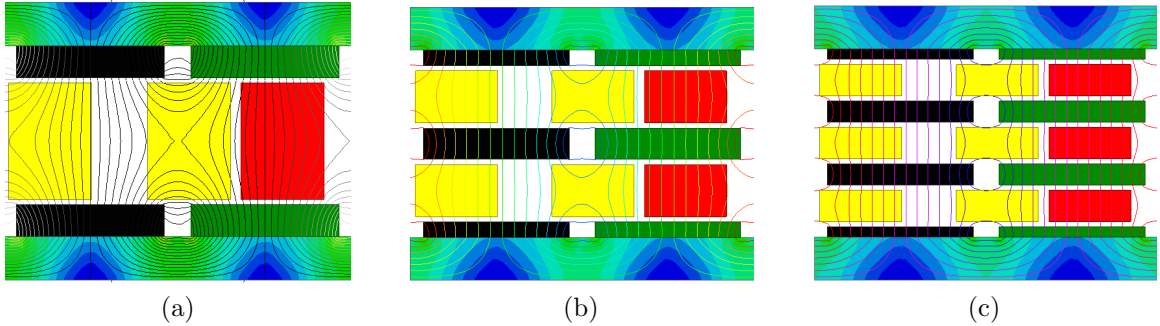


Figure 3.11: Flux lines of multi-disk AFPM machines with different number of disks.

3.2.3 Specifications and Design Considerations of the Coreless AFPM Motor

The coreless machine is considered to be employed for a two-driving wheel application, therefore, each of the motors should produce half the required torque within the same outer dimensions (diameter and axial length) as the conventional machine.

Selecting the Number of Disks:

The larger electromagnetic air-gap, caused by the elimination of stator core, reduces flux linkage and torque. This may be compensated for by the use of multiple

Table 3.2: Torque density and fundamental winding factor for 16 pole 12 coil topology with different number of stator disks.

Number of stator disks	1	2	3
Torque density [Nm/kg]	2.5	2.9	3.0
Winding factor	0.680	0.826	0.860

disks. The use of multiple coreless stator disks also reduces the coil thickness, improving the winding factor by increasing the distribution factor in axial direction as shown in (3.8).

In order to evaluate the appropriate number of stator disks—and accordingly the number of rotor disks— three models with one, two, and three stators are studied for an example coreless AFPM with 12 coils per stator disk and 16 poles. In the course of the comparison, the copper losses, air-gap, active volume, PM mass, and steel mass are kept constant.

The higher flux leakage and smaller winding factor for lower number of disks reduces torque density (Fig. 3.11 and Table 3.2). The designs with multiple stator disks demonstrate significant performance improvement with higher winding factor. For those reasons, the design with three stators is selected, although it may be noted that a higher number of disks may lead to difficulties in the manufacturing process.

Selecting the Combination of Poles and Coils:

A wide array of number of stator coil and rotor pole combinations is possible for this machine, and the comparative performance of some representative ones is studied. The electromagnetic air-gap is maintained the same for all designs by keeping the axial thickness of the coils, L_c , constant during the comparison. The total PM and steel mass are also kept the same. The thickness of the rotor core is dictated by mechanical

strength constraints, considering that back plates are also functioning as part of the frame.

A larger number of poles necessitates increasing number of coils to maintain a reasonable fundamental winding factor. For a diameter constrained application, the use of a large number of coils results in reduced coil width and end turn volume such that the total copper mass reduces. This can be quantified by estimating the mean turn length, l_{mt} ,

$$l_{mt} = (D_o - D_i) + \frac{\pi(D_o + D_i)}{N_c}, \text{ and } W_c = \frac{\pi D_i}{2N_c}, \quad (3.9)$$

where D_o and D_i are the outer and inner active diameter. Coil width, W_c , is constrained by inner diameter and is set on maximum possible value to reduce current density and improve DC copper loss. The total copper volume for 3 stator disks is calculable by

$$V_c = 3N_c W_c L_c L_{mt} = \frac{3\pi D_i}{2} L_c \left[(D_o - D_i) + \frac{\pi(D_o + D_i)}{N_c} \right] \quad (3.10)$$

where V_c is the copper volume. Thus, in the case of a constant fill factor, as N_c increases, V_c and consequently mass decrease.

Core losses in air-cored machines are small considering that steel is only used in the rotor. These losses can be further reduced and made negligible by approaches such as multi-layer windings that significantly decrease harmonics that only cause losses [98]. For those reasons, core losses are not accounted for in this comparison.

Litz wire is used to prevent skin effects at higher frequency, which can be quite substantial for this machine. Using such special conductor wires reduces the fill

Table 3.3: All the designed machines produce 28 Nm at 400 rpm.

Poles	8	10	16	20	30	32
Coils	6	6	12	12	18	24
k_{w1}	0.877	0.833	0.860	0.810	0.776	0.805
Cu mass [kg]	3.9	3.9	2.7	2.7	2.2	2.0
Cu loss [W]	288	305	221	239	245	236
Elec. eff. [%]	86	85	89	88	88	88

factor, and a 20% reduction is considered in the study. Assuming 120°C maximum winding temperature, increased copper resistance due to temperature rise is taken into account.

The electromagnetic torque of a non-salient AFPM machine can be estimated as

$$T = \frac{3p}{2} \lambda_m I ; \quad \lambda_m = \frac{2}{\pi} k_{w1} N_t k_{vg} \alpha_i B_{go} \tau_p L_{Fe} , \quad (3.11)$$

where p is pole number; λ_m , magnetizing flux linkage produced by PMs; N_t , number of turns per phase, which is constant for all the designs in Table 3.3; k_{vg} , the ratio of the amplitude of the fundamental wave to the average value of the air-gap flux density; α_i , pole arc to pole pitch ratio; B_{go} , the peak value of the open-circuit flux density; τ_p , pole pitch; and L_{Fe} , the core length. As the number of poles and coils increases, λ_m decreases, mainly due to reduced flux collecting area proportional to the pole arc, and partly because of higher leakage. Magnetizing flux linkage reduction due to lower τ_p is negated by higher number of poles while λ_m reduction due to increased leakage is compensated for by increasing current to produce constant torque.

The copper losses, P_{cu} , can be calculated from

$$R_{ph} = \frac{L_{mt} N_t}{\sigma W_c L_c S_{ff} / N_t} , \quad P_{cu} = 3 R_{ph} I_{rms}^2 = \frac{V_c J^2 F_f}{\sigma} , \quad (3.12)$$

where R_{ph} is the resistance of one phase winding; σ , is the copper conductivity; and F_f is the fill factor. Decrease in copper mass, due to reduction in the length of mean turn, and increase in J , to produce 28 Nm, results in minimum copper loss for 16 and 20 pole designs. The topology with 16 poles has higher winding factor. Other benefits of this topology are avoiding manufacturing complexities associated with higher number of poles, and relatively low copper mass. Therefore 16 pole and 12 coil topology is selected to be a good compromise. It is to be noted that for designs with space limitations, a higher number of poles will result in reduced total diameter due to decreased thickness of end coils.

3.2.4 Factors and Responses for DOE and RSM

The objectives to be met in case of both conventional and coreless topologies are to achieve least mass and losses while producing the required torque at the rated speed. It is assumed that cost is not a constraint.

Six independent factors, that considerably influence the performance of the conventional motor, are selected (Fig. 3.12a and Table 3.4), including: the mechanical air-gap, g , PM length, h_{pm} , tooth width to slot pitch ratio, k_{tw} , pole arc to pole pitch ratio, α , stator yoke length, h_{sy} , and rotor yoke length, h_{ry} . The outer and inner diameter, and total axial length are maintained the same as in the reference motor, limited by the wheel dimensions. In order to capture the non-linearities associated with the response surface, 3 levels for each factor are considered. A full factorial design for 6 factors with 3 levels requires 729 runs which is not feasible. Instead,

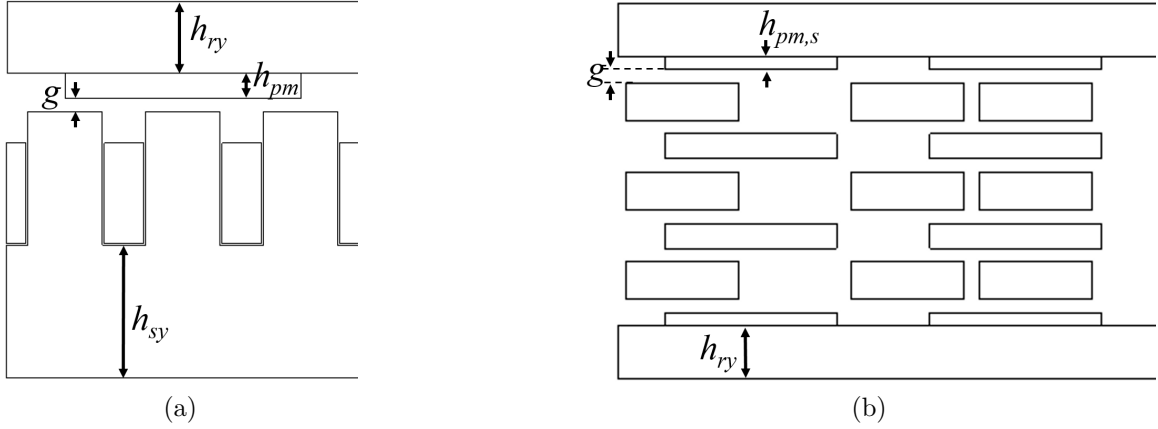


Figure 3.12: Dimensional variables selected as factors for DOE of (a) conventional, (b) coreless machine.

fractional factorial, Box-Behnken, or Central Composite designs may be used. Box-Behnken design requires less runs however it contains regions with poor prediction quality. Central Composite design provides relatively high quality predictions over the entire design space. For this case, face central composite design, with 6 factors and 3 levels, that needs only 100 runs, has been used. The FEA evaluations of these designs have been used to establish a regression model and then study above 4,000 designs.

In case of the coreless machine having no stator core or teeth, the number of factors is reduced to four, including the mechanical air-gap, g , the PM length on the rotor disks on two sides, $h_{pm,s}$, the pole arc to pole pitch ratio, α , and the stator yoke length, h_{sy} , as described in Table 3.5 and Fig. 3.12b. The PM length in the middle rotor disks $h_{pm,m}$, is set to be twice that in the ends, which results in higher torque. Due to the lower number of factors, full factorial DOE with the number of levels increased to 4 is employed. This requires 256 designs to be evaluated by FEA which is affordable. A full factorial design provides higher quality regression model.

Table 3.4: Geometrical input variables for the parametric model of the conventional (cored) machine.

Factor	Unit	Minimum value	Maximum value
$x_1 = g$	mm	1.8	5.0
$x_2 = h_{pm}$	mm	3.0	10.0
$x_3 = k_{tw}$		0.35	0.65
$x_4 = \alpha$		0.65	0.85
$x_5 = h_{sy}$	mm	9	18
$x_6 = h_{ry}$	mm	5	11

Table 3.5: Geometrical input variables for the parametric model of the coreless machine.

Factor	Unit	Minimum value	Maximum value
$x_1 = g$	mm	0.5	2.0
$x_2 = h_{pm,s}$	mm	1.0	3.5
$x_3 = \alpha$		0.65	0.85
$x_4 = h_{ry}$	mm	4.0	8.0

3.2.5 Selection of Best Designs

The result of DOE is used to fit a second order regression model for the responses including torque, mass, and losses (core and copper). In both cases, conventional and coreless machine, the overall volume is constant across all designs. Larger mass is a result of less space occupied by air, i.e. lower air-gap thickness, thicker magnets, more lamination, and/or more copper. All of these increase losses as well as the produced electromagnetic torque (Figs. 3.13 and 3.14).

The regression model results compared to FEA for selected designs (Table 3.6) show at most 6% error for mass estimation by regression model, 10% error for torque estimation, and 39% error for loss estimation. The errors may have been caused by the reduced number of designs and levels and also considering that core loss is more nonlinear, hence requires more levels. These errors can be addressed by using

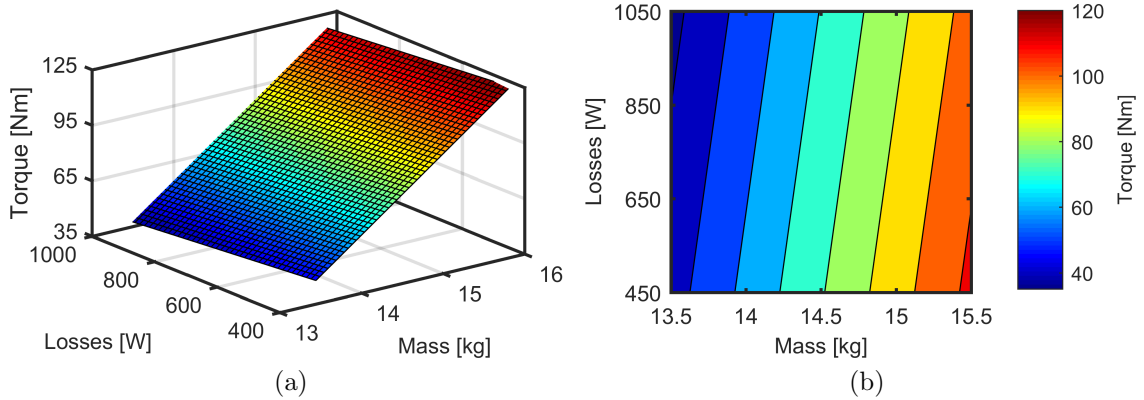


Figure 3.13: The responses of the conventional machine obtained from central composite DOE. (a) Three-dimensional plot and (b) the contour plot.

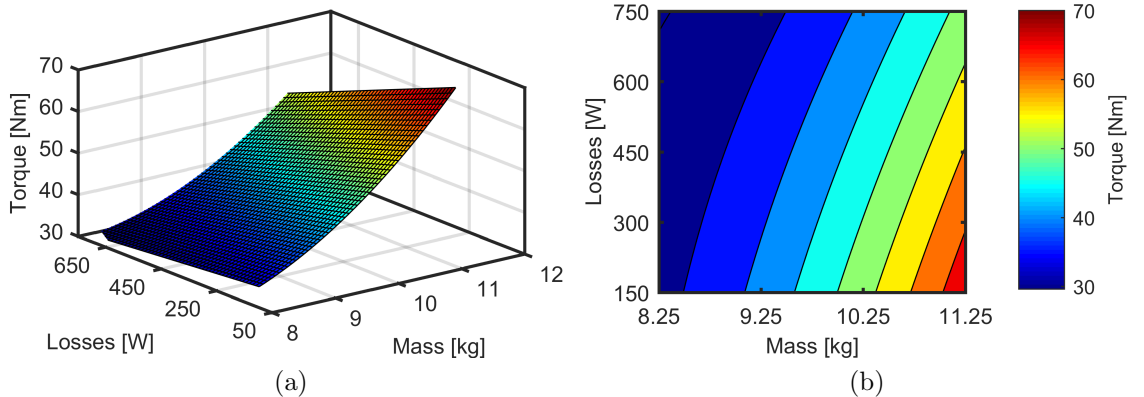


Figure 3.14: The responses of the multi-disk coreless machine obtained from full factorial DOE. (a) Three-dimensional plot and (b) the contour plot.

a correction factor in the regression model's estimations. Nevertheless, the main function of RSM, that is to identify the trends, is achieved.

Based on the regression models, hundreds of designs are studied. For each of two motors, three designs are selected to be analyzed in more detail via 2D FEA. The objectives are to produce the rated torque with the lowest mass and losses. The selected designs are marked in the scatter plots (Fig. 3.15). In case of the conventional machine, for the desired torque the active mass ranges between 13.6 kg and 14.2 kg while losses range between 400 W and 700 W. Designs with lower loss are assigned

Table 3.6: Reference model and selected designs for the conventional motor, at 400 rpm, for application with one driving wheel. Estimations are done using regression models and 2D and 3D FEA.

	Ref.	Design 1		Design 2		Design 3		
	3D FEA	Reg.	2D FEA	Reg.	2D FEA	Reg.	2D FEA	3D FEA
Air-gap [mm]	1.80	—	2.76	—	2.76	—	2.76	2.76
Torque [Nm]	54.3	57.2	63.5	57.6	59.9	58.8	60.9	58.2
Active mass [kg]	12.2	14.1	13.7	14.1	13.4	14.01	13.2	11.5
Core loss [W]	14	—	19	—	17	—	20	18
Copper loss [W]	398	—	325	—	319	—	302	351
Total losses [W]	411	423	343	452	336	450	322	369
Cogging torque [Nm]	13.8	—	21.8	—	11.9	—	5.5	6.9
Goodness [Nm/ \sqrt{W}]	2.7	—	3.5	—	3.3	—	3.4	3.0

Table 3.7: FEA results of the selected designs for the coreless motor for application with two driving wheels, at the rated speed of 400 rpm. All designs have mechanical air-gap of 1.85 mm.

	2D FEA			3D FEA
	D1	D2	D3	D1
Torque [Nm]	28.7	29.5	28.3	27.3
Active mass [kg]	9.4	8.8	9.0	10.5
Copper losses [W]	168	215	332	168
Goodness [Nm/ \sqrt{W}]	2.2	2.0	1.6	2.1

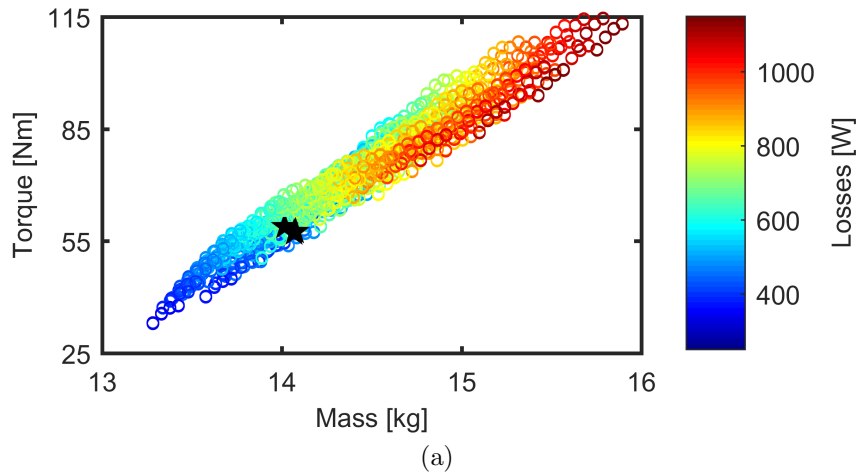


Figure 3.15: Projection of the DOE results and selected designs for the conventional motor. Designs marked with \star are selected in order to have approximately the same torque as the reference machine and minimum losses.

higher priority than those with lower mass.

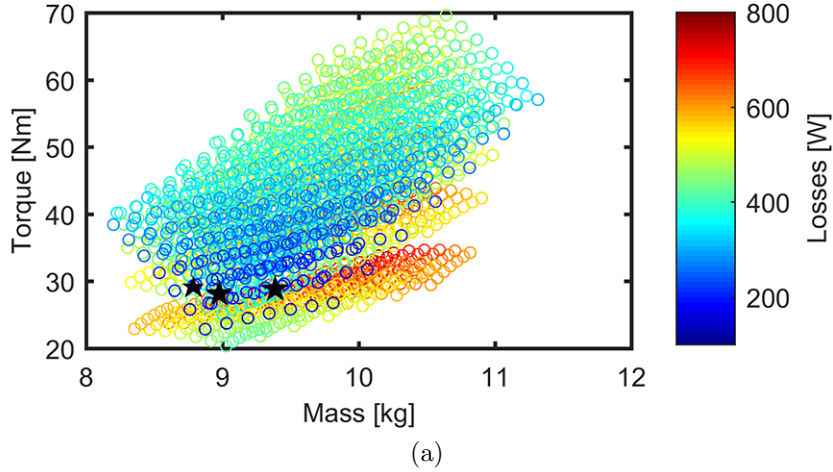


Figure 3.16: Projection of the DOE results and selected designs for the coreless motor. Designs marked with ★ are selected in order to have half the torque of the reference machine and minimum losses and mass.

The goodness of three selected designs, defined as $\frac{Torque}{\sqrt{losses}}$, are comparable. Design 3, being lighter with least losses, is selected to represent the conventional machine. Three-dimensional FEA is used for a more reliable performance estimation (Fig. 3.4a). For this design, the AC losses, including eddy current and proximity, are analytically estimated [99] to be 0.57 W at 400 rpm. Therefore, for this machine at rated speed, the AC losses are insignificant compared to the total losses and neglected.

Design 3, with an air-gap of 2.76 mm, achieves better performance than the reference design, which has a smaller air-gap of 1.85 mm (Table 3.6). Therefore, the required torque can be met with a larger air-gap and without compromising the performance.

The process is repeated for the coreless machine and three designs meeting the torque requirements have been selected (Fig. 3.16). The designs with lowest mass and loss are selected.

Due to the high quality of the full factorial DOE, and also robustness of coreless

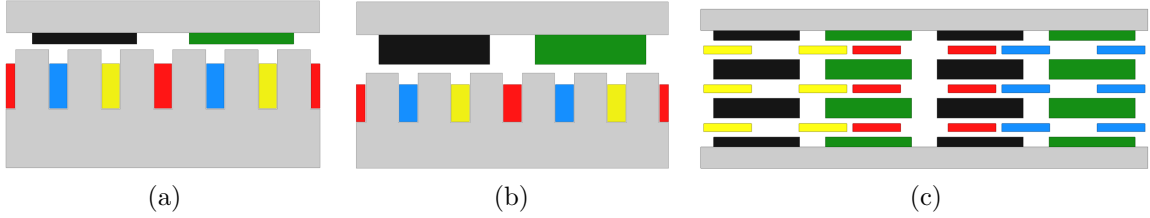


Figure 3.17: (a) The reference design, (b) the selected design 3 of conventional machine, (c) the selected design 1 of coreless machine. Taking advantage of the symmetrical geometry, only $\frac{1}{6}^{th}$ of the conventional machine and $\frac{1}{4}^{th}$ of the cored machine have been analyzed.

machines, the regression model's prediction of performance almost exactly matches that of 2D FEA. To avoid redundancy, only FEA results are presented in Table 3.7. The coreless motors have no cogging torque and their rotor core losses compared to copper losses are negligible. Comparing the goodness of the three selected designs, it is seen that Design 1 is superior to the others, and is thus selected. For this design it was analytically estimated [99] that using Litz wire with 40 strands per turn the winding AC losses are about 2.2 W and neglected.

An illustration of the contrast between dimensional properties of the reference model and the best designs of conventional and coreless motors is provided in Fig. 3.17. The 3D model of the selected best machines, i.e. design 3 of Table 3.6 and design 1 of Table 3.7, are in fact the designs presented in Fig. 3.4.

3.2.6 Comparison and Experimental Validation

On comparing the selected design of the conventional AFPM with the best design of the coreless machine, the combined weight of the two motors for the latter is higher, i.e. $10.5 \times 2 = 21$ kg compared to 11.5 kg, for the conventional machine. However, in

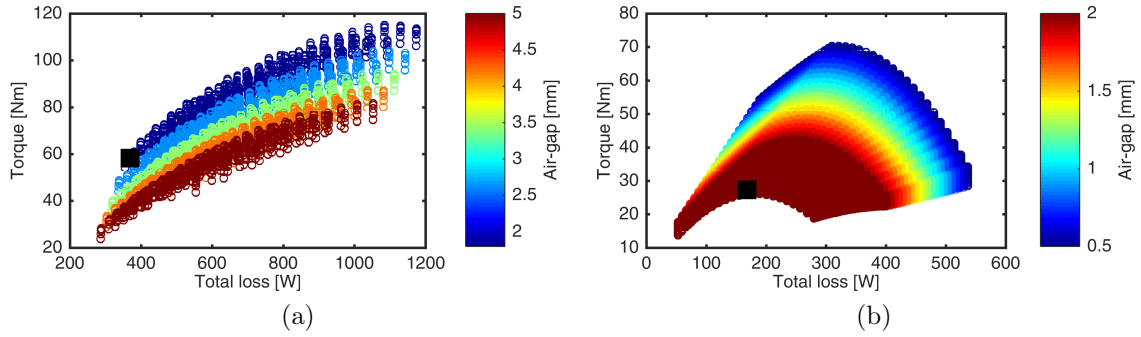


Figure 3.18: (a) Conventional and (b) coreless AFPM machine designs with changing air-gap. The selected design 3 in Table 3.6 and design 1 in Table 3.7 are marked with ■.

a two-wheel application, the mass is distributed between two wheels which reduces the pressure and also provides a better balance.

At the rated speed, the goodness of the conventional motor is higher than that of the coreless motor, presented in Tables 3.6 and 3.7. Nevertheless, at higher speeds, core losses increase in the conventional machine. In the coreless machine, the only steel employed is in the rotor back iron. The losses in magnets and steel, caused by harmonics in the stator MMF, are negligible because of the absence of slots. Thus, the rotor losses are insignificant. At higher speeds the rotor loss may be reduced by special winding techniques [98], not applicable for conventional configurations with slotted stator. As explained in the previous section, in the coreless machine, the conductor AC loss are mitigated by the use of Litz wire and transposition. At higher speeds, for the conventional design, considerable core losses increase is observed. Thus, the coreless machine may in fact outperform the conventional machine.

One of the objectives of the study is to achieve designs with larger air-gap in order to mitigate the mechanical problems associated with unsprung mass and arched axle.

In the conventional AFPM, the required torque can be met with a larger air-gap than used in the commercially available machine. The impact of the air-gap on torque and losses for both configurations, illustrated in Fig. 3.18a and 3.18b, shows for the desired torque production of the conventional machine, a larger air-gap results in considerable increase in the losses. Therefore, the selected design has a smaller air-gap in order to maintain an acceptable efficiency.

For the coreless machine design study, increasing the current beyond a threshold does not result in proportionally increased torque. This could be explained starting from the fact that the current density was fixed at 6.5 A/mm². It should be noted that, in principle, the study can be further expanded to consider specific cooling systems and particular thermal aspects, as discussed for example in [100]. In solar car applications, the motors are generally high efficiency for their volume such that the heat generated per volume is low and the thermal issues of a coreless machine design can be controlled.

In the current study, in order to increase the current, more copper wire is required to be used within the same geometrical envelope, which can be achieved, for example, by reducing the PM thickness, i.e. length in the direction of magnetization, which in turn results in decreased air-gap flux such that the electromagnetic torque does not increase although the current is higher. The selected design produces the required torque while attaining a relatively large air-gap and low losses (see Fig. 3.18b).

The coreless machine is generally lighter than the conventional one. This makes coreless machine suitable for vehicles with two driving wheels, as the total active mass

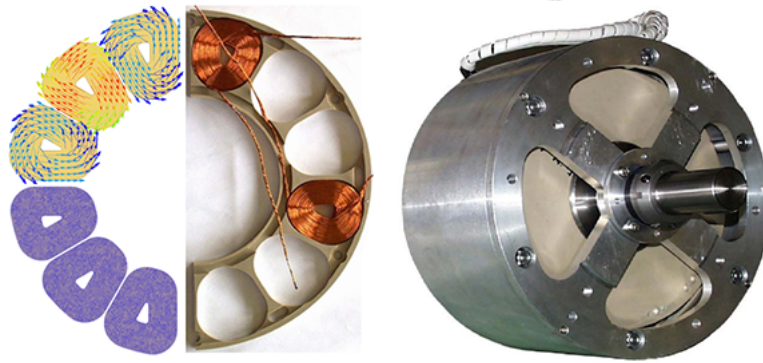


Figure 3.19: Special concentrated-winding multi-disk laboratory prototype employed for validating the 3D FEA parametric design study. The detailed fine finite element mesh and current density vectors in the coils calculated from 3D FEA are represented on the left.

in this case doubles, and conventional machines suitable for single in-wheel application, for the same reason. The coreless machine may also be selected for the single in-wheel application, however, the mechanical air-gap needs to be very small, below 1 mm, which is mechanically challenging, difficult to achieve and maintain. Utilizing conventional machines in double wheel vehicle results in much larger accumulated mass of rotors, on the other hand, considerably larger air-gaps could be used.

The design study based on electromagnetic 3D FEA has been validated with experimental data from a special concentrated-winding multi-disc laboratory prototype, which is shown in Fig. 3.19, and from two commercially available conventional and coreless AFPM machines, NGM and Marand, respectively, for solar powered vehicles. Marand topology has distributed air-cored winding and is represented in Fig. 3.20. NGM is the reference design and discussed in more detail in preceding sections. The main data for these machines is summarized in Table 3.8 and further details are available in [90, 92, 101, 102].

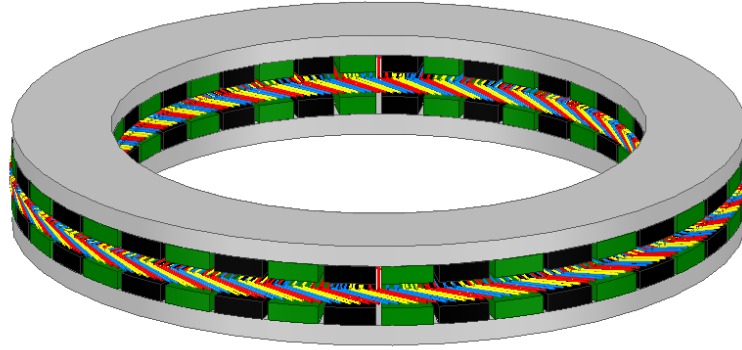


Figure 3.20: The 3D model of the commercially available distributed winding coreless AFPM machine produced by MARAND for in-wheel drive solar cars.

The experimental measurements and FEA results correlate favorably for the reference machines as illustrated in Fig. 3.21. The Marand machine is larger in active diameter and shorter in axial length. Considering that for axial flux machines the power is proportional to the cube of diameter, it is expected that Marand outperforms the NGM and all the other coreless machines designed for the dimensional limits similar to NGM. Also, Marand is benefited from distributed winding that improves its torque production capability.

It is observed that the coreless machine is distinctly lighter than the conventional design, and has lower loss, making it a better alternative for the double wheel configuration. The back iron portions of the rotors are also part of the wheel frame, hence the overall axial length is constant and fixed by the wheel dimensions. The maximum diameter available has been utilized to increase torque density. The identical wheel is used for configurations with single and double driving wheels.

Table 3.8: Main specifications of the reference machines considered for the experimental validation of the 3D FEA study.

		Multi-disk coreless	Marand	NGM
Speed	[rpm]	1000	1060	400
Diameter	[mm]	290	312	248
Axial length	[mm]	59	44.9	52.5
Rated torque	[Nm]	21	16.2	56

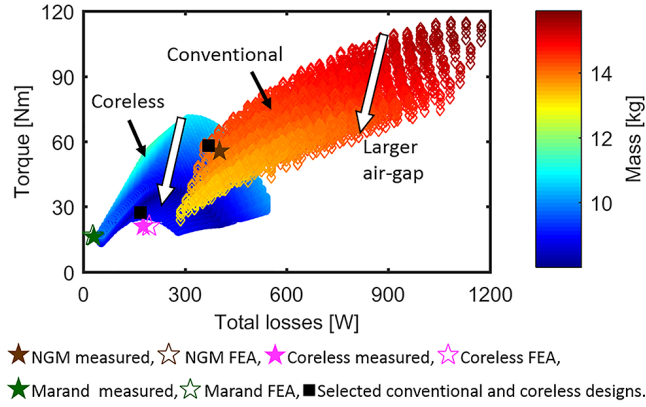


Figure 3.21: Torque versus total losses of conventional and coreless designs, compared to prototype and commercial machines employed in solar powered vehicles. Required torque is 56 Nm for single active wheel or 28 Nm for car designs with two active wheels, respectively.

3.2.7 Speed Range Extension of Coreless Machines

Coreless machines are known for their lower inductance, due to the relatively higher electromagnetic air-gap. The low inductance reduces the constant power operation speed range. In this section a dynamic method for increasing the constant power speed range, without employing a larger inverter rating, is proposed. The example coreless machine is a 2ph multiple disc machine with wave windings, as shown in Fig. 3.22

The extended speed range above the rated speed can be assessed through the

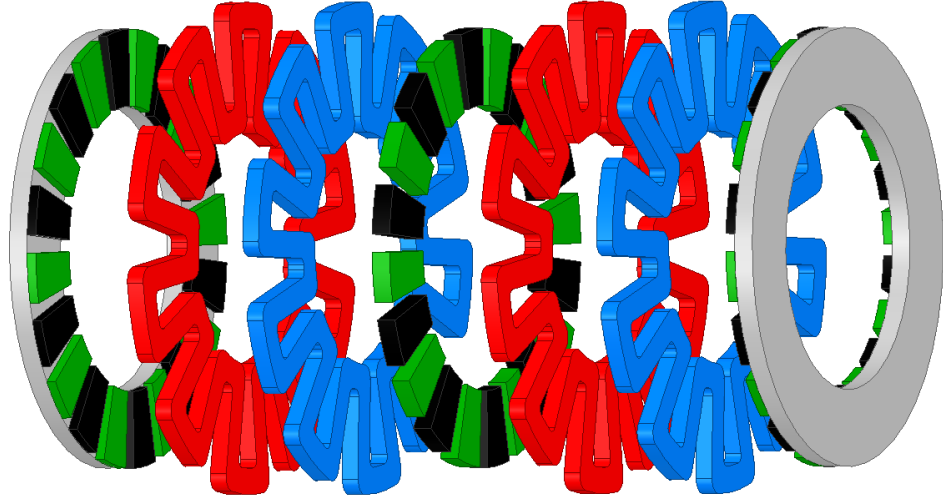


Figure 3.22: The exploded view of 3D FEA model for a two-phase AFPM motor with wave windings. Each of the two stators has a two-phase winding.

characteristic current, defined as

$$I_{ch} = \frac{\lambda_{pm}}{L_d} , \quad (3.13)$$

where L_d is the d-axis inductance and λ_{pm} is the permanent magnet flux linkage which can be calculated by

$$\lambda_{pm} = \frac{(D_o - D_i)k_{w1}N_t k_{vg} \alpha_i \tau_p B_r h_{pm}}{\pi g_e} , \quad (3.14)$$

where D_o and D_i are outer and inner active diameter; k_{w1} is the fundamental winding factor; N_t , number of turns per phase; k_{vg} , the ratio between the amplitude of the fundamental wave and the average value of the air-gap flux density; B_r , the magnet remanence; τ_p , pole pitch at the equivalent electromagnetic diameter; h_{pm} , the PM length in the magnetization direction; and α_i , the pole-arc to pole-pitch ratio. The electromagnetic air-gap, presented by g_e , for the conventional machine can be

estimated as

$$g_e = \frac{h_{pm}}{k_\sigma} + \mu_{mr} k_c k_{so} g , \quad (3.15)$$

and for the coreless machine and as

$$g_e = \frac{h_{pm}}{k_\sigma} + \mu_{mr} k_c k_{so} (g + L_c) , \quad (3.16)$$

where, k_c is Carter's coefficient; μ_{mr} , the relative permeability of the PM; k_{so} , the d-axis saturation factor at open-circuit operation; and k_σ , the leakage coefficient; g , the mechanical air-gap; and L_c is the coil height in axial direction.

The d-axis inductance, L_d , of an AFPM machine can be estimated as

$$L_d = \frac{m\mu_0\tau_p(k_{w1}N_t)^2(D_o - D_i)}{\pi^2 p k_{sd} g_e} , \quad (3.17)$$

where m is the number of phases and k_{sd} is d-axis saturation coefficient.

Theoretically, infinite speed can be achieved when $I_{ch} \leq I_r$, where I_r is the rated current limit. Lower values of I_{ch} adversely affect the delivered power. Therefore, ideally $I_{ch} = I_r$. This can be translated to $I_{ch} = 1 pu$.

The rated current of a two phase machine, exemplified in this section, with surface mounted PMs, for a given rated torque, can be evaluated through

$$I_r = \frac{2T_e}{p\lambda_{pm}} , \quad (3.18)$$

where T_e is the electromagnetic torque and p is the number of poles. Incorporating (3.13)-(3.18), the per-unit characteristic current can be estimated as

$$I_{ch,pu} = \frac{(1 - \alpha_d^2)(k_{vg}\alpha_i h_{pm} B_r)^2 p k_{sd}}{L_{ax}\mu_0 g_e T R V} , \quad (3.19)$$

where α_d is the split ratio; L_{ax} the axial length of the AFPM machine; and TRV is the torque ratio per volume. This indicates that if the machine has a high torque per active volume, $I_{ch,pu}$ reduces, meaning that it may be possible to design high torque density coreless machines with a low characteristic current. In particular, if the same torque per unit volume is obtained with the use of a low magnet volume or a lower remanence, reduced airgap flux density would lead to a low characteristic current. In other words, designs with high electric and low magnetic loading, and high torque per unit volume would lead to low characteristic current. These designs would have high loss, and low cost due to low magnet volume.

Two machines, one coreless and the other with stator cores, with similar torque per ampere are considered. Hence λ_{pm} is the same and, for the coreless machine, larger or stronger magnets need to be employed. Assuming both machines are employing the same magnet grade, based on (3.14) the amount of increase in magnet dimensions can be estimated. The coreless machine needs to employ $(1 + \frac{L_c}{g})$ times thicker magnets, i.e. larger h_{pm} , than a machine with stator core and the same rated torque. This will significantly increase $I_{ch,pu}$ as derived in (3.19). The estimated value for the coreless machine under study in this section is at least 8 pu .

The increased I_{ch} for the coreless machine limits its speed range. One solution is to employ an inverter with larger ratings [103]. Another method could be to dynamically reduce λ_{pm} of the coreless machine. According the approach employed in this section, this is obtained by utilizing multiple stator discs and rotating them relative to each other. In the proposed construction is represented for a two phase machine. Two stators are used, each comprising one wave coil per phase, as shown in Fig. 3.22. At

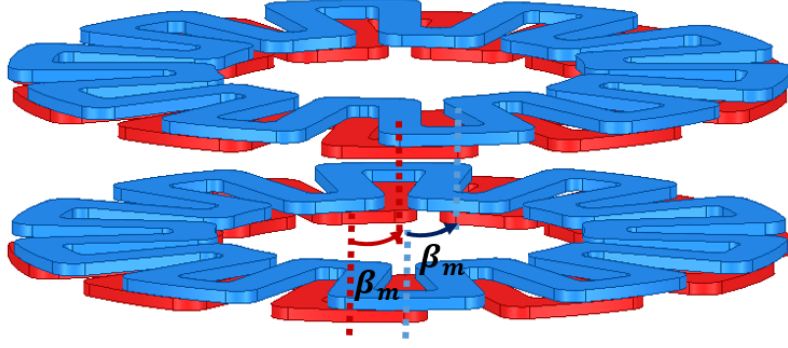


Figure 3.23: Illustration of the proposed technique for rotation of one of the stators with respect to the other for higher speed operation in constant power zone.

higher speeds one of the stators can be rotated to reduce the flux linkage and achieve constant power. The required flux linkage reduction at the speed of n where the rated speed is n_r can be estimated by

$$\frac{n_r}{n} = \frac{\sin \frac{kp\beta_m}{4}}{k \sin \frac{p\beta_m}{4}} = \frac{\sin \frac{p\beta_m}{2}}{2 \sin \frac{p\beta_m}{4}} = \cos \frac{p\beta_m}{4} ; \quad (3.20)$$

$$\beta_m = \frac{4}{p} \arccos \left(\frac{n_r}{n} \right) , \quad (3.21)$$

where k is the number of stator discs which equals 2 in this case study; p , the number of poles; and β_m is the mechanical rotation angle, as represented in Fig. 3.23.

This approach is employed for a 20 pole WAVED machine and the 3D FEA results are presented in Fig. 3.24. At speeds higher than the rated value, one of the stators is rotated with respect to the other, reducing the flux linkage and hence torque, resulting in constant power operation. The proposed method successfully achieves ideal high speed operation of the WAVED machine.

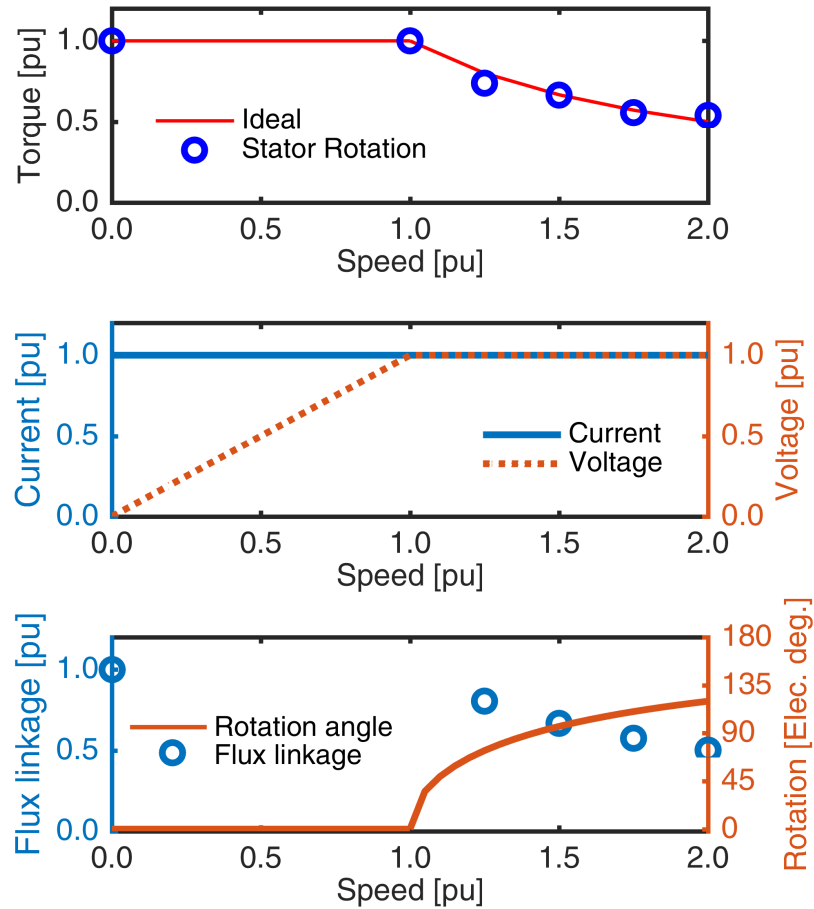


Figure 3.24: Traction characteristics of a WAVED coreless motor. The proposed stator rotation technique is employed in order to produce constant power operation by reducing the equivalent flux linkage.

3.3 A Systematic Study on the Effects of Dimensional and Materials Tolerances

In typical engineering practice, the experimentally measured performance of a new prototype electric machine may differ from design calculations and simulations. Provided that the numerical work has been conducted with well established procedures and software, such as high-fidelity FEA that has been proven in many previous instances to yield satisfactory agreement with experiments both in terms of values and

trends on other electric machines of the same type, questions are raised regarding the actual prototype hardware. More specifically, in this case, there is a need to identify any possible out of specification manufacturing and material properties tolerances that would represent the root cause for the noted differences.

In manufacturing practice, test performance may occasionally lie outside the specified tolerance bands, in which case the identification of the root causes is required based on a combination of theoretical and experimental methods. The current study addresses such issues, discusses the suitability of the IEEE Std 1812 procedures for these purposes, and exemplifies possible solutions.

In the process of designing and manufacturing an electrical machine, a systematic study of dimensional and material tolerances is of the utmost importance. Tolerances yield inevitable variations of output performance indices such as torque, losses, and efficiency. Establishing, under these conditions, the input to output system relationships is vital in order to ensure that performance is maintained within the specified limits around nominal values, and that, on the other hand, should these limits be exceeded, the root causes are traceable in terms of geometrical variables and/or material properties.

This section proposes a systematic method by which the effect of design specification variations on PM synchronous machine performance may be identified and quantified. The method combines design of experiments (DOE) techniques and open-circuit and short-circuit test results based on the recently approved IEEE Std 1812 testing guide. Case studies have been provided to demonstrate the proposed method for narrowing down the manufacturing tolerances.

A spoke-type rotor machine design is considered for which the manufacturing tolerances of the many geometrical independent variables and the variations of magnetic materials properties are systematically examined. The motor performance is simulated with these FEA models according to the test procedures described in the IEEE Std 1812. This approach, referred to as virtual tests, was preferred in order to enable a design of virtual experiments study with thirteen independent variables and three outputs that requires hundreds of model variations within the prescribed limits. This type of study is more relevant to early developments efforts that are typically focused on concept demonstration and employ only a reduced number of physical prototypes, rather than to production level processes, which are subject to very rigorous manufacturing quality control.

3.3.1 IEEE 1812 Testing Guide: Open-Circuit and Short-Circuit Tests

The newly approved IEEE Std 1812 testing guide contains general instructions for determining the performance characteristics of PM machines. The guide includes steady-state tests for open-circuit, short-circuit, load, and thermal performance, and transient tests for retardation and sudden short-circuit [104]. Virtual tests i.e. high fidelity FEA simulations, for the spoke-type PM machine and experimental measurements for the AFPM machine are conducted under the specified IEEE Std 1812 conditions.

According to the IEEE Std 1812 testing guide, section 4.3, the short-circuit test is conducted using a shorting switch and an optional external limiting impedance. The

current, I_{sc} , is measured after the steady-state short-circuit condition is achieved and then the synchronous reactance X_s can be calculated from:

$$I_{sc} = \frac{V_{oc}}{|jX_s + R_s + jX_{ex} + R_{ex}|}, \quad (3.22)$$

where R_s is the stator winding resistance. X_{ex} and R_{ex} are the external reactance and resistance, respectively. X_{ex} is negligible for the case under study.

Equation (3.22) employs the voltage from open-circuit test and the current from short-circuit test. Therefore, this synchronous reactance calculation approach may be regarded as an open for debate approximation; the non-linear electromagnetic field conditions and the flux pattern are largely different between open-circuit and short-circuit operation which impacts the results. This is particularly important for the study at hand that deals with small deviations.

3.3.2 Case Study for Dimensional and Material Tolerances

The case study is represented by an IPM spoke type radial flux machine with many possible tolerances for the geometrical specifications and magnetic material properties. This machine type was optimally designed with a record breaking high torque density of 12.2 Nm/kg, for application in Formula E racing cars and has an extremely high electrical and magnetic loading [105, 106]. It is a 100 hp motor with a spoke-type rotor containing 16 rare-earth (SmCo) PM poles and 18 slots, which has been successfully manufactured and tested. The associated FE models, such as those exemplified in Fig. 3.25, have been satisfactorily validated against experimental measurements as previously reported in [105, 106].

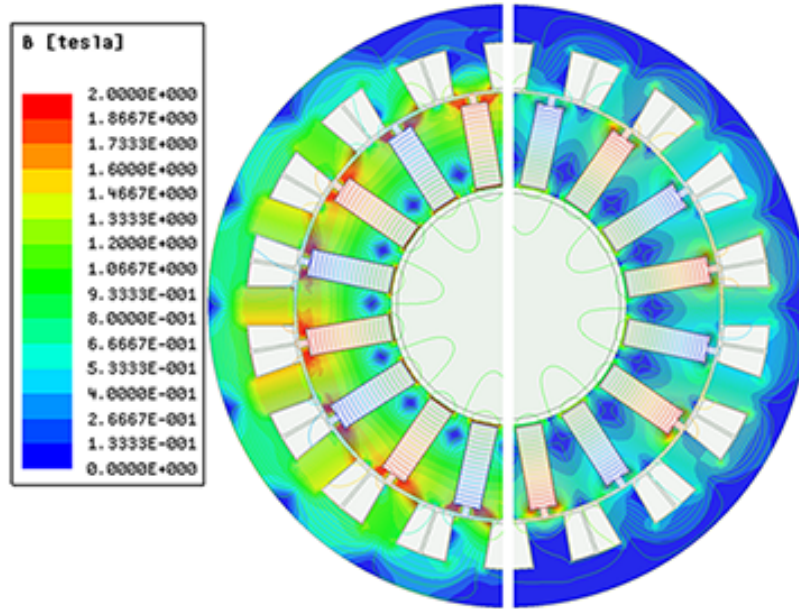


Figure 3.25: Flux density distribution and flux lines for the case studies: the spoke-type motor with high-energy rare-earth SmCo magnets (left) and the same design but with ceramic ferrite magnets (right).

A second case study employs the exact same dimensions as the first one, but with the only exception that it uses ceramic ferrites in order to investigate the spoke-type motor's performance at a more typical level of electromagnetic loading. The open-circuit voltage, open-circuit losses, short-circuit current, and d-axis inductance are the three performance indices considered for these two case studies.

The eleven geometrical input design variables considered in the first two studies are represented in Fig. 3.26 and specified in Table 3.9. A tolerance of ± 0.1 mm, typical for laser cutting prototyping, has been considered. A tolerance of $\pm 5\%$ is considered for the PM remanence in order to account for possible variations both in the material grade and in the external magnetization for prototypes. The specified material for the laminated core is M19 laminated silicon steel. As an example of deviation from the original specifications, an extreme case of inadvertently employing

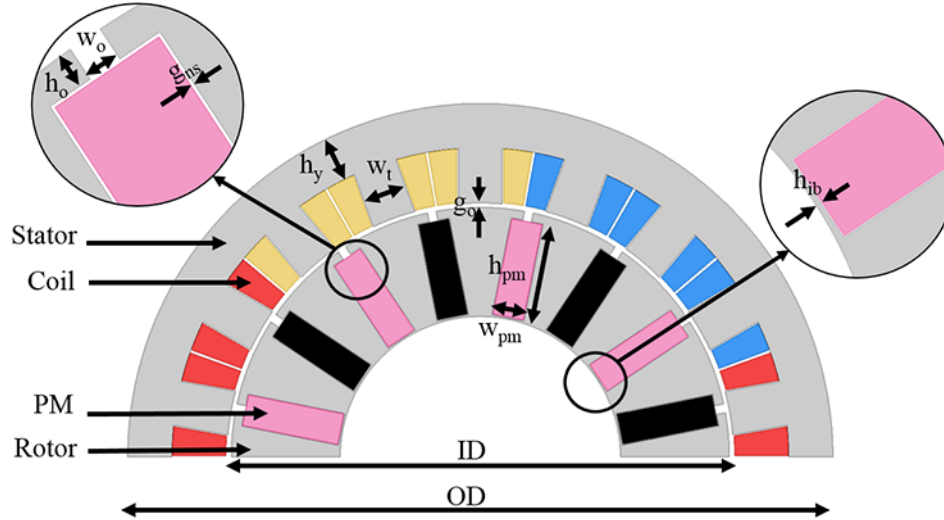


Figure 3.26: Overview of the geometrical design variables for the case studies. The model was analyzed with the ANSYS Maxwell software.

Table 3.9: Geometrical variables (fig. 3.26). A tolerance of ± 0.1 mm for geometrical variables has been considered.

Geometrical factors		Reference spec. [mm]
$x_1 = OD$	Outer diameter	160
$x_2 = h_y$	Yoke length	10
$x_3 = w_t$	Tooth width	10
$x_4 = h_{ib}$	Bridge height	0.5
$x_5 = g_o$	Air-gap	1
$x_6 = h_o$	Slot opening depth	3
$x_7 = w_{pm}$	PM width	7
$x_8 = h_{pm}$	PM height	22
$x_9 = w_o$	Slot opening width	2
$x_{10} = ID$	Inner diameter	115
$x_{11} = g_{ns}$	Nuisance gap	0.2

Table 3.10: SmCo rare-earth magnets and ceramic ferrites with a nominal remanence of 1.1 T and 0.4 T, respectively, have been studied together with the possible inadvertent substitution of the lamination grade.

Magnetic material factors		Reference	Tol./sub.
$x_{12} : B_r$	PM remanence	Nom.	$\pm 5\%$
$x_{13} : M$	Lamination	M19	M43

M43 with the same gauge is considered (see Table 3.10.)

3.3.3 Design of Experiments (DOE) and Virtual Tests

A main objective of the DOE studies in this section is to establish the motor performance sensitivity to varying dimensions and material properties due to manufacturing tolerances, in order to be able to determine the causes of out of specification performance. Data for the case studies was provided by virtual tests, i.e. FEA simulations of the open and short circuit tests for the spoke PM machine designs. This approach was preferred due to the very large effort associated with the large number of independent variables and performance indices requiring hundreds of experiments.

The first step in the DOE procedure includes the definition of the factors and their levels. Figure 3.26 shows 11 geometrical variables to capture the possible manufacturing deviations. In addition, magnet and laminated steel grades can also be affected by manufacturing tolerances. Hence, overall 13 factors are considered (Table 3.9 and 3.10). In order to ensure that all possible non-linearities are taken into account, geometrical factors and remanence are evaluated in three levels. The lamination grade is specified to be M19. Prototype manufacturing variations and material substitutions, due to unavailability or inadvertence, may further degrade the properties to those of M43. Hence 2 levels are considered for M .

A full factorial design will result, in the first two cases, in more than a million experiments, i.e. 1,062,882, per case which would be prohibitive even for FEA, let alone for costly hardware experimentation. Instead, a fractional factorial method, which only requires 376 experiments per study case, was preferred making at least virtual prototyping and testing with FEA parametric models and scripting possible

for sensitivity analysis with reasonable time and computational resources.

The response variables chosen for the DOE study include from the open-circuit test, the voltage (back emf) and core losses and from the short-circuit test, the current and the d-axis inductance. As per (3.22), unlike the measured short circuit current, the calculated d-axis inductance is correlated with the open-circuit voltage, which has implications in terms of the DOE mathematical formulation, i.e., the response variables must be independent. This is not the case for L_d , the evaluation of which is based on the recommended method for calculating X_s (3.22). Therefore, it is preferred to directly use I_{sc} as one of the performance parameters rather than L_d .

The sensitivity analysis is executed by fitting a 2^{nd} order regression curve demonstrated by a polynomial function as shown in (3.1). After fitting the preliminary second order regression model it was observed that for this study the interaction and higher order terms are negligible. Accordingly, the regression model is modified to fit a first order function. The regression coefficients are estimated using least-squares method. As an instance, V_{oc} , obtained from numerical analysis of the model with ferrite magnets can be estimated using the polynomial function,

$$\begin{aligned}
 Y_{(V_{oc})} = & 54.06 + 0.08X_{C1} - 0.02X_{C2} - 0.08X_{C3} - \\
 & 1.47X_{C4} - 3.83X_{C5} - 0.45X_{C6} + 0.38X_{C7} + \\
 & 0.08X_{C8} + 0.52X_{C9} + 0.10X_{C10} - 1.24X_{C11} + \\
 & 3.06X_{C12} - 0.42X_{C13} .
 \end{aligned} \tag{3.23}$$

When SmCo magnets are used β_0 is increased from 54.06 to 146.83, indicating higher open-circuit voltage, as expected. Per unit regression coefficients, defined as $\frac{\beta_i}{\beta_0}$ for the i^{th} factor, represent the percentage of variation in the response when all

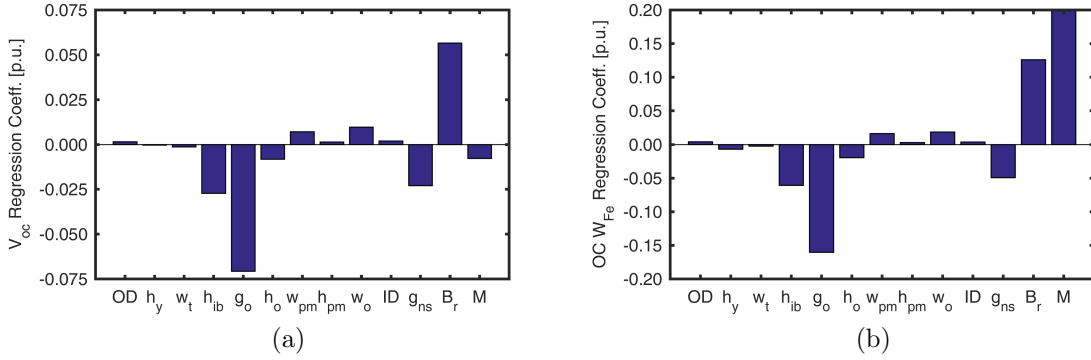


Figure 3.27: The per unit regression coefficients calculated for open-circuit based on FEA virtual tests for the motor with ceramic ferrite magnets; (a) back emf, i.e. voltage, (b) core losses. Note the different scales on the y-axis. The bar corresponding to lamination material, M , in (b) is truncated as it reaches up to 0.23.

factors are according to specifications ($X_{C_j} = 0 ; j = 1, 2, ..i - 1, i + 1, ...d_v$) except for one factor which is at its maximum studied deviation ($X_{C_i} = 1$). For instance, the p.u. regression coefficient of g_o for V_{oc} is -0.07 . This means that if $g_o = 1.1 \text{ mm}$ rather than its specified value of 1 mm and all other variables are according to specifications, V_{oc} would be $1 - 0.07 = 0.93$ times its rated value. Therefore, negative regression coefficients indicate that the response reduces upon increase in the corresponding factor. The larger the magnitude of the regression coefficients in Figs. 3.27-3.28, the more influential the factor.

Some important observations from Figs. 3.27-3.28 are:

- 1) Generally the output response parameters are more significantly sensitive to variations of the air-gap, g_o , remanence, B_r , bridge height, h_{ib} , and nuisance gap, g_{ns} , as well as the lamination grade. The impact of the rest of the factors is negligible.
- 2) Lamination material has an observable effect only on the core losses.
- 3) Open-circuit core loss is very sensitive. This may be understood by considering

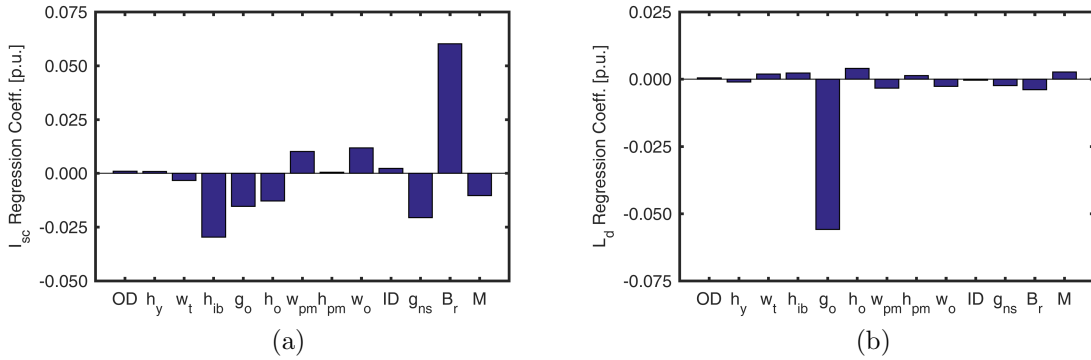


Figure 3.28: The per unit regression coefficients calculated for short-circuit based on FEA virtual tests for the motor with ceramic ferrite magnets; (a) d-axis inductance, (b) current. Note the different scales on the y-axis.

that while EMF is proportional to the flux density, core loss is proportional to its square, thus explaining its higher sensitivity to all variables that may affect flux density.

This machine at a different magnetic loading is also studied by replacing ferrite magnets with rare earth SmCo magnets. A comparison between regression coefficients of only significant factors, with values above 0.02 p.u., for the motor with ferrite and rare earth magnets is plotted in Fig. 3.29. The performance parameters of the motor with stronger magnet grade (rare earth magnets), Fig. 3.29a, represents lower sensitivity to changes in input variables, and negligible sensitivity to h_{ib} and g_{ns} . This motor operates under an exceptionally high magnetic loading such that the rotor core is saturated at the inner diameter. Therefore, for instance, a larger bridge height does not result in higher leakage flux and hence output performance is not considerably affected by its variations.

Another outcome of the regression models can be estimating the range within which a performance parameter may vary due to manufacturing tolerances. The

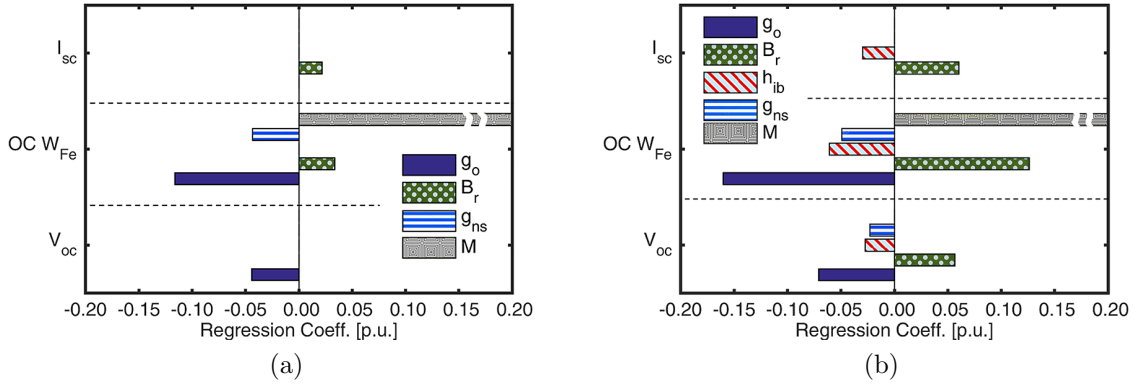


Figure 3.29: The per unit regression coefficients for the input factors most significantly affecting the output performance. Results based on FEA virtual tests for the spoke-type motor with (a) rare earth SmCo magnets, and (b) ceramic ferrite magnets.

Table 3.11: Theoretical Maximum Variations for the Open-circuit Voltage (Back EMF) and Core Losses.

Performance		Magnet	Ref.	Min	Max
V_{oc}	[V]	ferrite	51	41	62
		SmCo	133	116	150
$OC W_{Fe}$	[W]	ferrite	117	77	223
		SmCo	861	641	1456

limits of this variation are established by consideration of the improbable scenarios where all geometrical and magnetic variables are at their maximum or minimum value within the studied ranges, such that they cause either a cumulative reduction or increase in the value of a performance index. Table 3.11 represents these ranges for open-circuit voltage and core losses. The relatively tighter ranges noted for the motor with rare earth PMs is partially due to the stronger saturation of the magnetic circuit bridges, which minimizes flux leakage and reduces performance variability.

3.3.4 Discussion

In case of the comprehensive case study of the spoke-type machine, sensitivity analysis for responses from open-circuit — V_{oc} and W_{Fe} — and short-circuit tests— preferably I_{sc} — may be used to indicate possible sources of deviations from the nominal values. Each of these three responses can be more than, less than, or equal to the nominal values. In this section, a systematic approach for interpreting these deviations, with the purpose of identifying possible manufacturing tolerance(s), is introduced.

For the machine with SmCo magnets, regarding Fig. 3.29a, the relation between factors and response parameters' deviations can be represented in matrix form as,

$$\begin{bmatrix} \Delta V_{oc} \\ \Delta W_{Fe} \\ \Delta I_{sc} \end{bmatrix} = \begin{bmatrix} \beta_{v,g_o} & 0 & 0 & 0 \\ \beta_{w,g_o} & \beta_{w,B_r} & \beta_{w,g_{ns}} & \beta_{w,M} \\ 0 & \beta_{i,B_r} & 0 & 0 \end{bmatrix} \begin{bmatrix} \Delta g_o \\ \Delta B_r \\ \Delta g_{ns} \\ \Delta M \end{bmatrix}, \quad (3.24)$$

where ΔV_{oc} , is the difference between the measured and the nominal value of V_{oc} , i.e., $\Delta V_{oc} = V_{mes} - V_{nom}$; Δg_o , the normalized deviation of the specified g_o ; and β , the regression coefficients with the subscripts representing the relevant response and factor, respectively. The rest of the entries in (3.24) are defined similarly.

Equation (3.24) represents a system of 3 equations, with 4 unknowns, namely Δg_o , ΔB_r , Δg_{ns} , and ΔM . Such a system cannot be solved unless at least one of the unknowns is determined independently. For special scenarios, this might be possible using sensitivity analysis. For clarification, some examples are included below.

The first example is when measured V_{oc} and W_{Fe} match with their nominal values,

i.e., $\Delta V_{oc} = \Delta W_{Fe} = 0$ and only I_{sc} deviates, i.e., $\Delta I_{sc} \neq 0$. It can be concluded that all variables influencing V_{oc} and W_{Fe} are most probably as designed. Therefore, the only out of specification variable is B_r . Similarly, in case only V_{oc} deviates, it can be an indication of only g_o having out of specification tolerances. However, if only $\Delta W_{Fe} \neq 0$, a definite conclusion cannot be reached, as either or both g_{ns} and M may have manufacturing tolerances.

When more than one performance index deviates from design expectations, the certainty of conclusions deteriorate. For instance, if $\Delta W_{Fe} \neq 0$, $\Delta V_{oc} \neq 0$, and $\Delta I_{sc} = 0$, only the presence of out of specification tolerance in B_r can be eliminated and all the other variables may or may not be as specified by the design.

These examples show that the identification of design tolerances with certainty is possible, if the number of measurable responses equals the number of possible manufacturing tolerances. The narrowing down of the possible factors can be performed with sensitivity analysis and careful study of that particular scenario.

For a larger number of factors, it is more difficult to identify the deviation source(s). Adding another response, such as cogging torque, to such studies is only beneficial if the new response does not add another unknown to the system of equations. In the case study, it was observed that in addition to the factors included in Fig. 3.29, cogging torque is also influenced by ID , OD , and W_o , three parameters that do not affect other responses. Therefore, inclusion of cogging torque does not contribute additional information which can be used for distinguishing the out of specification design variables. On the other hand, in case cogging torque is the only response with deviation from expectation, it may be concluded that the out of specification

variables are limited to those three.

For the case of the spoke machine with ferrite magnets, the number of effective factors increases as seen in Fig. 3.29b. The relation between response parameters' deviations and design tolerances, can be formulated as

$$\begin{bmatrix} \Delta V_{oc} \\ \Delta W_{Fe} \\ \Delta I_{sc} \end{bmatrix} = \begin{bmatrix} \beta_{v,g_o} & \beta_{v,B_r} & \beta_{v,h_{ib}} & \beta_{v,g_{ns}} & 0 \\ \beta_{w,g_o} & \beta_{w,B_r} & \beta_{w,h_{ib}} & \beta_{w,g_{ns}} & \beta_{w,M} \\ 0 & \beta_{i,B_r} & \beta_{i,h_{ib}} & 0 & 0 \end{bmatrix} \begin{bmatrix} \Delta g_o \\ \Delta B_r \\ \Delta h_{ib} \\ \Delta g_{ns} \\ \Delta M \end{bmatrix}. \quad (3.25)$$

This represents a system of 3 equations, with 5 unknowns. Such a system cannot be solved unless at least two of the unknowns are determined independently.

In this machine, suppose $\Delta W_{Fe} \neq 0$, $\Delta I_{sc} = \Delta V_{oc} = 0$. This scenario is illustrated in Fig. 3.30. The parameter deviating from the nominal value is marked with ✖, while the parameters and variables matching with the design specifications are marked with ✓. The upward and downward arrows indicate a value larger and smaller than the design specification, respectively. The deviation direction is color coded to separate different cases. The dashed lines represent factors with less likely manufacturing tolerances. Lamination grade M is the only design variable that affects the loss with no measurable impact on the other two parameters. therefore, it can be concluded that M is most probably the only out of specification design variable.

In another example, $\Delta V_{oc} = \Delta W_{Fe} = 0$ and $\Delta I_{sc} \neq 0$, it follows that the source of deviation cannot be narrowed down with certainty to only tolerances in B_r , unlike in the previous case; those in h_{ib} also might be present. On the other hand, if only

		g_o	B_r	h_{ib}	g_{ns}	M
I_{sc}	✓	N/A	✓	✓	N/A	N/A
W_{Fe}	✗ ↑↓	↑↓	↑↓	↓↑	↑↓	↑↓
V_{oc}	✓	✓	✓	✓	✓	N/A

Figure 3.30: Example simple scenario for the spoke-type machine with ferrite magnets where only W_{Fe} is out of specification. As I_{sc} and V_{oc} comply with the design predictions, the design variables influencing their value are most probably as specified. This leaves lamination grade M the highest possible out of specification tolerance causing discrepancy in W_{Fe} .

		g_o	B_r	h_{ib}	g_{ns}	M
I_{sc}	✗ ↑↓	N/A	↑↓	↓↑	N/A	N/A
W_{Fe}	✗ ↑↓	↑↓	↑↓	↓↑	↓↑	↑↓
V_{oc}	✗ ↑↓	↑↓	↑↓	↓↑	↓↑	N/A

(a)

		g_o	B_r	h_{ib}	g_{ns}	M
I_{sc}	✗ ↑↓	N/A	↑↓	↓↑	N/A	N/A
W_{Fe}	✗ ↓↑	↑↓	↓↑	↑↓	↑↓	↑↓
V_{oc}	✗ ↓↑	↑↓	↓↑	↑↓	↑↓	N/A

(b)

Figure 3.31: Example scenarios for the spoke-type machine with ferrite magnets and illustrations of the simplifications employed in the identification process of non-conformant tolerances. I_{sc} out of specification values necessitates considering B_r and/or h_{ib} variations. If the other two geometrical parameters also deviate in the same direction (a), the possibilities of g_o and g_{ns} out of spec deviations are low; if they deviate in the opposite direction (b), all or part of the manufacturing tolerances are out of specification.

V_{oc} deviates from the nominal value, the possibility of having prototyped the motor with out of specification lamination material can be eliminated, but any of the other four factors or their combinations might exist.

Another example is when deviations are observed in all three performances indices, such that $\Delta I_{sc} > 0$, $\Delta W_{Fe} > 0$, and $\Delta V_{oc} > 0$. In this case, the possibility of out of specification values of either or both B_r and h_{ib} is higher, because these parameters affect all performance indices the same way (Fig. 3.31a). A different scenario arises if $\Delta I_{sc} > 0$, $\Delta W_{Fe} < 0$, and $\Delta V_{oc} < 0$. For example, an increase in B_r can cause the increased I_{sc} , but not the reduced W_{Fe} . Due to the dependence of ΔW_{Fe} on other factors information is required. Figure 3.31b is an illustration of this example.

The examined instance scenarios indicate that identification of out of specification variables strongly depends on the loadings and configuration of the machine. A comprehensive case-by-case sensitivity analysis accompanied by engineering judgment may help in narrowing down the possible manufacturing/prototyping tolerances.

3.4 Summary

Two cases of application of DOE and RSM in the field of electric machine design were presented. The first one is an elaboration of a design approach implemented for a coreless AFPM machine using DOE and RSM. The second case is a novel method for identifying the sources of discrepancy between the predicted performance in the design stage and the measurements. The proposed method is extensively employing DOE and RSM alongside virtual testing using FEA and IEEE 1812 standard.

Summary of Outcomes of Designing a Coreless AFPM Machine Using DOE and RSM:

It is observed that for the space constraints under study and for a given cooling system, the torque generation by both machine types is limited, and this torque limit for conventional machine is at a higher value. This is due primarily to the higher air gap in coreless machines.

Coreless machines may therefore be more suitable for use in a two-wheel drive version, at the cost of slightly reduced efficiency, and larger overall mass as compared with single wheel drives. These limitations are offset by the better mass distribution achieved in two wheel drives, for which the conventional machine may not be suitable

owing to large accumulated unsprung mass. Another advantage of a coreless AFPM construction is the limited investment required for stator tooling which is important when producing motors for the low volume solar car market.

Conventional AFPM topology could be used more efficiently with one driving wheel. The coreless machine may also be selected for single in-wheel configurations, although machine designs with very small air-gap are necessary to meet the torque requirement. Considering that the latest generation solar cars employ two-wheel drives, based on this study, it is recommended to consider the opportunities provided by coreless machine for such configurations. An additional contribution of this study is proposing a dynamic method for increasing the speed range applicable for low inductance coreless PM machines.

Summary of Outcomes of Studying Manufacturing Tolerances using DOE and Sensitivity Analysis:

A new systematic method aimed at quantifying the effect of tolerances on PM synchronous machine performance and identifying possible non-compliant dimensional variables and material characteristics is proposed. The study is based solely on the results of the open-circuit and short-circuit procedures incorporated in the newly approved IEEE Std 1812 standard, which are independent of the power electronics drive and control. The method is illustrated with three case studies and it is observed that through the combined comparative analysis of different tests, the non-conforming tolerances may be determined in some instances.

While the method itself is generally applicable in scope, it is also shown that,

as the electromagnetic loading greatly affects the sensitivity of the test outputs to tolerances, the careful consideration of the individual machine topology is required as part of the studies, limiting the simple generalization of quantitative conclusions. For example, for the case study motors that are identical with the exception of the permanent magnet type employed, i.e. SmCo and ferrite, the very same tolerances may lead to largely different variations of $\pm 13\%$ and $\pm 20\%$, respectively, for the open circuit voltage. Likewise, the same tolerances will result in open circuit core losses ranging from approximately 75% to 170% of the nominal design values for the SmCo magnet machine and from 65% to 200% for the machine with ferrite magnets.

Chapter 4

A New Two-level Surrogate Assisted Multi Objective Differential Evolution Optimization Algorithm

In this chapter a two level surrogate assisted optimization algorithm is proposed for electric machine design using 3D finite element analysis (FEA). The algorithm achieves the optima with much fewer FEA evaluations than conventional methods. It is composed of interior and exterior levels. The exploration is performed mainly in the interior level which evaluates hundreds of designs employing affordable surrogate meta-models known as kriging models. Then, the most promising designs are evaluated in the exterior loop with expensive 3D FEA models. The sample pool is constructed in a self-adjustable and dynamic way. A hybrid stopping criterion is used to avoid unnecessary expensive function evaluations.

4.1 Introduction

Electric machine design requires an optimization algorithm to achieve the best result. Conventional optimization algorithms often use thousands of design evaluations. Hence, 3D FEA is not affordable. However, 2D models are not accurate for machines with 3D flux paths, such as axial flux or transverse flux machines, or for studying skew angle, overhang, or end coils. One solution is to use surrogate models, although the accuracy of these can decline in a wide and nonlinear search space. Another solution utilizes algorithms with a minimum number of designs evaluations. A combination of these two solutions is proposed here.

Currently, for the optimal design of electric machines, population based evolutionary algorithms are widely used with the differential evolution (DE) method being a typical choice [107, 108]. According to DE, following initialization of a random population, offspring multiple successive generations are created by differential mutation, an operation achieved by adding a scaled difference of two previous designs to a third parent design. The resulting children will survive to the next generation if they achieved improvement for all multi-objective performance indices considered as part of the optimal design problem. Only a minimum number of control parameters, namely the scaling factor and crossover probability, are considered in the DE algorithm and the global optimum can be achieved regardless of the initial designs. Nevertheless, a major disadvantage of conventional DE is that it requires the evaluation of a very large number of generations and candidate designs, which for electrical machines are typically based on computational expensive FE models [69, 109, 110]. For example, a

previous optimal design problem with five independent variables employed more than four thousand candidate designs [109], while using the novel algorithm proposed in this chapter this number can be reduced by one order of magnitude, to only a few hundreds.

Surrogate modeling is a suitable replacement for expensive measurements. The response surface methodology (RSM) is a popular example of surrogate model application in electric machine design; these mathematically estimate the performance of a design, and can be classified into global or local meta-models. A global surrogate model is a regression model built from a predetermined function, as is with RSM. Local surrogate interpolations are obtained from spatial functions passing through all sample points. The Gaussian process, known as kriging, is an example of local surrogate models where a greater weight is put on closer sampled data points [111]. Kriging models gained popularity in geostatistics [112] and proved to be a practical estimation tool. Other fields, including electric machine design optimization, have taken advantage of this method.

Kriging-based optimization has emerged in the design of electromagnetic devices, and more recently electric machines [113–116]. Further contributions are made by a special two-level optimization algorithm which eliminates the estimation errors on significant designs. The algorithm has a dynamic sample pool with self-adjusting capabilities for problems with different levels of complexity, thus avoiding unnecessary evaluations. The proposed algorithm particularly saves significant time for multi-objective optimization problems, which have a higher level of complexity with several objectives, such as losses, mass, cost, etc., to be simultaneously considered.

4.2 Kriging Surrogate Modeling

Kriging is a local fitting model that, unlike other methods, does not use one predetermined polynomial function to estimate every unsampled design. It has two components: trend and residual. The benefits of kriging models rise from the residual component that addresses the error between the actual data points and the general trend. There are different types of kriging modeling methodologies mostly categorized by the trend component [117]. The universal kriging model is the most complicated and accurate, and is used here. The kriging estimation methods can be expressed as

$$\hat{Y} = \hat{X}\beta + r^T R^{-1}(Y - X\beta) ; \quad (4.1)$$

$$r_i = \exp[-\sum_{t=1}^k \theta_t |\hat{x}_t - x_{i,t}|^2] ; \quad i, j = 1, \dots, n, \quad (4.2)$$

$$R_{i,j} = \exp[-\sum_{t=1}^k \theta_t |x_{i,t} - x_{j,t}|^2] ; \quad i, j = 1, \dots, n. \quad (4.3)$$

where \hat{Y} is the unsampled design to be predicted, based on known sample designs, i.e. X and Y ; β is the regression coefficients that can be obtained using methods such as least squares; n is the number of sampled designs; and k the number of optimization variables. Kriging weights, r^T and R^{-1} are derived from a covariance function or semivariogram and a maximum likelihood estimation (MLE) [118].

In order to assess the prediction accuracy of kriging models versus global surrogate models, i.e., second order regression and Eureka [119, 120], the magnet eddy losses of an example axial flux machine was studied. Fifty designs were evaluated using 3D FEA. The RMS estimation error for 15 unsampled designs were compared to

Table 4.1: The RMS estimation error of predictions made by 3 surrogate models, for magnet eddy losses of an example AFPM machine.

Surrogate model	2^{nd} order regression	Eureqa	kriging
RMS estimation error	48.5%	143.5%	13.5%

FEA calculations. As presented in Table 4.1, kriging estimations are more accurate than the others. Henceforth, predictions made by the kriging surrogate model will be referred to as inexpensive evaluations, and calculations made by the 3D FEA as expensive evaluations.

4.3 Novel Optimization Algorithm

The proposed approach composes an exterior level evolutionary algorithm, replacing the mutation with an interior level complete DE optimization. After the first generation of the main loop (exterior), parents are, in fact, estimated Pareto (non-dominated) designs, hence, close to the actual Pareto front. The exterior loop uses expensive function evaluations for the estimated Pareto designs to correct the estimation errors made by the interior loop. The optimization algorithm flowchart is given in Fig. 4.1 and explained as follows.

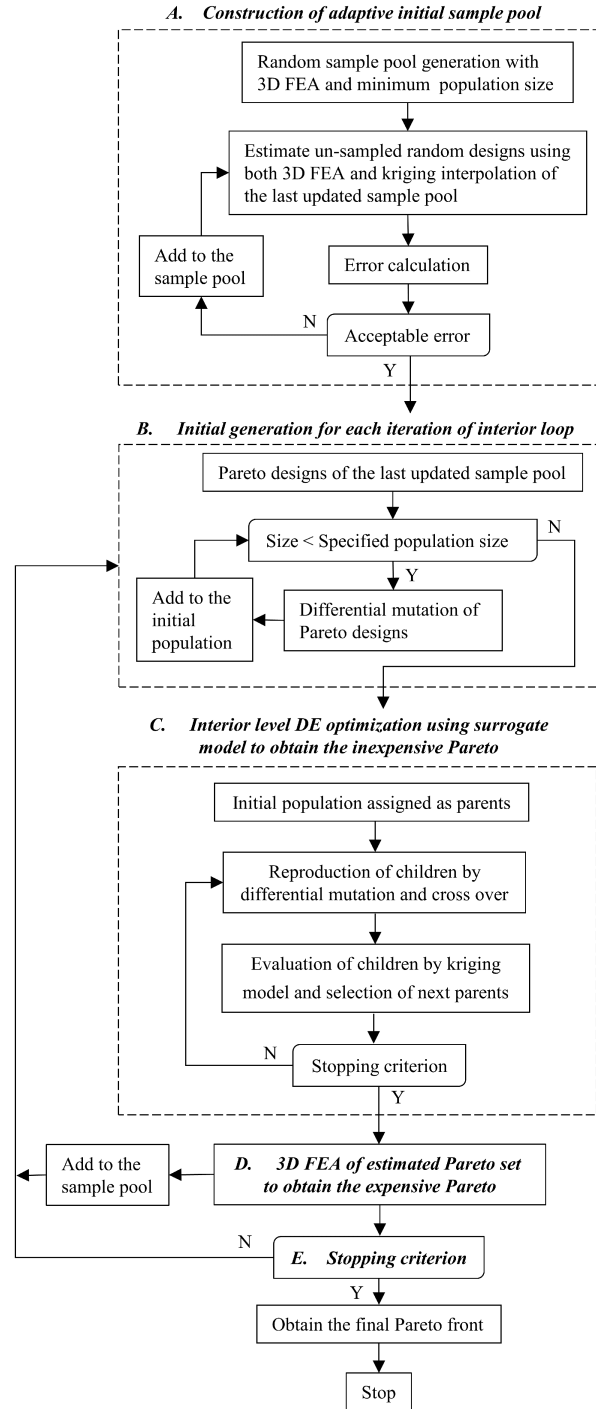


Figure 4.1: The two-level optimization algorithm with an interior loop based on DE and kriging surrogate models.

4.3.1 Initial sample pool

To efficiently generate the sample pool, the number of designs and their locations need to be considered. Larger number of samples is ideal; however, for each sample, computational effort should be performed, so it is important to reduce the samples through effectively locating them.

Sampling strategies can be categorized in two groups: (1) space filling methods for exploration purposes, and (2) sequential infilling sampling that improves exploitation [121]. In local surrogate model based optimization, infilling samples are very important. In this algorithm, infilling is performed in two stages: in the initial sample construction and after each generation. After generating the minimum sample size, the performance of a limited number of unsampled designs, e.g. 10, is evaluated with the kriging model as well as simulated with FEA and an estimation error is calculated. If the error is larger than a pre-set limit, e.g. %5, these designs are added to the pool and a new batch of unsampled designs are evaluated. This process constantly increases the sample pool size until satisfactory estimations are achieved for all test designs. As each outer level generation ends, the sample pool size increases only in the promising parts of the search space.

It should be mentioned that Design of Experiment (DOE) can be utilized as a systematic approach to generate the initial sample pool. However, when the search space is large, designs span over a wide range and nonlinearity is expected, so a higher number of levels for acceptable resolution is required; hence, a large number of designs are required by DOE to achieve reasonable resolution.

4.3.2 Initial generation for each iteration of interior loop

The initial population of the interior DE optimization is the Pareto designs of the latest sample pool. If the number of Pareto designs is more than the population size, extra designs are randomly eliminated; if they are less, additional designs are obtained using differential mutation.

4.3.3 Interior level

The interior level is a conventional DE optimization using inexpensive function evaluations. The output of this block is an estimated Pareto.

4.3.4 3D FEA of promising designs

It is expected to have some estimation error for the inexpensive Pareto front. To correct that, the Pareto designs are evaluated with 3D FEA and replaced with estimations.

4.3.5 Stopping criterion:

Multi-objective optimizations usually set a maximum number of function evaluations or maximum number of generations as the termination criterion. For the algorithms that converge to the optima very fast, this criterion can cause many dispensable generations which is vital to avoid, in order to reduce expensive evaluations. Here, a hybrid stopping criterion is used. Negligible improvement in the tips and the middle point of the Pareto front, for a few consecutive generations, will satisfy the third stopping criterion. Meeting any of these criteria, stops the algorithm.

Table 4.2: The results of the optimization algorithm presented in Fig. 4.1 for the test function (DTLZ2) with different number of objectives and variables. The results are the average of 5 runs for each scenario.

Variables	4		8		12	
Algorithm	DE	2L SA	DE	2L SA	DE	2L SA
1 objective; the population size of each generation is 5						
Generations	39.8	4	51	4	65.3	5
Func Evals	199	64	255	90	326.5	122.2
2 objectives; the population size of each generation is 10						
Generations	46.4	4	70.2	7 4.3	84.8	5.8
Func Evals	464	170	702	384.7	848	429.4
3 objectives; the population size of each generation is 15						
Generations	46.4	4	52.4	4	63.8	4
Func Evals	696	440	786	800	957	1060

4.4 Algorithm Implementation, Validation and Design Examples

The proposed optimization algorithm is implemented and validated using the test function DTLZ2 [122]. This function is capable of assessing the algorithm for problems with different levels of complexity, i.e., number of optimization variables and objectives. DTLZ2 functions with 1-3 objective and 4-12 variables were studied. Table 4.2 represents the average results of 5 runs for each scenario. Even for high number of variables, the proposed algorithm outperforms the conventional. For very complex problems with more than 3 objectives and 12 variables, the sample pool construction needs almost as many function calls as the total evaluations in conventional DE algorithm. Hence, their performances are comparable.

Two implementations of the algorithm for axial flux permanent magnet (AFPM)

Table 4.3: Optimization variables of the conventional machine.

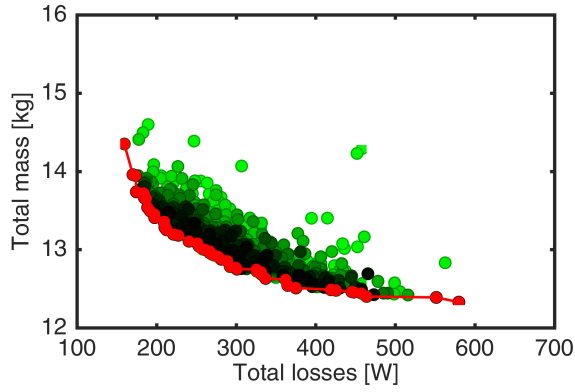
Variable	Unit	Minimum	Maximum
Air-gap	mm	1.8	5.0
Magnet thickness	mm	3.0	10.0
Tooth width / pitch		0.35	0.65
Pole arc / pitch		0.65	0.85
Statot yoke	mm	9	18
Rotor yoke	mm	5	11

Table 4.4: Optimization variables of the coreless machine.

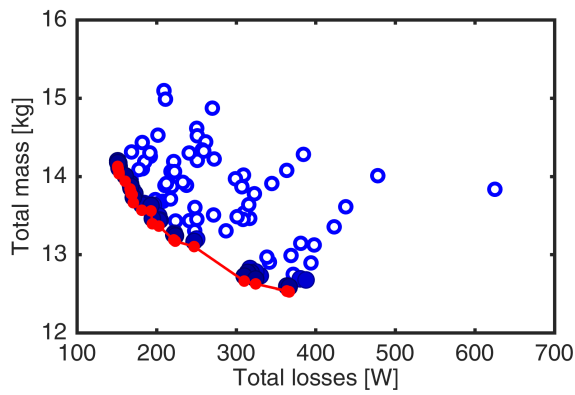
Variable	Unit	Minimum	Maximum
Air-gap	mm	0.5	2.0
Magnet thickness	mm	1.0	3.5
Pole arc / pitch		0.65	0.85
Rotor yoke	mm	4.0	8.0

machines with different numbers of variables were also studied: a commercially available conventional AFPM motor with single-rotor single-stator topology [90], and a multi-disc coreless machine with 2 stators [123]. The number of optimization variables are 4 and 6 for the coreless and conventional machines, respectively, represented in Table 4.3 and 4.4. The minimization of two objectives is simultaneously considered for the multi-objective design studies: active material mass and total losses at rated operation. All designs are evaluated at the rated torque and speed.

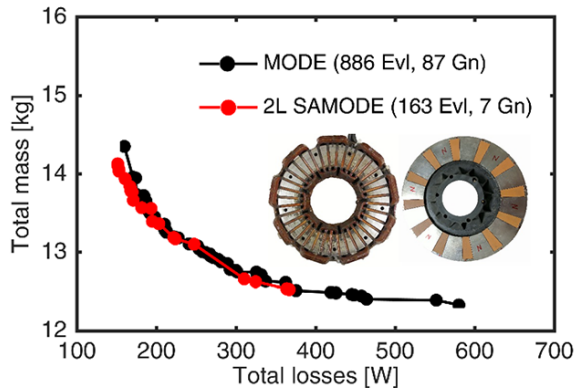
The optimization progress and Pareto front obtained from the conventional multi-objective DE (MODE) and the two-level surrogate assisted algorithm (2L SAMODE) are shown in Figs. 4.2 and 4.3. Darker colored designs evolved in more recent generations. The hollow data points represent designs in the initial sample pool.



(a)

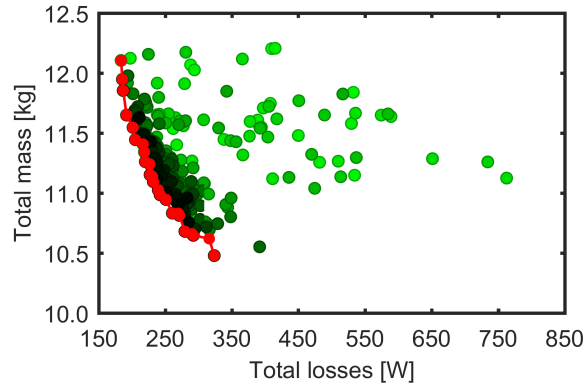


(b)

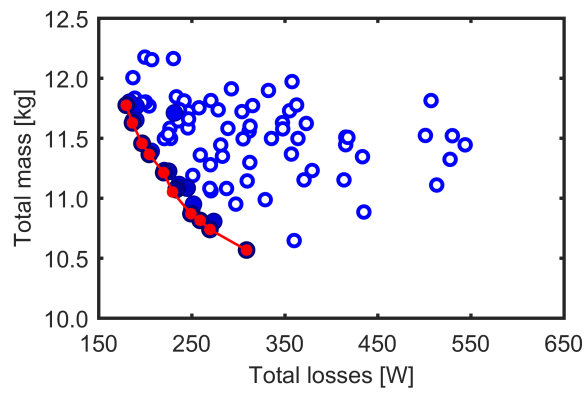


(c)

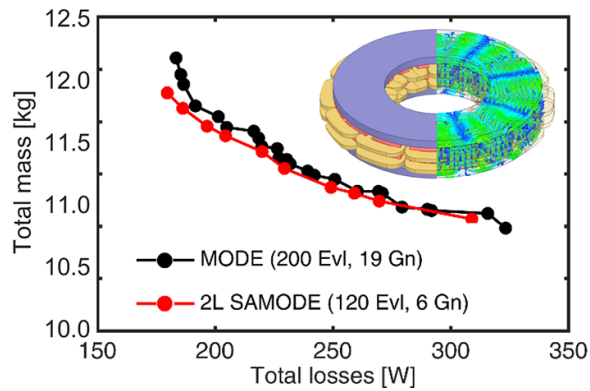
Figure 4.2: The optimization results for the commercial motor at the rated torque of 56 Nm, using (a) the conventional MODE, (b) the 2 level SAMODE, and (c) the Pareto fronts obtained from the two algorithms. The darker colors in (a) and (b) represent the designs evolved in more recent generations.



(a)



(b)



(c)

Figure 4.3: The optimization results for a coreless AFPM motor at the rated torque of 28 Nm, using (a) the conventional MODE, (b) the 2 level SAMODE, and (c) the Pareto fronts obtained from the two algorithms. The darker colors in (a) and (b) represent the designs evolved in more recent generations.

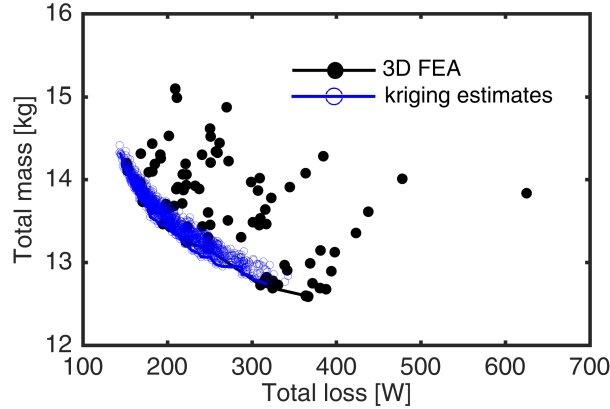


Figure 4.4: Employing the surrogate model is estimating designs in order to fill in the gaps in Pareto front.

4.5 Comparing Optimization Results

Both MODE and 2L SAMODE have achieved relatively similar Pareto front, which proves them to be the true Pareto front. In the coreless machine case, the MODE algorithm has terminated prematurely and needs a more strict stopping criterion. The reason can be explained by considering that total number of function calls in two-level optimization is the sum of the interior loop (inexpensive) and the exterior loop (expensive) function evaluations. This sum will be orders of magnitude more than the conventional algorithm, which improves exploration and exploitation; hence, it is likely that Pareto designs are achieved faster.

In case of the AFPM motor in Fig. 4.2c, the proposed 2L SAMODE achieves the Pareto front with only 163 3D FEAs, while conventional MODE needs 886 FEAs. For the coreless machine, Fig. 4.3c, the problem is less complicated, due to fewer number of variables and eliminated possible saturation in teeth. The Pareto front is obtained with 120 FEAs for 2L SAMODE, and 200 FEAs for MODE.

It is desired to include more designs in the Pareto front, in order to provide more

alternatives in the design selection. The kriging model can be used to fill in the gaps. This is demonstrated in Fig. 4.4, using the 2L SAMODE results in Fig. 4.2b. First, the variables range is limited to the designs in the Pareto front. Then thousands of designs within that range are estimated using the kriging model. Relatively accurate estimations are expected, since the sample pool has a better resolution closer to the Pareto. In case of MODE, to have a more complete Pareto front, the population of each generation should be increased, which requires even more FEAs.

4.6 Reference Design and Search Space Specification

The optimization algorithms with the ranges of design variables as wide as possible, need a large number of function evaluations in order to arrive at the final solution. It is expected that by properly narrowing down the search space the algorithm acquires the Pareto front quicker and this results into an ultra fast method. In this section methods of narrowing down the search space are proposed and compared with a reference approach which employs a broader search space. All the studied methods for assigning the optimization search space are included in the flowchart of Fig. 4.5.

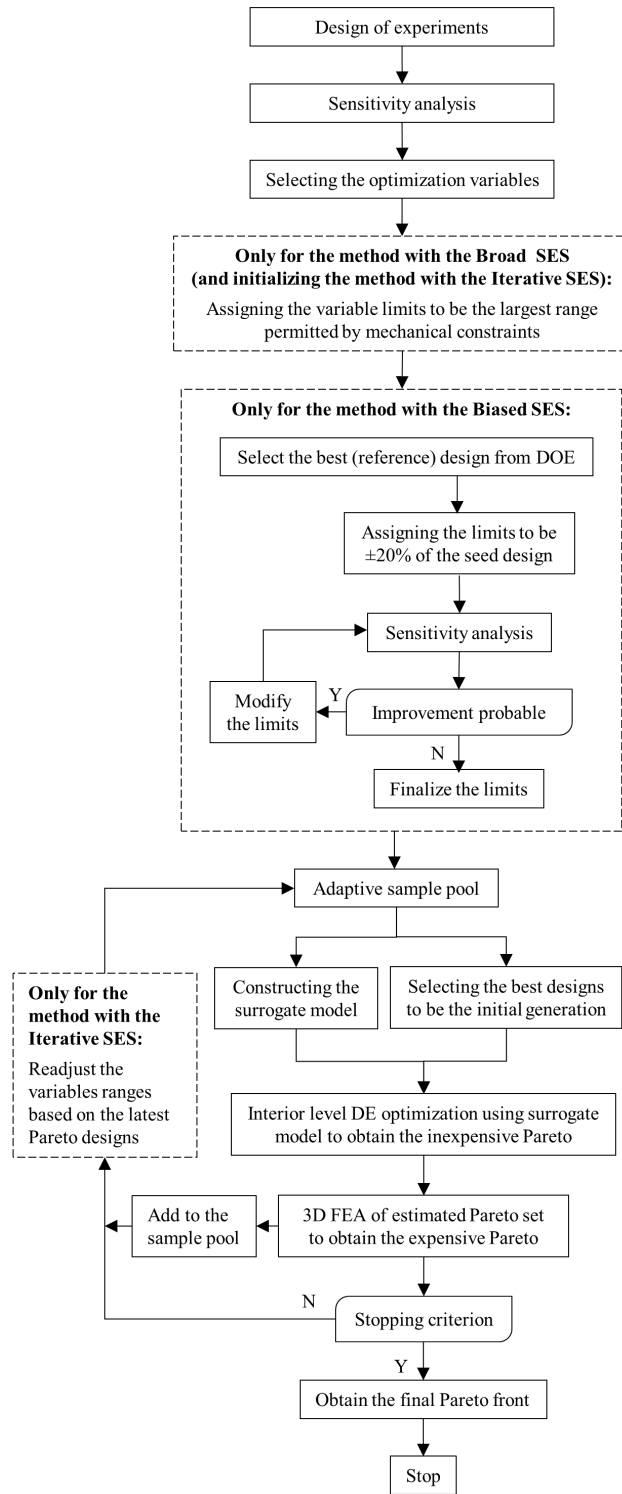


Figure 4.5: Three different methods of specifying search space are illustrated in the flowchart of the two-level kriging surrogate assisted optimization algorithm. The steps in dashed boxes are specific for different search space assignment approaches.

Defining the limits of optimization variables can greatly affect the speed of the optimization algorithm and the final design. If the search space is as wide as possible, a large number of designs would need to be evaluated, making the computation time prohibitively large. On the other hand, with the design limits clustered in a small area, the best trade-off of the objectives may not be achieved. Therefore, the proper specification of the search space is crucial. In this section, three methods for defining the search space are compared.

4.6.1 Broad search space specification

The first method (Broad SES) includes the widest possible ranges for variables' limits. A thorough exploration which may ensure the global optimum result is achieved at the cost of a large number of design evaluations.

4.6.2 Iterative search space specification

The second method (Iterative SES) is proposed to start with similar wide variable ranges and progressively modify them based on the latest Pareto designs. Consequently, the search space shrinks and the speed of the optimization improves. This can be seen as a greedier method and may miss some of the Pareto front designs, compared to the previous approach.

4.6.3 Biased search space specification

The third method (Biased SES) has narrower ranges for the variables, defining these ranges by taking advantage of DOE outcomes. In contrast with commonly used

approaches, the results from the DOE are used here for establishing a reference design and the search space, as explained in the following.

The designs specified by the DOE, conducted over an initially large range, are evaluated using 3D FEA, and in an example study in this section, the one with the lowest loss is selected as the reference design. The sensitivity analysis for this design is performed within a specified range, in this case, $\pm 20\%$ of its variables. As the obtained optimization variable ranges depend on the selected reference design, the search space is biased by its reference. This range is further modified based on sensitivity analysis.

4.6.4 Example Study and the Biased Search Space Definition

In order to clarify the biased search space definition and example spoke-type axial flux machine with 5 optimization variables, as shown in Fig. 4.6 and Table 4.5, are considered. The 40 pole 48 slot spoke-type AFPM machine under study is to be optimally designed with minimum active material cost and electromagnetic loss. The optimization objective functions are defined for the total loss, F_l , and active material cost, F_c :

$$F_l = W_{Cu} + W_c , \quad (4.4)$$

$$F_c = m_c + m_{pm} + 3 \cdot m_{Cu} , \quad (4.5)$$

where W_{Cu} , and W_c stand for the copper and core losses. PM eddy losses are not significant as ferrite magnets are employed. The total mass of the stator and rotor

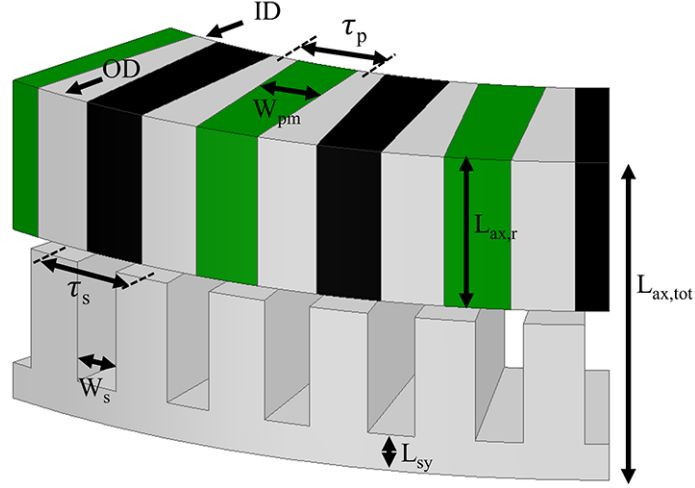


Figure 4.6: The geometrical variables employed in design optimization.

Table 4.5: The optimization variables and their assigned limits.

Variable	Definition	Search space assignment method	
		Broad and initially the Iterative SES	Biased SES
k_{sy}	$\frac{L_{sy}}{L_{ax,tot}}$	[0.11 , 0.40]	[0.11 , 0.18]
k_{rl}	$\frac{L_{ax,r}}{L_{ax,tot}}$	[0.20 , 0.50]	[0.34 , 0.47]
k_{pm}	$\frac{W_{pm}}{\tau_p}$	[0.30 , 0.90]	[0.55 , 0.90]
k_{sw}	$\frac{W_s}{\tau_s}$	[0.45 , 0.90]	[0.78 , 0.90]
λ	$\frac{OD}{ID}$	[0.40 , 0.85]	[0.42 , 0.75]

core are represented with m_c , and the copper and magnet mass, with m_{Cu} and m_{pm} , respectively. The mass is calculated in kg and the steel cost per kg is considered as the one-unit reference.

The results of sensitivity analysis for $\pm 20\%$ range, shown in Fig. 4.7 with dark blue bars, indicate that reduction in some design variables (k_{sy} and k_{rl}) and increase in others (k_{pm} , $k_{sw,id}$, and λ) decrease the loss. The extended ranges for the variables are defined based on these findings. For instance, the primary range for k_{rl} is 0.34-0.47, and sensitivity analysis indicates that lower values result in smaller losses. In order to investigate if further reduction in the value of k_{rl} is beneficial, an extended range is

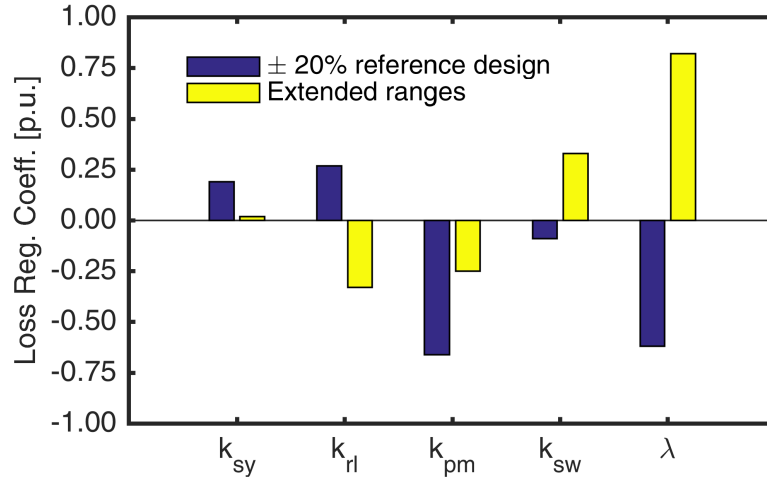


Figure 4.7: The sensitivity analysis within the range of $\pm 20\%$ of the reference design variables, and within an extended range to examine the possibility of further reduction in loss.

examined within 0.2-0.34. It is observed that the polarity of the regression coefficient changes, as seen in Fig. 4.7, concluding that further reduction in k_{rl} increases the losses, and hence, the variable is limited between 0.34-0.47. The ranges of other variables to be used for the optimization study are established similarly (Table 4.5). The steps above are exemplified for a spoke-type machine. The consideration of mechanical constraints may also be incorporated in this process.

4.6.5 Comparing the Result of Different Search Space Assignment Methods

The optimization study is conducted with the three discussed methods for defining the search space. The Pareto front is obtained using each of these methods (Fig. 4.8). The number of 3D FEA design evaluations for each of the methods is given (Table 4.6). It may be noted that the initial design space for the Broad and Iterative methods are identical, hence, both have an equal number of initial samples. The Biased method,

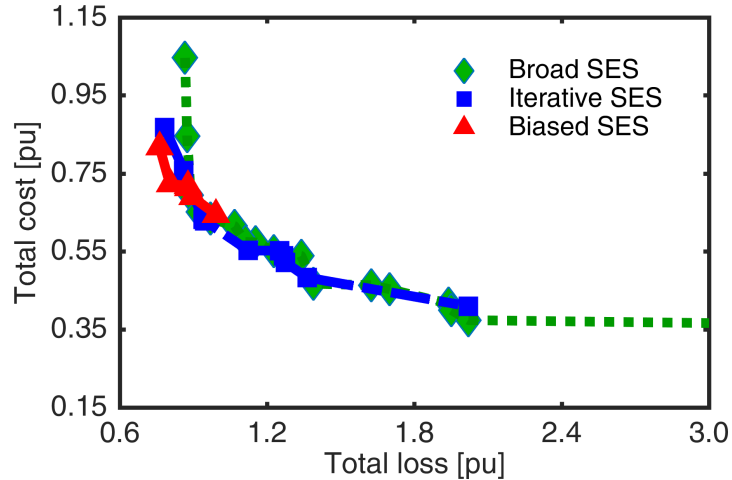


Figure 4.8: The Pareto front designs obtained from the two-level surrogate assisted optimization with three different methods for search space assignment. The reference design is providing the per-unitization base.

Table 4.6: The number of 3D FEA design evaluations by the surrogate assisted optimization.

Search space assignment	Number of FEA design evaluations		
	Initial samples	After initialization	Total
Broad	110	70	180
Iterative	110	45	155
Biased	70	45	115

having a smaller design space, needs a smaller number of initial FEAs. It is observed that, for the studied optimization problem of the spoke-type AFPM machine, the total number of FEA evaluations is the least when the Biased design space is used. It should be noted that the designs are evaluated using time consuming 3D FEAs and therefore, even the smallest amount of reduction in the number of evaluations is valuable.

The Broad SES assignment, identifies an extended Pareto front and provides various alternative optimum designs to choose between. The absolute limits of the machine design, taking the problem constraints and ratings into account, can be

identified using this wide design space, albeit at the cost of larger number of design evaluations.

The Pareto front obtained from proposed Iterative method has fewer designs, nonetheless, it can still provide several optimum options for the designer to select among and it requires fewer FEA runs. The exploitation capability of the optimization algorithm is improved at the cost of the exploration capability (Fig. 4.8).

The obtained Pareto front highly depends on the location of the search space, which in the third method is biased by the reference design. The design with the least loss from the DOE was selected as the initial reference design for this example, and thus, the search space location is inclined toward the low-loss high-cost zone (Fig. 4.9). On the other hand, if the reference design was a lower cost and higher loss machine, the search space would be located differently and consequently the Pareto front would yield a different set of optimum designs. Thus, the reference design may be selected based on which of the considered objectives is more important. As a result of the smaller search space, the number of FEA evaluations reduces, as presented in Table 4.6. Due to utilization of a surrogate assisted algorithm, the number of required FEA design evaluation is much smaller than a conventional optimization which usually needs thousands of design evaluations. However, as 3D models are employed, even the smallest amount of reduction in number of analysis saves significant amount of time.

In the example problem, although the emphasis was on obtaining a low loss machine, single-objective optimization was not recommended as cost was also an objective in the second place of priority. In such cases, employing the Biased SES is

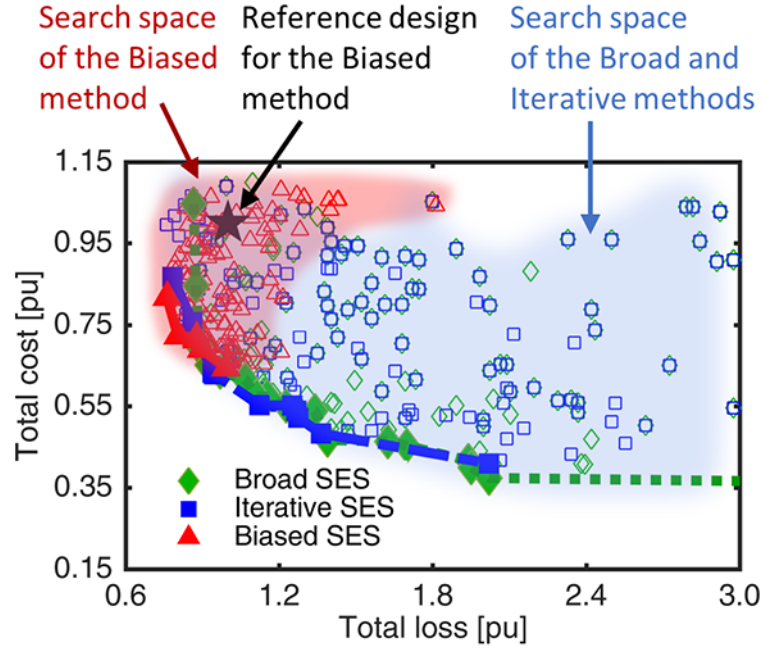


Figure 4.9: The search space defined with different methods, for the multi-objective optimization of the spoke machine design. All the designs shown in the plot are evaluated with 3D FEA. The reference design is providing the per-unitization base.

recommended as a specified location of the Pareto front is of more interest, resulting in fewer 3D FEAs.

Figure 5.11 represents the distribution of variables for the Pareto front designs. The ranges of the variables for the optimum designs obtained from the Broad SES are the widest, while the Biased SES has tighter ranges. As the designs in the Biased method are inclined toward higher efficiency, it can be deduced that for the studied machine, within the constrained envelope and specified ratings, in order to achieve a higher efficiency, thinner stator yoke and thicker magnets can be used. The rest of the parameters need to be selected through optimization.

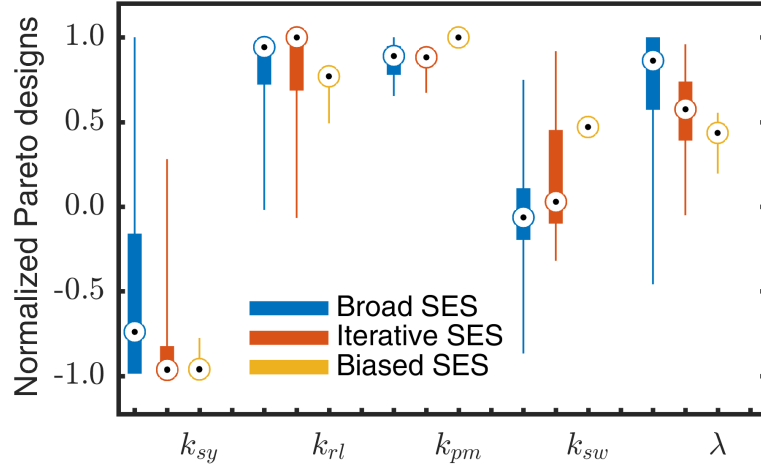


Figure 4.10: The distribution of variables for the Pareto front designs obtained using different search space assignments.

4.7 Summary

A two-level surrogate-assisted DE based optimization is proposed for use with electric machine design problems with 3D FEA. The results show that the algorithm outperforms conventional methods as it requires substantially fewer design evaluations. The two-level evaluation of Pareto designs results in an efficient exploration and exploitation approach so that the global optima can be located within the first few generations, depending on the accuracy of the kriging model.

This algorithm, unlike most surrogate assisted optimizations, does not solely rely on estimated values; it has a dynamic sample pool that stops increasing in size once the estimation error is sufficiently small, and gradually improves the kriging model resolution only around Pareto designs. These make it possible to achieve accurate final results, avoid unnecessary expensive evaluations, and converge faster. The constructed kriging model can also be used for post processing purposes, such as developing a full Pareto front, and thereby allowing selection from a larger number of

optimum designs. If the sample pool is large enough, any FEA calculation for further purposes may become dispensable and replaced with the highly accurate kriging surrogate model.

In addition, different methods for the search space definition in multi-objective optimization are proposed and compared. One of these new methods progressively narrows down the variable limits, enhancing the exploitation. The other approach relies on novel applications of the DOE methodology and biases the search space definition based on a reference design and sensitivity analysis. This is especially useful when it is known beforehand which of the objectives is more important. Ultimately resulting in a smaller design space, reducing the number of evaluations, thereby greatly improving the speed of the optimization.

Chapter 5

Optimization Case Studies

5.1 Introduction

In this chapter two detailed example studies are included, both taking advantage of the introduced optimization algorithm in the previous chapter. The first study is dedicated to optimally designing surface mounted AFPM machines for different slot/pole combinations. The study is extensive and extracts the general design guidelines to achieve the best machine performance and the best choice for the pole count. The second study systematically compares two AFPM machine configurations: yokeless and segmented armature (YASA) machine and more simple single-stator single-rotor AFPM machine configuration. Both cases are representing a comparative and systematic design approach with outcomes that can be used for understanding the path taken by the optimization algorithm toward the best design for given envelope size and ratings.

5.2 Systematic Exploration of the Effects of Pole Count on Optimum Design of Ultra-high Efficiency Fractional hp Axial Flux PM Machines

Optimizing the design of electric machines is a vital step in ensuring the economical use of active materials. In addition to the time consuming 3D analyses and large number of design evaluations required by general optimization algorithms, adding the pole count as a variable to be assigned and also increasing the range of each variable in order to have a more comprehensive search space, are all the reasons necessitating the use of a more efficient algorithm in optimally designing the machine in this case study.

The proposed algorithm in the previous chapter is employed to optimally design an AFPM machine within a specified envelope, and to identify the limits of cost and efficiency. In order to obtain these limits, the variables' ranges are assigned to be as wide as possible, resulting in a vast design space, the study of which was enabled by the developed special algorithm. Additionally, optimized designs with different rotor polarities are systematically compared in order to form the basis for a set of generalized design rules.

5.2.1 Problem Formulation for Analysis and Optimization

The design and optimization of axial flux permanent magnet (AFPM) machines are of great interest due to many of their advantages such as higher torque density and efficiency. Their disc shape makes it practical to achieve designs with a larger

diameter and a higher number of poles. The possibility to have a higher pole count leads to potential performance improvements. Determining the number of rotor poles and subsequently stator slots greatly impacts the outcomes of the electric machine design optimization [124]. This section is a systematic investigation of those impacts for a surface mounted AFPM machine.

Recently, the fractional slot concentrated winding (FSCW) has attracted attention for its application in surface mounted PM machines [125–127]. Its main advantages include shorter end coils, a simple structure, and improved fault tolerance. The use of double layer FSCW, as opposed to its single layer counterpart, can mitigate the core and PM losses. Also, in case of axial flux configurations, the double layer winding can yield an increased active diameter within a constrained total diameter, due to the reduction in coil thickness.

Studies on surface mounted PM machines (SPM) with a concentrated winding provide the principles for selecting the best combinations for the number of slots and poles. They propose a slot per pole per phase less than or equal to 0.5 [128], $N_s = N_p \pm 1$ or $N_s = N_p \pm 2$ [129–132], and $N_s > N_p$ [133], where N_s and N_r are the number of slots and poles, respectively. Based on the above guidelines, four slot/pole combinations (12/10, 24/20, 36/30, 48/40) with a double layer concentrated winding are selected.

The main shortcomings of the studies conducted on the effect of slot/pole combinations is that they rely on simplistic assumptions, such as a constant yoke thickness, and the use of analytical approaches and/or 2D models for machines with 3D flux paths [126, 134–138], which results in comparing topologies that are not truly optimal

designs for their pole count. This section addresses the issue by considering several pole counts and optimally designing the machine for each case.

The axial flux machine under study is designed to produce the rated torque of 5.4 Nm at 1050 rpm. The optimization study is comprehensive and considers all possible designs within the limitations of this problem, i.e. geometrical dimensions, mechanical limits, etc., in order to reach the absolute limit of each objective function.

The envelope size, including axial length and total outer diameter are constant and fixed at their maximum value while number of poles and other geometrical variables are investigated to achieve the most favorable design. The optimal design problem is elaborated in the following.

Objectives:

Considering that cost competitiveness and design efficiency are the most important criteria from the perspective of manufacturers and customers, the optimization objectives are considered to be the total loss and cost [139]. The two optimization objective functions are defined for the total loss, F_l , and active material cost, F_c :

$$F_l = W_{Cu} + W_c + W_{pm} , \tag{5.1}$$

$$F_c = m_c + 3 \cdot m_{Cu} + 24 \cdot m_{pm} ,$$

where W_{Cu} , W_c , and W_{pm} stand for the copper, stator core, and PM eddy losses.

The preliminary studies showed that the rotor core loss is a negligible portion of the total loss in this study, and is therefore not considered in the analysis. The low rotor core losses can be attributed to the relatively low fundamental frequency, as well as reduced rotor core flux density harmonics due to application of surface mounted PMs.

The magnet losses can be reduced by segmentation.

The total mass of the stator and rotor core are represented with m_c , and the copper and magnet mass, with m_{Cu} and m_{pm} , respectively. The mass is calculated in kg and the steel cost per kg is considered as the one-unit reference [140]. This per-unitized method of defining the cost function makes the calculations independent of the impact of using various vendors and currencies, while still including a correct representation of the cost trends needed for design comparison.

It is expected that the best compromise design varies for different pole counts. One of the goals of this study is to investigate those varying factors in order to identify generalized rules for a suitable initial design of SPM machines with different polarities.

Generally, as the number of poles and slots increases, the copper loss decreases, due to the reduced end winding length. On the other hand, the increase in the fundamental frequency causes more core losses. Therefore, a pole count which achieves a proper trade-off between copper and core losses, for a given application and dimensional constraints exists, and should be identified.

Parametric 3D FEA Models:

The AFPM machines to be optimized are single stator single rotor configurations with surface mounted Neodymium magnets and concentrated non-overlapping windings. The stator core is laminated. In order to include the effect of varying number of poles, different optimization studies are conducted for four slot/pole combinations i.e. 12/10, 24/20, 36/30, and 48/40. The total axial height and the total outer diameter including the end coils are kept the same in all the studied topologies. Figure 5.1 illustrates the 3D parametric model, exemplified for the 40 pole configuration. All of

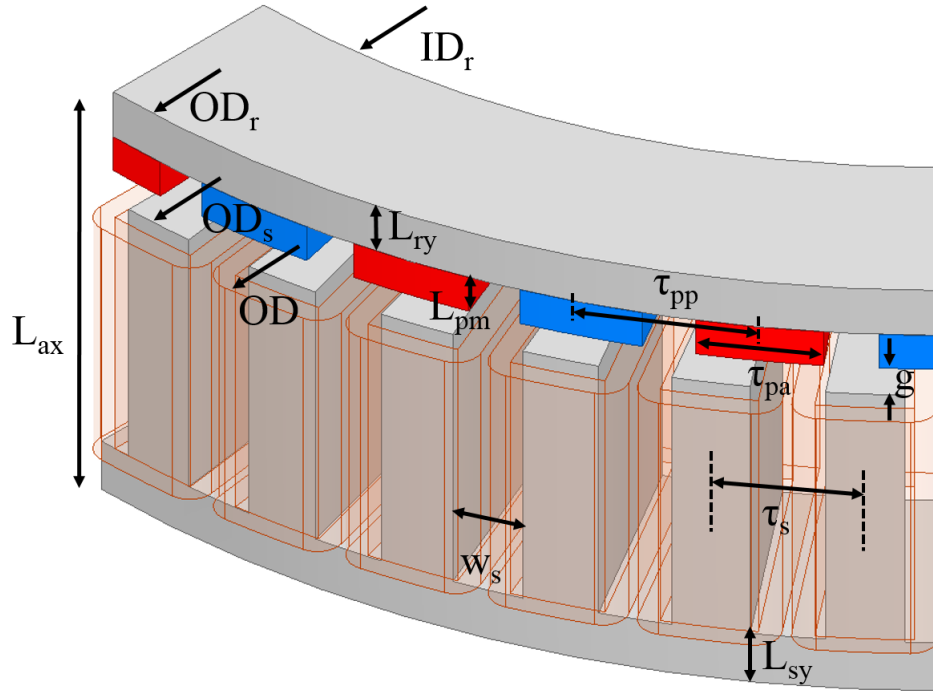


Figure 5.1: The geometrical independent variables included in the process of design optimization. The variables are introduced to the algorithm as ratios.

the FEA results are obtained from time-transient 3D models with motion.

Optimization Variables:

The search space for the optimal design is assigned to be very large, i.e., the ranges of the optimization variables are as wide as possible, with only geometrical limitations taken into account, to include the absolute limits of the minimum cost and loss achievable. Therefore, the variables are limited either to prevent the intersection of various geometrical components or to address mechanical constraints such as the minimum air-gap or yoke thickness.

Eight geometrical variables are selected as optimization variables, as illustrated in Fig. 5.1 and Table 5.6. The flux lines distribution for the 40 pole topology, as an instance, is presented in Fig. 5.2. The variables are defined as ratios to ensure their independence. Only the air-gap is defined as an absolute value, in mm. The variables

Table 5.1: Independent optimization variables and corresponding limits, exemplified for the configuration with 40 poles.

Variable	Description	Min	Max
g	<i>Air-gap</i> [mm]	1.50	4.00
k_{ry}	rotor yoke ratio = $\frac{L_{ry}}{L_{ax}}$	0.07	0.25
k_{sy}	stator yoke ratio = $\frac{L_{sy}}{L_{ax}}$	0.07	0.25
k_{pm}	magnet length ratio = $\frac{L_{pm}}{L_{ax}}$	0.06	0.25
k_{ds}	split ratio = $\frac{ID_s}{OD_s}$	0.48	0.80
k_{oh}	over hang ratio = $\frac{(OD_r - OD_s)}{(OD - OD_s)}$	-1.00	1.00
k_{sw}	slot width to slot pitch ratio = $\frac{w_s}{\tau_{s,id}}$	0.45	0.90
k_p	pole arc to pole pitch ratio = $\frac{\tau_{pa}}{\tau_{pp}}$	0.60	0.95

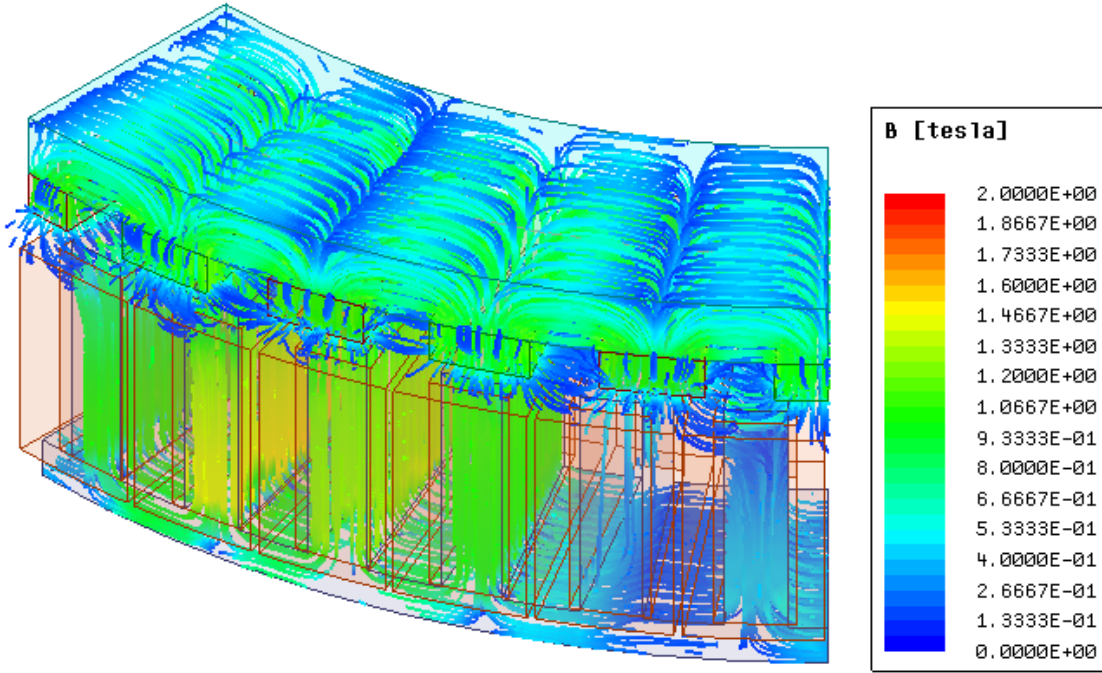


Figure 5.2: The 3D flux lines distribution of an exemplified design with 40 poles.

in the axial direction are divided by the total axial length, L_{ax} . The slot depth is calculated for a constant overall axial length.

The over-hang ratio, k_{oh} , is defined to take values between -1 and $+1$. The positive values indicate over-hang, that is, the magnet radial length is greater than the stator radial length with the same average radius. The negative values represent under-hang, that is, the magnet radial length is less than the stator radial length with

the same average radius. Taking over-hang into account, particularly in cost sensitive designs, is helpful in potential PM volume reduction. It is ensured that all designs produce the rated torque at the rated speed through a two-pass analysis. First the design is analyzed using a preassigned current density. Then, based on the produced torque and the required torque, the current density is adjusted and the design is re-evaluated to ensure the rated torque is obtained.

Sensitivity Studies:

The effects of the optimization variables on the performance of the designs with different number of poles are investigated by studying regression coefficients, which are obtained by conducting a design of experiments study. Negative and positive regression coefficients indicate that the absolute value of the response reduces and increases, respectively, upon increase in the corresponding factor. The larger the magnitude of the regression coefficients, the more influential the factor.

The influence of variations in the optimization variables on dc copper loss, stator core loss, and cost function are illustrated in (Fig. 5.3, Fig. 5.22b, and Fig. 5.5). The magnet loss comprises a smaller fraction of the total losses. In the case of the specific ratings and envelope constraints in this study, it may be observed from these figures that the general trend is that the copper losses increase upon increasing the air-gap (g), and split ratio (k_{ds}). On the other hand, by increasing magnet thickness (k_{pm}), slot width (k_{sw}) and pole arc (k_p), the copper loss reduces. This is attributed to the higher magnetic loading achieved by an increase in these parameters, and therefore, a lower current density can be employed to produce the rated torque. The rotor yoke (k_{ry}) appears to be influential only in case of the machine with the lowest pole count,

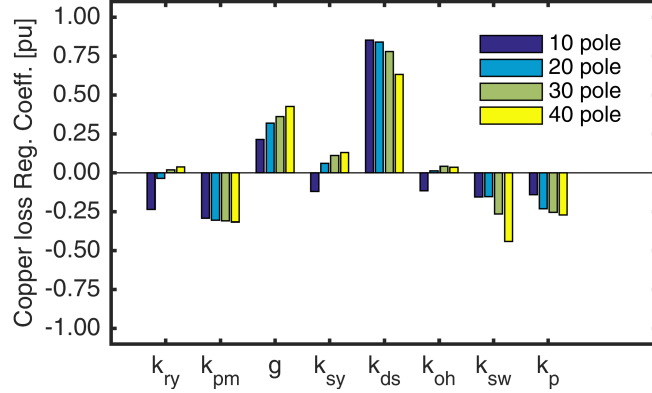


Figure 5.3: The effects of optimization variables on dc copper loss of designs with different pole count, represented by per-unitized regression coefficients.

which may be owing to its higher saturation, considering the larger pole pitch.

It is observed that the degree of the impacts varies for different pole counts. With fixed axial length, the increase in yoke thickness can be achieved by reducing the slot depth. This may alter the leakage pattern and/or the harmonic spectrum and hence core losses in a non-straightforward way. Figure 5.5 shows that the effect of overhang ratio (k_{oh}) is more considerable in cost function and more so in case of the machines with lower number of poles. This design of experiments based study shows that the selected studied variables have significant effects on objectives. Therefore, the optimization is performed with all eight discussed variables.

5.2.2 Optimization Results and Discussion

The two-level surrogate assisted optimization is performed on the AFPM machines with different number of poles. For all cases, the population size is set at ten designs per generation. The number of generations is dynamic and not fixed; the optimization terminates once further improvement is not achieved. The number of total FEA runs

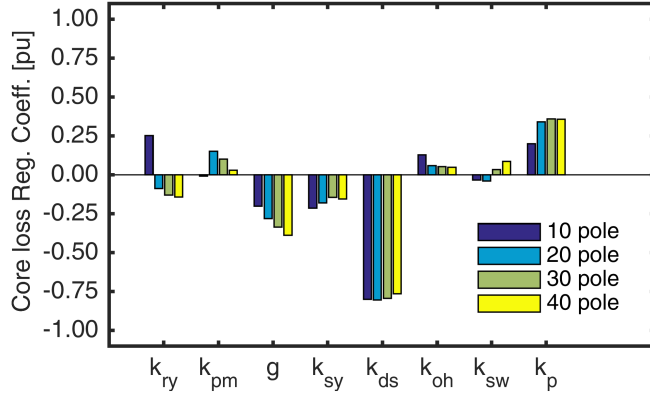


Figure 5.4: The effects of optimization variables on core loss of designs with different pole count, represented by per-unitized regression coefficients.

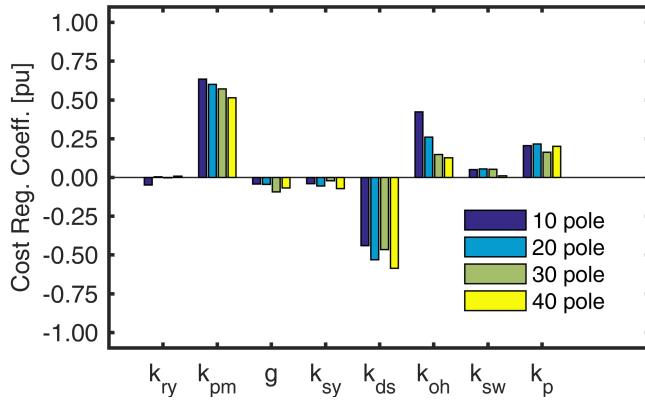


Figure 5.5: The effects of optimization variables on cost function of designs with different pole count, represented by per-unitized regression coefficients.

is also variable because it depends on factors such as the acceptable sample pool resolution, the number of generations, and the number of new proposed promising designs in each generation. The number of generations, FE models, and kriging surrogate model design evaluations for each optimization set-up is provided in Table 5.2.

As expected, because each generation includes hundreds of design candidates evaluated with ultra-fast kriging meta models, even the total number of generations is much lower than for typical DE optimization algorithms, resulting in a substantial

Table 5.2: Number of generations, FE models, and kriging surrogate models for each optimization study.

Poles	40	30	20	10
Generations	5	7	5	9
FE models	211	207	164	300
Kriging models	3130	3120	2040	5640

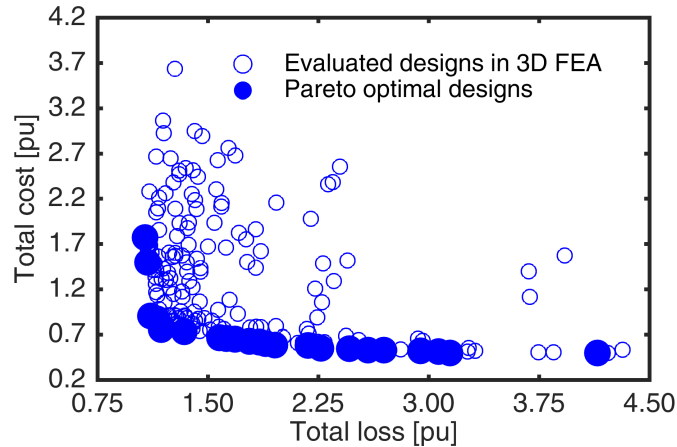


Figure 5.6: All designs evaluated in 3D FEA for the 30 pole configuration and the Pareto optimal designs represented by filled circles.

reduction of the computational effort. Only a relatively low number of 3D FE models are employed, each solved with the ANSYS/Maxwell software in approx. 30 minutes on a desktop PC workstation with 10 cores, Intel(R) Xeon(R) CPU E5-2687W v3 @ 3.10 GHz, and much faster on HPC systems with large scale parallel processing capabilities. As an example for the 30 pole machine, Fig. 5.6 includes all the 207 candidates evaluated with 3D FEA and for clarity does not include the results for the 3120 Kriging models.

5.2.3 Optimal Design Selection

The final product of a multi-objective optimization, after reaching termination criteria, is a set of non-dominated designs, referred to as Pareto optimal designs. A

design is Pareto optimal if there exists no other feasible design within the defined search space which would improve one objective without concurrently worsening at least one other objective [141]. Mathematically, designs variables' vector \vec{x}^* is called a Pareto optimal design, if no other vector x exists that satisfies both the following conditions [142]:

$$\begin{aligned} f_j(\vec{x}) &\leq f_j(\vec{x}^*) \quad \text{for all } j \in (1, 2, \dots, m) ; \\ f_j(\vec{x}) &< f_j(\vec{x}^*) \quad \text{for at least one } j \in (1, 2, \dots, m). \end{aligned} \tag{5.2}$$

where f represents the objective function and m is the number of objective functions, for this study $m = 2$. An example Pareto front obtained for the 30 pole topology and 2 objectives of this study is plotted in Fig. 5.6. The Pareto designs closer to the knee region of the Pareto front provide a trade-off between the two objectives while the designs further away from the knee point represent the superiority of one of the objectives over the other.

The final design should be selected among the Pareto front optimal designs. This can be done by approaches such as ranking and rating the alternatives, dividing the Pareto front solutions into clusters of preferences, defining a weighted metric, pseudo-weighted vectors, reference point method, or filtering the Pareto front designs through additional constraints such as robustness [143–147]. While these help with narrowing down the choices, they may not result in one single final selection unless the process is iteratively repeated until only one solution is left. The existing methods may also add difficulties in convergence of the optimization results [144, 146]. In this section, a systematic solution is proposed which may quantify the preferences and facilitate final design selection.

The relation between the two objectives can be captured by fitting a curve on the Pareto front. The general format of the fitted curve can be described as

$$\hat{f}_2 = \frac{a}{\hat{f}_1 - b} + c, \quad (5.3)$$

where \hat{f}_1 and \hat{f}_2 are the two objective functions on the fitted curve (loss and cost, respectively, in this study), and constants a , b , and c are positive values that can be assigned based on the exact shape of the obtained Pareto front.

The final design selection can be performed by quantifying the superiority of objectives over one another. This quantification can be expressed by a factor T ; any percentage-wise further improvement in one objective should cause less than T times deterioration in the other, that is:

$$\frac{\Delta \hat{f}_{t1}}{\hat{f}_{t1}} = -\frac{\Delta \hat{f}_{t2}}{\hat{f}_{t2}} \times T \xrightarrow{\Delta f \rightarrow 0} \frac{d\hat{f}_{t2}}{d\hat{f}_{t1}} = -\frac{1}{T} \times \frac{\hat{f}_{t2}}{\hat{f}_{t1}}. \quad (5.4)$$

Equation (5.4) in combination with (5.3) can be solved for \hat{f}_{t1} and \hat{f}_{t2} that are the the objective values of the desired design. The closest design on Pareto to $(\hat{f}_{t1}, \hat{f}_{t2})$ can be selected as the final design.

The knee point can be defined as the point where $T = 1$. This means any percentage-wise improvement in one of the objectives results into the exact amount of percentage-wise deterioration in the other, and is therefore representative of a best-compromise design. The calculated knee point is marked with a star in Fig. 5.7. Two other examples, prioritizing loss and cost, are also included and marked. In one example, with $T = 0.2$, further percentage-wise reduction of loss will cause at least 5 times ($1/0.2 = 5$) more percentage-wise increase in cost. As another example, where

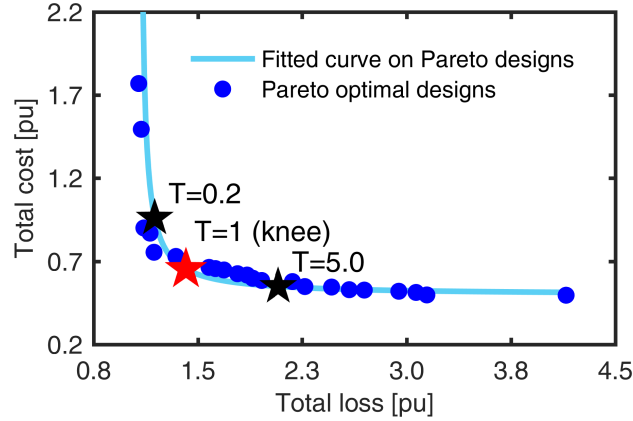


Figure 5.7: The fitted curve on the Pareto front and the calculated knee point, based on (5.4), marked with the red star symbol (★). The point $T = 0.2$ is where further reduction in loss causes at least 5 ($\frac{1}{0.2} = 5$) times more increase in the cost. The point $T = 5$ is where further reduction of cost causes at least 5 times more increase in loss.

$T = 5$, further reduction in cost leads to at least 5 times more increase in the loss.

5.2.4 Identification of Trends

The representative optimum design for each pole count is selected to be on the knee point of the Pareto front, marked with a star in Fig. 5.8. The breakdown of active material mass, cost, and loss for these designs is shown in Table 5.3 and Fig. 5.9. Table 5.3 also includes the global performance parameters, i.e., power density, torque density, and goodness defined as Nm per loss unit, in order to provide comparison indices with other designs.

It is observed that for the optimum design with a lower number of poles and slots, the copper and steel mass increase. The PM mass is affected by several variables including the split ratio, overhang, PM thickness, and PM arc ratio and it comprises a smaller portion of the total mass.

It is also seen that copper losses of the knee point design reduce initially upon

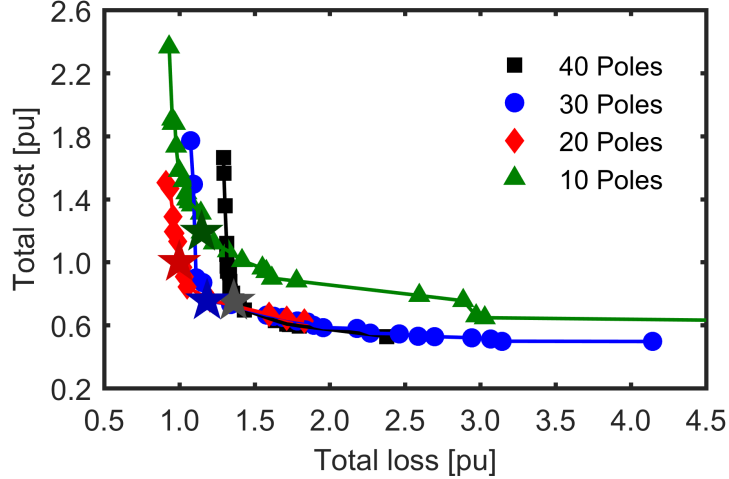
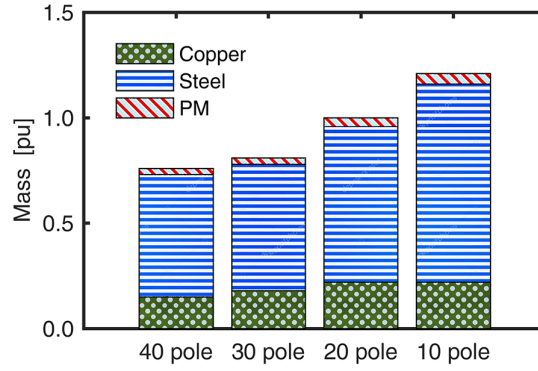


Figure 5.8: Pareto fronts obtained for the machines with different pole count, employing 3D FEA models. A representative design of each topology is marked with a star symbol (★). The per-unit system is based on the representative design with the highest efficiency which is the 20 pole topology marked with a red star symbol (★).

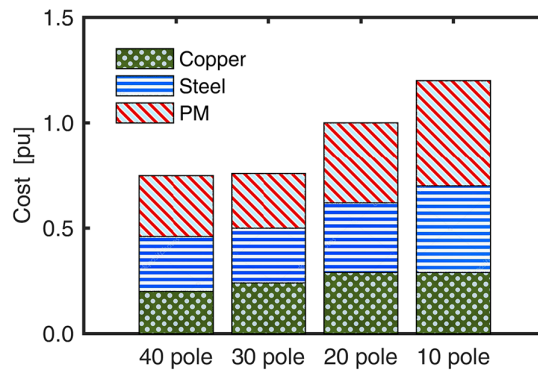
Table 5.3: The per-unit value of representative optimum designs for different pole counts. The total mass, cost, and loss of the selected 20 pole design represent the base.

Number of poles		40	30	20	10
Mass	Copper	0.15	0.18	0.22	0.22
	Steel	0.58	0.60	0.74	0.94
	PM	0.03	0.03	0.04	0.05
	Total	0.76	0.81	1.00	1.21
Cost	Copper	0.20	0.24	0.29	0.29
	Steel	0.26	0.26	0.33	0.41
	PM	0.29	0.26	0.38	0.50
	Total	0.75	0.77	1.00	1.21
Loss	Copper	0.71	0.67	0.49	0.75
	Core	0.63	0.43	0.37	0.22
	PM	0.03	0.07	0.14	0.17
	Total	1.36	1.17	1.00	1.14
Emag. efficiency [%]		92.7	93.7	94.6	93.9
Power density [W/kg]		217.5	205.5	165.4	136.8
Torque density [Nm/kg]		2.0	1.9	1.5	1.2
Goodness [Nm/ \sqrt{W}]		0.79	0.86	0.93	0.87

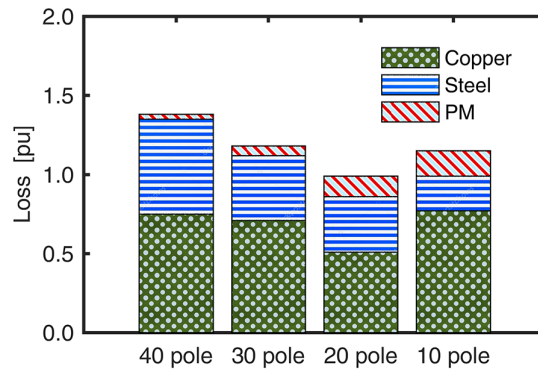
increasing pole count, and then increase. This trend may in part be explained by considering that as the number of poles and slots reduces, the end turn length increases,



(a)



(b)



(c)

Figure 5.9: The mass, cost, and loss components of the design on the knee point of the Pareto front obtained from the optimization studies with different number of poles.

while the current density reduces. The minimum copper loss is obtained for the design with 20 poles, given the specifications and ratings of this study. The core loss is lower for optimum designs with lower number of poles. This can be attributed to the

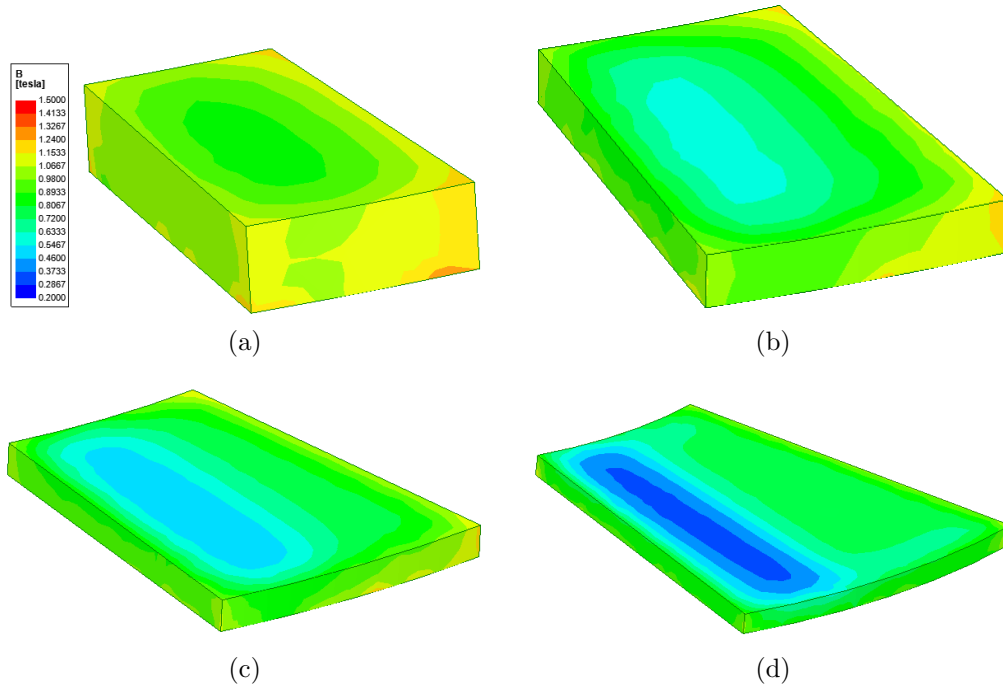


Figure 5.10: Flux density distribution in magnets of the optimum designs with (a) 40, (b) 30, (c) 20, and (d) 10 poles at the rated load. Note that the color scale is identical and ranges from 0.2 T to 1.5 T.

Table 5.4: Minimum flux density within Neodymium magnets of the optimum designs selected on the knee of the Pareto front.

Number of poles	40	30	20	10
Open-circuit [T]	0.57	0.45	0.39	0.30
Load 1 pu [T]	0.57	0.45	0.39	0.28
Load 2 pu [T]	0.57	0.41	0.36	0.20

reduced electrical frequency. The magnet loss increases for lower pole counts; magnet segmentation is not considered in the optimization process, therefore lower pole counts with larger pieces of magnets may increase the magnet eddy current losses. Magnet segmentation would affect the cost function which adds to the complications of setting up a systematic optimization algorithm. It also should be noted that, compared to the other two loss components, magnet loss is a smaller portion of the total losses.

In order to evaluate the PM demagnetization situation, the minimum flux density within the entire PM space is recorded and presented in Table 5.4. The evaluations are carried for open-circuit, rated and double the rated load. The flux density distribution at the rated operating condition is illustrated in Fig. 5.10. The optimization results suggest thicker magnets for the designs with higher pole count. Therefore, the lowest flux density of 0.3 T is observed in case of the machine with the lowest pole count and thinner magnets which have a lower permeance coefficient. The magnets of the machine with 40 poles have minimum flux density of 0.57 T. The demagnetization curve of employed Neodymium PM exhibits a knee at about 0.35 T for 75°C. The results show that for this design problem, optimum designs with higher pole count have a lower risk of demagnetization.

5.2.5 Characteristics of Optimum Designs

The box plot in Fig. 5.11 illustrates the distribution of variables for designs on the Pareto fronts. This plot can be used to identify certain characteristics of optimum designs as discussed in the following. The PM thickness of the optimal designs located on the Pareto front tends towards their smaller values and more so for lower pole counts. Generally, the PM arc ratios are larger for the lower pole counts. This implies that when the number of poles is lower, a design with thinner PMs and larger pole arc to pole pitch ratio will be more beneficial. The optimization algorithm reduces the thickness of the PMs with wider arcs that may result in reduction of the PM volume and eddy losses. The stator yoke in optimum designs is generally larger for topologies with lower pole counts. This can be to reduce the flux density in the

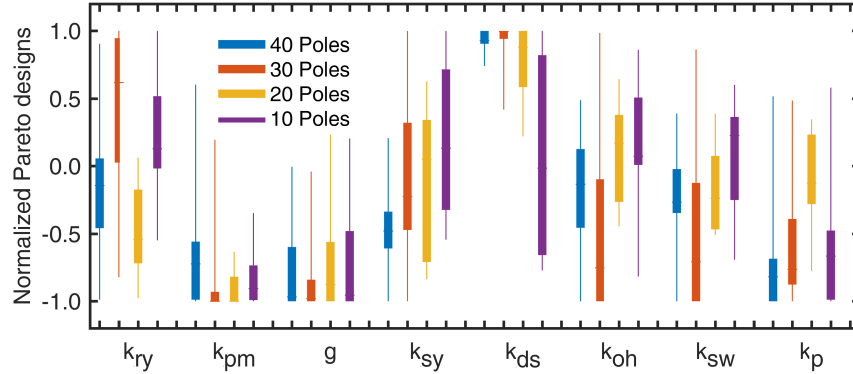


Figure 5.11: Distribution of the design variables for the Pareto front designs obtained with different pole counts.

yoke and hence core loss.

The split ratio of the Pareto front designs is generally inclined toward their greater value and more so for higher pole and slot counts. A larger split ratio reduces the active material weight and cost and provides a larger tooth width in the inner diameter, mitigating the risk of saturation. The increased number of slots necessitates larger split ratio for core loss reduction.

To examine the extreme Pareto designs which are located on the tips of the Pareto front, the 30 pole topology is exemplified because of its extended and asymptotic Pareto front. The Pareto front is divided into three zones shown in Fig. 5.12.

The division of Pareto designs into three zones is conducted using the factor T , as explained by (5.4). Zone 1 is selected to be where further reduction of loss causes at least 5 times more increase in cost which corresponds to $T < 0.2$. Zone 3 is where further reduction in cost leads to at least 5 times more increase in loss, corresponding to $T > 5$. Zone 2 includes the Pareto designs in between. Therefore, designs in zone 1 and 3 are optimized with an emphasis on minimizing the loss and cost, respectively, while the designs in zone 2 display a preference of balance between the two objectives.

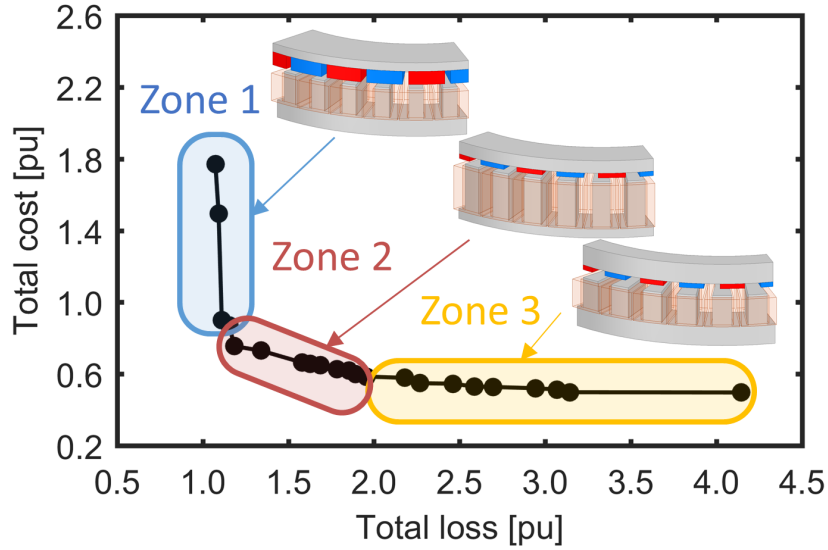


Figure 5.12: Pareto front obtained for the machine with 30 poles, divided into three zones, the vertical section (zone 1) where further reduction in loss requires at least 5 times more increase in cost, the knee in the middle (zone 2), and the horizontal section (zone 3) where further reduction in cost requires at least 5 times more increase in loss.

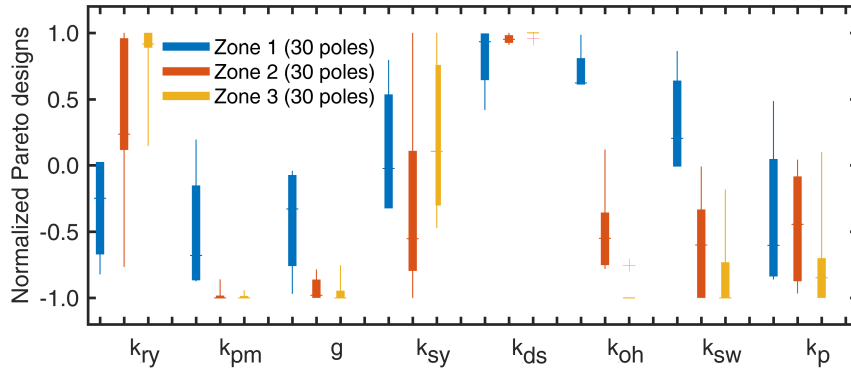


Figure 5.13: Distribution of the design variables at different zones of the Pareto front for the topology with 30 poles. This topology is selected due to its extended asymptotic Pareto front on both sides, illustrated in Fig. 5.12.

Based on Fig. 5.13, the high efficiency designs in zone 1 have a thinner yoke and a larger air-gap. However, the use of more magnet material results in costly designs. More efficient designs also have wider slots, smaller current density and copper loss. The less expensive, albeit less efficient, designs in zone 3 are achieved by reducing the

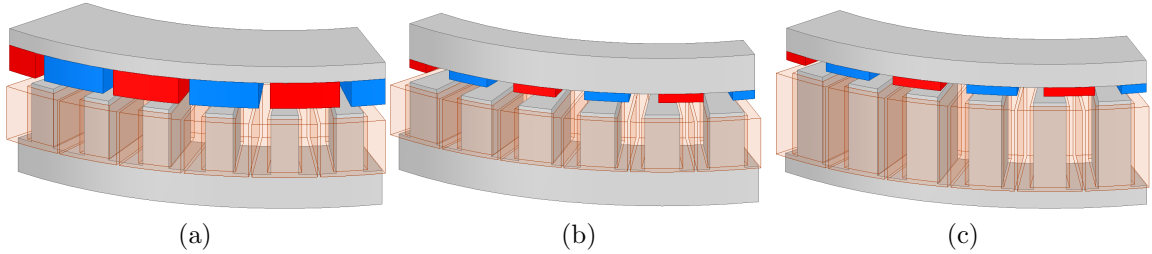


Figure 5.14: The optimum designs obtained for the configuration with 30 poles. (a) The design with minimum loss on the Pareto front, (b) the design with minimum cost on the Pareto front, (c) the design on the knee of the Pareto front with a trade-off between cost and loss.

PM thickness, the PM arc, and the overhang ratio, and also by increasing the split ratio.

Extreme cases of designs, with the lowest loss and with the lowest cost, along with the knee designs that achieves trade-off between loss and cost are presented in Fig. 5.14. The design with the least loss in Fig. 5.14a has thick PMs and a thin yoke such that the cost is mostly associated with the PMs at about 78% of the total cost. Copper and core losses are both equal, at about 17 W. The design in Fig. 5.14b has the minimum cost and employs very thin PMs and a very thick yoke. The copper loss accounts for most of the total loss with 134 W out of 140 W, while the cost is distributed evenly among the materials. The results illustrate that the designs in the knee zone, i.e. the best trade-off region, have balanced cost and loss components, a characteristic typically associated with robust optimal designs.

5.2.6 Prototyping and Experimental Validation

All the designs evaluated for the four slot/pole combinations along with the Pareto front obtained are represented in Fig. 5.15. A lower loss design can be obtained from the 20 pole configuration, while a less expensive design can be achieved with 30 or 40

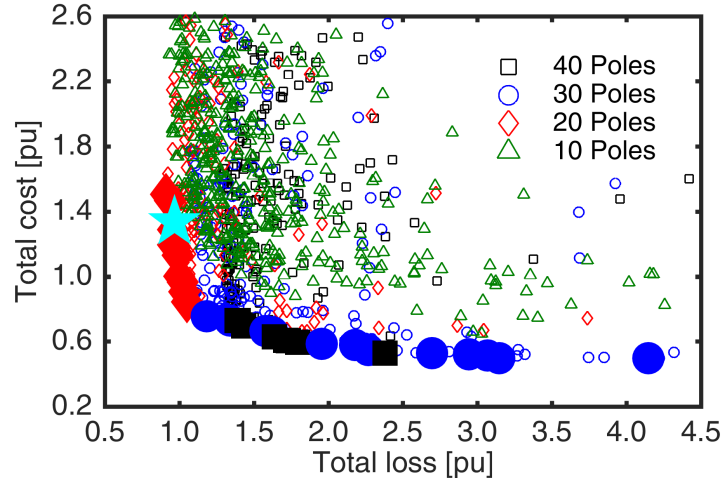


Figure 5.15: The overall Pareto front (filled markers) and all of the evaluated designs (hollow markers). The prototyped design is selected to have a high efficiency, marked with a star symbol (★).

poles. A machine with 20 poles and 24 slots which achieves the ultra high efficiency in excess of 94% is selected for prototyping and marked with a star in Fig. 5.15. The manufactured prototype is presented in Fig. 5.16.

The estimated performance using the 3D FEA model is verified with measurements and represented in Table 5.5 [2]. The spinning loss includes mechanical losses, such as friction and windage, stator core losses, and PM losses. The calculated efficiency uses copper and core losses obtained from the FEA and 6 W mechanical losses. The results for the measurements and the FEA are in agreement and serve as the basis for the satisfactory validation of the study.

The performance of the motor is investigated at different speed and torque values. The efficiency map is measured and plotted in Fig. 5.17. The calculated efficiency map within the same speed and torque range matches satisfactorily with the measurements. The performance of the machine at the rated torque and speed is marked.

Table 5.5: The experimental and calculated results for the ultra high efficiency axial flux SPM machine rated at 0.75 hp. The calculated value of the efficiency uses 3D FEA results and a 6 W mechanical loss component.

		Calculated	Measured
Torque Constant	[Nm/A]	1.4	1.4
Phase resistance	[Ω]	0.39	0.37
Conductor loss	[W]	17.4	15.3
Core loss	[W]	10.9	—
Mechanical loss	[W]	6	—
Spinning loss	[W]	—	17.3
Total loss	[W]	34.3	32.6
Efficiency	[%]	94.5	94.3

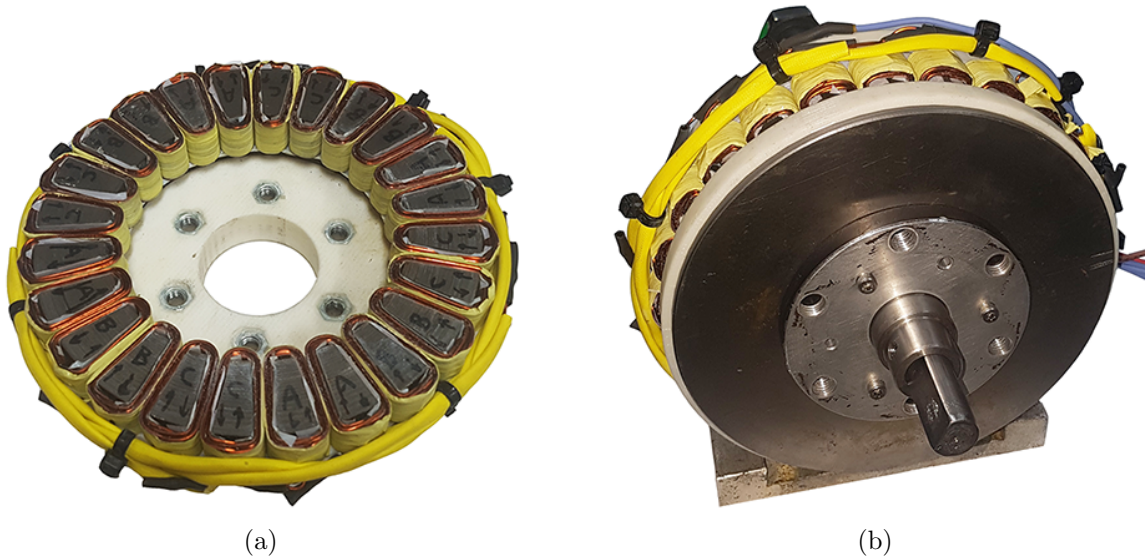


Figure 5.16: The ultra high efficiency AFPM machine, rated for 5.4 Nm at 1050 rpm, selected for prototyping based on the comprehensive optimization study with 3D FEA models. (a) The stator with a core OD of approx. 170 mm and (b) the assembled motor.

5.3 Systematic Optimization and Comparison of Single-sided and Double-sided AFPM Machines

The disc shape of axial flux permanent magnet (AFPM) machines have opened up many configuration possibilities including yokeless and segmented armature (YASA).

The YASA machine can be regarded as a next generation Torus type AFPM machine

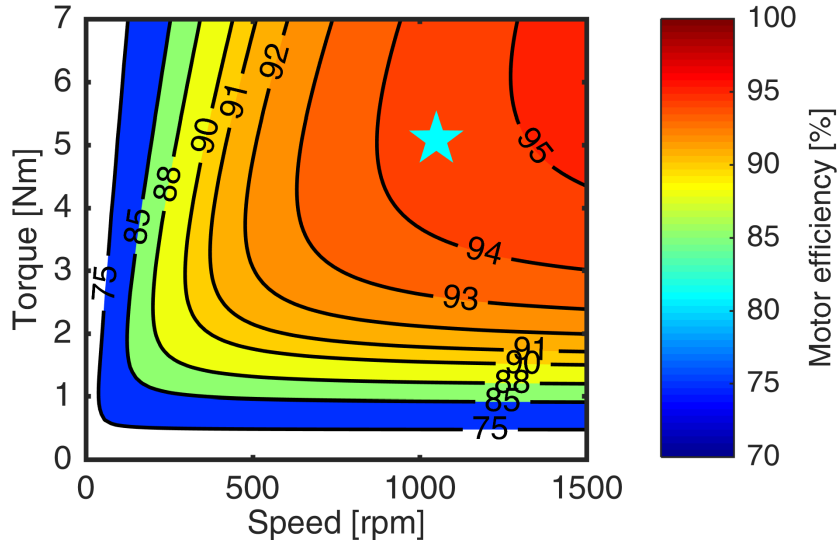


Figure 5.17: The measured efficiency map of the prototyped machine. The performance of the machine at its rated torque and speed is marked with a star symbol (★).

[148, 149] that combines winding arrangements of the NN and NS type Torus machines. The YASA structure has been proposed for traction application [7] and gained attention due to its high torque density and the segmented stator teeth structure that facilitates higher slot fill factor.

The mechanical challenges of the YASA topology remain its major drawbacks and are twofold. Firstly, if the segmented stator sections are to be made of laminated steel and stacked radially, they should increase in circumferential width from the inner to the outer radius. That is, to carry the axially directed flux, each single lamination must be differently shaped. This can be addressed by methods such as punching reduced width laminations, or using soft magnetic composite (SMC) materials [150–152]. The second drawback is the difficulty of holding the individual stator segments in place while maintaining a balanced air-gap [153]. This can be resolved by utilizing annular plates containing openings the same size as the shoe of the stator segments

[152], or by incorporating ring holders [151].

A comparative study conducted on transverse flux, radial flux, and YASA machines with identical dimensions and the same PM mass concluded that the transverse flux topology performs better when a low speed, a high torque, and small electric loadings are desired. However, in case of limited axial lengths, YASA is found to be superior [154]. In another study, YASA, single sided, and TORUS machines were compared [155], showing that the torque density (Nm/m^3) of YASA is higher than the others at the rated specifications of an electric vehicle. These studies have compared the performance of the YASA machine with other axial and radial flux machines. However, optimal designs have not been considered, which may make the outcomes of such comparisons debatable. In this regard, this section presents a systematic comparison for an example traction application of the two machine structures shown in Fig. 5.18.

Optimization studies for both machines are performed to simultaneously achieve the objectives of minimum active material mass and minimum electromagnetic loss, including the stator core loss and the dc copper loss. The optimization algorithm capable of handling 3D FEAs is proposed in the previous chapter. A comparative study is conducted for the optimum designs located on the Pareto front.

5.3.1 Analytical Evaluation

In order to clarify the general differences in electromagnetic performance of the YASA and single sided machine, three machine designs are considered in this section: 1) a YASA structure, 2) a single sided machine with half the total magnet volume of

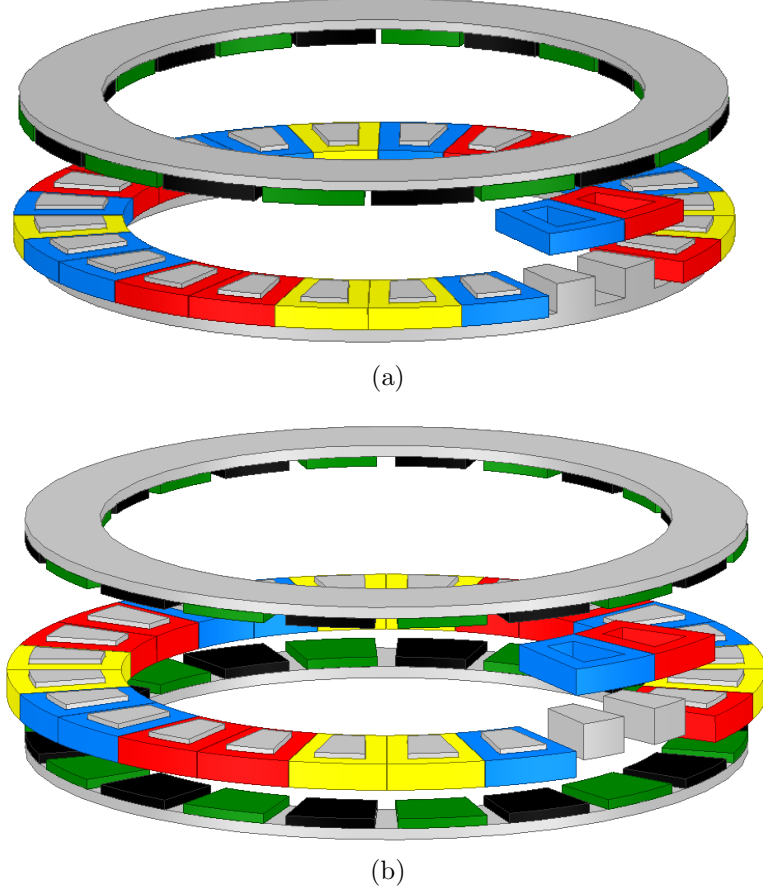


Figure 5.18: The 3D parametric models of the two AFPM machines under study: (a) single-stator single-rotor, and (b) YASA with two rotors.

the YASA machine (S1M), and 3) a single sided machine with the same total magnet volume as the YASA structure (S2M). The parametric models are presented in Fig. 5.19.

The electromagnetic torque of an AFPM machine with a pure q-axis current excitation, i.e. $i_d = 0$, can be estimated from

$$T_e = \frac{3p}{2} \lambda_d i_q ; \quad \lambda_d = \lambda_{mo} - L_e \cdot i_q , \quad (5.5)$$

where p is the number of poles; λ_d , the d-axis flux linkage; λ_{mo} , the open circuit flux produced by the magnets; and L_e is an equivalent inductance to capture the drop in d-axis flux linkage due to the q-axis current [156]. Figure 5.20 plots λ_d versus i_q . It

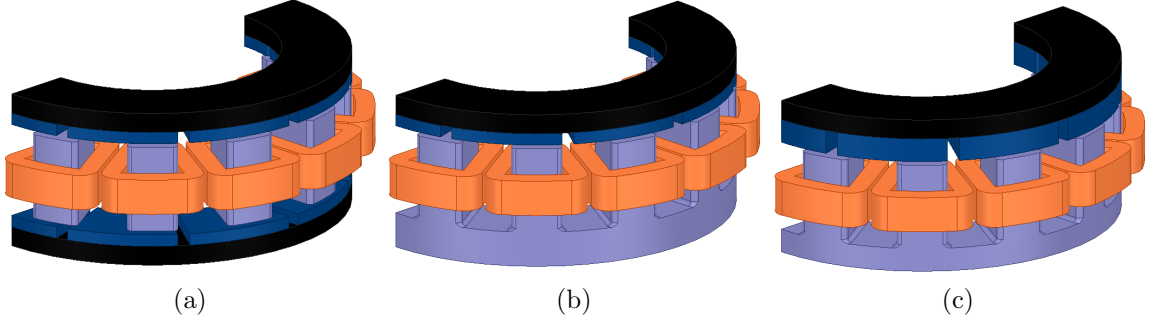


Figure 5.19: The 3D FEA parametric model of three topologies considered for preliminary evaluations; (a) the YASA structure, (b) the single sided machine with half the total magnet volume as the YASA (S1M), and (c) the single sided machine with the same total magnet volume as the YASA (S2M).

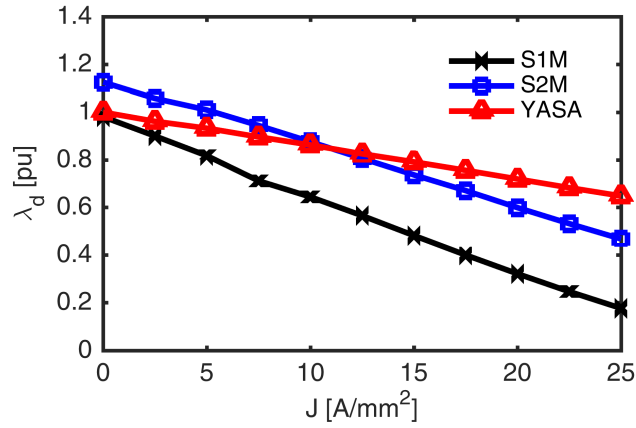


Figure 5.20: D-axis flux linkage at different q-axis currents, per-unitized based on λ_d of the YASA machine at open-circuit. The reduction in λ_d due to i_q is considerably higher for the single sided machines due to greater saturation.

can be seen that this drop is fairly linear and the slope can be represented by L_e as

$$L_e = \frac{\Delta\lambda_d}{\Delta i_q} . \quad (5.6)$$

L_e has a larger value for machines with a higher saturation level, as shown in Figs. 5.21a and 5.21b, resulting in a sharper decline in the d-axis flux in the load operation. This results in non-linear torque-current characteristics, which will be further discussed.

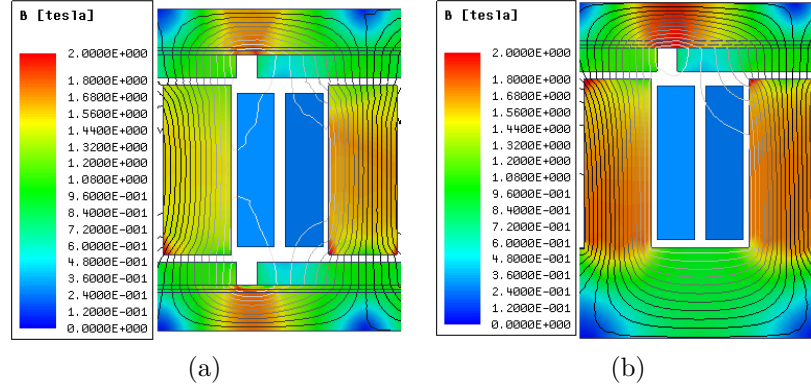


Figure 5.21: Flux density distribution with pure q-axis excitation for (a) the YASA machine, and (b) the S1M machine, at the current density of 25 A/mm^2 . The stator teeth and rotor core operate in saturation, which explains the reduction in d-axis flux at high q-axis currents.”

The magnet flux, λ_{mo} , can be estimated as [127]

$$\lambda_{mo} = \frac{2}{\pi} k_{w1} N_t k_{vg} \alpha_i B_{go} \tau_p L_{Fe} ; \quad B_{go} = \frac{B_r}{\frac{1}{k_\sigma} + \frac{\mu_{mr} k_c k_{so} g}{L_{pm}}} , \quad (5.7)$$

where k_{w1} is the fundamental winding factor; N_t , the number of turns per phase; k_{vg} , the ratio between the amplitude of the fundamental wave and the average value of the air-gap flux density; B_{go} , the peak value of the open-circuit flux density; τ_p , the pole pitch; L_{Fe} , the inner diameter subtracted from the outer diameter in case of an axial air-gap machine; B_r , the remanence of the magnets; L_{pm} , the magnet thickness in the direction of magnetization; α_i , the pole-arc to pole-pitch ratio; g , the air-gap length; k_c , Carter’s coefficient; μ_{mr} , the relative permeability of the PM; k_{so} , the d-axis saturation factor in the open-circuit operation; and k_σ is the leakage coefficient.

Based on (5.7), for an unsaturated machine with negligible leakage and fringing (k_σ , k_c , and $k_{so}=1$), λ_{mo} is proportional to the ratio of the total magnet thickness to the total electromagnetic air-gap, i.e. $\frac{L_{pm}}{\mu_{mr} \cdot g + L_{pm}}$. The S1M machine has half the

air-gap and half the magnet thickness of the YASA machine, while the S2M machine has half the mechanical air-gap of the YASA for the same overall magnet thickness. Therefore, $\frac{L_{pm}}{\mu_{mr}g+L_{pm}}$ is identical for S1M and YASA, while it is higher for S2M. This leads to a higher λ_{mo} for S2M and comparable values for YASA and S1M, as observed in Fig. 5.20 (λ_d at $i_q = 0$).

Another phenomenon affecting torque production, particularly at higher currents, is the armature reaction which strongly influences the displacement power factor. The stator inductance, L_s ($L_q = L_d = L_s$), may be estimated by

$$L_s = \frac{m\mu_0(k_{w1}N_t)^2\tau_p L_{Fe}}{\pi^2 p(k_{cg} + \frac{L_{pm}}{\mu_{mr}})} \cdot \frac{1}{k_{sd}}, \quad (5.8)$$

where m is the number of phases, and k_{sd} the saturation coefficient with values larger than 1 for higher saturation levels. A larger electromagnetic air-gap results in a lower inductance, and thus a smaller armature reaction and a higher power factor. Therefore, the armature reaction effect would be lowest in case of the YASA machine and highest for the S1M. This is to the YASA's advantage, particularly at higher loadings.

A common argument is that the eliminated stator yoke in the YASA machine provides extra space for the stator and copper, resulting in a higher torque within the same volume. Nevertheless, not all of this space can be used by copper since some room must be provided for the second rotor disc. However, such an argument may be more credible in cases where the stator employs a thicker yoke for mechanical and/or electromagnetic reasons. sided machine necessitate a thick stator yoke.

The torque production principles can also be explained with shear stress and the

air-gap surface area [110]. The electromagnetic torque of any electric machine can be defined as the product of the electromagnetic force, F , and the radius:

$$T_e = Fr ; F = \sigma a_a ; \sigma = BA , \quad (5.9)$$

where r is the radius; σ , the electromagnetic air-gap shear stress; a_a , the air-gap area; B , the magnetic loading; and A , the electric loading defined as the ampere-turns per unit of periphery. Although in the YASA configuration a_a is twice that of the single sided AFPM machine, A and consequently F for each air-gap is reduced by half. Therefore, doubling the air-gap surface area in the YASA structure does not double the torque.

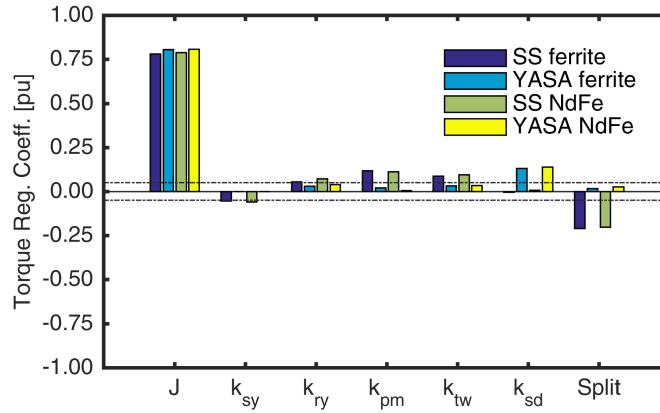
5.3.2 Sensitivity Analysis

The primary intent of the sensitivity analysis in this case is to study the impact of the loadings on the performance indices. To perform a systematic study, the performance indices (responses) and their corresponding variables (factors) are selected. Then, several designs are selected employing the design of experiments methodology. The responses selected are the electromagnetic torque, the stator core losses, and the displacement power factor. For each response, 7 variables are selected, including: the current density, J ; the stator yoke to the total axial length ratio, k_{sy} ; the rotor yoke to the total axial length ratio, k_{ry} ; the magnet thickness to the total axial length ratio, k_{pm} ; the slot depth to the total axial length ratio, k_{sd} ; and the split ratio defined as the inner to the outer diameter ratio. Figure 5.22 represents the results, where positive values indicate a proportional increase in the response when the factor

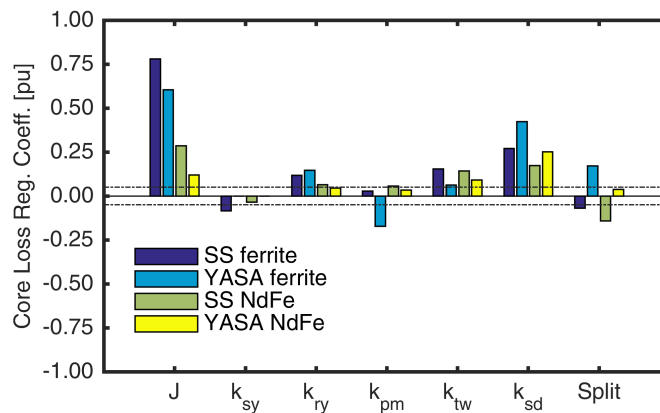
is increased, while negative values represent a proportional decrease. Larger values indicate a stronger sensitivity.

The sensitivity is conducted for machines with both ferrite and Neodymium magnets. The magnet volume is identical in all cases. Some considerable outcomes of the sensitivity analysis, demonstrated in Fig. 5.22, are as follows:

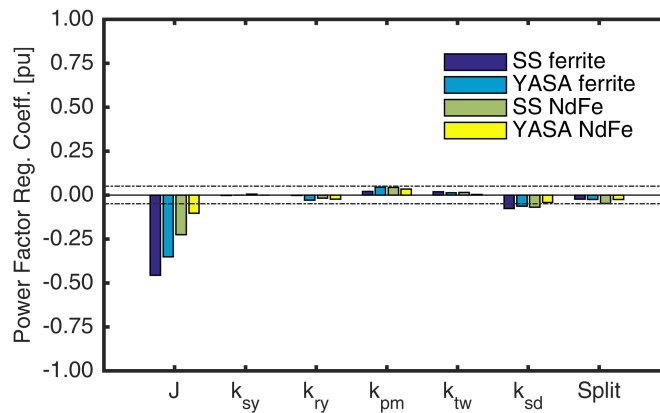
- 1) An increase in the ampere-turns improves the electromagnetic torque more significantly in the YASA compared to the single sided machine, which is due to the YASA's lower armature reaction.
- 2) The stator and rotor yoke thicknesses have negligible effects, indicating that the yokes are not saturated within the studied range.
- 3) In case of an increased slot depth, the improvement in torque production is considerable only in the YASA machine. This can be attributed to the increased flux leakage in the single sided machines with deeper slots.
- 4) Due to the larger volume of the stator core in the single sided machines and the larger armature reaction, the effect of the current on core loss is higher.
- 5) The reduction in the displacement power factor due to the increased current density is more significant for the single sided machine. This is due to smaller armature reaction of the YASA machine.
- 6) Higher magnetic loading causes less reduction in the displacement power factor at overload operation. This is in line with expectations, due to the smaller per unit reactance with NdFeB magnets than with ferrites.



(a)



(b)



(c)

Figure 5.22: The sensitivity analysis of the (a) electromagnetic torque, (b) stator core loss, and (c) power factor for single sided and YASA topologies. The horizontal dashed lines distinguish the insignificant factors with maximum effect being less than 5% variation in the response, within the studied range.

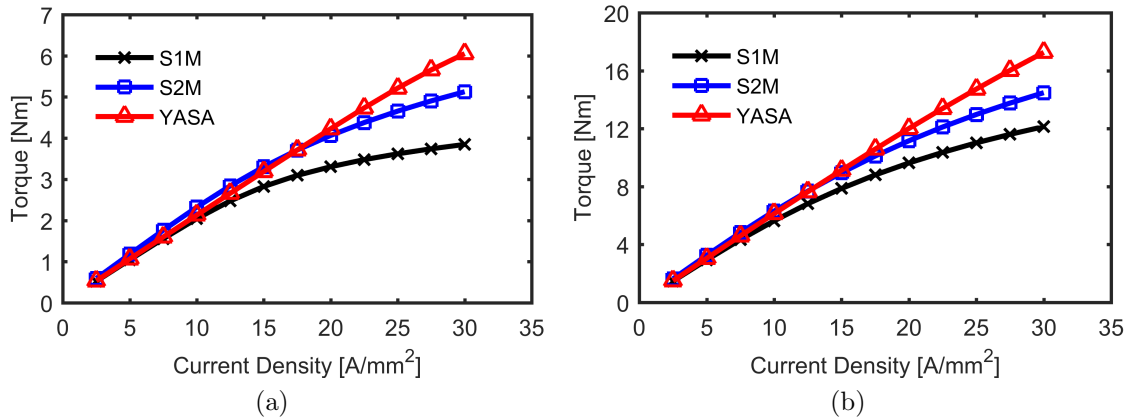


Figure 5.23: The torque production of YASA, S1M and S2M topologies (a) with ferrite magnets, and (b) with Neodymium magnets.

5.3.3 Overload Capability

The torque production and loss of the machines are evaluated at a range of magnetic and electric loadings using 3D FEAs. Figure 5.23 represent the torque at different currents with ferrite and rare earth magnets. The torque produced by S1M at higher currents declines very quickly because of saturation at very high loads. S2M remains slightly better than YASA for a wider range until YASA produces more torque, at very high loadings.

The torque-ampere turn characteristics of the single sided machine, start to bend at smaller currents as compared with the YASA. This indicates that the saturation of stator core of single sided machine happens at smaller currents. Therefore, the d-axis flux linkage declines more, shown in Fig. 5.20. The lower saturation of the YASA machine can be seen from the flux density distribution plots in Fig. 5.24.

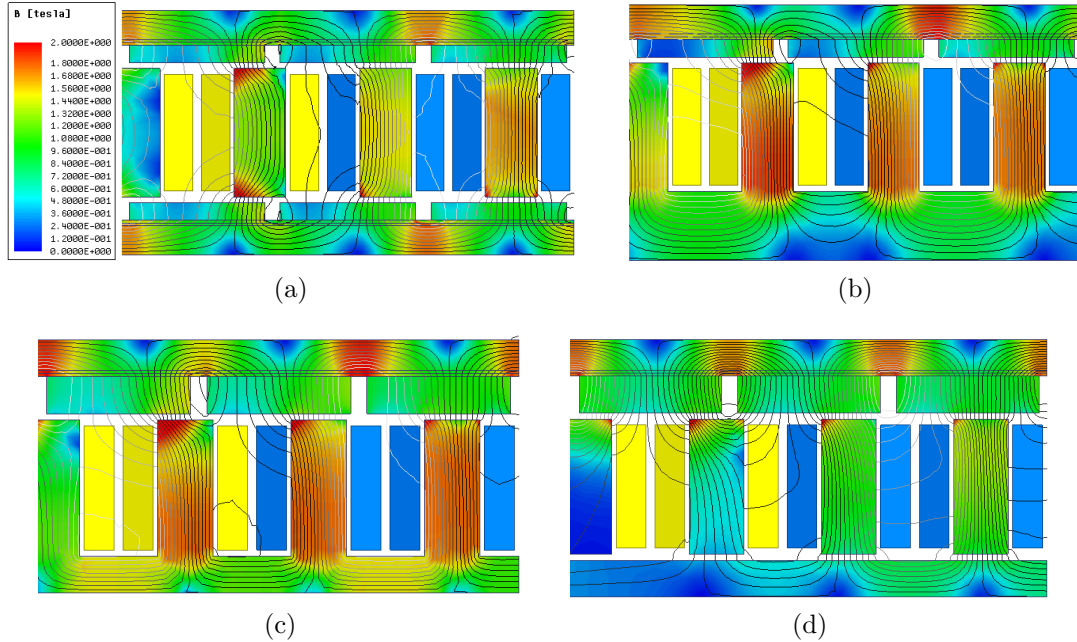
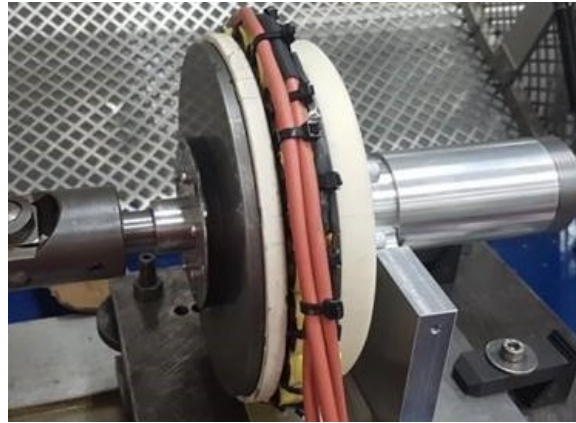


Figure 5.24: Flux density distribution at high magnetic and electric loading, current density of 25 A/mm^2 with Neodymium magnets. Figure (d) and (c) are similar except for an additional air-gap in the latter.

5.3.4 Design Topologies and Optimization Setup

The study reported here includes two AFPM machines, namely, a surface mounted (SPM) single sided 1–stator 1–rotor machine, shown in Fig. 5.18a, and a YASA machine configuration, represented in Fig. 5.18b. The motors are optimally designed for application in formula student design competition cars by the society of automotive engineers (SAE). Both machines have ratings of 70 Nm at 6500 rpm. The reference single sided AFPM machine has been manufactured and presented in Fig. 5.25. The test results as shown in Fig. 5.26 present a good agreement between the 3D FEA and measurements, which attests to the accuracy of calculations.

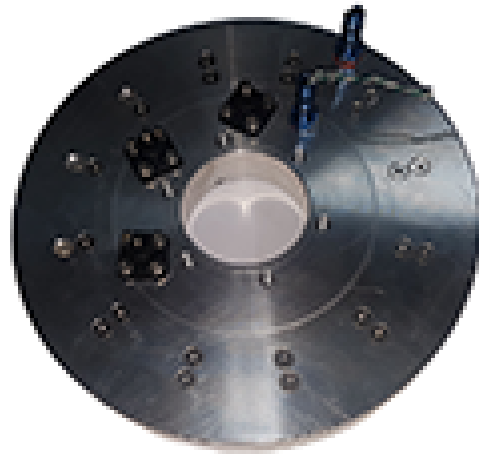
In the optimization study, the current density is varied from design to design such that all produce the rated torque. Both machines incorporate 24 slots and 20 poles,



(a)



(b)



(c)

Figure 5.25: The reference AFPM motor employed for the base design and experimental validation: (a) the test set-up, (b) the stator, (c) the oil cooling jacket.

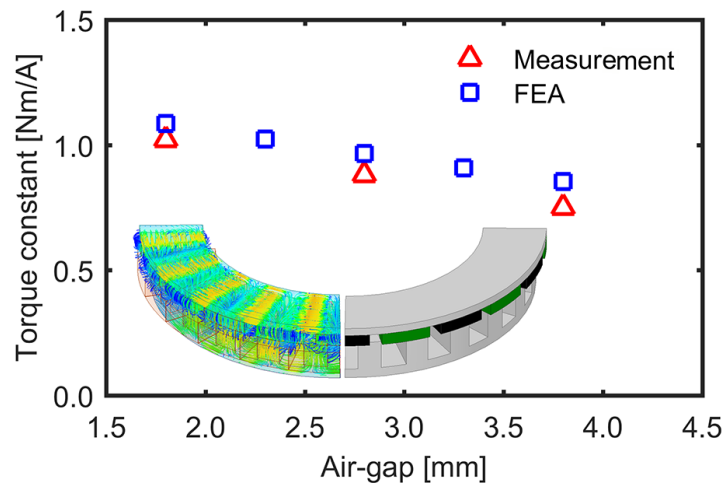


Figure 5.26: The experimental validation of the FEA simulations.

Table 5.6: Independent optimization variables and their corresponding limits.

Variable	Description	Min	Max
L_{ax}	Total axial length [mm]	25.0	40.0
k_{ry}	rotor yoke ratio = $\frac{L_{ry}}{L_{qx}}$	0.1	0.16
k_{sy}	stator yoke ratio = $\frac{L_{sy}}{L_{ax}}$	0.13	0.20
k_{pm}	magnet length ratio = $\frac{L_{pm}}{L_{ax}}$	0.18	0.24
k_{ds}	split ratio = $\frac{ID_s}{OD_s}$	0.58	0.86
k_{oh}	over hang ratio = $\frac{(OD_r - OD_s)}{(OD - OD_s)}$	-1.00	1.00
k_{sw}	slot width to slot pitch ratio = $\frac{w_s}{\tau_{s,id}}$	0.58	0.88
k_p	pole arc to pole pitch ratio = $\frac{\tau_{pa}}{\tau_{pp}}$	0.64	0.96

concentrated winding and surface mounted magnets. The use of open slots and the application of bobbin wound coils result into the same high fill factor for the single sided machine as the YASA.

The motors are optimized employing accurate 3D FEA models for design evaluations. The objectives are to minimize active material mass and the electromagnetic loss, including the stator core loss and the dc copper loss. The winding and PM eddy current losses are estimated for the selected optimum designs.

The optimization process takes 8 variables for the single sided topology and 7 for the YASA, which features one less due to the absence of the stator yoke. The independent optimization variables are listed in Table 5.6.

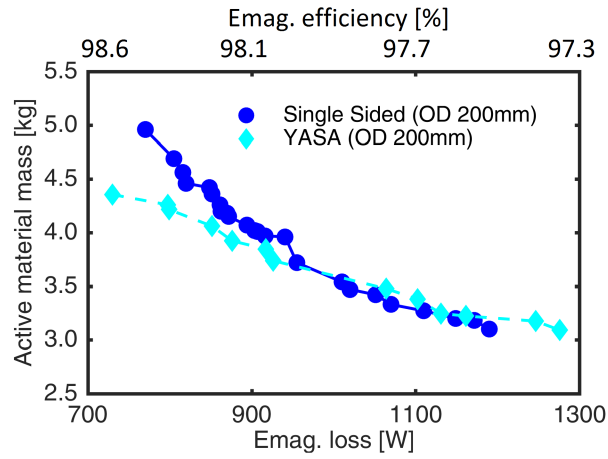
The diameter being the most influential design variable, the optimization is conducted for two constraint diameters. The outer diameter is fixed at 200 mm and 300 mm for two sets of studies. This incorporates the effect of the motor's physical dimensions on the best choice. The non-dominated or Pareto front optimum designs are obtained and plotted (Fig. 5.27). Elaborated comparative discussions in the following sections are based on the optimal designs on the Pareto front.

5.3.5 Pareto front designs

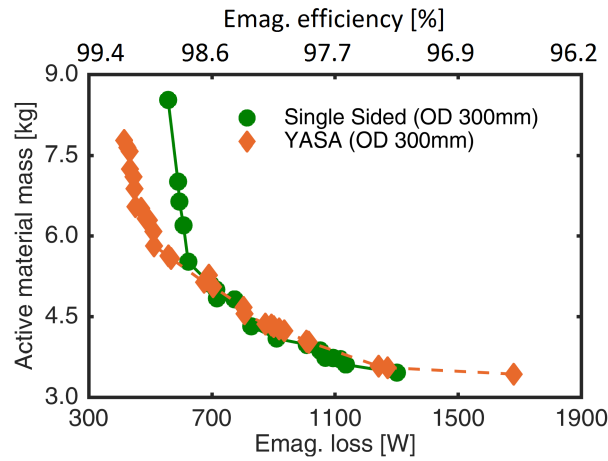
The optimum designs from Fig. 5.27 produce the same rated torque, therefore a design with higher active material mass has lower specific torque (Nm/kg). It can be observed that for the designs with electromagnetic efficiency greater than about 98%, the YASA topology has a higher specific torque compared to the single sided one. On the other hand, this high efficiency zone of the design space includes heavier machines. In applications where the mass is a vital concern, the right side of the plots in Fig. 5.27 would be more of interest. In this case, the single sided machine has slightly higher specific torque. Based on these results, it may be noted that generally claiming higher specific torque for the YASA topology does not hold true, as it is the case only for very low loss designs.

For both the envelope dimensions studied, i.e. OD of 200 mm and 300 mm, the comparative performance represents a similar trend: for a mass sensitive application, the single sided topology may be at an advantage. On the other hand, if very efficient designs are of interest, higher specific torque can be gained by employing the YASA topology. The machines designed at a larger diameter constraint, can achieve even larger efficiency, albeit at the cost of increased mass.

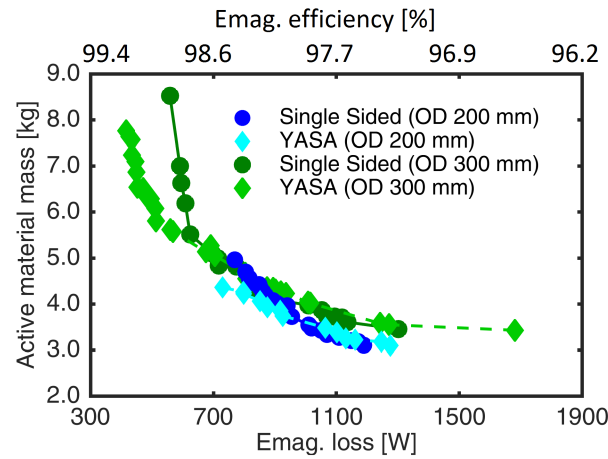
The detailed distribution of optimization variables for the designs on the Pareto front is provided in Fig. 5.28. Some of the observations specific to this study are that the optimally designed YASA compared to single sided machines tend toward larger split ratios and slot widths. This may be explained by considering that the YASA topology has a lower stator core loss, due to the absence of the yoke, and hence



(a)

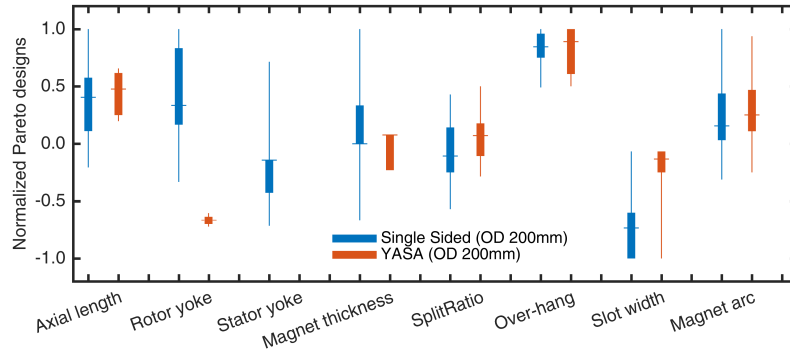


(b)

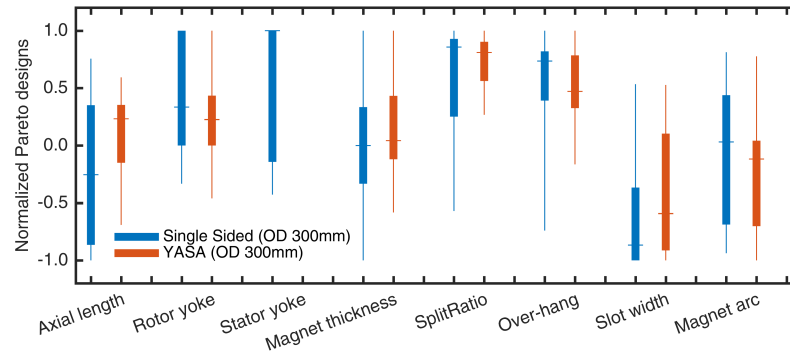


(c)

Figure 5.27: The Pareto fronts for the topologies optimally designed for different envelopes: (a) outer diameter of 200 mm, (b) outer diameter of 300 mm, and (c) both diameters.



(a)



(b)

Figure 5.28: The distribution of variables for optimum designs with total outer diameter of (a) 200 mm, (b) 300 mm.

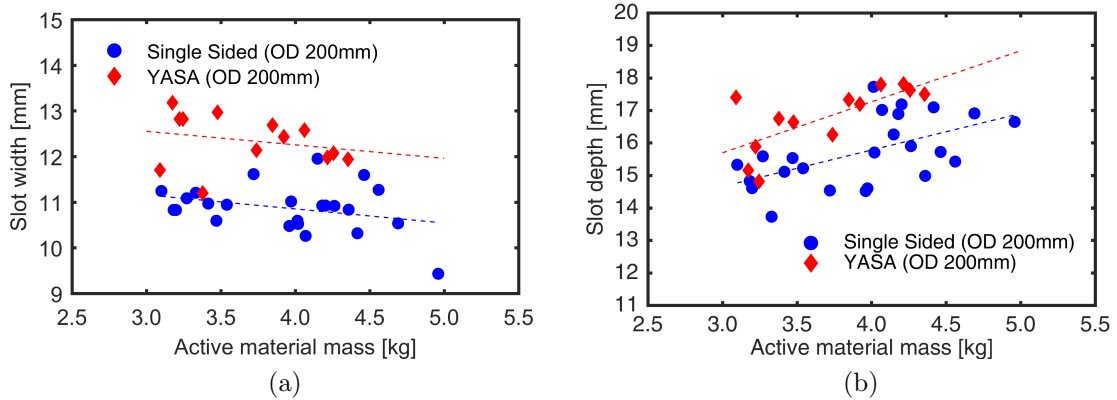


Figure 5.29: The slot width and depth variation of Pareto front designs of (a) the single sided and (b) the YASA machine.

higher flux density in the stator may be permissible, and thus, the machine can afford thinner teeth and therefore larger slot widths and split ratios.

In order to derive more general design guidelines and establish the limitations

of the two topologies, the geometrical variables of the obtained Pareto designs are carefully investigated. For instance, the slot width and depth of the YASA machines were found to be larger than for the single sided ones, as shown in Fig. 5.29. A larger slot depth in the case of the single sided machine may not be beneficial as this also increases the leakage, more significantly than in the YASA machine. Considering the slope of the trend lines in Fig. 5.29, it can be inferred that lower loss and higher mass designs on the Pareto front generally have deeper slots and reduced slot width.

The performance of the evaluated designs in the optimization are later investigated in three most frequent operating points. These points include the rated condition (70 Nm at 6500 rpm) which the optimization was performed at, as well as 14 Nm and 35 Nm. Then each objective function for each design is calculated based on a weighted sum of that objective value in the three operating points. The weights are assigned according to an estimated operation duration. It was observed that the selected designs remain very close to the Pareto front.

5.3.6 Mass components breakdown

The breakdown of mass components for designs on the Pareto front is shown in Fig. 5.30. The copper mass required for optimum designs of the YASA machine is larger than for the single sided machine throughout the whole Pareto front. The magnet mass required for the optimum YASA design is also larger, except in designs with low total losses. The stator core mass of the YASA is smaller due to the elimination of the yoke, on the other hand it has higher rotor mass due to including two rotors.

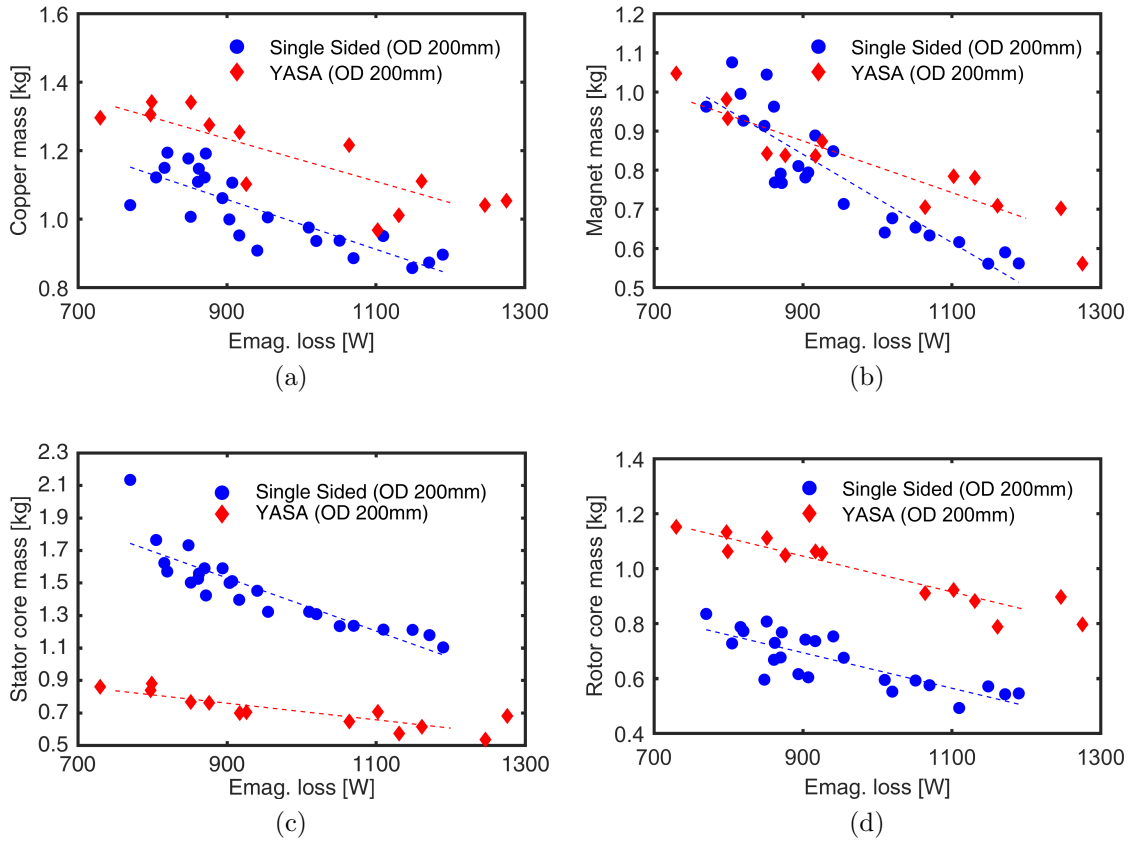


Figure 5.30: The breakdown of mass components for the Pareto front designs of the topologies studied for an outer diameter of 200 mm. Similar trends were observed for the machines designed for the larger envelope with an outer diameter of 300mm.

5.3.7 Loss components breakdown

The breakdown of loss components for designs on the Pareto front is presented in Fig. 5.31. It is observed that the copper loss is dominant in the case of both topologies with the ratings and envelope size under study. The copper loss of the optimally designed YASA machines is higher than that of the single sided ones, except for the very heavy and high efficiency designs. The stator core loss of the single sided topology is larger than the YASA for all the designs on the Pareto front.

Two machines with similar mass and efficiency are selected in order to compare

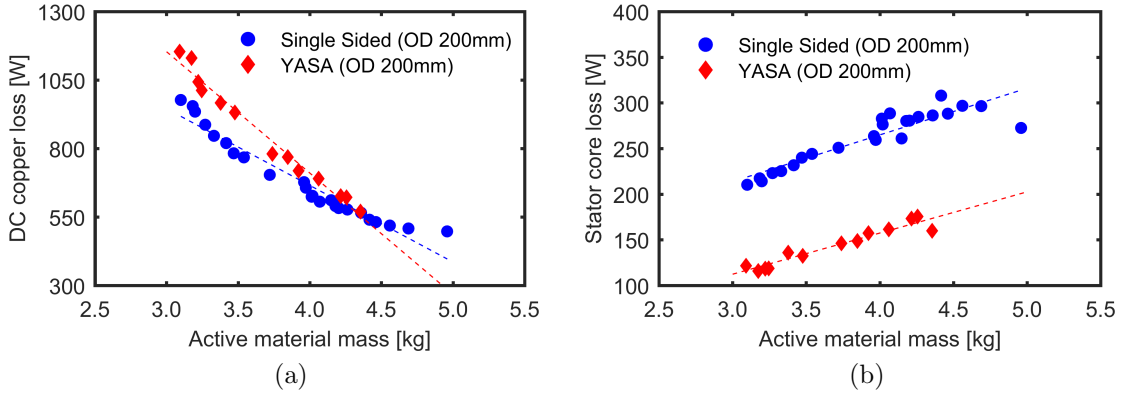


Figure 5.31: The breakdown of loss components for Pareto front designs of the topologies studied for an outer diameter of 200 mm. Similar trends were observed for the machines designed for the larger envelope with an outer diameter of 300mm.

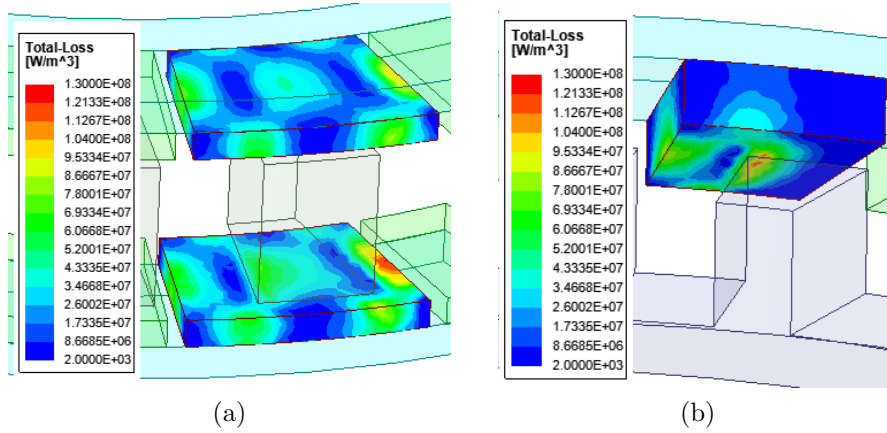


Figure 5.32: Distribution of eddy current losses in the magnets of (a) the selected YASA optimal design and (b) the selected single-sided AFPM machine optimal design.

their PM and winding eddy current losses, and also obtain their efficiency map. Eddy current losses are not considered in the optimization in order to accelerate the 3D design evaluation process. These losses are assessed for the two selected optimal designs as follows.

The topology under study employs sintered Neodymium magnets. Magnet eddy current loss calculation with 3D time-transient FEA for the selected optimally designed YASA and single-sided machines are shown in Fig. 5.32. Should only one

magnet per pole be used in the rotor, the eddy-current losses would be extremely high at 1kW for the selected single sided topology and about twice that for the selected YASA topology. In the practical design each pole is segmented in 8 magnet pieces, resulting in a drastic reduction of losses. Including the magnet loss results in 95.6% and 93.9% electromagnetic efficiency for the single sided and YASA machines, respectively.

The reasons for larger PM loss for the YASA machine topology include, thinner magnets that reduce the permeance coefficient and also doubled magnet surface area facing the air-gap that is more exposed to the flux density harmonics. These show that for this design problem, magnet segmentation or other magnet loss reduction methods need to be taken into account, particularly for the YASA machine.

The winding eddy current losses for the two selected optimum designs at rated operating conditions are calculated using 2D FEA. The calculations are conducted for scenarios with different numbers of turns, all with AWG 12, and shown in Fig. 5.33. The current density is readjusted for the rated torque. Example FEA results for the selected YASA machine is presented in Fig. 5.34 and 5.35 which include the flux lines and the distribution of total winding losses.

The winding eddy current losses for the two machines are very close to each other except for the case with highest number of turns where the magnet passing eddy current losses are significant. This is mainly due to the larger slot depth for the YASA machine specified by the optimization algorithm. With identical conductors and number of turns, for the YASA machine with larger slot depth the conductors are located further away from the magnets, reducing flux density variation in conductors

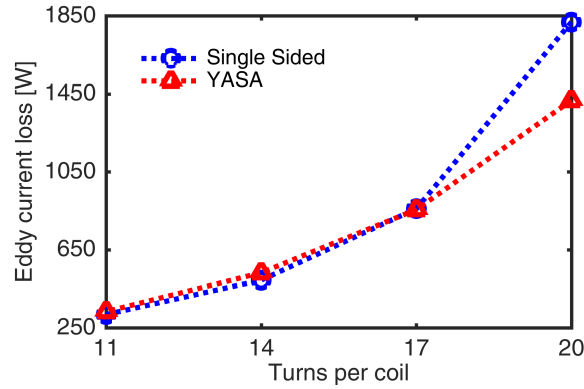


Figure 5.33: The additional winding losses due to eddy currents at rated load for the selected single sided and YASA optimum designs.

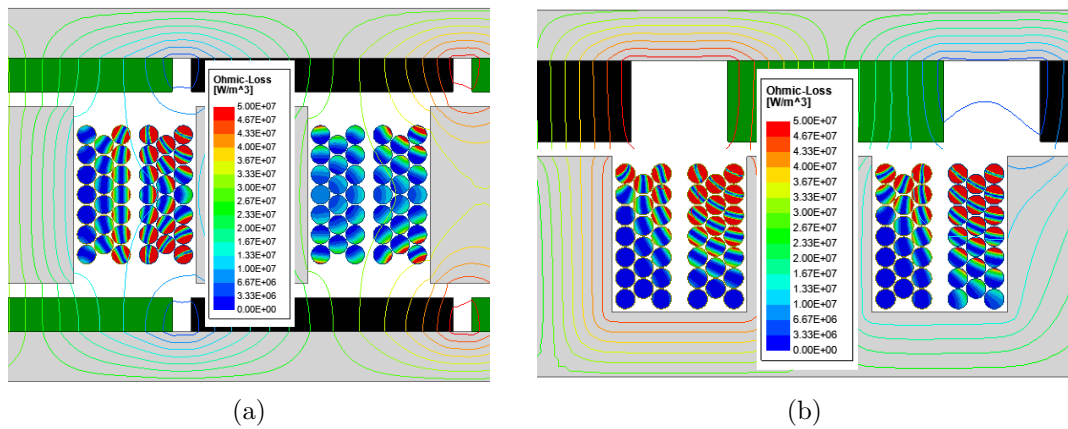


Figure 5.34: Distribution of eddy current losses in the winding with 20 turns per coil of (a) the selected YASA optimal design and (b) the selected single sided AFPM machine optimal design.

and hence mitigating the losses. It is expected that with identical slot depth, the YASA machine has larger winding eddy current losses as it features two air-gaps.

5.3.8 Efficiency Maps

The efficiency maps for the selected optimum designs are calculated with 3D FEA and shown in Fig. 5.36. High efficiency performance is consistent at wider speed range as well. In order to simplify the comparison of the two efficiency maps a third plot is obtained by subtracting them, presented in Fig. 5.36c. The positive values

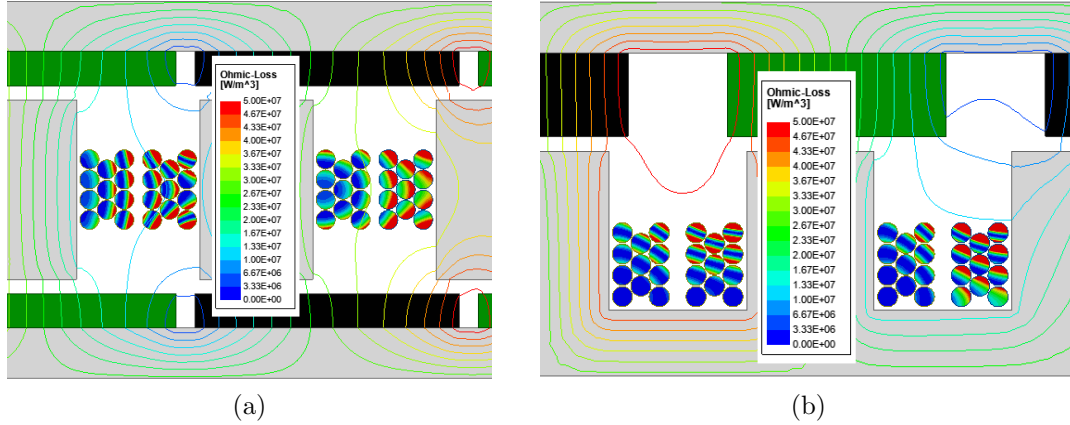


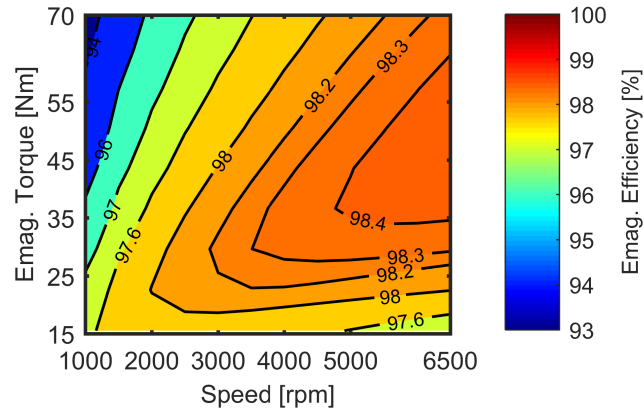
Figure 5.35: Distribution of eddy current losses in the winding with 11 turns per coil of (a) the selected YASA optimal design and (b) the selected single sided AFPM machine optimal design.

of this plot indicates higher efficiency of the single sided machine while the negative values show a higher efficiency for the YASA topology.

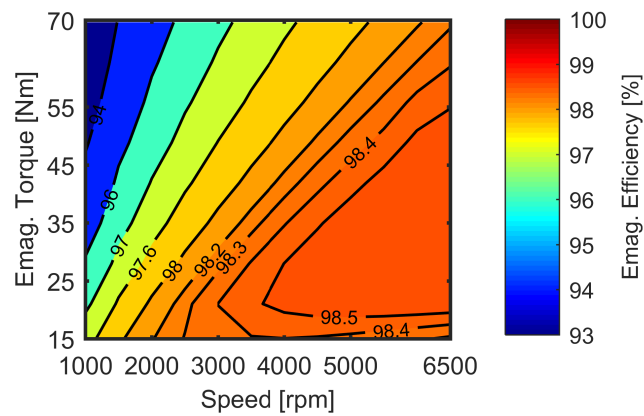
It can be seen that for the two selected designs, assuming identical cooling methods, the single-stator single-rotor machine performs favorably at higher torque and lower speed operating points where the copper loss is more significant. Therefore, it may perform better for driving cycles with more torque requirement while the YASA machine is better for traction motors with higher speed and lower torque requirements.

5.4 Summary

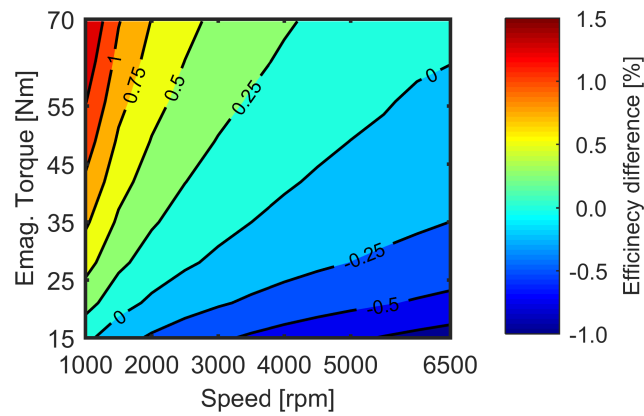
Two example case studies of employing the two-level surrogate assisted optimization algorithm employing 3D FEA for the systematic and accurate design and comparative investigation of AFPM machines are presented. The following is summary and conclusion of each case.



(a)



(b)



(c)

Figure 5.36: The electromagnetic efficiency maps calculated by 3D FEA for the two representative designs with similar mass and loss: (a) single sided design, (b) the YASA design, and (c) the difference between efficiency maps of the two designs (the efficiency of the YASA machine subtracted from the single sided).

Outcomes of the Systematic Study of the Effects of Pole Count on Optimally Designed AFPM Machines:

The absolute performance limits that can be achieved by fractional horse power AFPM machines with surface magnets within a given envelope are explored. This necessitates the study of a large number of designs spanning a wide design space, and having different slot-pole combinations, and the problem is further complicated due to the three-dimensional nature of the machine geometry. In this regard, the new two-level surrogate assisted multi-objective optimization algorithm is utilized. In addition, a systematic method for selecting the optimum designs for multi-objective optimization problems is proposed.

Approximately horizontal and vertical lines obtained on the extremes of the Pareto front indicate that within the geometrical limitations further improvement in efficiency and cost is not probable. The results confirmed that the designs with the best trade-off between the two objectives of loss and mass split the core and copper losses nearly equally.

The combined Pareto front with pole counts ranging from 10 to 40 illustrates that the highest efficiency is obtained for designs employing 20 poles. An ultra high efficiency axial flux SPM design with 20 poles rated for 0.75 hp is prototyped, demonstrating a measured efficiency of 94.3%.

Furthermore, the effect of the pole count on the optimum design variables is examined to find a relative trend. For instance, it is observed that thinner PMs with a larger pole arc to pole pitch ratio are generally more beneficial for lower pole counts.

Within the studied frame size and ratings, a bigger air-gap, a thinner yoke, and a larger slot width result in more efficient, albeit more expensive, designs. Learning such trends can serve as a basis for developing generalized design rules and as a reference for the preliminary stages of the optimum design process, ultimately making the optimization results more accurate as well as computationally affordable.

Outcomes of the Systematic Optimization and Comparison of Single-sided and Double-sided AFPM Machines:

This section systematically compared two axial flux permanent magnet (AFPM) machines designed for a university student racing car application: a double-rotor single-stator yokeless and segmented armature (YASA) structure, and a single-stator single-rotor configuration. Both machines were optimized for minimum loss and active weight using 3D finite element analysis and the highest performing candidate designs are compared in more detail. The studies indicate that the benefits offered by the YASA configuration over the single-stator single-rotor machine are achieved only for specific designs that are heavier. For the design space with lower mass, albeit with increased losses, the Pareto front designs overlap which shows the performance of the two machines is very close to each other.

For identical heat transfer capabilities, reflected in the same temperature rises for the stators and rotors, respectively, the very high efficiency YASA designs are lighter than their single sided counterparts of comparable torque and loss performance. On the other hand, single sided machines may be preferable for applications in which lower mass is of the essence, at the inevitable expense of increased electromagnetic

losses.

Within the entire design space considered, the optimally designed YASA machines require heavier copper windings and rotor cores, and lower stator core mass, as compared with the single-stator single-rotor machines. The YASA machines also require increasingly more magnet mass within the design space region with higher loss and lower mass. Lower core loss and higher copper loss are noted for the YASA optimal designs over the entire design space. The winding eddy current losses are comparable for the two machine configurations, while the YASA machines have higher magnet eddy current losses.

The preferred axial flux PM motor topology may depend on the torque and speed driving cycle requirements. The efficiency maps of two representative designs with comparable loss and mass show that, at the operating points with higher torque and lower speed, the single sided machine exhibits a higher efficiency, while for higher speed and lower torque, the YASA design is more efficient.

Chapter 6

Conclusions

In this chapter, the conclusions and contributions resulted from this dissertation are summarized. Future research is recommended in order to facilitate further progress on the same topics as the ones included in this work.

6.1 Summary and Conclusions

In chapter 2, a new hybrid analytical-FEA method for calculating ac eddy current losses in electrical machine windings has been proposed. It is shown that the previously existing analytical and hybrid methods significantly overestimate these losses while the numerical methods are either also overestimating (detailed 2D FEA) or unpractical due to the lengthy calculations time (detailed 3D FEA). The proposed approach brings a major improvement upon more conventional FEA based hybrid methods by considering the variation of the flux density in a 3D dimension, using only a general 3D FEA where the windings are modeled as a crude one-turn coil. This achieves a trade-off between speed and precision, making it suitable for different stages of the design process of an electrical machine. The developed analytical

equation has minimum simplifying assumptions and is taking other complicating aspects of winding eddy current loss calculation into account, such as the potential variations in the eddy current path and the eddy current at the end turns. Should the time consuming detailed 3D FEA with meticulous wire-by-wire model be used, recommendations for effective reduction in the mesh size, and consequently computational time, is proposed. In the same chapter, an approach for the measurement of ac winding loss is proposed and conducted for an open slot AFPM machine. The measurements are in close agreement with the results from 3D FEA. Other matters discussed include the selection of the number of turns and the comparison of circular and square conductors.

Chapter 3 appropriates DOE and RSM principles in two different machine design related perspectives. The first one is a more typical method to achieve optimum design with evaluating only a certain and minimum number of specified designs. The second study is innovatively using outcomes of RSM studies and extensive sensitivity analysis to trace down manufacturing tolerances and out of specification properties of fabricated machines.

In the first study of chapter 3, a coreless and a conventional AFPM machine are comparatively and optimally designed for the same application in a solar car. It is observed that for the space constraints under study and for a given cooling system, the torque generation by both machine types is limited, and this torque limit for conventional machine is at a higher value. Therefore, the coreless machines may be more suitable for use in a two-wheel drive version, at the cost of slightly reduced efficiency, and larger overall mass as compared with single wheel drives.

Conventional AFPM topology could be used more efficiently with one driving wheel. Weight advantages obtained by the coreless design may assist in mass distribution, which is particularly important for in-wheel application.

The second study in chapter 3 is devoted to a new systematic method aimed at quantifying the effect of tolerances on PM synchronous machine performance and identifying possible non-compliant dimensional variables and material characteristics. The method is greatly using DOE, RSM, and sensitivity analysis. While the method itself is generally applicable in scope, it is also shown that, as the electromagnetic loading greatly affects the sensitivity of the test outputs to tolerances, the careful consideration of the individual machine topology is required as part of the studies, limiting the simple generalization of quantitative conclusions.

One of the main contributions of this dissertation is included in chapter 4, which proposes a two-level surrogate-assisted DE based optimization for use with 3D FEA. This method employs kriging surrogate models in combination with FEA, reducing the number of overall finite element design evaluations. Two example machine design problems are shown, one conventional and the other coreless AFPM machines. The example machines are optimally designed with conventional DE and proposed algorithm. The results are very similar Pareto fronts, which attest to the effectiveness of the proposed approach. It is also observed that the algorithm outperforms conventional methods as it is computationally less expensive and requires substantially fewer design evaluations. The constructed kriging model can also be used for post processing purposes. This is an additional benefit of the surrogate-assisted algorithm

which is not present in conventional approaches. This chapter also dives into proposing and comparing methods of defining the search space. One of these new methods progressively narrows down the variable limits, enhancing the exploitation. The other approach relies on novel applications of the DOE methodology and biases the search space definition based on a reference design and sensitivity analysis. This is especially useful when it is known beforehand which of the objectives is more important. Ultimately resulting in a smaller design space, reducing the number of evaluations, thereby greatly improving the speed of the optimization.

After proposing the two-level surrogate-assisted optimization method in the previous chapter, extensive and elaborated electric machine design optimization problems are included in chapter 5 to showcase the full advantages of the new method.

The absolute performance limits that can be achieved by fractional horse power AFPM machines with surface magnets within a given envelope are explored. This necessitates the study of a large number of designs spanning over a wide search space, and having different slot-pole combinations. The problem is further complicated due to the three-dimensional nature of the AFPM machine geometry. Approximately horizontal and vertical lines obtained on the extremes of the Pareto front indicate that within the geometrical limitations further improvement in efficiency and cost is not probable. The results confirmed that the designs with the best trade-off between the two objectives of loss and mass split the core and copper losses nearly equally. The combined Pareto front with pole counts ranging from 10 to 40 illustrates that the highest efficiency is obtained for designs employing 20 poles. An ultra high efficiency axial flux SPM design with 20 poles rated for 0.75 hp is prototyped, demonstrating

a measured ultra-high efficiency of 94.3%. It is observed that thinner PMs with a larger pole arc to pole pitch ratio are generally more beneficial for lower pole counts. Within the studied frame size and ratings, a bigger air-gap, a thinner yoke, and a larger slot width result in more efficient, albeit more expensive, designs. Learning such trends can serve as a basis for developing generalized design rules and as a reference for the preliminary stages of the optimum design process. In addition, a systematic method for selecting the optimum designs of a multi-objective optimization problem is proposed. With respect to this, a factor is introduced that quantifies the trade-off between counteracting objectives, ultimately making the post-processing of a multi-objective optimization problem more systematic.

Another benchmark study compares two optimally designed axial flux permanent magnet (AFPM) machines: a YASA and a single sided configuration. The difference in properties of these two machines is highly three-dimensional. For instance, increased stator teeth flux density in inner diameter is more tolerable for the YASA machine as it has generally lower core losses. Therefore, a fair comparison not only needs to be conducted for optimal designs, but also the optimization needs to employ 3D models. This is achieved through the proposed algorithm. The comparison indicates that the benefits offered by the YASA configuration over the single-sided machine are achieved only for specific designs that are heavier. For the design space with lower mass, albeit with increased losses, the Pareto front designs overlap which shows the performance of the two machines is very close to each other. Within the entire design space considered, the optimally designed YASA machines require heavier copper windings and rotor cores, and lower stator core mass, as compared with

the single-sided AFPM machines. The YASA machines also require increasingly more magnet mass within the design space region with higher loss and lower mass. Lower core loss and higher copper loss are noted for the YASA optimal designs over the entire design space. Efficiency maps comparison attests that at the operating points with higher torque and lower speed, the single sided machine exhibits a higher efficiency, while for higher speed and lower torque, the YASA design is more efficient.

6.2 Original Contributions

The main contributions of this dissertation can best be summarized as follows:

1. A comparison between various existing methods for estimating winding eddy current losses is conducted. It is shown that faster approximate methods overestimate the losses. Several recommendations for reducing the computational effort of the most accurate and the most expensive eddy current loss evaluation approach, i.e. 3D FEA with a detailed wire-by-wire model, are proposed. The study includes two case study machines known for their high winding ac losses: a PM machine with open slots and a coreless design. (chapter 2)
2. A hybrid analytical/numerical method for estimation of winding eddy current losses taking 3D effects into account is proposed. The target outcome is to obtain a method applicable in the optimization process which has a balance between accuracy and computational time. Such a method is developed and presented with multiple example studies. (chapter 2)

3. Utilization of DOE and RSM methodologies for systematic electric machine design purposes is elaborated. Then, the information provided by DOE, RSM, and sensitivity analysis is innovatory used to narrow down the out of specification causes and manufacturing tolerances. (chapter 3)
4. Developments on AFPM coreless machine design for traction application are presented. These studies include comparison of pros and cons of using a coreless AFPM design versus a conventional AFPM machine for in-wheel traction application, recommendations for the best practices of employing a coreless machine, a proposed method to overcome the challenges of a small inductance and limited constant power speed range, and a proposed method for accurate winding factor calculation of coreless machines. (chapter 3)
5. A Two-level surrogate assisted optimization algorithm is introduced that requires one order of magnitude less number of design evaluations through FEA. This enables application of time consuming 3D FEA models in optimization algorithm and hence established a well-grounded design method for machine topologies that otherwise were not confidently designed at their highest potential performance. (chapter 4)
6. Three methods for assigning the limits of the optimization variables are proposed and investigated. These include: assigning the broadest possible ranges, starting with very wide ranges and later iteratively redefine and narrow them down as the optimization progresses, and assigning the range biased by a reference design and sensitivity analysis. The *Broad* search space results into

more options on the Pareto front while the *Biased* search space results in faster optimization. (chapter 4)

7. Systematically exploring the limits of efficiency and cost of a fractional hp AFPM machine by exploring a very large search space. Asymptotic horizontal and vertical lines obtained on two ends of the Pareto front represent that further improvement within the constraints of the design problem is not possible. The best compromise design achieves at a pole count with the best balance between loss components. In the same study, the best practices of assigning design variables for machines with different number of poles is introduced. Through the application of the proposed design method, an ultra-high efficiency fractional hp AFPM machine is prototyped and tested. (chapter 5)
8. The guidelines for selecting the best single-stator AFPM machine topology with one or two rotor discs is established. The study is comprehensive and systematic and includes only the optimized machines. The design spaces where single rotor AFPM or double rotor YASA machine outperforms the other are identified. In the same study, an approach for selecting a design among the Pareto front designs is proposed by introducing a factor to quantify the improvement and deterioration of objectives relative to each other. With this method the designer can specify how much deterioration in one objective can be afforded in return for improvement in the other. If all optimization objectives are equally desired, the knee point of the Pareto front can be mathematically calculated. (chapter 5)

6.3 Recommendations for Future Work

Based on the results of this dissertation and earlier research conducted by others, possible further research may include the following:

1. The outcomes of a systematic optimization process, such as the ones included in chapter 5, are not limited to the optimized design. Additionally, it provides information that can be utilized as guidelines for best practices in designing the machine. Such insights can help with a very good initial design and further increase the speed of optimization. As a next step of this work, similar guidelines can be obtained for less mature machine topologies, for example vernier type or MAGNUS, claw pole, switched reluctance, transverse flux, spherical, PCB stators, and PM machines combining radial and axial air-gap structure, etc. Most of these machine structures are high 3D and hence can benefit from the proposed optimization algorithm.
2. Electric machines working based on flux modulation principles, referred to as MAGNUS or vernier type, have been studied relatively more in their radial form than axial. A systematic comparison of the Pareto front designs for radial and axial MAGNUS machines with different envelope dimensions can be performed to highlight their strengths and weaknesses against each other. Such comparisons for usual radial and axial flux PM machines conducted in the past, have successfully enlightened the path ahead and therefore can prove beneficial for the MAGNUS type counterpart.

3. Coreless AFPM machines with printed circuit board (PCB) stators are promising alternatives with very compact and light structure. These machines have very thin conductor cross sections that increases the mesh size. With the use of the proposed optimization algorithm, coreless AFPM machines can be designed optimally and to their highest potential.
4. The machines with PCB stators can have high winding ac losses if not designed properly or the loss estimation method is not accurate. Through the winding loss calculation method proposed in this dissertation, such loss components can be studied to improve upon the performance of PCB stators. Another step, in the same line, can be to optimally design the copper trace of PCB for minimum loss or incorporate flexible PCBs and try innovative uncommon layouts.
5. The proposed machine design optimization algorithm may be even more improved upon via several techniques:
 - The initial sample pool construction is already randomized to enable application for design problems with many variables. However, this can be done with systematic approaches such as design of experiments (DOE), which is also discussed. It is predicted that DOE would require a large sample pool size when the design problem has many variables. The practicality of using DOE for the best number of variables can be tested.
 - As the proposed method facilitates study of large design problems, multiphysics optimization can be performed which includes simultaneous electromagnetic, thermal, and mechanical performance estimation.

- The algorithm can become more hybrid by calculating some components of fitness functions using analytical methods, some with 2D FEA, some with 3D FEA, and the rest with kriging surrogate model. The suitable approach can be decided based on the level of non-linearity of the component.
- An accurate surrogate model can replace any further FEA calculation, either for optimization or other purposes. Different surrogate models and the ways they improve their estimation can lead into an approach that replaces and eliminates the need for FEA calculations.
- Some other potential studies and extensions of the optimization algorithm include examination of a constrained optimization problem as opposed to an unconstrained one where the same constraints are defined as fitness functions to be minimized or maximized, also adding noise to variables to identify the robust designs and penalize the rest.

References

- [1] M. Rosu, P. Zhou, D. Lin, D. M. Ionel, M. Popescu, F. Blaabjerg, V. Rallabandi, and D. Staton, *IEEE Press Series on Power Engineering*. IEEE, 2018. [Online]. Available: <https://ieeexplore-ieee-org.ezproxy.uky.edu/document/8233737>
- [2] G. Heins, D. M. Ionel, D. Patterson, S. Stretz, and M. Thiele, “Combined experimental and numerical method for loss separation in permanent-magnet brushless machines,” *IEEE Transactions on Industry Applications*, vol. 52, no. 2, pp. 1405–1412, March 2016.
- [3] J. F. Gieras, R.-J. Wang, and M. J. Kamper, *Axial Flux Permanent Magnet Brushless Machines*. Springer, 2005.
- [4] N. Tesla, “Electro-magnetic motor,” UNITED STATES PATENT OFFICE. 405 858.
- [5] M. Aydin, S. Huang, and T. A. Lipo, “Axial flux permanent magnet disc machines: A review,” in *Research Report, Wisconsin Electric Machines and Power Electronics Consortium*, 2004.
- [6] C. C. Chan, “Axial-field electrical machines design and applications,” *IEEE Transactions on Energy Conversion*, vol. EC-2, no. 2, pp. 294–300, June 1987.
- [7] T. J. Woolmer and M. D. McCulloch, “Analysis of the yokeless and segmented armature machine,” in *2007 IEEE International Electric Machines Drives Conference*, vol. 1, May 2007, pp. 704–708.

- [8] M. Aydin, Surong Huang, and T. A. Lipo, "Design and 3d electromagnetic field analysis of non-slotted and slotted torus type axial flux surface mounted permanent magnet disc machines," in *IEMDC 2001. IEEE International Electric Machines and Drives Conference (Cat. No.01EX485)*, June 2001, pp. 645–651.
- [9] A. Parviainen, M. Niemela, and J. Pyrhonen, "Modeling of axial flux permanent-magnet machines," *IEEE Transactions on Industry Applications*, vol. 40, no. 5, pp. 1333–1340, Sep. 2004.
- [10] M. Aydin, S. Huang, and T. A. Lipo, "Design, analysis, and control of a hybrid field-controlled axial-flux permanent-magnet motor," *IEEE Transactions on Industrial Electronics*, vol. 57, no. 1, pp. 78–87, Jan 2010.
- [11] M. Aydin and M. Gulec, "A new coreless axial flux interior permanent magnet synchronous motor with sinusoidal rotor segments," *IEEE Transactions on Magnetics*, vol. 52, no. 7, pp. 1–4, July 2016.
- [12] B. Tekgun, T. Husain, S. Das, Y. Sozer, and M. Hamdan, "Design of a novel interior permanent magnet axial flux machine," in *2017 IEEE Energy Conversion Congress and Exposition (ECCE)*, Oct 2017, pp. 314–320.
- [13] P. Campbell, "Principles of a permanent-magnet axial-field d.c. machine," *Proceedings of the Institution of Electrical Engineers*, vol. 121, no. 12, pp. 1489–1494, December 1974.
- [14] E. Spooner and B. J. Chalmers, "'torus': a slotless, toroidal-stator, permanent-magnet generator," *IEE Proceedings B - Electric Power Applications*, vol. 139, no. 6, pp. 497–506, Nov 1992.
- [15] Ronghai Qu, M. Aydin, and T. A. Lipo, "Performance comparison of dual-rotor radial-flux and axial-flux permanent-magnet bldc machines," in *IEEE International Electric Machines and Drives Conference, 2003. IEMDC'03.*, vol. 3, June 2003, pp. 1948–1954 vol.3.

- [16] D. J. Patterson, G. Heins, M. Turner, B. J. Kennedy, M. D. Smith, and R. Rojoza, “An overview of the compactness of a range of axial flux pm machines,” in *2015 IEEE International Electric Machines Drives Conference (IEMDC)*, May 2015, pp. 96–101.
- [17] F. Caricchi, F. Crescimbin, F. Mezzetti, and E. Santini, “Multistage axial-flux pm machine for wheel direct drive,” *IEEE Transactions on Industry Applications*, vol. 32, no. 4, pp. 882–888, July 1996.
- [18] R. J. Hill-Cottingham, P. C. Coles, J. F. Eastham, F. Profumo, A. Tenconi, and G. Gianolio, “Multi-disc axial flux stratospheric aircraft propeller drive,” in *Conference Record of the 2001 IEEE Industry Applications Conference. 36th IAS Annual Meeting (Cat. No.01CH37248)*, vol. 3, Sept 2001, pp. 1634–1639 vol.3.
- [19] M. Aydin, M. Gulec, Y. Demir, B. Akyuz, and E. Yolacan, “Design and validation of a 24-pole coreless axial flux permanent magnet motor for a solar powered vehicle,” in *2016 XXII International Conference on Electrical Machines (ICEM)*, Sept 2016, pp. 1493–1498.
- [20] D. Hanselman, *Brushless Permanent Magnet Motor Design*. Magna Physics Publishing, 2006. [Online]. Available: <https://books.google.com/books?id=rilVPgAACAAJ>
- [21] T. Nakata, N. Takahashi, and K. Uehara, “Analysis of magnetic characteristics of a brushless dc motor taking into account the distribution of magnetization,” *IEEE Transactions on Magnetics*, vol. 22, no. 5, pp. 1084–1086, Sep. 1986.
- [22] T. F. Chan, Lie-Tong Yan, and Shao-Yuan Fang, “In-wheel permanent-magnet brushless dc motor drive for an electric bicycle,” in *IEEE International Electric Machines and Drives Conference. IEMDC’99. Proceedings (Cat. No.99EX272)*, May 1999, pp. 407–409.
- [23] J. M. Seo, S. H. Rhyu, I. S. Jung, and H. K. Jung, “A design of multi flux permanent-magnet machine for electric bicycles,” in *2015 9th International*

Conference on Power Electronics and ECCE Asia (ICPE-ECCE Asia), June 2015, pp. 1457–1461.

- [24] D. Lim, Y. Cho, J. Ro, S. Jung, and H. Jung, “Optimal design of an axial flux permanent magnet synchronous motor for the electric bicycle,” *IEEE Transactions on Magnetics*, vol. 52, no. 3, pp. 1–4, March 2016.
- [25] P. J. Masson, M. Breschi, P. Tixador, and C. A. Luongo, “Design of hts axial flux motor for aircraft propulsion,” *IEEE Transactions on Applied Superconductivity*, vol. 17, no. 2, pp. 1533–1536, June 2007.
- [26] D. Moreels and P. Leijnen, “Turning the electric motor inside out: A belgian startup’s axial-flux motor for evs is small, light, and powerful,” *IEEE Spectrum*, vol. 56, no. 10, pp. 40–45, Oct 2019.
- [27] F. Profumo, Zheng Zhang, and A. Tenconi, “Axial flux machines drives: a new viable solution for electric cars,” *IEEE Transactions on Industrial Electronics*, vol. 44, no. 1, pp. 39–45, Feb 1997.
- [28] K. M. Rahman, N. R. Patel, T. G. Ward, J. M. Nagashima, F. Caricchi, and F. Crescimbeni, “Application of direct-drive wheel motor for fuel cell electric and hybrid electric vehicle propulsion system,” *IEEE Transactions on Industry Applications*, vol. 42, no. 5, pp. 1185–1192, Sep. 2006.
- [29] E. Muljadi, C. P. Butterfield, and Yih-Huie Wan, “Axial-flux modular permanent-magnet generator with a toroidal winding for wind-turbine applications,” *IEEE Transactions on Industry Applications*, vol. 35, no. 4, pp. 831–836, July 1999.
- [30] T. F. Chan and L. L. Lai, “An axial-flux permanent-magnet synchronous generator for a direct-coupled wind-turbine system,” *IEEE Transactions on Energy Conversion*, vol. 22, no. 1, pp. 86–94, March 2007.
- [31] K. Schmidt and D. J. Patterson, “Performance results for a high efficiency tropical ceiling fan and comparisons with conventional fans:

- Demand side management via small appliance efficiency,” *Renewable Energy*, vol. 22, no. 1, pp. 169 – 176, 2001. [Online]. Available: <http://www.sciencedirect.com/science/article/pii/S0960148100000562>
- [32] W. Wu, E. Spooner, and B. J. Chalmers, “Design of slotless torus generators with reduced voltage regulation,” *IEE Proceedings - Electric Power Applications*, vol. 142, no. 5, pp. 337–343, Sep. 1995.
- [33] Surong Huang, Jian Luo, F. Leonardi, and T. A. Lipo, “A comparison of power density for axial flux machines based on general purpose sizing equations,” *IEEE Transactions on Energy Conversion*, vol. 14, no. 2, pp. 185–192, June 1999.
- [34] A. B. Proca, A. Keyhani, A. El-Antably, Wenzhe Lu, and Min Dai, “Analytical model for permanent magnet motors with surface mounted magnets,” *IEEE Transactions on Energy Conversion*, vol. 18, no. 3, pp. 386–391, Sep. 2003.
- [35] M. Lukaniszyn and R. Wrobel, “A study on the influence of permanent magnet dimensions and stator core structures on the torque of the disc-type brushless dc motor,” *Electrical Engineering*, vol. 82, no. 3, pp. 163–171, Mar 2000. [Online]. Available: <https://doi.org/10.1007/s002020050007>
- [36] W. Tong, S. Wang, S. Dai, S. Wu, and R. Tang, “A quasi-three-dimensional magnetic equivalent circuit model of a double-sided axial flux permanent magnet machine considering local saturation,” *IEEE Transactions on Energy Conversion*, vol. 33, no. 4, pp. 2163–2173, Dec 2018.
- [37] V. Rallabandi, P. Han, M. G. Kesgin, N. Taran, and D. M. Ionel, “Axial-field vernier-type flux modulation machines for low-speed direct-drive applications,” in *2019 IEEE Energy Conversion Congress and Exposition (ECCE)*, Oct 2019.
- [38] V. Rallabandi, N. Taran, D. M. Ionel, and I. G. Boldea, “Magnus — an ultra-high specific torque pm axial flux type motor with flux focusing and modulation,” in *2017 IEEE Energy Conversion Congress and Exposition (ECCE)*, Oct 2017, pp. 1234–1239.

- [39] —, “Axial-flux pm synchronous machines with air-gap profiling and very high ratio of spoke rotor poles to stator concentrated coils,” in *2017 IEEE International Electric Machines and Drives Conference (IEMDC)*, May 2017, pp. 1–7.
- [40] N. Taran and D. M. Ionel, “A hybrid analytical and FE-based method for calculating AC eddy current winding losses taking 3D effects into account,” in *2019 IEEE Energy Conversion Congress and Exposition (ECCE)*, Oct 2019.
- [41] N. Taran, D. M. Ionel, and D. G. Dorrell, “Two-level surrogate-assisted differential evolution multi-objective optimization of electric machines using 3-d fea,” *IEEE Transactions on Magnetics*, vol. 54, no. 11, pp. 1–5, Nov 2018.
- [42] N. Taran, V. Rallabandi, G. Heins, and D. M. Ionel, “Systematically exploring the effects of pole count on the performance and cost limits of ultra-high efficiency fractional hp axial flux pm machines,” *IEEE Transactions on Industry Applications*, pp. 1–10, 2019.
- [43] N. Taran, V. Rallabandi, D. M. Ionel, P. Zhou, M. Thiele, and G. Heins, “A systematic study on the effects of dimensional and materials tolerances on permanent magnet synchronous machines based on the ieee std 1812,” *IEEE Transactions on Industry Applications*, vol. 55, no. 2, pp. 1360–1371, March 2019.
- [44] N. Taran, V. Rallabandi, G. Heins, and D. M. Ionel, “Coreless and conventional axial flux permanent magnet motors for solar cars,” *IEEE Transactions on Industry Applications*, vol. 54, no. 6, pp. 5907–5917, Nov 2018.
- [45] N. Taran, G. Heins, V. Rallaband, D. Patterson, and D. M. Ionel, “Systematic comparison of two axial flux PM machine topologies: Yokeless and segmented armature versus single sided,” in *2019 IEEE Energy Conversion Congress and Exposition (ECCE)*, Oct 2019.
- [46] N. Taran, V. Rallabandi, and D. M. Ionel, “Waved: A coreless axial flux pm motor for drive systems with constant power operation,” in *2019 IEEE Transportation Electrification Conference and Expo (ITEC)*, June 2019, pp. 1–6.

- [47] N. Taran, V. Rallabandi, D. M. Ionel, G. Heins, D. Patterson, and P. Zhou, “Design optimization of electric machines with 3d fea and a new hybrid doede numerical algorithm,” in *2019 IEEE International Electric Machines Drives Conference (IEMDC)*, May 2019, pp. 603–608.
- [48] N. Taran, V. Rallabandi, D. M. Ionel, G. Heins, and D. Patterson, “A comparative study of methods for calculating ac winding losses in permanent magnet machines,” in *2019 IEEE International Electric Machines Drives Conference (IEMDC)*, May 2019, pp. 2265–2271.
- [49] N. Taran, G. Heins, V. Rallabandi, D. Patterson, and D. M. Ionel, “Torque production capability of axial flux machines with single and double rotor configurations,” in *2018 IEEE Energy Conversion Congress and Exposition (ECCE)*, Sep. 2018, pp. 7336–7341.
- [50] N. Taran, V. Rallabandi, G. Heins, and D. M. Ionel, “Exploring the efficiency and cost limits of fractional hp axial flux pm machine designs,” in *2018 IEEE Energy Conversion Congress and Exposition (ECCE)*, Sep. 2018, pp. 3272–3277.
- [51] N. Taran, V. Rallabandi, D. M. Ionel, and G. Heins, “A comparative study of coreless and conventional axial flux permanent magnet synchronous machines for low and high speed operation,” in *2017 IEEE Energy Conversion Congress and Exposition (ECCE)*, Oct 2017, pp. 321–327.
- [52] N. Taran, V. Rallabandi, G. Heins, and D. M. Ionel, “A comparative study of conventional and coreless axial flux permanent magnet synchronous motors for solar cars,” in *2017 IEEE International Electric Machines and Drives Conference (IEMDC)*, May 2017, pp. 1–7.
- [53] N. Taran, V. Rallabandi, D. M. Ionel, and P. Zhou, “On the effect of design tolerances on the performance of synchronous pm machines evaluated according to the ieee std 1812,” in *2017 IEEE International Electric Machines and Drives Conference (IEMDC)*, May 2017, pp. 1–7.

- [54] L. J. Wu and Z. Q. Zhu, "Simplified analytical model and investigation of open-circuit ac winding loss of permanent-magnet machines," *IEEE Transactions on Industrial Electronics*, vol. 61, no. 9, pp. 4990–4999, Sept 2014.
- [55] P. Ponomarev, I. Petrov, J. Pyrhonen, and N. Bianchi, "Additional losses in stator slot windings of permanent magnet synchronous machines," 2015, doi:[10.13140/RG.2.1.2081.9368](https://doi.org/10.13140/RG.2.1.2081.9368).
- [56] A. Al-Timimy, P. Giangrande, M. Degano, M. Galea, and C. Gerada, "Investigation of ac copper and iron losses in high-speed high-power density PMSM," in *2018 XIII International Conference on Electrical Machines (ICEM)*, Sept 2018, pp. 263–269.
- [57] C. R. Sullivan, "Computationally efficient winding loss calculation with multiple windings, arbitrary waveforms, and two-dimensional or three-dimensional field geometry," *IEEE Transactions on Power Electronics*, vol. 16, no. 1, pp. 142–150, Jan 2001.
- [58] P. B. Reddy, T. M. Jahns, and T. P. Bohn, "Modeling and analysis of proximity losses in high-speed surface permanent magnet machines with concentrated windings," in *2010 IEEE Energy Conversion Congress and Exposition*, Sep. 2010, pp. 996–1003.
- [59] L. J. Wu, Z. Q. Zhu, D. Staton, M. Popescu, and D. Hawkins, "Analytical model of eddy current loss in windings of permanent-magnet machines accounting for load," *IEEE Transactions on Magnetics*, vol. 48, no. 7, pp. 2138–2151, July 2012.
- [60] P. Mellor, R. Wrobel, D. Salt, and A. Griffio, "Experimental and analytical determination of proximity losses in a high-speed pm machine," in *2013 IEEE Energy Conversion Congress and Exposition*, Sep. 2013, pp. 3504–3511.
- [61] D. C. Hanselman and W. H. Peake, "Eddy-current effects in slot-bound conductors," *IEE Proceedings - Electric Power Applications*, vol. 142, no. 2, pp. 131–136, March 1995.

- [62] P. Zhang, G. Y. Sizov, J. He, D. M. Ionel, and N. A. O. Demerdash, “Calculation of magnet losses in concentrated-winding permanent-magnet synchronous machines using a computationally efficient finite-element method,” *IEEE Transactions on Industry Applications*, vol. 49, no. 6, pp. 2524–2532, Nov 2013.
- [63] M. R. Shah and A. M. EL-Refaie, “Eddy-current loss minimization in conducting sleeves of surface pm machine rotors with fractional-slot concentrated armature windings by optimal axial segmentation and copper cladding,” *IEEE Transactions on Industry Applications*, vol. 45, no. 2, pp. 720–728, March 2009.
- [64] P. H. Mellor, R. Wrobel, and N. McNeill, “Investigation of proximity losses in a high speed brushless permanent magnet motor,” in *Conference Record of the 2006 IEEE Industry Applications Conference Forty-First IAS Annual Meeting*, vol. 3, Oct 2006, pp. 1514–1518.
- [65] M. Popescu and D. G. Dorrell, “Proximity losses in the windings of high speed brushless permanent magnet ac motors with single tooth windings and parallel paths,” *IEEE Transactions on Magnetism*, vol. 49, no. 7, pp. 3913–3916, July 2013.
- [66] D. A. Gonzalez and D. M. Saban, “Study of the copper losses in a high-speed permanent-magnet machine with form-wound windings,” *IEEE Transactions on Industrial Electronics*, vol. 61, no. 6, pp. 3038–3045, June 2014.
- [67] I. Petrov, M. Polikarpova, P. Ponomarev, P. Lindh, and J. Pyrhönen, “Investigation of additional ac losses in tooth-coil winding pmsm with high electrical frequency,” in *2016 XXII International Conference on Electrical Machines (ICEM)*, Sept 2016, pp. 1841–1846.
- [68] N. Aliyu, G. Atkinson, N. Stannard, and M. Kimiabeigi, “Assessment of AC copper loss in permanent magnet axial flux machine with soft magnetic composite core,” in *2018 IX International Conference on Power Electronics Machines and Drives (PEMD)*, Apr 2018.

- [69] A. Fatemi, D. M. Ionel, N. Demerdash, D. A. Staton, R. Wrobel, and Y. C. Chong, “Computationally efficient strand eddy current loss calculation in electric machines,” *IEEE Transactions on Industry Applications*, pp. 1–1, 2019.
- [70] G. Volpe, M. Popescu, F. Marignetti, and J. Goss, “Modelling ac winding losses in a pmsm with high frequency and torque density,” in *2018 IEEE Energy Conversion Congress and Exposition (ECCE)*, Sept 2018, pp. 2300–2305.
- [71] O. A. Mohammed and S. Ganu, “FE-circuit coupled model of electric machines for simulation and evaluation of EMI issues in motor drives,” *IEEE Transactions on Magnetics*, vol. 46, no. 8, pp. 3389–3392, Aug 2010.
- [72] R. L. Russell and K. H. Norsworthy, “Eddy currents and wall losses in screened-rotor induction motors,” *Proceedings of the IEE - Part A: Power Engineering*, vol. 105, no. 20, pp. 163–175, April 1958.
- [73] J. R. Hendershot and T. J. E. Miller, *Design of brushless permanent-magnet motors / J.R. Hendershot, Jr., T.J.E. Miller*. Magna Physics Pub. ; Clarendon Press Hillsboro, OH : Oxford, 1994.
- [74] R.-J. Wang and M. J. Kamper, “Calculation of eddy current loss in axial field permanent-magnet machine with coreless stator,” *IEEE Transactions on Energy Conversion*, vol. 19, no. 3, pp. 532–538, Sep. 2004.
- [75] D. J. Patterson, J. L. Colton, B. Mularcik, B. J. Kennedy, S. Camilleri, and R. Rohoza, “A comparison of radial and axial flux structures in electrical machines,” in *2009 IEEE International Electric Machines and Drives Conference*, May 2009, pp. 1029–1035.
- [76] A. G. Jack, B. C. Mecrow, G. Nord, and P. G. Dickinson, “Axial flux motors using compacted insulated iron powder and laminations - design and test results,” in *IEEE International Conference on Electric Machines and Drives, 2005.*, May 2005, pp. 378–385.

- [77] D. Patterson and R. Spee, "The design and development of an axial flux permanent magnet brushless dc motor for wheel drive in a solar powered vehicle," *IEEE Transactions on Industry Applications*, vol. 31, no. 5, pp. 1054–1061, Sep 1995.
- [78] A. Joss and P. J. Randewijk, "Design and optimisation of an ironless double-rotor radial flux permanent magnet machine," in *2016 XXII International Conference on Electrical Machines (ICEM)*, Sept 2016, pp. 1473–1479.
- [79] A. Daghigh, H. Javadi, and H. Torkaman, "Design optimization of direct-coupled ironless axial flux permanent magnet synchronous wind generator with low cost and high annual energy yield," *IEEE Transactions on Magnetics*, vol. 52, no. 9, pp. 1–11, Sept 2016.
- [80] R.-J. Wang, M. J. Kamper, K. V. der Westhuizen, and J. F. Gieras, "Optimal design of a coreless stator axial flux permanent-magnet generator," *IEEE Transactions on Magnetics*, vol. 41, no. 1, pp. 55–64, Jan 2005.
- [81] C. Schumann, T. Müller, E. Stein, and M. Pacas, "Axial-flux-machine with an ironless fractional slot winding," in *IECON 2014 - 40th Annual Conference of the IEEE Industrial Electronics Society*, Oct 2014, pp. 424–430.
- [82] K. Latoufis, K. Troullaki, T. Pazios, and N. Hatziargyriou, "Design of axial flux permanent magnet generators using various magnetic materials in locally manufactured small wind turbines," in *2016 XXII International Conference on Electrical Machines (ICEM)*, Sept 2016, pp. 1545–1551.
- [83] M. Chirca, S. Breban, C. A. Oprea, and M. M. Radulescu, "Analysis of innovative design variations for double-sided coreless-stator axial-flux permanent-magnet generators in micro-wind power applications," in *2014 International Conference on Electrical Machines (ICEM)*, Sept 2014, pp. 385–389.
- [84] H. C. Lovatt, V. S. Ramsden, and B. C. Mecrow, "Design of an in-wheel motor for a solar-powered electric vehicle," in *1997 Eighth International Conference on Electrical Machines and Drives (Conf. Publ. No. 444)*, Sep 1997, pp. 234–238.

- [85] S. De, M. Rajne, S. Poosapati, C. Patel, and K. Gopakumar, “Low-inductance axial flux bldc motor drive for more electric aircraft,” *IET Power Electronics*, vol. 5, no. 1, pp. 124–133, January 2012.
- [86] N. Taran, V. Rallabandi, G. Heins, and D. M. Ionel, “Coreless and conventional axial flux permanent magnet motors for solar cars,” *IEEE Transactions on Industry Applications*, vol. 54, no. 6, pp. 5907–5917, Nov 2018.
- [87] N. Chayopitak and D. G. Taylor, “Performance assessment of air-core linear permanent-magnet synchronous motors,” *IEEE Transactions on Magnetics*, vol. 44, no. 10, pp. 2310–2316, Oct 2008.
- [88] D. Montgomery, *Design and analysis of experiments*. Wiley, 1997. [Online]. Available: <https://books.google.com/books?id=ehvvAAAAMAAJ>
- [89] M. Rosu, P. Zhou, D. Lin, D. M. Ionel, M. Popescu, F. Blaabjerg, V. Rallabandi, and D. Staton, *Automated Optimization for Electric Machines*. IEEE, 2018. [Online]. Available: <https://ieeexplore-ieee-org.ezproxy.uky.edu/document/8233742>
- [90] NuGen Mobility Inc., “SCM150-XXX axial flux, brushless pm motor specifications,” 2007.
- [91] R. J. Hill-Cottingham, P. C. Coles, J. F. Eastham, F. Profumo, A. Tenconi, G. Gianolio, and M. Cerchio, “Plastic structure multi-disc axial flux pm motor,” in *Conference Record of the 2002 IEEE Industry Applications Conference. 37th IAS Annual Meeting (Cat. No.02CH37344)*, vol. 2, Oct 2002, pp. 1274–1280 vol.2.
- [92] F. Profumo, A. Tenconi, M. Cerchio, J. F. Eastham, and P. C. Coles, “Axial flux plastic multi-disc brushless pm motors: performance assessment,” in *Applied Power Electronics Conference and Exposition, 2004. APEC '04. Nineteenth Annual IEEE*, vol. 2, 2004, pp. 1117–1123 vol.2.

- [93] M. J. Kamper, R. J. Wang, and F. G. Rossouw, "Analysis and performance of axial flux permanent-magnet machine with air-cored nonoverlapping concentrated stator windings," *IEEE Transactions on Industry Applications*, vol. 44, no. 5, pp. 1495–1504, Sept 2008.
- [94] B. Xia, J. X. Shen, P. C. K. Luk, and W. Fei, "Comparative study of air-cored axial-flux permanent-magnet machines with different stator winding configurations," *IEEE Transactions on Industrial Electronics*, vol. 62, no. 2, pp. 846–856, Feb 2015.
- [95] A. Mohammadpour, A. Gandhi, and L. Parsa, "Winding factor calculation for analysis of back emf waveform in air-core permanent magnet linear synchronous motors," *IET Electric Power Applications*, vol. 6, no. 5, pp. 253–259, May 2012.
- [96] S. G. Min and B. Sarlioglu, "Analytical calculation of back emf waveform for linear pm motors in slotted and slotless structures," *IEEE Transactions on Magnetics*, vol. 53, no. 12, pp. 1–10, Dec 2017.
- [97] N. Chayopitak and D. G. Taylor, "Performance assessment of air-core linear permanent-magnet synchronous motors," *IEEE Transactions on Magnetics*, vol. 44, no. 10, pp. 2310–2316, Oct 2008.
- [98] V. Rallabandi, N. Taran, and D. M. Ionel, "Multilayer concentrated windings for axial flux pm machines," *IEEE Transactions on Magnetics*, vol. 53, no. 6, pp. 1–4, June 2017.
- [99] C. R. Sullivan, "Computationally efficient winding loss calculation with multiple windings, arbitrary waveforms, and two-dimensional or three-dimensional field geometry," *IEEE Transactions on Power Electronics*, vol. 16, no. 1, pp. 142–150, Jan 2001.
- [100] D. N. Mbidi, K. van der Westhuizen, R. Wang, M. J. Kamper, and J. Blom, "Mechanical design considerations of a double stage axial-flux pm machine," in

Conference Record of the 2000 IEEE Industry Applications Conference. Thirty-Fifth IAS Annual Meeting and World Conference on Industrial Applications of Electrical Energy (Cat. No.00CH37129), vol. 1, 2000, pp. 198–201 vol.1.

- [101] Axial flux surface mount motor kit for solar vehicle applications, application notes. [Online]. Available: <http://lati-solar-car.wikispaces.com/file/view/Application+Notes+-+Surface+Mount+Kit+Motor+-+Augst+2011.pdf>
- [102] V. Rallabandi, N. Taran, D. M. Ionel, and J. F. Eastham, “On the feasibility of carbon nanotube windings for electrical machines case study for a coreless axial flux motor,” in *2016 IEEE Energy Conversion Congress and Exposition (ECCE)*, Sept 2016, pp. 1–7.
- [103] D. Lawhorn, N. Taran, V. Rallabandi, and D. M. Ionel, “A comparative study of constant power operation techniques for low inductance machines,” in *2018 IEEE Transportation Electrification Conference and Expo (ITEC)*, June 2018, pp. 638–643.
- [104] “IEEE trial-use guide for testing permanent magnet machines,” *IEEE Std 1812-2014*, pp. 1–56, Feb 2015.
- [105] A. Fatemi, D. M. Ionel, M. Popescu, and N. A. O. Demerdash, “Design optimization of spoke-type pm motors for formula e racing cars,” in *2016 IEEE Energy Conversion Congress and Exposition (ECCE)*, 2016.
- [106] A. Fatemi, D. M. Ionel, M. Popescu, Y. C. Chong, and N. Demerdash, “Design optimization of a high torque density spoke-type PM motor for a race drive cycle,” *IEEE Transactions on Industry Applications*, pp. 1–1, 2018.
- [107] R. Storn and K. Price, “Differential evolution – a simple and efficient heuristic for global optimization over continuous spaces,” *Journal of Global Optimization*, vol. 11, no. 4, pp. 341–359, Dec 1997. [Online]. Available: <https://doi.org/10.1023/A:1008202821328>

- [108] K. Price, R. Storn, and J. Lampinen, *Differential Evolution: A Practical Approach to Global Optimization*, ser. Natural Computing Series. Springer, 2005.
- [109] Y. Duan and D. M. Ionel, “Nonlinear scaling rules for brushless pm synchronous machines based on optimal design studies for a wide range of power ratings,” *IEEE Transactions on Industry Applications*, vol. 50, no. 2, pp. 1044–1052, March 2014.
- [110] D. M. Rosu, D. P. Zhou, D. D. Lin, D. D. M. Ionel, D. M. Popescu, D. F. Blaabjerg, D. V. Rallabandi, and D. D. Staton, *Multiphysics Simulation by Design for Electrical Machines, Power Electronics and Drives*. Wiley-IEEE Press, 2017.
- [111] C. E. Rasmussen and C. K. I. Williams, *Gaussian Processes for Machine Learning*. MIT Press, 2006.
- [112] G. Matheron, “Principles of geostatistics,” *Economic Geology*, vol. 58, no. 8, p. 1246, 1963. [Online]. Available: [+http://dx.doi.org/10.2113/gsecongeo.58.8.1246](http://dx.doi.org/10.2113/gsecongeo.58.8.1246)
- [113] L. Lebensztajn, C. A. R. Marretto, M. C. Costa, and J. L. Coulomb, “Kriging: a useful tool for electromagnetic device optimization,” *IEEE Transactions on Magnetics*, vol. 40, no. 2, pp. 1196–1199, March 2004.
- [114] F. Bittner and I. Hahn, “Kriging-assisted multi-objective particle swarm optimization of permanent magnet synchronous machine for hybrid and electric cars,” in *2013 International Electric Machines Drives Conference*, May 2013, pp. 15–22.
- [115] J. C. Yu and Suprayitno, “Evolutionary reliable regional kriging surrogate and soft outer array for robust engineering optimization,” *IEEE Access*, vol. 5, pp. 16 520–16 531, 2017.

- [116] B. Xia, Z. Ren, K. Choi, and C. S. Koh, “A novel subregion-based multidimensional optimization of electromagnetic devices assisted by kriging surrogate model,” *IEEE Transactions on Magnetics*, vol. 53, no. 6, pp. 1–4, June 2017.
- [117] J. P. C. Kleijnen, “Design and analysis of simulation experiments.” Springer Publishing Company, Incorporated, 2007, ch. 5, pp. 139–156.
- [118] T. W. Simpson, T. M. Mauery, J. J. Korte, and F. Mistree, “Kriging models for global approximation in simulation-based multidisciplinary design optimization,” *AIAA Journal*, vol. 39, no. 12, pp. 2233–2241, 2001.
- [119] M. Schmidt and H. Lipson, “Distilling free-form natural laws from experimental data,” *Science (New York, N.Y.)*, vol. 324, no. 5923, April 2009.
- [120] Eureka, the AI powered modeling engine. [Online]. Available: <https://www.nutonian.com/products/eureka/>
- [121] J. Eason and S. Cremaschi, “Adaptive sequential sampling for surrogate model generation with artificial neural networks,” *Computers and Chemical Engineering*, vol. 68, pp. 220–232, 2014. [Online]. Available: <http://www.sciencedirect.com/science/article/pii/S0098135414001719>
- [122] K. Deb, L. Thiele, M. Laumanns, and E. Zitzler, “Scalable multi-objective optimization test problems,” in *Evolutionary Computation, 2002. CEC '02. Proceedings of the 2002 Congress on*, vol. 1, May 2002, pp. 825–830.
- [123] N. Taran, V. Rallabandi, D. M. Ionel, and G. Heins, “A comparative study of coreless and conventional axial flux permanent magnet synchronous machines for low and high speed operation,” in *2017 IEEE Energy Conversion Congress and Exposition (ECCE)*, Oct 2017, pp. 321–327.
- [124] M. Rosu, P. Zhou, D. Lin, D. M. Ionel, M. Popescu, F. Blaabjerg, V. Rallabandi, and D. Staton, *Multiphysics Simulation by Design for Electrical Machines, Power Electronics and Drives*. Wiley-IEEE Press, 2017.

- [125] S. Santoso and H. W. Beaty, *Standard Handbook For Electrical Engineers, Seventeenth Edition*. McGraw Hill, 2018, pp. 919–960.
- [126] N. Bianchi, S. Bolognani, M. D. Pre, and G. Grezzani, “Design considerations for fractional-slot winding configurations of synchronous machines,” *IEEE Transactions on Industry Applications*, vol. 42, no. 4, pp. 997–1006, July 2006.
- [127] N. Taran, V. Rallabandi, G. Heins, and D. M. Ionel, “Coreless and conventional axial flux permanent magnet motors for solar cars,” *IEEE Transactions on Industry Applications*, vol. 54, no. 6, pp. 5907–5917, Nov 2018.
- [128] J. Cros and P. Viarouge, “Synthesis of high performance PM motors with concentrated windings,” *IEEE Transactions on Energy Conversion*, vol. 17, no. 2, pp. 248–253, Jun 2002.
- [129] D. Ishak, Z. Q. Zhu, and D. Howe, “Permanent-magnet brushless machines with unequal tooth widths and similar slot and pole numbers,” *IEEE Transactions on Industry Applications*, vol. 41, no. 2, pp. 584–590, March 2005.
- [130] K. F. Konecny, “Compact three-phase permanent magnet rotary machine having low vibration and high performance,” U.S. Patent 4 774 428A, May 15, 1987.
- [131] T. Katsuma and M. Kitoh, “Brushless motor having permanent magnet rotor and salient pole stator,” U.S. Patent 4 719 378A, 23, 1984.
- [132] K. Wang, Z. Q. Zhu, and G. Ombach, “Synthesis of high performance fractional-slot permanent-magnet machines with coil-pitch of two slot-pitches,” *IEEE Transactions on Energy Conversion*, vol. 29, no. 3, pp. 758–770, Sept 2014.
- [133] K. Ahsanullah, R. Dutta, and M. F. Rahman, “Analysis of low-speed IPMMs with distributed and fractional slot concentrated windings for wind energy applications,” *IEEE Transactions on Magnetics*, vol. 53, no. 11, pp. 1–10, Nov 2017.

- [134] C. Tang, W. L. Soong, G. S. Liew, and N. Ertugrul, “Effect of pole and slot number changes on the performance of a surface PM machine,” in *2012 XXth International Conference on Electrical Machines*, Sept 2012, pp. 220–227.
- [135] Y. S. Chen, Z. Q. Zhu, and D. Howe, “Vibration of PM brushless machines having a fractional number of slots per pole,” *IEEE Transactions on Magnetics*, vol. 42, no. 10, pp. 3395–3397, Oct 2006.
- [136] C. C. Mi, G. R. Slemon, and R. Bonert, “Minimization of iron losses of permanent magnet synchronous machines,” *IEEE Transactions on Energy Conversion*, vol. 20, no. 1, pp. 121–127, March 2005.
- [137] S. M. Castano, J. W. Jiang, B. Bilgin, A. Sathyan, H. Dadkhah, and A. Emadi, “An investigation of slot-pole combinations for interior permanent magnet synchronous machines with different magnet topologies,” in *2017 IEEE International Electric Machines and Drives Conference (IEMDC)*, May 2017, pp. 1–8.
- [138] Y. Liu, Z. Zhu, C. Gan, S. Brockway, and C. Hilton, “Comparison of optimal slot/pole number combinations in fractional slot permanent magnet synchronous machines having similar slot and pole numbers,” in *International Conference on Power Electronics, Machines and Drives (PEMD)*, Apr. 2018.
- [139] Y. Duan and D. M. Ionel, “Nonlinear scaling rules for brushless PM synchronous machines based on optimal design studies for a wide range of power ratings,” *IEEE Transactions on Industry Applications*, vol. 50, no. 2, pp. 1044–1052, March 2014.
- [140] A. Fatemi, D. M. Ionel, N. A. O. Demerdash, and T. W. Nehl, “Optimal design of IPM motors with different cooling systems and winding configurations,” *IEEE Transactions on Industry Applications*, vol. 52, no. 4, pp. 3041–3049, July 2016.
- [141] C. A. C. Coello, G. B. Lamont, D. A. Van Veldhuizen *et al.*, *Evolutionary algorithms for solving multi-objective problems*. Springer, 2007, vol. 5.

- [142] Y. Duan and D. M. Ionel, “A review of recent developments in electrical machine design optimization methods with a permanent magnet synchronous motor benchmark study,” in *2011 IEEE Energy Conversion Congress and Exposition*, November 2011.
- [143] V. Veerappa and E. Letier, “Understanding clusters of optimal solutions in multi-objective decision problems,” in *2011 IEEE 19th International Requirements Engineering Conference*, Aug 2011, pp. 89–98.
- [144] A. Gaspar Cunha, J. C. Ferreira, J. A. Covas, and G. Recio, “Selection of solutions in multi-objective optimization: Decision making and robustness,” in *2014 IEEE Symposium on Computational Intelligence in Multi-Criteria Decision-Making (MCDM)*, Dec 2014, pp. 16–23.
- [145] E. Zitzler and L. Thiele, “Multiobjective evolutionary algorithms: a comparative case study and the strength pareto approach,” *IEEE Transactions on Evolutionary Computation*, vol. 3, no. 4, pp. 257–271, Nov 1999.
- [146] K. Deb, “Multi-objective optimization using evolutionary algorithms: An introduction,” *KanGAL Report Number 2011003*, pp. 1–24, Feb 2011.
- [147] O. Augusto, B. Fouad, and S. Caro, “A New Method for Decision Making in Multi-Objective Optimization Problems,” *Pesquisa Operacional*, vol. 32, no. 3, pp. 331–369, Dec. 2012. [Online]. Available: <https://hal.archives-ouvertes.fr/hal-00914025>
- [148] P. D. Evans and J. F. Eastham, “Disc geometry homopolar synchronous machine,” *IEE Proceedings*, vol. 127, no. 5, Sept 1980.
- [149] E. Spooner and B. J. Chalmers, “Torus: A slotless, toroidal-stator, permanent-magnet generator,” *IEE Proceedings*, vol. 139, no. 6, Nov 1992.
- [150] P. Sergeant, H. Vansompel, and L. Dupre, “Performance and implementation

- issues considering the use of thin laminated steel sheets in segmented armature axial-flux pm machines,” in *2014 International Conference on Electrical Machines (ICEM)*, Sept 2014, pp. 1363–1369.
- [151] W. Fei, P. C. K. Luk, and K. Jinupun, “A new axial flux permanent magnet segmented-armature-torus machine for in-wheel direct drive applications,” in *2008 IEEE Power Electronics Specialists Conference*, June 2008, pp. 2197–2202.
- [152] B. Zhang, T. Seidler, R. Dierken, and M. Doppelbauer, “Development of a yokeless and segmented armature axial flux machine,” *IEEE Transactions on Industrial Electronics*, vol. 63, no. 4, pp. 2062–2071, April 2016.
- [153] A. D. Gerlando, G. M. Foglia, M. F. Iacchetti, and R. Perini, “Parasitic currents in stray paths of some topologies of yasa afpm machines: Trend with machine size,” *IEEE Transactions on Industrial Electronics*, vol. 63, no. 5, pp. 2746–2756, May 2016.
- [154] B. Zhang, T. Epskamp, M. Doppelbauer, and M. Gregor, “A comparison of the transverse, axial and radial flux pm synchronous motors for electric vehicle,” in *2014 IEEE International Electric Vehicle Conference (IEVC)*, Dec 2014, pp. 1–6.
- [155] N. J. Stannard, J. G. Washington, and G. J. Atkinson, “A comparison of axial field topologies employing smc for traction applications,” in *2016 19th International Conference on Electrical Machines and Systems (ICEMS)*, Nov 2016, pp. 1–6.
- [156] D. M. Ionel, M. J. Balchin, J. F. Eastham, and E. Demeter, “Finite element analysis of brushless dc motors for flux weakening operation,” *IEEE Transactions on Magnetics*, vol. 32, no. 5, pp. 5040–5042, Sep 1996.

Vita

Narges Taran, PhD Candidate

Department of Electrical and Computer Engineering, University of Kentucky

Narges Taran is a Ph.D. candidate in the SPARK Laboratory, Electrical and Computer Engineering Department, University of Kentucky. She started her studies at UK in 2016 after receiving her M.S. degree in Power Electronics and Electrical Machines from K. N. Toosi University of Technology, Tehran, Iran, in 2014. She has published more than 25 papers, including one that received a Best Paper Award at IEEE ECCE 2016, the largest joint technical conference of the Power Electronics and Industry Applications Societies. She has also co-authored two chapters of the latest edition of the widely circulated Standard Handbook for Electrical Engineers published in 2018 by McGraw Hill. At the UK ECE Graduate Research Symposium in 2018, Narges received the award for Outstanding Graduate Poster and in April 2019, she received the UK College of Engineering Dean's award for Outstanding PhD Student. Since joining UK, she has been working as a research assistant on projects sponsored by NSF and industrial companies, and as a summer intern for Borg Warner, Inc. Her current research focuses on electric machines and power electronic drives including new topologies and materials, electromagnetic field finite-element analysis, and large-scale optimization methods.